Fabrication and High Speed Optoelectronic Characterization of Semiconductor Devices

Ivair Gontijo, B. Sc., M. Sc.

A thesis submitted to the Faculty of Engineering of the
University of Glasgow
for the degree of

Doctor of Philosophy

April 1992

ProQuest LLC.
789 East Eisenhower Parkway
P.O. Box 1346
Ann Arbor, MI 48106 – 1346

For Possi.

Acknowledgements

The financial help from CNPq - Conselho Nacional de Desenvolvimento Científico e Tecnológico is gratefully acknowledged.

I thank all members of the Academic and Technical staff of the Department of Electronics & Electrical Engineering of Glasgow University who contributed directly or indirectly for the completion of this work.

I thank my wife for her help and understanding.

Table of contents

List of Figures

List of Tables

Summary

This work is an investigation on the use of high speed optoelectronic techniques for the characterization of semiconductor devices. A low-frequency electrooptic probe station was demonstrated as well as the optoelectronic sampling scheme. The optoelectronic sampling technique relies on fast photoconductive switches for its operation. The autocorrelation signal detected in optoelectronic sampling was compared with signal detection by conventional techniques employing a sampling oscilloscope and a network analyser.

The optoelectronic techniques described in this work depend critically on short-pulse lasers for the measurement of high speed devices. A fibre-grating pulse compressor was set-up to shorten the 120 ps pulses produced by a mode-locked Nd:YAG laser. Compression by a factor of 40 was demonstrated and nearly transform limited pulses of 3 ps duration were obtained. However, the output of the pulse compressor is very noisy and the output power is not high enough to enable electrooptic sampling experiments, in a jitter-free scheme. The same Nd:YAG laser was frequency doubled and used to synchronously pump a rhodamine 6G dye laser. Autocorrelation measurements obtained with the dye laser are again, very noisy and with poor reproducibility. The noise problems with the pulse compressor and with the dye laser were traced back to the Nd:YAG pump laser. It is concluded that this laser should be avoided as the source of short pulses for the electrooptic and optoelectronic measurement techniques. The use of a feedback loop is likely to reduce the noise in this laser, but drift in the intensity in a long time scale would still be present.

A mode-locked Ti:Sapphire laser was also used for measurements in this project. Autocorrelation measurements taken with this laser are totally reproducible and contain little or no noise.

The devices measured in this project were made by a combination of electron-beam lithography and photolithography. The use of these two lithography techniques together was made possible by the design of a mask set with alignment marks which can be used for registration in a mask aligner and in the electron beam lithography machine.

Discrete devices were made and characterized by electrical techniques. Fabrication procedures were developed for resistors, Metal-Insulator-Metal (MIM) capacitors and for the Optoelectronic Sampling Device (OSD). Discrete Mesfets were fabricated on MBE grown epilayers and their I-V characteristics were measured. A simplified optoelectronic sampling device was designed and made in a single lithographic

step. It provides a quick way of producing devices in which autocorrelation measurements can be performed to determine the carrier lifetime in the substrate material.

The optoelectronic sampling devices were made on four different substrate materials. The first one is a high purity, MBE grown GaAs epilayer, with very long lifetime (2ns). The control samples were made on "standard" semi-insulating GaAs, whose carrier lifetime is $\approx$ 200 ps. Proton implantation in some of these devices made on SI GaAs substrate was used as a means of shortening the carrier lifetime, to produce fast turn-off times in the photoconductive switches. The lifetime after implantation of 4 x 10^{14} protons/cm^2 was estimated from an optoelectronic sampling measurement, to be around 40 ps. This is still a very long lifetime for the photoconductive switches. It is thought that self-annealing of the deep electron traps, caused by the lack of temperature control in the implanter, prevented the achievement of short lifetime in the switches.

GaAs epilayers were grown by MBE at a temperature around 250°C, with a high group III to group V beam equivalent pressure. This type of growth conditions can produce an incorporation of up to 1 or 2% excess arsenic in the lattice. Upon annealing, the excess As precipitates into metallic As clusters which act as very fast recombination centres. The material grown in this work was characterized by X ray diffraction and photoluminescence at room temperature and at 4K. The carrier lifetime in photoconductive switches (simplified Optoelectronic Sampling Devices) made on these materials was measured using a sampling oscilloscope and high-frequency probes. The shortest lifetime obtained was roughly 70ps. Based on very recent results published after the completion of this work, it is suggested that the growth temperature of the MBE epilayers should be reduced to 200°C. At temperatures around or below 200°C, the low temperature GaAs epilayers can have a lifetime in the sub-picosecond regime.

Thus, optoelectronic techniques for the characterization of semiconductor devices were demonstrated in this project. Different lasers and substrate materials for device fabrication were investigated. Some more work is still needed to optimize the characteristics of the semiconductor materials used for device fabrication.

Chapter I - Introduction

1) -High speed semiconductor devices and their characterization

Over the years, the speed of semiconductor devices has been continuously increasing. As novel material structures appear and fabrication processes improve, new devices can be made, which operate at higher speeds with less noise and power consumption. This in turn has an enormous influence on establishing new technological applications for such devices. There are now advertisements showing that the front-end receiver of a satellite TV antenna includes a low noise HEMT (High Electron Mobility Transistor) for pre-amplification of very weak signals.

In order to cope with the ever increasing speed of semiconductor devices, the bandwidth of electronic instrumentation needed to measure them has also been widening. Sampling oscilloscopes can already resolve rise times of about 25 ps. Commercial network analysers can routinely measure the response of devices up to a frequency of 26.5 GHz. It is possible to push the bandwidth of network analysers up to 60 GHz and even 100 GHz, by adding external frequency multipliers, mixers and waveguide connectors to the measurement apparatus[1] . Unfortunately however, this introduces losses and reflections, specially at the very high frequencies of particular interest. Thus, the task of de-embedding the operation characteristics of the device from the retrieving response of the measurement system becomes much harder as frequencies are increased. Another point of concern is the invasiveness of the measurement probes, since they introduce shunt capacitances and series inductances. These parasitic impedances can seriously affect the accuracy of any of the present day measurement systems operating in the millimetre wave range.

The challenge posed by the new generation of devices, however, is even greater than the outstanding performance of the electronics instrumentation outlined above.

GaAs Mesfets fabricated in this department[2] and elsewhere[3] have demonstrated cut-off frequencies Fmax (extrapolated) above 110 GHz. Pseudomorphic InGaAs/AlGaAs MODFETs have an extrapolated F_{max} of nearly 200 GHz[4], obtained from a power gain versus bandwidth plot. In addition, photoconductive switches with sub-picosecond response times have recently been demonstrated[5].

In order to characterize this type of device fully, new measurement techniques are required. Fortunately the generation of ultra-short laser pulses has undergone an astonishing improvement over the last decade. Laser pulses as short as 8 fs have already been generated[6] with the wavelength in the near infrared. Such pulses contain only four optical cycles.

1.1) - Electrical Characterization techniques

Some of the most common instruments for the electric characterization of semiconductor devices have already been mentioned above, namely, spectrum and network analysers and sampling oscilloscopes. These instruments do not have a wide enough bandwidth or short enough time resolution for the characterization of state-of-the-art devices. Another limitation of this type of instrument is their inability to test the internal nodes of IC's. The connection between these instruments and an IC is made via probes which are large compared to most of the internal components of an IC. Therefore, only input/output measurements at the pads are possible.

Another way of measuring voltage in an IC is to analyse secondary electron emission[7,8]. A voltage contrast SEM based on this concept, was developed to measure voltage logic levels in Silicon chips, by researchers at Siemens, in Germany[7]. The electron beam in a SEM is focussed onto the device to be tested, which is biased to its operating conditions. The e-beam produces strong secondary electron emission from the device metallization. If the particular metal part of the device which is being tested is at ground or negative electrical potential, the secondary electrons will have enough energy to escape from the device and reach the secondary electron detector. The detector is located behind an energy analyser, which is held at a certain potential. The parts of the device under test which are at a positive potential produce secondary electrons having lower energies, thus decreasing the number of electrons which are detected. The number of detected electrons is thus inversely proportional to the voltage present on the metal line which is being probed.

Because of the small voltages present in IC's, the detected signal is usually very weak and must be time averaged to improve the signal-to-noise ratio. To increase the time resolution, the voltage levels are sampled by electron beam pulses.The technique

has a bandwidth of about 2 GHz (or 220 ps time resolution)[7]. The voltage sensitivity is around 10 mV and the spatial resolution is determined by the electron-beam spot size to about 20 nm. There is a trade-off between spatial resolution and sensitivity. The smaller the spot size, the lower the e-beam current is, which reduces the sensitivity.

The time resolution is also connected to the sensitivity through the gating of the SEM cathode. When the e-beam pulses are shortened to increase the time resolution, the average current decreases, worsening the instrument sensitivity. In general, the time resolution is of the order of hundreds of picoseconds for detectable average electron beam currents. This technique has been improved by using a photocathode triggered by an intense picosecond laser pulse which produces high average current pulses[9]. This promises a time resolution below 10 ps, but the main problems with this technique remain, which are its high cost and complexity. Another reason for concern is that the technique is somewhat invasive due to charging effects of the device under test.

1.2) - Optoelectronic Techniques

Much research has been carried out to use short-pulse lasers for the characterization of electronic devices. The laser beams can interact with semiconductor devices in a wide variety of ways.

Perhaps, the two most used techniques are electrooptic and optoelectronic sampling, using photoconductive switches. These two techniques will be thoroughly described in the next chapter. Both of them were demonstrated in this work and their use will also be reported in chapter II. The main aim of this introduction is to present a general overview of the optoelectronic techniques that have been developed for measurement of silicon, InP and GaAs devices.

In the case of Silicon devices, the electrooptic effect cannot be used to provide the interaction between light and the electrical signals. As silicon is a centrosymmetric crystal, it does not exhibit an electrooptic effect. Other methods of making light and electric signals to interact are therefore required for silicon devices. It is well known that free carriers in an active device perturb the index of refraction and the absorption coefficient in the device. Free carrier absorption is negligible in the near infrared wavelength region but the small perturbations in the index of refraction change the optical path length for the light wave, producing measurable phase modulation. A specially designed phase contrast Nomarski interferometer can detect the phase modulation. Such an instrument was employed by Heinrich[10] in the measurement of integrated circuits in silicon. In that apparatus, a laser beam from a cw 1.3μm YAG laser passes through a polarizing beam splitter and a Nomarski prism where it splits into a

probe and reference beam. These beams enter through the back of the Si device under test. The reflected probe beam (that contains the phase modulation) and the reference beam interfere before detection by a photodiode. It can be shown that the free carrier density is proportional to the phase modulation[10].

This charge detection system was first demonstrated in silicon. The charge stored in a large area (0.5mm x 0.5mm) abrupt p-n junction diode was detected at zero and forward bias. The minimum detectable signal at forward bias is 51 $\mu V/\sqrt{Hz}$, for 1 mA of photocurrent. A 0.8V , 1MHz signal superimposed on the dc bias was also successfully recovered in single shot, real time measurements. Signals of up to 100 MHz have subsequently been detected in Si bipolar junction transistors. For this measurement a 20 mW, cw, 1.3 μm Nd:YAG laser was employed.

The charge sensing scheme has been extended to measure charge density and voltage in GaAs devices, by Kolner et al[11]. The polarization of the incoming laser beam has to be adjusted to cancel out the electrooptic effect present in GaAs. Frequencies up to 20 MHz were detected in this experiment.

That is a promising technique, specially for Si and other non-electrooptic materials. Continuous wave (cw) lasers have been used so far. To improve the bandwidth of the technique, laser pulses must be used, with some signal averaging technique. This poses a great challenge to the charge sensing scheme, because of the inherent jitter between the laser pulses and the signal to be measured. The synchronization of microwave synthesizers and pulsed mode-locked lasers will have to be greatly improved to make this technique a viable option for testing high speed devices.

In conclusion, various alternative measurement techniques for semiconductor devices have been tried over the years. Many of them were demonstrated to work at least at low frequencies, up to 100 MHz. In order to cope with the ever increasing speed of the devices, much work is needed to improve the characterization techniques. Electrooptic and optoelectronic sampling seem to be the most promising ones. They will be discussed in chapter II.

1.3) - Aims of this project

This project is an investigation on the fabrication and testing, by optoelectronic techniques, of semiconductor devices. The final aims are to produce an optoelectronic integrated circuit, to implement electrooptic and optoelectronic sampling and to use these techniques to measure the optoelectronic devices.

Because of the interdisciplinary nature of the project, three main areas of activity were pursued:

A - Design and fabrication of the devices:

Both photolithography and electron beam lithography were used in fabrication. Optical masks were designed and manufactured for the "large" device features. Electron beam lithography was used to define the high resolution features, such as the gates of the Mesfets. The aim of the fabrication process is to produce the optoelectronic integrated circuit containing 4 photoconductors, 4 capacitors, 2 resistors, coplanar waveguide transmission lines (CPW) for the interconnections and a short gate length Mesfet. Process control devices are also included in the optical masks for the evaluation of the material quality and fabrication figures of merit.

B - Theoretical and experimental studies on the production of short laser pulses, both in the visible and in the near infrared.

C - Implementation of electrooptic and optoelectronic sampling schemes to investigate the advantages and disadvantages of these techniques in the characterization of high speed semiconductor devices.

- Measurements of the above devices using the optoelectronic techniques. The results thus obtained should be compared with conventional measurements done with sampling oscilloscopes and a network analyser.

1.4) - Overview of the thesis

Electrooptic and optoelectronic sampling will be described in chapter II. Theoretical and practical aspects of these two techniques will be considered and a low-frequency electrooptic probing station will be demonstrated.

One of the key points in any optoelectronic scheme is the laser source employed. In chapter III, the use of various laser sources and the associated techniques for generation of picosecond laser pulses will be investigated.

Chapter IV deals with the modelling of coplanar waveguide (CPW) optoelectronic circuits. A model for electrical pulse propagation will be presented. Ultra fast photoconductors used for generation of short electric pulses will also be investigated.

Details of design and fabrication of the CPW optoelectronic sampling device (OSD) are reported in chapter V, as well as fabrication procedures for the individual devices which make up the OSD.

The devices were tested both electrically and optoelectronically. The results are presented in chapters V and VI.

In Chapter VII one finds a review of a growth procedure, electrical and optical characterization of GaAs epilayers grown by MBE at low temperatures. This material has been found to exhibit very short carrier lifetime, which makes it attractive for the fabrication of photoconductive switches. Growth and characterization of these epilayers are also reported in chapter VII, as well as measurements of devices made onto them.

The conclusions to be drawn from the present work and suggestions for further improvements of the sampling techniques can be found in chapter VIII.

1.5) - References

1 - A 60 GHz network analyser is currently in operation at Duisburg University (Germany). This apparatus has been used by our group for some measurements of Mesfets.

2 - J. A. Adams, "*Fabrication and scaling effects of very short gate-length GaAs Mesfets*", PhD thesis, Glasgow University, April, 1990.

3 - H. Q. Tserng and B. Kim, "110 GHz GaAs FET oscillator", Electronics Letters, Vol. 21, 178-179, 1985.

4 - T. Henderson, M. I. Aksun, et. al., "Microwave performance of a quarter-micrometer gate low-noise pseudomorphic InGaAs/AlGaAs modulation-doped field effect transistor", IEEE Electron Devices Letters, Vol. EDL-7, 649-651, 1986.

5 - P. M. Downey, "Subpicosecond response times from ion bombarded InP photoconductive switches", in Topical Meeting of Picosecond Optoelectronics, Technical Digest, March 1985, paper ThAG-1 , Springer-Verlag, NY, 1985.

6 - W. H. Knox, R. L. Fork, et. al., "Optical pulse compression to 8 fs at a 5 KHz rate", Applied Physics Letters, Vol. 46, 1120-1121, 1985.

7 - "Electron beam testing of VLSI chips gets practical", Electronics, 51-54, March 24, 1986.

8 - R. Iscoff,"E-beam probing systems: filling the submicron gap", Semiconductor Int., 62-68, September 1985.

9 - P. May, J. M. Halbout et. al."Laser pulsed e-beam system for high speed IC testing", in *Picosecond Electronics and Optoelectronics*, NY, Springer-Verlag, 1987.

10 - H. K. Heinrich, D. M. Bloom and B. R. Hemenway, "Noninvasive sheet charge density probe for integrated silicon devices", Applied Physics Letters, 48, (16), 1066, 1986.

11 - U. Keller, S. K. Diamond, B. A. Auld, and D. M. Bloom, "Noninvasive sheet charge density probe for integrated silicon devices", Applied Physics Letters, 53(5), 388,1988.

Chapter II - Electrooptic and Optoelectronic Sampling

2.1) - Electrooptic Effect in GaAs

The electrooptic effect is the change in the index of refraction of a non-centrosymmetric crystal, caused by and proportional to an applied electric field. This effect can be exploited as a way of modulating light beams by electric fields. This leads to useful light modulators in a large variety of crystals, including GaAs[1,2].

GaAs does not possess inversion symmetry and thus exhibits the linear electrooptic effect. It has the same crystal structure as zincblende, i.e., it belongs to the $4\bar{3}m$ group and its electrooptic tensor is very simple and given by:[3]

$$T = \begin{pmatrix} 0 & 0 & 0 \\ 0 & 0 & 0 \\ 0 & 0 & 0 \\ r_{41} & 0 & 0 \\ 0 & r_{41} & 0 \\ 0 & 0 & r_{41} \end{pmatrix} \qquad (2.01)$$

The coefficient r_{41} is, in general, a function of the wavelength of the input light. Values of r_{41} for four wavelengths, together with the respective refractive indices are quoted below, from ref.4, unless otherwise stated.

Table 2.1 - The electrooptic coefficient for GaAs for four different wavelengths.

λ	r_{41}	n_0
(μm)	(10^{-12} m/V)	-
0.9	1.1	3.60
1.06	1.4	3.60 *
1.15	1.43	3.43
3.39	1.24	3.3

* - From ref. 7

The electrooptic effect can be conveniently described by the index ellipsoid, which for zincblende, takes the form:[3]

$$\frac{x^2}{n_0^2} + \frac{y^2}{n_0^2} + \frac{z^2}{n_0^2} + 2r_{41}(yzE_x + xzE_y + xyE_z) = 1 \qquad (2.02)$$

Where n_0 is the zero field refractive index, r_{41} is the electrooptic coefficient and $E_{x,y,z}$ are the components of the applied electric field. The X,Y and Z directions in eq.(2.02) correspond to the <100> directions of the cubic Bravais lattice of GaAs.

The intersection of the index ellipsoid with the plane containing the origin and perpendicular to the propagation direction defines an ellipse whose major and minor axes give the two new refractive indices and the two eigenvector polarization directions.[5]

For light propagating in the X direction, the ellipse equation is obtained by substituting x = 0 into the previous equation. The resulting ellipse equation can be transformed to its principal coordinate system by diagonalizing its associated 2 x 2 matrix M, which is given by $M_{11} = M_{22} = n_0^{-2}$ and $M_{21} = M_{12} = r_{41}.E_x$. The eigenvalues and eigenvectors of this matrix (and of the electrooptic effect) give the new refractive indices and the directions of the axes of the ellipse:

$$\begin{aligned} Y = Z \quad (Y') \qquad & n_{y'} = n_0 + \frac{1}{2} n_0^3 r_{41} E_x \\ Y = -Z \quad (Z') \qquad & n_{z'} = n_0 - \frac{1}{2} n_0^3 r_{41} E_x \end{aligned} \qquad (2.03)$$

Fig. (2.1) below shows the old (XYZ) and new (X'Y'Z') coordinate systems and the <100> directions of the Bravais lattice for GaAs.

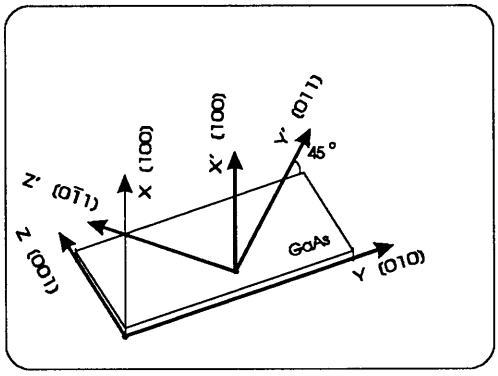

(2.1) - The principal axes and the "electrooptic effect coordinate system" for GaAs.

A light beam propagating through such an anisotropic medium will suffer a phase shift between the two orthogonal polarizations Y' and Z', given by:

$$\Delta\phi = k_0 \Delta n\, t = \frac{2\pi}{\lambda_0} n_0^3 r_{41} E_x t = \frac{2\pi}{\lambda_0} n_0^3 r_{41} V \qquad (2.04)$$

Where t is the thickness of the chip, $\Delta n = n_{y'} - n_{z'}$ and $V = E_x.t$ is the applied voltage. Therefore, if linearly or circularly polarized light enters and propagates through the crystal, its polarization state will be affected by the phase shift. For both input polarizations the output will be, in general, elliptically polarized. The phase shift is proportional to the applied voltage, according to (2.04). This can be converted into intensity modulation by passing the light through an analyser as in a Pockels cell modulator.[4]

The intensity modulated output of a Pockels cell light modulator can be written as:

$$I(v) = I_0 \sin^2\left[\frac{\Delta\phi}{2}\right] = I_0 \sin^2\left[\frac{\pi}{2}\frac{v}{v_\pi}\right] \qquad (2.05)$$

Where I_0 is the light intensity at the input of the modulator and

$$V_\pi = \frac{\lambda_0}{2 n_0^3 r_{41}} \qquad (2.06)$$

is the voltage necessary to make $\Delta\phi = \pi$ in (2.04). This is usually a very high voltage, in the Kilovolts range. For $\lambda_0 = 1.15$ μm, in GaAs, $V_\pi = 9.9$ KV.

This type of modulator is normally "optically biased" by a quarter wave plate to the $V_{\pi/2}$ point, to make the output scale linearly with the applied voltage. If the function in (2.05) is expanded in Taylor series to first order, around $V = V_{\pi/2}$, one gets:

$$I(v) = \frac{I_0}{2}\left[1 + \pi\frac{v}{v_\pi}\right] \qquad (2.07)$$

How this simple theory of the electrooptic effect can be used to design an electrooptic modulator will be shown in the next section.

2.2) - Low frequency electrooptic modulation in GaAs.

Before attempting wide bandwidth measurements with the electrooptic technique, a low frequency electrooptic probe station was set up to demonstrate the technique and assess the difficulty of signal detection and alignment of the laser beam to the device. A cw He-Ne laser operating at $\lambda = 1.15$ μm, with $\approx$ 10 mW of output power was used as the light source. A schematic diagram of the experiment is shown in fig. (2.2).

GaAs chips were patterned for this experiment with pairs of rectangular pads of 100 x 150 μm, separated by a 10 μm gap . The pads (ohmic contacts) were formed by depositing Au, Ge and Ni. A 10KHz, 10Vpp square wave was applied between the two rectangles to generate an oscillating electric field inside the GaAs chip. This signal can be recovered with the electrooptic prober by making the infrared laser beam enter through the backside of the chip, reflect off the metal of the contact pads and go back on itself, as shown in fig.(2.2). The polarizing beamsplitter and the two waveplates provide an effective way of controlling the polarization of the input and output laser beams. Fig. (2.3) shows the polarization controller.

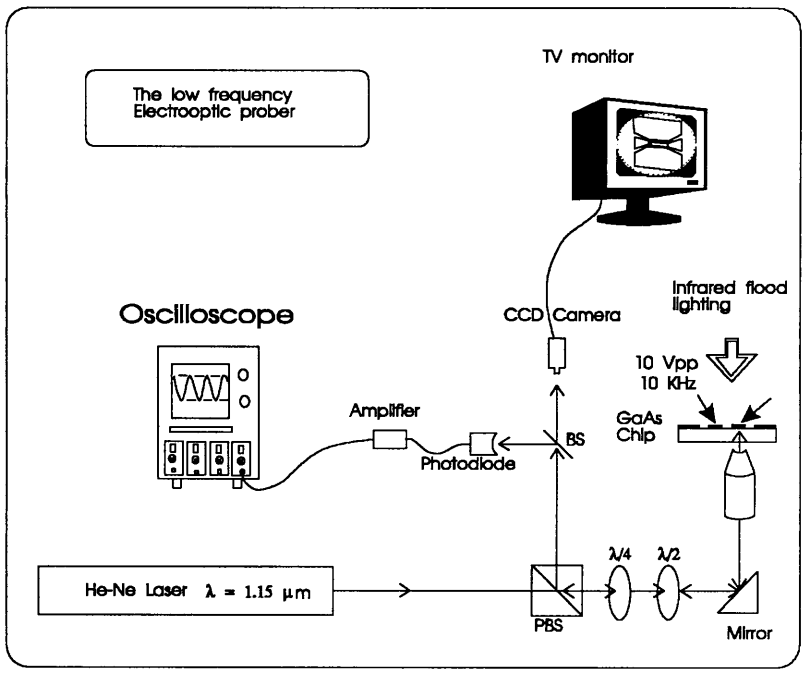

Fig.(2.2) - The Electrooptic Prober. The sample (GaAs chip) is mounted on a XYZ stage (not shown here) to allow for alignment of the device to the laser beam. The CCD camera and TV make this alignment very easy. The sample is flood lit from above with an infrared light source. GaAs is transparent to this lighting, but the metallizations deposited on the chip are not. Thus, an image of the devices and of the laser spot can be formed by the CCD camera on the TV monitor. The sample is then moved to align a particular device to the laser beam. λ\2 and λ\4 are the two waveplates. BS is a beamsplitter and PBS is a polarizing beamsplitter.

The incoming beam has its polarization adjusted so that the reflected beam, containing the modulation produced by the electric field inside the crystal, is deflected by the polarizing beam splitter (PBS), at 90° towards the CCD camera and photodiode. The best way to describe the polarization changes through all the components is by using Jones Matrix calculus[6]. The calculations are straightforward. One matrix is written for each optical component of the polarization controller. The propagation of light through each element is described by multiplying its associated matrix by the light's electric field vector. In order to maximize the electrooptic interaction inside the GaAs crystal and have the reflected beam directed (by the PBS) to the detector, the waveplates have their axes deliberately aligned at an angle to each other and to the X axis. It is then necessary to perform many rotations of the coordinate system, during the calculations, to account for these angles. That makes the calculations somewhat tedious and thus they will not be repeated here.

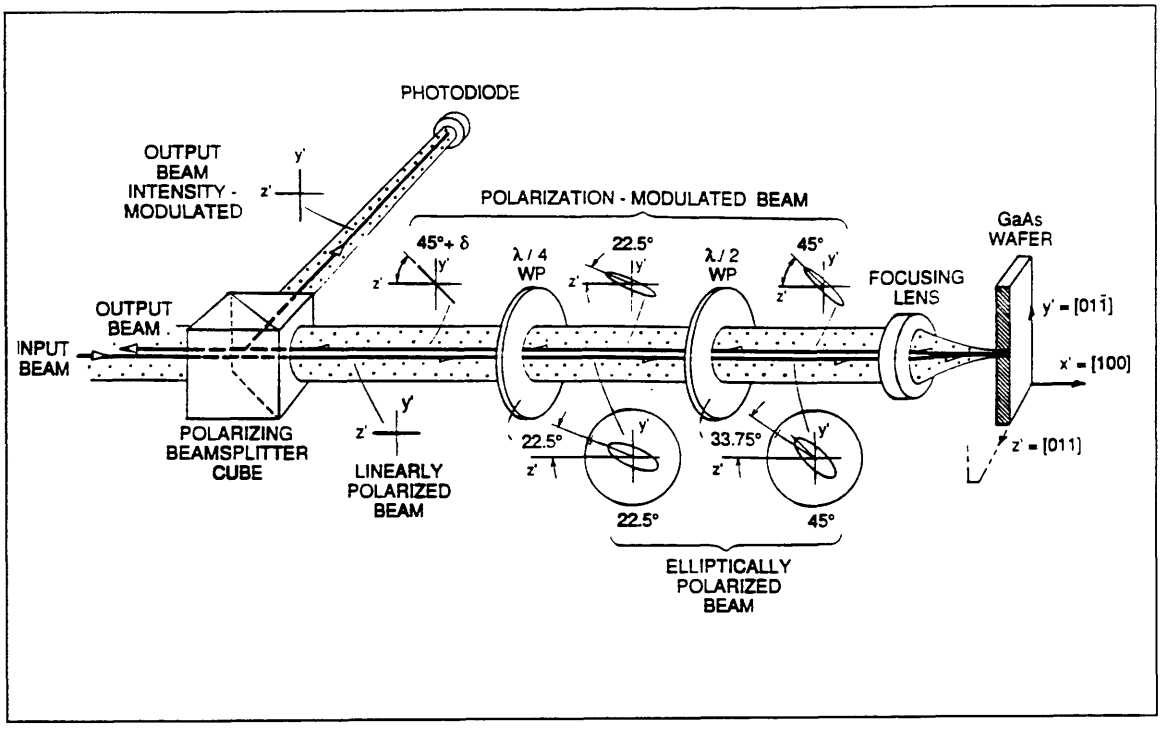

Fig.(2.3) - The polarization controller, after ref. 7. λ\2 and λ\4 are a half and a quarter wave plate. The polarization state of the light after each optical element is indicated in the diagram.

The polarization control set-up was described qualitatively by Kolner as follows.[7] The linearly polarized beam from the beamsplitter passes through a λ/4 plate aligned at 22.5° to the beamsplitter axis, producing elliptical polarization. A λ/2 plate, oriented at 33.75° to the axis of the beamsplitter, rotates the elliptical polarization by 22.5° and aligns the major axis of the ellipse to the [011] direction of the GaAs substrate. The beam is then focussed onto the chip, entering through the backside. The reflected beam comes back on itself, and passes through the lens and waveplates, where its polarization state is further changed. The laser beam after the waveplates is linearly polarized at 45° to the axis of the polarizing beamsplitter (PBS) and the polarization component at 90° is reflected onto a photodiode. The voltage probed in the GaAs chip changes the linear polarization angle at 45° by a small angle δ, through the electrooptic effect. This small change is then converted into intensity modulation of the reflected beam by the polarizing beamsplitter.

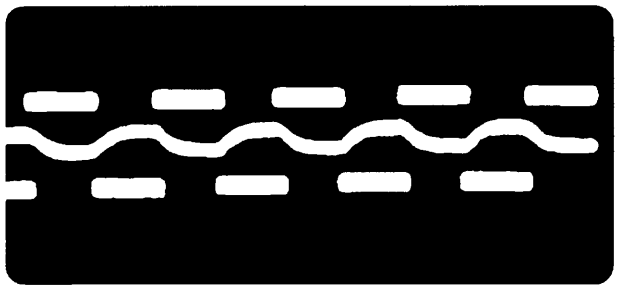

Fig.(2.4) - Oscilloscope picture of the output of the electrooptic prober. The signal produced by the photodiode was connected directly to the oscilloscope, without the amplifier depicted in fig.(2.3). The square wave was applied to the GaAs chip and successfully recovered by the electrooptic prober as shown by the other curve. The distortion of the curve is explained in the text. The frequency of the square wave is 10KHz and its amplitude is 8Vpp. The signal is 2 mVpp.

Real time measurements of the oscillating electric field *inside* the GaAs chip were obtained with this set-up. The square wave in fig.(2.4) was used as the driving signal. It was recovered by electrooptic probing in "single shot" measurements as shown by the other curve in fig. (2.4). Some harmonic distortion is evident in this curve. It is caused by the time constant associated with the 100 pF/m capacitance of the coaxial cable used and the 1 MΩ input impedance of the oscilloscope. That gives a time constant of 0.1 ms, producing a low pass filter that attenuates the harmonics of the originally square waveform.

Simple tests were carried out by varying the applied voltage and measuring the change in the amplitude of the detected signal. It was found that the signal varies linearly with v, in accordance with eq.(2.07).

2.3) - Theory of Operation of the electrooptic sampling system.

Having demonstrated the electrooptic sampling prober at low frequencies, the possibility of using it at microwave and millimetre wave frequencies will now be discussed. Obviously, the simplest approach would be to repeat the electrooptic modulation experiment, using this time, a high frequency voltage source. There are many problems with this approach. Firstly, one would be limited to a 26.5 GHz bandwidth if, for example a conventional network analyser was to be used as the rf source. It would be possible to go up to 40 GHz or more with increased cost, complexity and inaccuracy of the system. If one intends to do measurements above 100 GHz, then the generation, transmission and delivery of such wide bandwidth signals would impose severe

challenges to the apparatus. It has to be said however that the non-linear transmission lines which are being investigated at Stanford University[8,9] could improve considerably upon conventional rf signal generators. In these lines a high frequency sine wave is made to propagate through a nonlinear transmission line, which leads to electric shock wave formation. Risetimes of 3.5 ps have already been measured by electrooptic sampling. If sawtooth-like waves with very short falltimes can be generated, wide bandwidth signals could be attained. This technique could then become a good choice for the generation of wide bandwidth signals for device characterization. This is certainly a promising approach but it was not pursued in this investigation.

Another problem with the technique outlined above is that the detection of the electrooptically modulated signal would be very difficult. Assuming again a 100 GHz signal, it would be necessary to have a photodiode capable of < 5 ps time resolution. Yet, the fastest commercially available photodiodes have rise times of the order of 25 ps.

One way of modifying the system is to replace the cw laser with a mode-locked laser capable of producing ultra-short light pulses. The train of pulses could then be used in a sampling scheme, provided that the jitter between the waveform to be measured and the laser pulses can be controlled. This approach has already been tried and demonstrated to work, by Kolner et al[7] and Weingarten et. al[10]. This can be done by a phase-lock-loop. Rodwell[11] et al managed to reduce the 0.25Hz-25KHz pulse timing fluctuations of a Nd:YAG cw-mode-locked laser from 20.6 ps to less than 0.3 ps rms by an electronic phase-lock-loop. A similar system has been used in an electrooptic sampling experiment with InP integrated circuits[12].

By using a different approach, the jitter problem can be completely avoided. If a near infrared short pulse laser has part of its output frequency-doubled, two beams, one above and another below the bandgap of GaAs can be produced. The "above bandgap" beam can be used to trigger photoconductors (Auston switches[13]) to generate short electric pulses. These voltage pulses are then used to bias a device in a way analogous to the 10KHz square wave of fig.(2.4). Then, these pulses can be electrooptically sampled at the output of the device by the infrared, "below bandgap" beam produced by the laser.

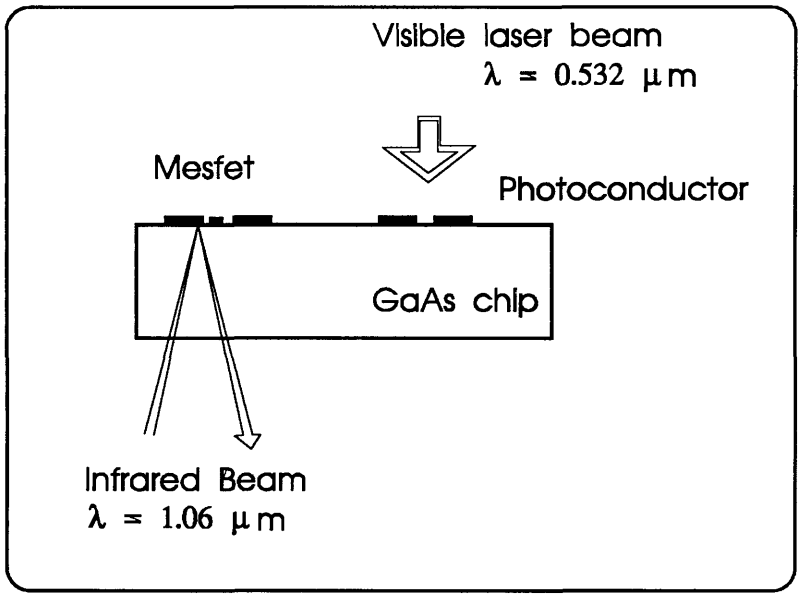

Fig.(2.5) - The jitter-free electrooptic sampling scheme.

Fig. (2.5) shows a situation where the frequency doubled beam (above the bandgap of GaAs) is used to illuminate a biased photoconductor. A short electrical pulse is produced and transferred to the gate of the FET. The electric pulse could be sampled *inside* the FET channel or at the drain side by the infrared beam through electrooptic interaction. As the two laser beams used for generation and sampling were produced by the same laser, there is no jitter between them. The generation of short laser pulses will be discussed again in chapter 3.

2.3.1) - Time resolution, voltage sensitivity and Signal-to-noise (S/N) ratio

Fig. (2. 5) shows the interaction between an electric and a laser pulse inside a Mesfet. The pulses are assumed to be rectangular in shape to make it easier to understand the sampling scheme. The laser pulse enters the device, propagating in the +Y direction. It reflects off the metallizations at the top and then goes backwards in the -Y direction. Meanwhile, an electric pulse is travelling from the gate to the drain contact. The laser beam will accumulate a polarization change proportional to its overlap with the electric pulse. This overlap is controlled by the delay τ (ps), introduced in the infrared laser beam path. The function $I_{sig}(t,\tau)$ is proportional to the output intensity of the sampling beam after being affected by the electrooptic retardation. The measured output voltage is

$$C(\tau) = \int I_{sig}(t,\tau)\, dt \qquad (2.08)$$

The integration accounts for the fact that a slow photodetector is used to collect the intensity modulated light. Normally, the photodetector is not fast enough to record the true waveform in real time t.

The electric and laser pulses are not infinitely short and thus transit times are associated with their interaction. This in principle reduces the time resolution of the electrooptic technique. Kolner analysed the resolution limitations by studying each transit time separately. His scheme will be outline here and modified to apply to the longitudinal sampling geometry of interaction in a Mesfet.

A - Optical transit time effect (OTT)

It takes a small but finite time interval for the optical sampling pulse to propagate upwards, reflect at the top metallizations and turn back on itself. During this time the electric pulse is also propagating, i.e., moving away, down the coplanar waveguide (CPW). Hence, the sampling beam does not probe a fixed point of the electrical waveform. It, in fact, measures an average of the electric pulse amplitude over that short time interval. By assuming that the electrical waveform is a propagating rectangular impulse function and that the optical beam diameter is negligible, this averaging effect can be estimated. The sampling optical pulse would experience uniform retardation during the interaction with the electric pulse and zero retardation otherwise. That results in a rectangular impulse response for the sampling system. The FWHM of this impulse response and the -3 dB bandwidth was calculated by Kolner:[7]

$$\Delta\tau_{OTT} = \frac{2\,n\,L}{c} \qquad \upsilon_{-3dBOTT} = 0.441\,\frac{c}{2\,n\,L} \qquad (2.09)$$

where

$\Delta\tau_{OTT}$ is the FWHM of the optical transit time effect.

n is the refractive index of the substrate.

L is the depth of the FET channel or, more generally, the depth of penetration of the electric field to be sampled.

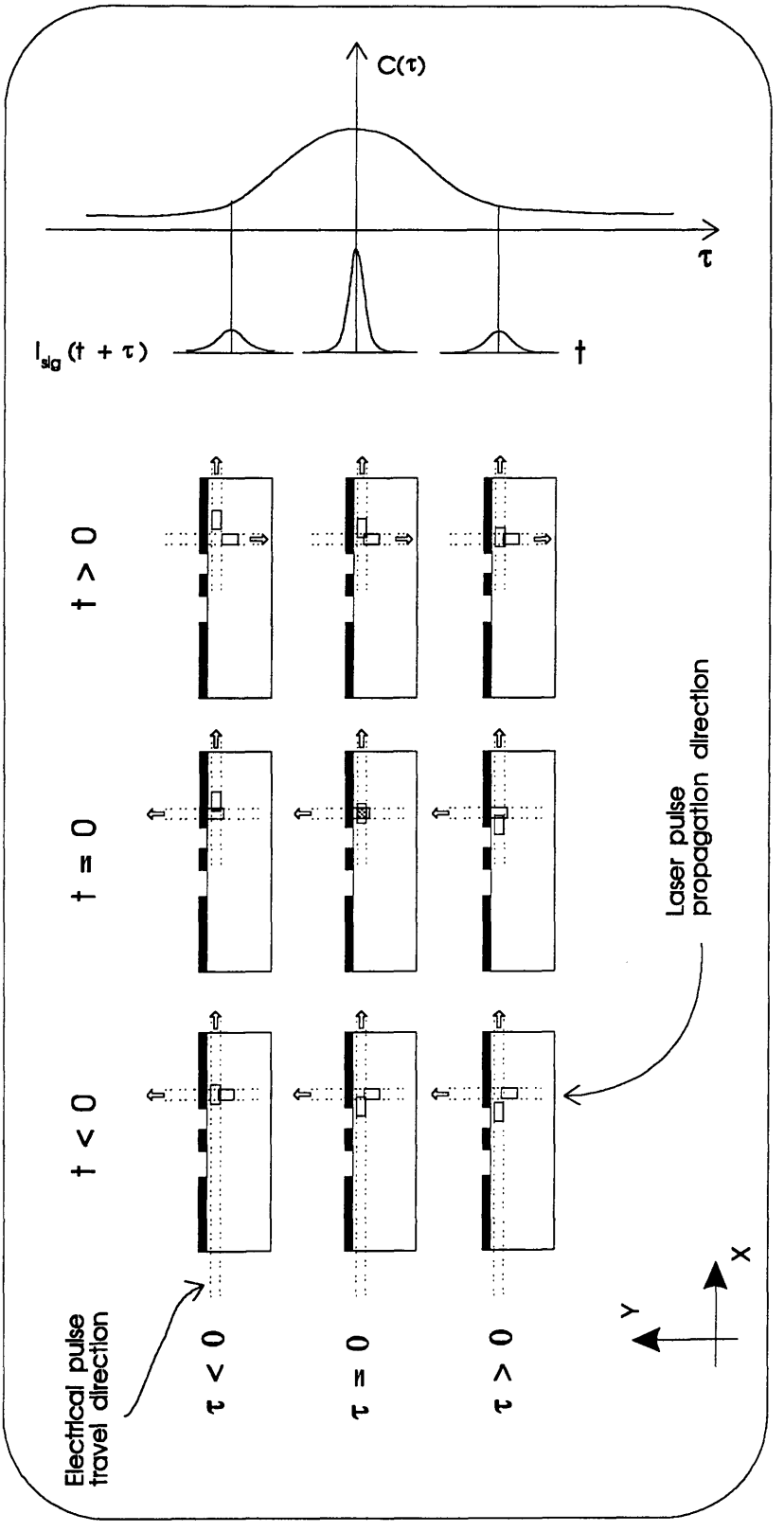

Fig.(2.6) - The electrooptic interaction of the electrical and optical pulses inside the channel of a Mesfet. The intensity of the modulated light, $I_{sig}(t,\tau)$ depends on the overlap between the fields. For $\tau = 0$, the overlap is maximum. The measured signal is $C(\tau)$, which is equal to $I_{sig}(t,\tau)$ integrated over a certain time interval Δt.

B - Electrical Transit Time Effect (ETT).

Another degradation of the impulse response occurs because the electrical pulse has to propagate across the laser beam spot, which does not have a constant intensity. Assuming now that the electrical pulse is a delta function and that the radial intensity distribution of the sampling beam is a lowest order gaussian mode, one obtains[7]:

$$\Delta\tau_{ETT} = \frac{\omega}{c}\sqrt{2\ln(2)\,\varepsilon_{eff}}$$

$$\text{and } \upsilon_{-3dBETT} = \frac{c}{\pi\omega}\sqrt{\left[\frac{\ln 2}{\varepsilon_{eff}}\right]} \qquad (2.10)$$

where
$\Delta\tau_{ETT}$ is the electrical transit time
ω is the gaussian beam radius
ε_{eff} is the effective dielectric constant of the coplanar waveguide, to be defined in the next chapter
c is the speed of light in vacuum

C - Optical pulsewidth Limit (OPW)

So far, the optical sampling pulses have been considered to be delta functions in time. To account for their time duration, the other field will be assumed to have infinitesimal spatial and temporal extents. If the optical sampling beam is taken to have a gaussian time profile, with a FWHM pulsewidth τ_o, then the impulse response broadening is given by:[7]

$$U(\tau) = \exp[-4\ln 2\,(\tau/\tau_o)^2] \qquad (2.11)$$

and

$$\upsilon_{-3dBOPW} = \frac{0.441}{\tau_o}$$

The time duration of the sampling pulse is the "time window" through which the electric field measurement is made. The wider it is, the lower the time resolution of the electrooptic prober.

Using equations (2.09) through (2.11), the time resolution for a particular circuit measurement can be calculated. Suppose a Mesfet is being probed and consider the following experimental parameters:

$n = 3.5$	(refractive index of GaAs)
$L = 1\ \mu m$	(channel depth - penetration of E field)
$\varepsilon_{eff} \cong 7$	(effective dielectric constant)
$\omega = 2\ \mu m$	(laser beam radius)
$\tau_o = 5$ ps	(laser beam pulsewidth)

then

$\delta\tau_{OTT} = 23$ fs $\qquad \upsilon_{-3dB(OTT)} = 19$ THz

$\delta\tau_{ETT} = 21$ fs $\qquad \upsilon_{-3dB(ETT)} = 15$ THz

$\tau_o = 5$ ps $\qquad \upsilon_{-3dB(OPW)} = 100$ GHz

The laser pulsewidth is by far, the dominant factor in the time resolution degradation. This is usually the case in most experimental arrangements.

Minimum Detectable Voltage

The minimum detectable voltage is the voltage that, through the electrooptic effect, would produce a signal in the receiver equal to the sum of all noise contributions. Johnson noise and shot noise are always present and in electrooptic probing there is also noise due to the laser. Since these noise components are uncorrelated, the total mean noise power is the sum of the individual mean noise power contributions. The total noise current can be written in terms of the individual noise current spectral densities as:[7]

$$\overline{i_{TN}^2} = \overline{i_{SN}^2} + \overline{i_{JN}^2} + \overline{i_{LN}^2} \qquad (2.12)$$

where

$\overline{i_{TN}^2}$ = Total Noise current squared and averaged

$\overline{i_{SN}^2} = 2\,e\,i_{av}$ A^2/Hz (Shot Noise)

$\overline{i_{JN}^2} = \frac{4\,K_B\,T}{R_L}$ A^2/Hz (Johnson Noise)

$\overline{i_{LN}^2}$ = Laser Noise A^2/Hz

i_{av} = average photodiode current
K_B = Boltzman constant
e = electronic charge
R_L = photodiode load resistor.

If the laser noise can be reduced to a negligible level by signal processing, then a simple expression for the signal to noise ratio (S/N) results. Following this procedure, Kolner[7] obtained an expression for S/N, from which the minimum detectable voltage V_{min} is obtained on equating S/N = 1:

$$V_{min} = 4\frac{V_\pi}{\pi}\sqrt{\left[\frac{e}{i_{av}}\right]} \qquad V/\sqrt{Hz} \qquad (2.13)$$

If the average current generated in the photodiode which detects the intensity modulated light is, say, 1 mA for a detection bandwidth of 1 Hz, then

$$V_{min} = 161\ \mu V/\sqrt{Hz}$$

The electrooptic prober is therefore an instrument capable of unprecedented wide bandwidth, very high time resolution and high sensitivity measurements. The main concern when using this technique is the performance of the probe laser. If short, stable and relatively high power laser pulses cannot be obtained, a serious degradation in detection efficiency will occur, which can eventually make the technique unworkable.

2.4) - Optoelectronic Sampling

2.4.1) - Historical Background

This technique relies on picosecond optoelectronic switching in semiconductors. The physical basis of this type of measurement is the change of the semiconductor into a "quasi-metallic" condition by a very short and intense light pulse.

This is by no means a new concept in semiconductor Physics. Haynes and Schockley used in 1951, light pulses to measure carrier drift mobility and lifetime in germanium.[14] In silicon, picosecond optoelectronic switching was first demonstrated by Auston[15] and co-workers.[16] By 1977, GaAs chips were being used as optical switching elements in high power lines.[17] Voltages up to 0.6 KV were switched across a GaAs slab in those experiments. Silicon was also used in high power optoelectronic switching by LeFur and Auston.[18] Electrical pulses of 1.5 KV were switched into and propagated down their transmission lines. Since then, Ge, Si, SOS, InP and GaAs have been used in a wide variety of high speed picosecond photoconductive applications.

Johnson and Auston[16] used picosecond laser pulses to switch a microwave signal into transmission lines made on silicon. Shortly after fast electrical pulses were generated and detected, they were used to study real devices. One of the earliest examples of this was the switching of a resonant tunnelling diode, triggered by a picosecond photoconductor, and its measurement using electrooptic sampling. The switching characteristics of GaAs FET logic gates were studied by optically induced logic level switching.[19] Laser pulses of 80 fs duration were used in a "sliding contact" technique to short a charged coplanar transmission line and generate subpicosecond electric pulses.[20,21] Very recently, a new integrated structure was proposed and demonstrated by C. Rauscher for time domain reflectometry with GaAs substrates.[22]

This work is primarily concerned with the measurement of GaAs Mesfets by time-domain reflectometry using picosecond photoconductors. Many different experiments have already been tried elsewhere, some as early as 1981. All of them have at least one feature in common: The device to be measured is bonded to another (or a pair of) device(s) containing photoconductors and transmission lines. The photoconductors are triggered by picosecond laser pulses and the electrical pulses generated are transmitted to the device under test, through bonding wires. This was the approach taken by Smith and Auston[23] in 1981 and is still the one used ten years later by Matloubian et al[24] in their 100 GHz bandwidth measurements. Despite the success of such measurements, the hybrid nature of the circuitry poses limitations to the accuracy and speed of the sampling scheme employed. Much more accurate measurements would result if the losses and reflections introduced by bond wires could be avoided. The task of integrating the measurement

circuit and the device to be tested onto a single chip has proved to be difficult. Some steps towards this integration will be reported later, in chapter V.

2.4.2) - Theory of Scattering Parameter measurements by Optoelectronic Sampling

High speed Mesfets are normally characterized by measuring the four scattering parameters (or S-parameters) of the device. In such measurements, an automatic network analyser is used and the device is considered to have two ports, namely the gate and drain. Fig.(2.7) shows schematically a two-port network and its associated scattering parameters.

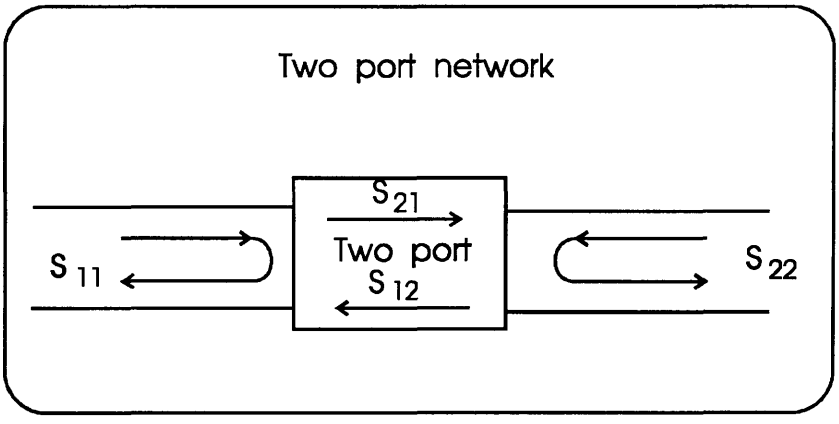

Fig.(2.7) - Schematic representation of a two-port network with its associated scattering parameters.

The scattering parameters for a two port network are defined in terms of the following variables:

$$a_1 = V_{i1}/\sqrt{Z_o} \qquad b_1 = V_{r1}/\sqrt{Z_o}$$

$$a_2 = V_{i2}/\sqrt{Z_o} \qquad b_2 = V_{r2}/\sqrt{Z_o}$$

The V_{iN} and V_{rN} are the voltages incident or reflected at ports 1 and 2. Z_o is the characteristic impedance of the connecting transmission line. The a_N and b_N represent normalized complex voltage waves incident and reflected at the Nth port, respectively. The

square modulus of these variables has dimensions of power. Therefore, $|a_1|^2$ is the power incident on port 1 and $|b_1|^2$ is the reflected power in that same port.

The scattering parameters S_{ij} are then defined by:

$$b_1 = S_{11}.a_1 + S_{12}.a_2$$
$$b_2 = S_{21}.a_1 + S_{22}.a_2 \qquad (2.14)$$

In Optoelectronic measurements, the scattering parameters are not measured directly. The data obtained gives instead, the impulse response of the device, i. e., it is in the time domain. It is possible to convert this data into frequency domain, using a procedure first developed by Auston[25] and modified by Lee and co-workers.[26]

Fig. (2.8) is a diagram of an individual optoelectronic sampling circuit. It consists of a Mesfet in the centre, connected by coplanar waveguide transmission lines (CPW) to photoconductors and bias lines. The photoconductors are simply gaps in the metallic structure and protons were implanted in this area to reduce the carrier lifetime of electrons and holes. The fabrication of photoconductors will be thoroughly discussed later, in chapter 5. From now on, the device at the centre of the structure will be called the Device Under Test, or DUT for short. It can be either a Mesfet, a short or open circuit or a straight through connection. At both ends of the CPW there are monolithically integrated 50Ω termination resistors. The whole structure can be viewed and modelled as a two port network.

The dimensions of the device are indicated in the figure. The time of ≈ 50 ps in parenthesis near the 2.5mm distance is the time taken by an electrical waveform to travel to the centre of the device and reflect back to the photoconductor. By analogy, the 100 ps time in the figure is immediately understood.

In a typical measurement, the side-line A is biased to a constant voltage V_b. A picosecond laser pulse, whose photon energy is above the bandgap of GaAs is fired onto P_1. When the laser pulse is absorbed, a large concentration of electrons and holes is generated, creating a plasma in that region, which connects the bias line to the central conductor line. After the laser pulse, the electrons and holes recombine quickly, switching OFF the voltage transfer. Thus, a short voltage pulse is transferred to the central line and starts propagating in both directions in that line. If the carriers lifetime is sufficiently short, the electrical pulse can have a pulsewidth comparable to the laser pulsewidth. Auston[25,27] showed that this voltage pulse can be detected by firing a second laser pulse

onto P_2 (between side-line B and the central line), synchronized with the first laser pulse, to transfer a small sample of the voltage to the detection side-line. In this way, the voltage pulse in the central line is used as the bias voltage for the photoconductor 2. The modelling of photoconductors and pulse propagation in transmission lines will be discussed later, in chapter 4.

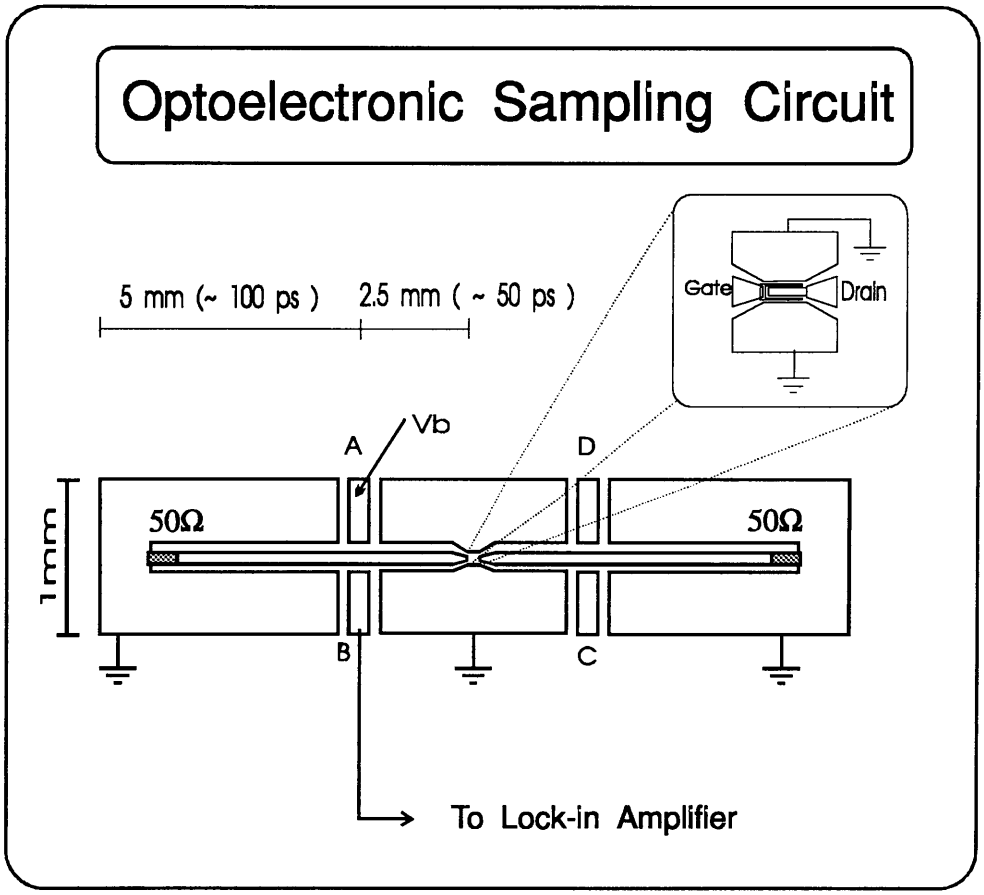

Fig.(2.8) - Schematic diagram of an integrated optoelectronic sampling circuit. The gaps between the side-lines A,B,C and D and the central lines of the device form the four photoconductors P_1 , P_2, P_3 and P_4. The inset drawing above shows the DUT (a Mesfet in this case), which is made at the centre of the sampling circuit.

For a fixed difference in arrival time between the two laser pulses, a fixed portion of the voltage waveform will be transferred to the detection line. By varying the arrival time of the second laser pulse on the sampling photoconductor P_2, the whole voltage pulse can be sampled out to the detection line. One (or both) of the laser pulses is (are) chopped by a mechanical wheel to generate a known modulation and reference

signal. The voltage sampled to the detection line is preamplified in a current amplifier and then applied to a lock-in amplifier.

Fig. (2.9) presents a diagram of the experimental set-up. The incoming laser pulses have a small sample of their intensity directed by the beamsplitter BS1 to an autocorrelator, for laser diagnostics. The main beam is split at BS2 into the two beams, which follow routes 1 and 2 and are used in the experiment. The beam reflected (route 1) by BS2 follows a path L_{a1} in air and is coupled into a single-mode optical fibre whose length is L_{f1}. The transmitted beam (route 2) is directed to a retroreflector, travelling a distance L_{a2} in air and is eventually coupled into a second piece of single-mode fibre, with length L_{f2}. For a certain position of the retroreflector mounted on a translation stage, the two pulses arrive at the *output* of the fibres at the same time. That will happen when $L_{a1} + n.L_{f1} = L_{a2} + n.L_{f2}$, or when

$$L_{a2} = L_{a1} + n.\Delta L_f$$

$\Delta L_f = L_{f1} - L_{F2}$ is the difference in fibre lengths.
n is the refractive index of the fibre core.

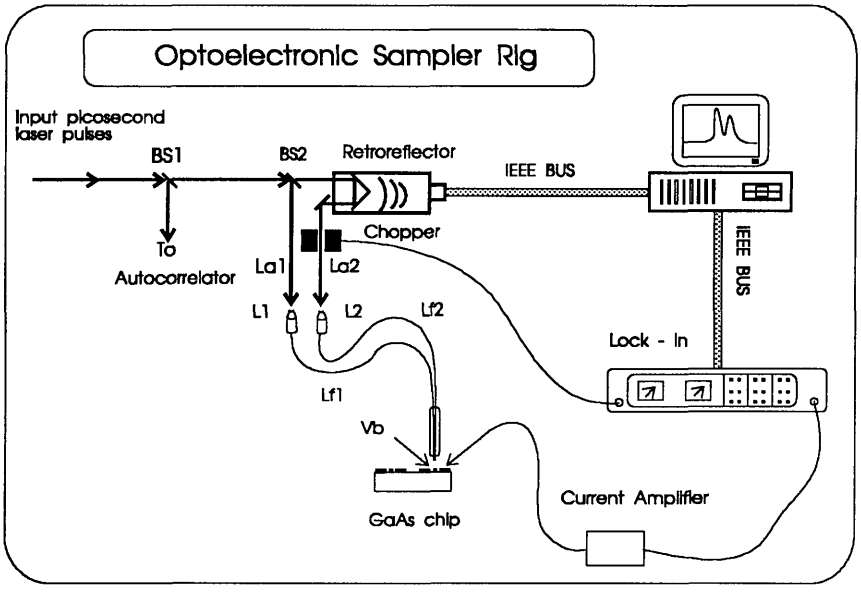

Fig.(2.9) - The optoelectronic sampling schematic diagram. The laser beam following route 1 travels a distance la_1 in air and lf_1 in the first optical fibre. The other beam goes through route 2 and travels a distance la_2 in air and lf_2 in the second fibre. BS1 and BS2 are beamsplitters and L_1 and L_2 are 10x microscope objectives. The single mode optical fibres have lengths lf_1 and lf_2.

During a measurement, the computer moves the retroreflector a certain number of steps (thus changing L_{a2} and the arrival time of the second laser beam) and then takes a measurement from the lock-in amplifier, moves the stage again and takes another measurement and so on. The data is recorded on disc in ASCII format. The mathematical analysis of the experiment now follows.

2.4.3) - Mathematical Treatment of the Optoelectronic Sampling Technique

As there are many non-equivalent definitions of Fourier transforms, Convolution and Correlation, the definitions used here are given below, according to Champeney[28]. The allowed forms of f(t) and g(t) will not be stated here as they can be found in any good book on Fourier Analysis. The time domain functions encountered in this work are all well behaved, in the sense that the definitions below can be applied to them.

Fourier Transforms:

$$F(\omega) = \frac{1}{2\pi} \int_{-\infty}^{+\infty} e^{-i\omega t} f(t)\, dt$$

$$f(t) = \int_{-\infty}^{+\infty} e^{+i\omega t} F(\omega)\, d\omega \qquad (2.15)$$

Convolution:

$$f(t) \otimes g(t) = \int_{-\infty}^{+\infty} f(\tau)\, g(t - \tau)\, d\tau \qquad (2.16)$$

Cross-correlation:

$$f(t) * g(t) = \int_{-\infty}^{+\infty} f^*(\tau)\, g(t+\tau)\, d\tau \qquad (2.17)$$

$f^*(t)$ is the complex conjugate of $f(t)$. All time domain waveforms in this work are real functions,thus we can take $f^*(t) = f(t)$.

From (2.16) and (2.17), it follows that:

$$f(-t) \otimes g(t) = f(t) * g(t) \qquad (2.18)$$

Going back now to fig.(2.8), one can consider the optoelectronic sampling device as a two port network, with photoconductors A and B as port 1 and C and D as port 2. The voltage switched across two photoconductors (say A and B) can be described by the cross-correlation between the two photoconductors:

$$g_{1i}(t) = \int_{-\infty}^{+\infty} f_A(\tau)\, f_B(t+\tau)\, d\tau \qquad (2.19)$$

where $g_{1i}(t)$ is the voltage appearing on port 1, $f_A(t)$ is the voltage pulse generated at the photoconductor A and $f_B(t)$ is the voltage pulse incident on photoconductor B.

The first subscript in function g(t) refers to the port identification and the second refers to incident (i), reflected (r) or transmitted (t) signal. It is assumed in (2.19) that only the incident signal appears on the photoconductor B. In practice this is done by choosing a time window for the sampling so that the reflected signal does not have enough time to reach port 1 before the sampling pulse is fired. Obviously this can only be done if the incident and reflected waveforms are totally resolved in time at port 1. If the photoconductors are identical, then $f_A(t) = f_B(t)$ and (2.19) represents the autocorrelation of the voltage pulses generated in the photoconductor A.

From (2.18) and (2.19), one has:

$$g_{1i}(t) = f_i(-t) \otimes f_i(t) \tag{2.20}$$

where it is assumed that $f_A(t) = f_B(t) = f_i(t)$. Taking the Fourier transform of equation (2.20) and applying the convolution theorem, one gets:

$$G_{1i}(\omega) = |F_i(\omega)|^2 \tag{2.21}$$

which is the power spectrum of the incident pulse.

The reflected time-domain waveform is obtained by choosing the sampling time window so that only the reflections from discontinuities (or from the end of the transmission line) are sampled out at port 1. In such case, one has:

$$g_{1r}(t) = f_i(-t) \otimes f_r(t) \tag{2.22}$$

Again, by taking Fourier transforms and applying the convolution theorem:

$$G_{1r}(\omega) = F_i^*(\omega) \cdot F_r(\omega) \tag{2.23}$$

$F_i^*(\omega)$ is the complex conjugate of $F_i(\omega)$.

At the photoconductor C, the voltage pulse is given by the incident pulse convolved with the impulse response h(t) of the device under test:

$$f_o(t) = h(t) \otimes f_i(t) \tag{2.24}$$

As all four photoconductive switches are identical, the sampling function of photoconductors C or D is the same as the generation and sampling functions of photoconductors A and B. This means that the sampled signal at C or D is given by the cross-correlation of $f_i(t)$ with $f_o(t)$:

$$g_{2t}(t) = f_i(-t) \otimes f_o(t) = f_i(-t) \otimes [\, h(t) \otimes f_i(t) \,] \tag{2.25}$$

and

$$G_{2i}(\omega) = |F_i(\omega)|^2 \cdot H(\omega) \tag{2.26}$$

$H(\omega)$ is the complex transfer function of the DUT

The input reflection coefficient and the forward transmission coefficient for port 1 of the device under test (DUT) are then given by:

$$S_{11}(\omega) = \frac{G_{1r}(\omega)}{G_{1i}(\omega)} \tag{2.27}$$

and

$$S_{21}(\omega) = \frac{G_{2t}(\omega)}{G_{1i}(\omega)} \tag{2.28}$$

In equations (2.27) and (2.28) above, the phase reference planes are defined at the photoconductors B and C. In order to move the reference planes to the input and output of the DUT, the propagation constant β of the coplanar waveguide has to be measured. The signals are then multiplied by a phase factor given by $e^{-j\beta\omega}$.

Now, if port 2 (photoconductive switches C and D) is used as the input port, we can immediately write, in analogy with (2.21), (2.23) and (2.26) that:

$$\begin{aligned} G_{2i}(\omega) &= |F_i(\omega)|^2 \\ G_{2r}(\omega) &= F_i^*(\omega) \cdot F_r(\omega) \\ G_{1t}(\omega) &= |F_i(\omega)|^2 \cdot J(\omega) \end{aligned} \tag{2.29}$$

The function $J(\omega)$ is, in general, different from $H(\omega)$, in (2.26). This is the case for example, of a Mesfet, where the gain of the device is built into $H(\omega)$.

The other two scattering parameters can now be written as:

$$S_{12}(\omega) = \frac{G_{1t}(\omega)}{G_{2i}(\omega)} \tag{2.30}$$

$$S_{22}(\omega) = \frac{G_{2r}(\omega)}{G_{2i}(\omega)} \tag{2.31}$$

These scattering parameter measurements depend critically on the laser used to excite the photoconductors. In the next chapter, issues regarding picosecond laser pulses generation will be investigated. The advantages and disadvantages of different laser systems will be highlighted as well as some of the experiments performed with these lasers.

2.5) - References to Chapter2

[1] - T. E. Walsh, " Gallium-Arsenide electro-optic modulators", RCA Review, 323-335, September, 1966.

[2] - A. Yariv, C. A. Mead, J. V. Parker, " 5C3 - GaAs as an electrooptic modulator at 10.6 microns", IEEE Journal of Quantum Electronics, Vol. QE-2, 243-245, 1966.

[3] - S. Namba, "Electro-optical effect of zincblende", Journal of the Optical Society of America, Vol. 51, No.1, 76-79, 1961.

[4] - A. Yariv: "*Optical Electronics*", Holt-Saunders Int. Editions, NY, chapter9, 1985.

[5] - M Born and E Wolf: "*Principles of Optics*", Chapter XIV, Sixth edition, Perganon Press, Oxford, 1980.

[6] - F. L. Pedrotti and L. S. Pedrotti: "*Introduction to Optics*", chapter 17, 337-358, Prentice-Hall International Inc., NJ, 1987.

[7] - B. H. Kolner, D. M. Bloom, "Elec trooptic sampling in GaAs integrated circuits", IEEE Journal of Quantum Electronics, Vol. QE 22 No 1, 79-93, 1986.

[8] - C. J. Madden, M. J. Rodwell, R. A. Marsland, D. M. Bloom and Y. C. Pao, "Generation of 3.5 ps Fall-time shock waves on a monolithic GaAs nonlinear transmission line", IEEE Electron Device Letters, Vol. 9, No.6, 303-305, 1988.

[9] - C. J. Madden, R. A. Marsland, J. J. Rodwell, D. M. Bloom and Y. C. Pao, "Hyperabrupt-doped GaAs nonlinear transmission line for picosecond shock-wave generation", Applied Physics Letters, Vol. 54, No. 11, 1019-1021, 1989.

[10] - K. J. Weingarten, M. J. W. Rodwell and D. Bloom, "Picosecond Optical sampling of GaAs integrated circuits", IEEE Journal of Quantum Electronics, Vol.24, No.2, 198-220, 1988.

[11] - M. J. W. Rodwell and D. M. Bloom, "Subpicosecond laser timing stabilization", IEEE Journal of Quantum Electronics, Vol.25, No.4, 817-827, 1989.

[12] - J. M. Wiesenfeld, R. S. Tucker, A. Antreasyan, C. A. Burrus and A. J. Taylor, "Electro-optic Sampling measurements of high speed InP integrated circuits", Applied Physics Letters, 50(19),1310-1312, 1987.

[13] - For a collection of papers on ultrafast optoelectronics see "*Picosecond Optoelectronic Devices*", edited by Chi H. Lee, Academic Press, Inc, Orlando, Florida, 1984.

[14] - J. R. Haynes and W. S hockley, "The mobility and life of injected holes and electrons in germanium", Physical Review, 81, 835, 1951.

[15] - D. H. Auston, "Picosecond Optoelectronic switching and gating in Silicon", Applied Physics Letters, 26, 101, 1975.

[16] - A. M. Johnson and D. H. Auston, "Microwave switching by picosecond photoconductivity" IEEE Journal of Quantum Electronics, QE11, No.6, 283-287, 1975.

[17] - Chi H. Lee, "Picosecond Optoelectronic switching in GaAs", Applied Physics Letters, Vol.30, No2, 84-86, 1977.

[18] - P. LeFur and D. H. Auston, "A kilovolt picosecond optoelectronic switch and Pockel's cell", Applied Physics Lettes, Vol.28, No.1, 21-23, 1976.

[19] - K. J. Ravinder and D. E. Snyder, "Switching characteristics of logic gates addressed by picosecond light pulses", IEEE Journal of Quantum Electronics, Vol. QE19, No4, 658-663, 1983.

[20] - M. B. Ketchen, D. Grischkowsky, T. C. Chen, C. C. Chi, I. N. Duling N. J. Halas, J. M. Halbout, J. A. Kash and G. P. Li, "Generation of subpicosecond electrical pulses on coplanar transmission lines", Applied Physics Letters, 48,(12), 751-753, 1986.

[21] - D. R. Grischkowsky, M. B. Ketchen , C. C. Chi, I. N. Duling, "Generation and detection of subpicosecond electrical pulses on coplanar transmission lines", IEEE Journal of Quantum Electronics, Vol.24, No2, 221-225, 1988.

[22] - C. Rauscher, "Optoelectronic Approach to on-chip device and circuit characterization at microwave and millimeter-wave frequencies", IEEE Transactions on Microwave Theory and Techniques, MTT vol.39, No. 7, 1179-1193, 1991.

[23] - P. R. Smith, D. H. Auston and W. M. Augustyniak, "Measurement of GaAs field-effect transistor electronic impulse response by picosecond optical electronics", Applied Physics Letters, 39 (9), 739-741, 1981.

[24] - M. Matloubian, S. E. Rosenbaum, H. R. Fetterman and P. T. Greiling, "Wide-band millimeter wave characterization of sub 0.2 micrometer gate-length AlInAs/GaInAs HEMTs", IEEE Microwave and Guided Wave Letters, Vol.1, No2, 32-34, 1991.

[25] - D. H. Auston, "Impulse response of photoconductors in transmission lines", IEEE Journal of Quantum Electronics, Vol. QE 19, 639-648, 1983.

[26] - H. A. Hung, P. Polak-Dingels, K. J. Webb, T. Smith, H. C. Huang and C. H. Lee, "Millimeter-wave monolithic integrated circuit characterization by a picosecond optoelectronic technique", IEEE Transactions on Microwave Theory and Techniques, MTT, Vol.37, No8, 1223-1230, 1989.

[27] - D. H. Auston, "Picosecond Photoconductors: physical properties and applications", in *Picosecond Optoelectronic Devices*, edited by Chi H. Lee, Academic Press, Orlando, 1984.

[28] - D. C. Champeney, " *Fourier Transforms and their Physical Applications*", Academic Press, London, 1973.

Chapter III - Laser considerations in Optical Measurements.

3.1) - An Study of Self-Phase Modulation in Single Mode Optical Fibres

3.1.1) - A simple Theory of pulse propagation

A rigourous treatment of optical pulse propagation in nonlinear and dispersive media like optical fibres involves in general the solution of the nonlinear Schrödinger equation.[1,2] This is not the approach taken here. A very simple theory to explain Self-Phase Modulation (SPM) will be presented and compared with experimental results. Group velocity dispersion *in the fibre* will be considered negligible. Group velocity dispersion *produced by a pair of diffraction gratings* on the other hand, will be thoroughly discussed later in this chapter.

Shimizu[3] studied in 1967, the frequency broadening of short pulses of a Q-switched ruby laser in a carbon disulfide liquid cell. The model proposed to explain the broadening is essentially the same still in use today for the study of frequency broadening in optical fibres. A short and sufficiently intense laser pulse can modulate its own phase in a nonlinear medium like an optical fibre through a third order nonlinearity which gives rise to the intensity dependent refractive index:

$$n(t) = n_0 + n_2.I(t) \tag{3.01}$$

where n_0 is the linear (dark) refractive index of the medium and n_2 is the nonlinear Kerr coefficient[4]. I(t) is the envelope of the laser pulse. If I(t) is a very intense and peaked function, different parts of the laser pulse (i.e., different initial intensities) will experience different refractive indices and optical path lengths in the medium. A phase shift inside the pulse will develop, given by:

$$\Delta\phi(t) = \frac{2\pi}{\lambda_0} \Delta n(t).L_{eff} \tag{3.02}$$

where λ_0 is the vacuum wavelength
$\Delta n(t) = n(t) - n_0 = n_2.I(t)$ and
L_{eff} is the effective length of the fibre, due to absorption.

$$L_{eff} = \int_0^L e^{-\alpha l}\, dl = \frac{1 - e^{-\alpha L}}{\alpha} \tag{3.03}$$

α is the linear absorption coefficient of the fibre, in [length]$^{-1}$ and L is the actual length of the fibre.

The phase shift in eq.(3.02) is changing rapidly with time, following the time changes in the intensity I(t). This translates into a frequency shift:

$$-\frac{d}{dt}\Delta\phi(t) = \Delta\omega(t) = -\frac{2\pi}{\lambda_0} \cdot L_{eff}\, n_2 \cdot \frac{d}{dt} I(t) \tag{3.04}$$

If I(t) is a gaussian pulse, then

$$I(t) = I_0\ e^{-(4\ \ln 2).(t/\tau)^2}$$

and

$$\Delta\omega(t) = 2\ (4\ \ln 2)\ \frac{t}{\tau}\ \frac{\Delta\phi_{max}}{\tau}\ e^{-(t/\tau)^2} \tag{3.05}$$

$$\Delta\phi_{max} = n_2\, k\, L_{eff}\, I_0$$

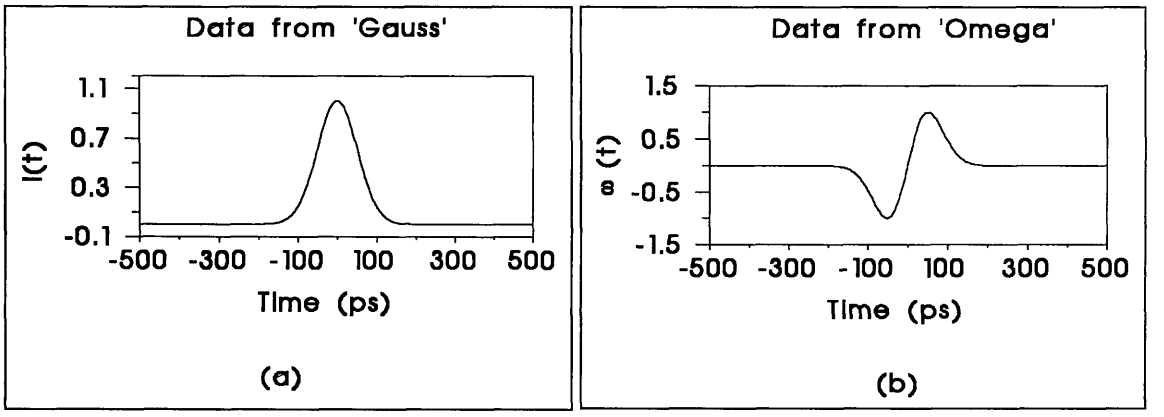

Fig.(3.1) - Effect of Self-Phase Modulation on the frequency content of a gaussian pulse. In (a) a 120 ps FWHM gaussian pulse in shown. The "instantaneous frequency" ω(t) after propagation through 150 m of optical fibre is shown in (b) as a function of time.

Fig.(3.1) shows I(t) and $\Delta\omega(t)$, the instantaneous frequency profile of the pulse. The leading edge of the pulse has its frequency downshifted while the trailing edge is upshifted.

The important concept of group velocity dispersion (GVD) will now be introduced for further reference. The second derivative of the propagation parameter β is:

$$\beta'' = \frac{d^2\beta(\omega)}{d\omega^2} = \frac{4\pi^2 c_0}{\omega^3} \cdot \frac{d^2 n(\lambda_0)}{d\lambda_0^2} = -\frac{1}{v_g^2} \cdot \frac{dv_g(\omega)}{d\omega} \qquad (3.06)$$

Dispersive optical materials are characterized by a plot of $n(\lambda_0)$ x λ_0. When $d^2n(\lambda_0)/d\lambda\omega^2$ is positive, the material is said to have a positive GVD. The negative GVD situation follows by analogy. From eq.(3.06) it is clear that negative GVD means $d^2n(\lambda_0)/d\lambda\omega^2 < 0$ and $dv_g(\omega)/d\omega > 0$.[4]

An interesting effect happens when SPM and *negative* GVD are both present, distributed along an optical fibre. Under these conditions, SPM will produce a frequency broadened pulse, with low frequencies at the leading edge of the pulse and higher frequencies at the trailing edge. Negative GVD, on the other hand, will make the higher frequencies travel faster than lower frequencies. The trailing edge, travelling faster, will catch up with the leading edge producing a very short pulse. A soliton can then be

formed by the interplay of SPM and negative GVD distributed along the fibre[2]. In such cases the fibre acts as its own pulse compressor.

For wavelengths where GVD is positive in the fibre, $dv_g(\omega)/d\omega < 0$ and the lower frequencies (leading edge) travel faster than the higher frequencies of the trailing edge. This leads to pulse spreading and a short sech (t) pulse evolves into a rectangular pulse in the fibre[2]. For the laser wavelength employed in this work GVD is positive[4], but the relatively short fibre length makes its effect negligible. This will be shown " a posteriori", by the good agreement between the SPM theory and experimental results.

3.1.2) - Experiments in Self-Phase Modulation

The spectral power density for the frequency broadened laser pulse can be calculated by a Fourier transform of I(t) with appropriate phase shifts:[5]

$$P(\omega) = \frac{1}{2\pi} \cdot \int_{-\infty}^{+\infty} I(t)^{0.5} \, . \, e^{i\Delta\phi(t)} \, . \, e^{-i(\omega - \omega_0)t} \, dt \qquad (3.07)$$

I(t) is taken as the gaussian pulse in eq.(3.04), $\Delta\phi(t)$ is given in (3.02) and $\omega_0 = 2\pi c/\lambda_0$. The peak intensity I_0 is given by:

$$I_0 = \frac{P_{peak}}{A_{eff}}$$

where P_{peak} is the peak power of the laser pulse and A_{eff} is the fibre effective area[5].

The spectral content of a gaussian pulse after propagating through a single-mode optical fibre was calculated using eq.(3.07) for a number of laser peak powers. The parameters used in such calculations are the following:

$\tau = 120$ ps
$a = 2.25$ μm (fibre core radius)
$n_2 = 3.0 \times 10^{-20}$ m²/W
$\alpha = 5$ dB/Km $= 1.15$ Km^{-1}
$L = 150$ m or $L_{eff} = 138$ m
$A_{eff} = 2.2\, A_{core}$
$\lambda_0 = 1.064$ μm
$A_{core} = \pi a^2$

The results of these calculations were found to be in quantitative agreement with experimental results. The experimental results were obtained by using a Nd:YAG laser and 150 m of single mode optical fibre. The laser is a model 416 Quantronix mode locked laser producing pulses of 120 ps at 76 MHz repetition rate. The average output power is 7W and the wavelength is 1.064 μm. The optical fibre is a non-polarization

preserving SM800 optical fibre supplied by York Technology. Its attenuation is $\alpha_{dB} = 5$ dB/Km which gives a linear attenuation coefficient of $\alpha = 1.15$ Km^{-1}. The fibre NA is 0.13 and the core diameter is 4.5 μm. For the laser wavelength and the parameters above, the V number is V = k a NA = 1.70, so a single mode is propagated. The laser beam was coupled into the fibre using a 10x microscope objective. By adjusting the XYZ positioner upon which the objective (and fibre) is mounted, the amount of power coupled into the fibre can be varied. The light exiting the fibre is split into two beams by the beamsplitter BS as shown in fig.(3.2).

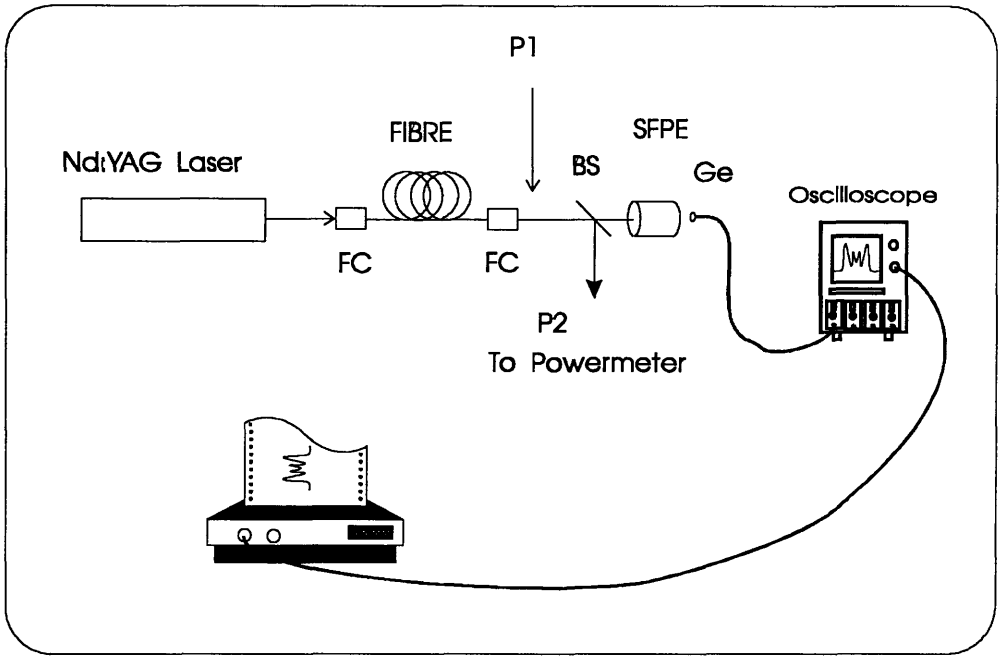

Fig.(3.2) - Experimental set-up for the measurement of Self-Phase Modulation in an optical fibre. P1 and P2 are the two positions where the laser average power is measured. BS is a beamsplitter, FC is the fibre coupler, SFPE is the Scanning Fabry-Perot Etalon and Ge is a Germanium photodiode. The spectra are recorded in the storage oscilloscope and sent to the chart recorder.

One beam goes to a power meter and the other, to a planar scanning Fabry-Perot interferometer. The readings from the powermeter were calibrated by measuring the power before and after the beamsplitter (positions P1 and P2 respectively in fig. (3.2)). Therefore, during the experiment, the power is measured only at position 2 and the calibration is used to work out the total power exiting the fibre.

The planar scanning Fabry-Perot interferometer has a Free Spectral Range (FSR) of 150 GHz and a Finesse of about 30. The light after the Fabry-Perot interferometer is collected by a Ge photodiode and the voltage signal is fed to a storage oscilloscope connected to a chart recorder.

Some of the plots obtained are shown in fig (3.3), together with the theoretical plots obtained through equations (3.02) and (3.07). The qualitative agreement is evident. Moreover, the spectral width of the theoretical and experimental plots are in good quantitative agreement. The width of the experimental plots is measured using the FSR calibration of the F-P etalon. The two outermost major peaks in the measured spectra are separated by one FSR, i.e., 150 GHz. In other words, the last peak at right on fig. (3.3.A.2) for example, is a repetition of the first peak at left on that same picture. The spectral widths for both, measured and calculated results are indicated in fig.(3.3). The input power to the fibre was varied and many spectra were recorded, to compare with the theoretical model.

Fig. (3.4) is a plot of the spectral width (FWHM) versus power of the light exiting the fibre, for the measured and calculated results. One can say from fig.(3.4) that the straight lines upon which the measured and calculated results fall, have slightly different slopes. The calculated points were obtained from eq.(3.07), where the value of n_2 was taken to be 3.0×10^{-20} m^2/W. This linear dependence of the bandwidth on the laser intensity can be predicted by the simple theory of Self-Phase Modulation put forward before. The instantaneous frequency in eq. (3.04) can be easily converted into an instantaneous wavelength by:

$$\Delta\lambda(t) = \frac{\Delta\omega(t)}{2\pi c} \cdot \lambda^2 \qquad (3.08)$$

therefore

$$\Delta\lambda(t) = \frac{8\ln 2}{c} \cdot \frac{n_2 \lambda L_{eff} I_0}{\tau} \cdot \frac{t}{\tau} \cdot e^{-4\ln 2(t/\tau)^2} \qquad (3.09)$$

The maximum shift in wavelength can now be calculated by

$$\Delta\lambda_{max} = \Delta\lambda_i + \delta\lambda \qquad (3.10)$$

Where $\Delta\lambda_i$ is the bandwidth of the laser pulses before entering the fibre and $\delta\lambda$ equals the distance between the maximum and the minimum of $\Delta\lambda(t)$. Taking a time derivative of $\Delta\lambda(t)$ and making it equal to zero to obtain the maximum and minimum of the function in (3.09), $\Delta\lambda_{max}$ is then found to be:

Fig. (3.3) Theoretical and Experimental plots of Self-Phase Modulation (SPM).

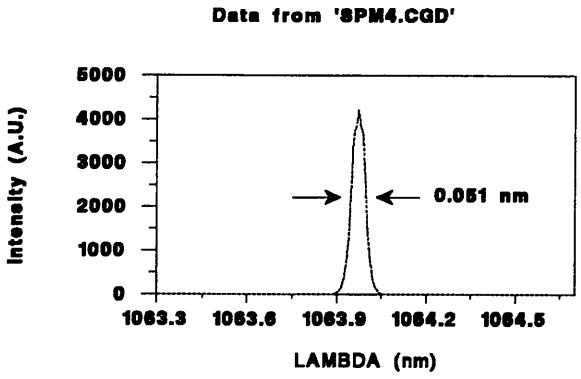

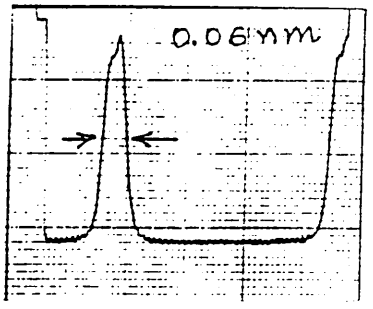

Peak Power = 4 W

A.1) A.2)

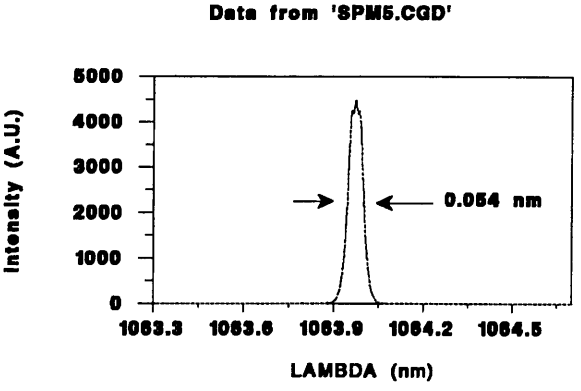

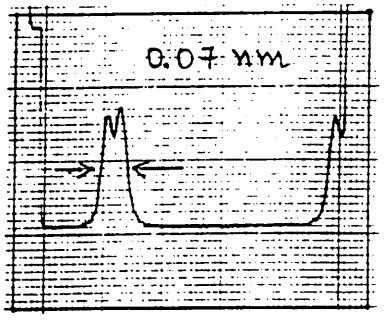

Peak Power = 5 W

B.1) B.2)

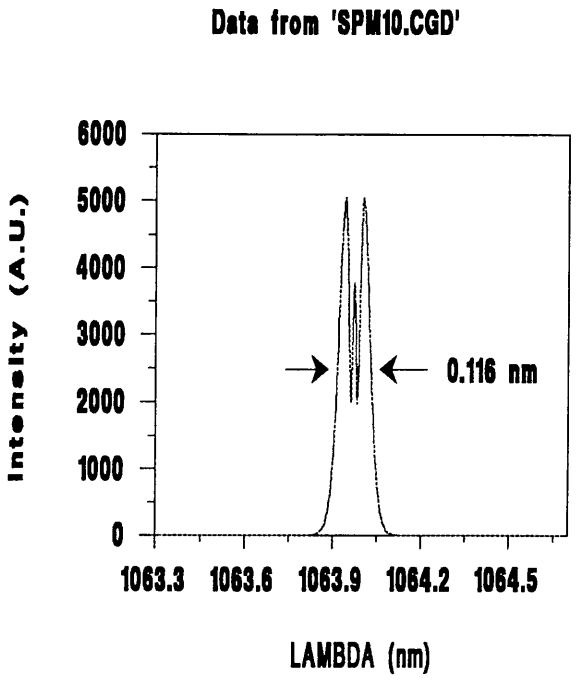

Peak Power = 10 W

C.1)

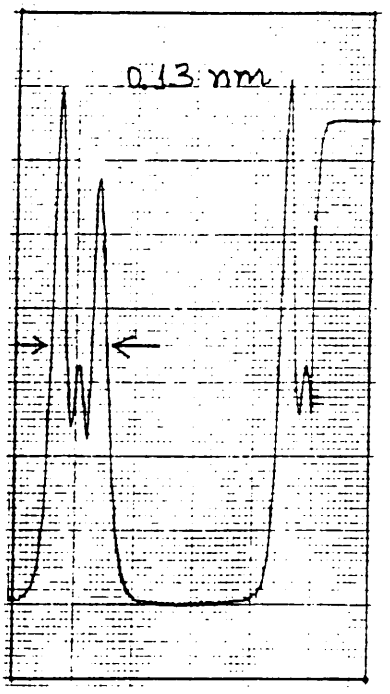

C.2)

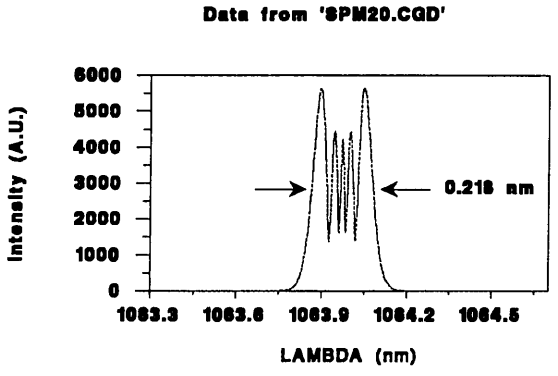

Peak Power = 20 W

D.1)

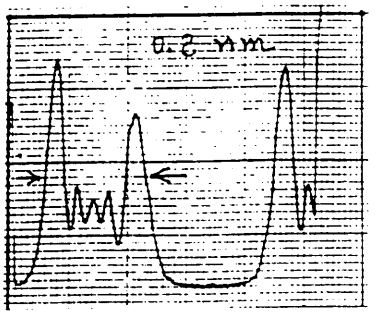

D.2)

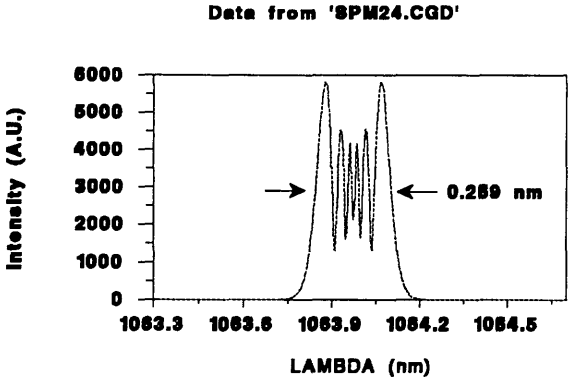

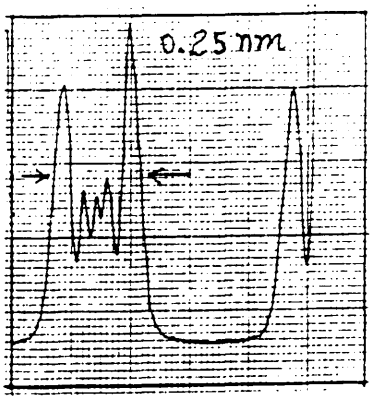

Peak Power = 24 W

E.1) E.2)

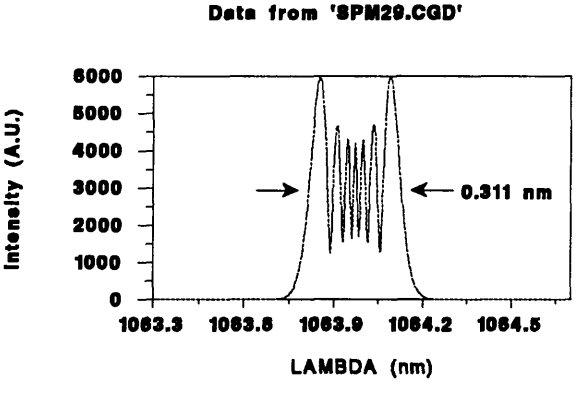

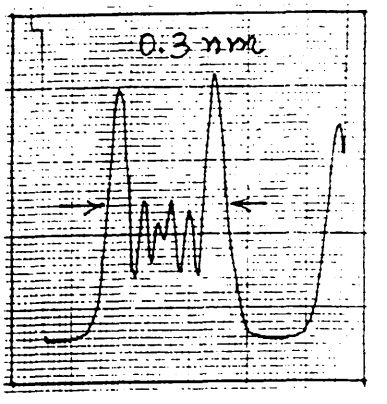

Peak Power = 29 W

F.1) F.2)

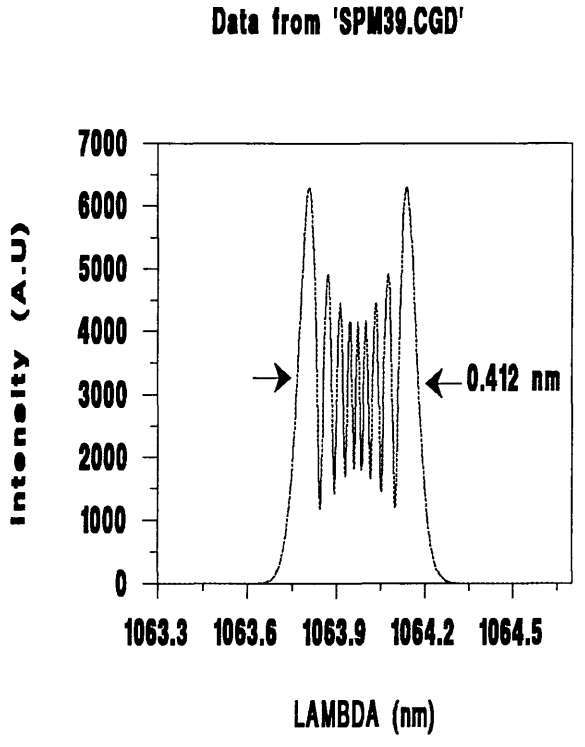

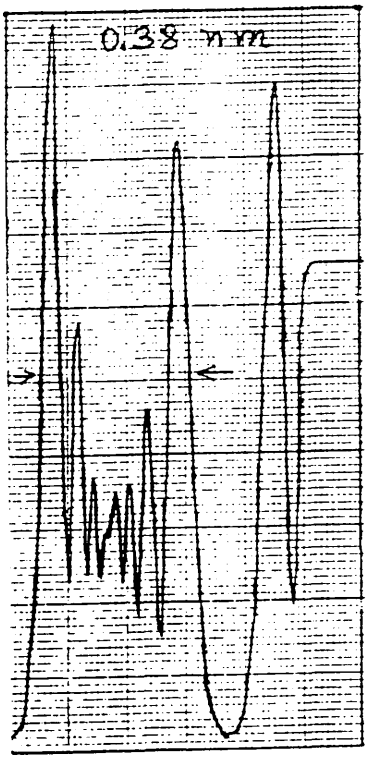

Peak Power = 39 W

G.1) G.2)

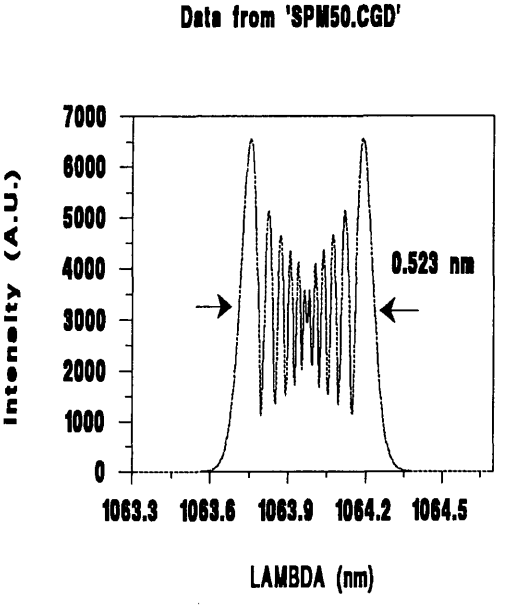

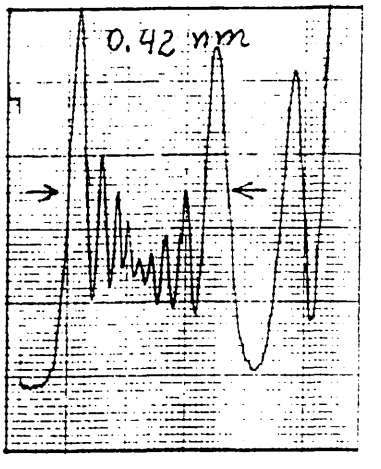

Peak Power = 50 W

H.1) H.2)

$$\Delta\lambda_{max}(P) = \Delta\lambda_i + 4\sqrt{\frac{2\ln 2}{e}} \cdot \frac{n_2 I_0 L_{eff}}{c A_{eff}} \cdot \frac{P}{\tau} \qquad (3.11)$$

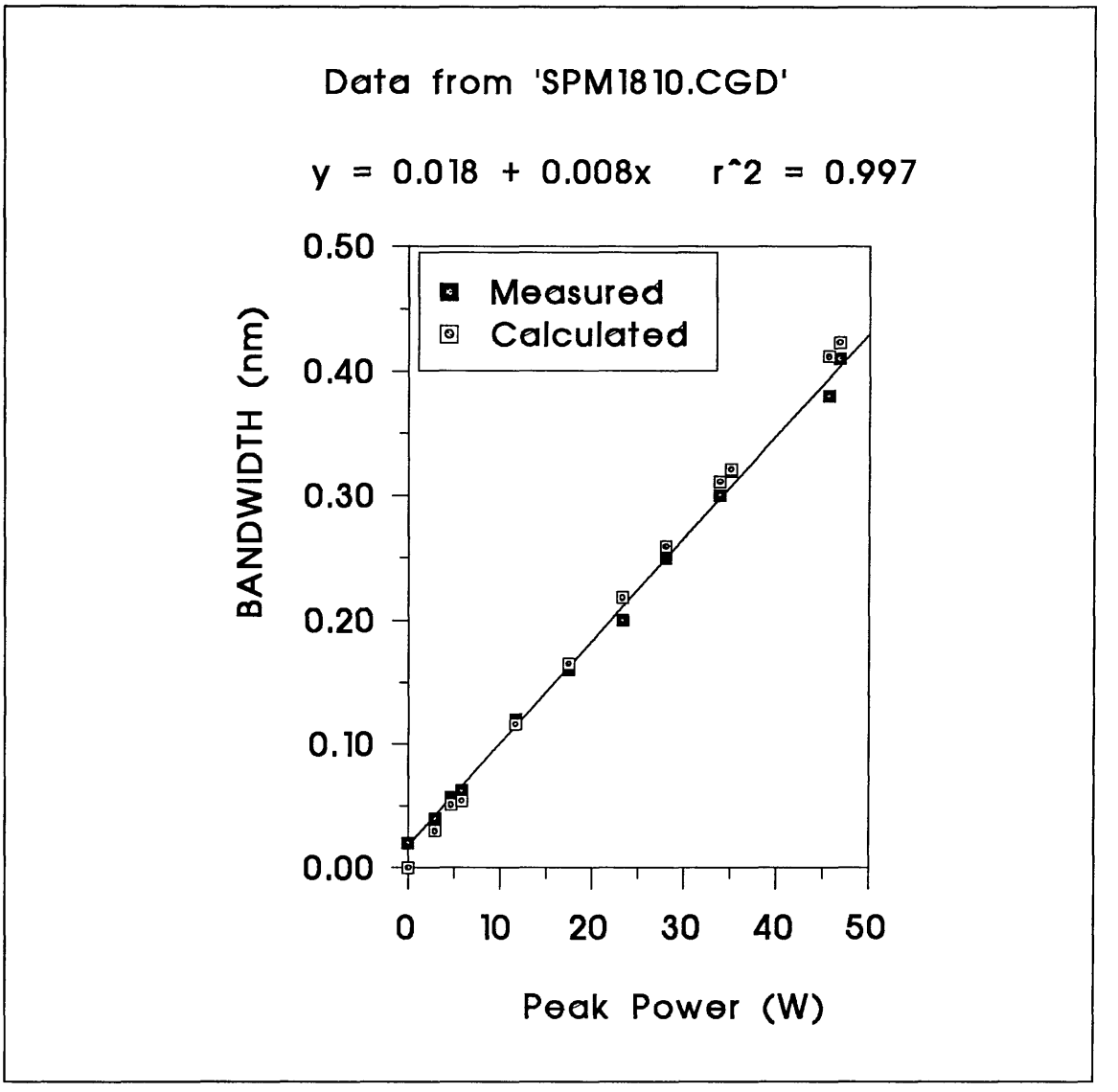

Fig.(3.4) - Measured and calculated bandwidths of laser pulses versus Peak power, after propagating through 150 m of single mode optical fibre. A least square straight line was fitted to the measured data and its equation is given above.

The least-squares fit of the data in fig.(3.4) gives a value of $\Delta\lambda_{max}(0) = \Delta\lambda_i =$ 0.18 Å. The spectral width of the laser without passing the light through the fibre was measured with a double pass spectrometer and the bandwidth obtained was $\Delta\lambda_i$ = 0.2 Å. The agreement between theory and experiment is therefore excellent. The slope of the

straight line fit gives the value of $n_2 = 2.5 \times 10^{-20}$ m²/W. As the polarization is scrambled in the fibre, a reduced value for n_2 is obtained. This effect can be accounted for by an average correction factor of 6/5, which takes linear and circular polarizations into account.[5] The value obtained for n_2 is then $n_2 = 3 \times 10^{-20}$ m²/W. This is in good agreement with values of n_2 obtained by other researchers[6].

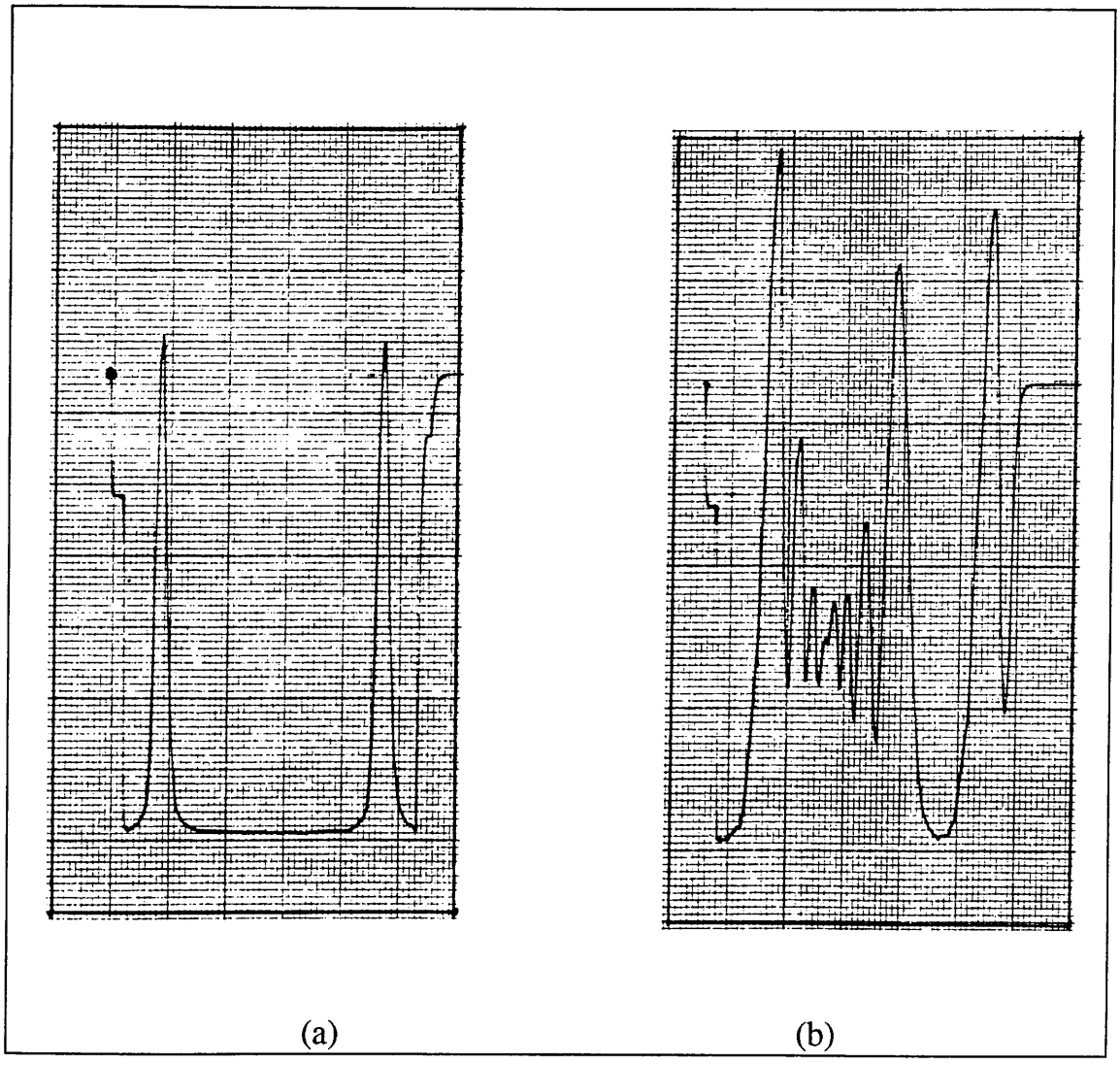

Fig.(3.5) - The power spectrum of the light exiting the single mode optical fibre, measured by a scanning Fabry-Perot interferometer. The distance between the two peaks in (a) is one FSR, which equals 150 GHz. In (a) the laser mode-locker is off and the laser power is 390 mW, which does not produce SPM. The spectrum is then gaussian. When the mode-locker is on, as in (b), the peak power increases by a factor of ≈ 100. SPM acting along the fibre broadens the spectrum of the laser, producing the characteristic oscillations shown in (b).

A final demonstration of the dependence of the bandwidth of the light exiting the fibre, on the laser peak power is provided by fig. (3.5). In (3.5.a) the laser light is being guided through the fibre, but the mode-locker was turned OFF. The power exiting the fibre is 390 mW of cw light, which does not produce SPM. When the mode-locker is turned ON, the laser produces one 120 ps pulse every 12 ns. As the average power measured by a powermeter is still the same, the peak power in each pulse is roughly 100 times larger than the average power, i.e., 39W. The spectrum of the laser broadens drastically and breaks up into SPM oscillations as shown in (3.5.b).

3.2) - Laser Pulse Compression

Having produced frequency broadened laser pulses by SPM, these pulses were "focussed in time" by a dispersive line. This line is composed of two diffraction gratings in tandem used at grazing angle of incidence as first described by Treacy[7].

A pair of gratings with their faces and rulings parallel to one another has the important property of producing a time delay that is an increasing function of the wavelength. One can write a time delay τ as $\tau = d/v_g$ where d is the distance travelled by a laser pulse with group velocity v_g. Taking a derivative with respect to λ, one gets:

$$\frac{dv_g}{d\lambda} = -\frac{d}{\tau^2} \cdot \frac{d\tau}{d\lambda}$$

If $\frac{d\tau}{d\lambda} > 0$ as said above, then $\frac{dv_g}{d\lambda} < 0$. Now

$$\frac{dv_g}{d\lambda} = -\frac{2\pi c}{\lambda^2} \cdot \frac{dv_g}{d\omega}$$

Therefore, $\frac{d\tau}{d\lambda} > 0$ translates into $\frac{dv_g}{d\omega} > 0$. This fact, together with eq.(3.06) means that the grating pair forms a dispersive line with *negative* group velocity dispersion. It can therefore be used to compress chirped (frequency broadened) laser pulses.

The expression for the time delay can be easily obtained as shown by Treacy[7] . The diagram in fig. (3.6) defines some important parameters. The angle of incidence is

Γ, i.e., the angle between the incident laser beam and the normal to the first grating. θ is the angle between the incident and diffracted rays. b is the slant separation between the two gratings. The X axis is taken parallel to the incident rays and the plane X = 0 is shown in the diagram to intercept both the input and output beams.

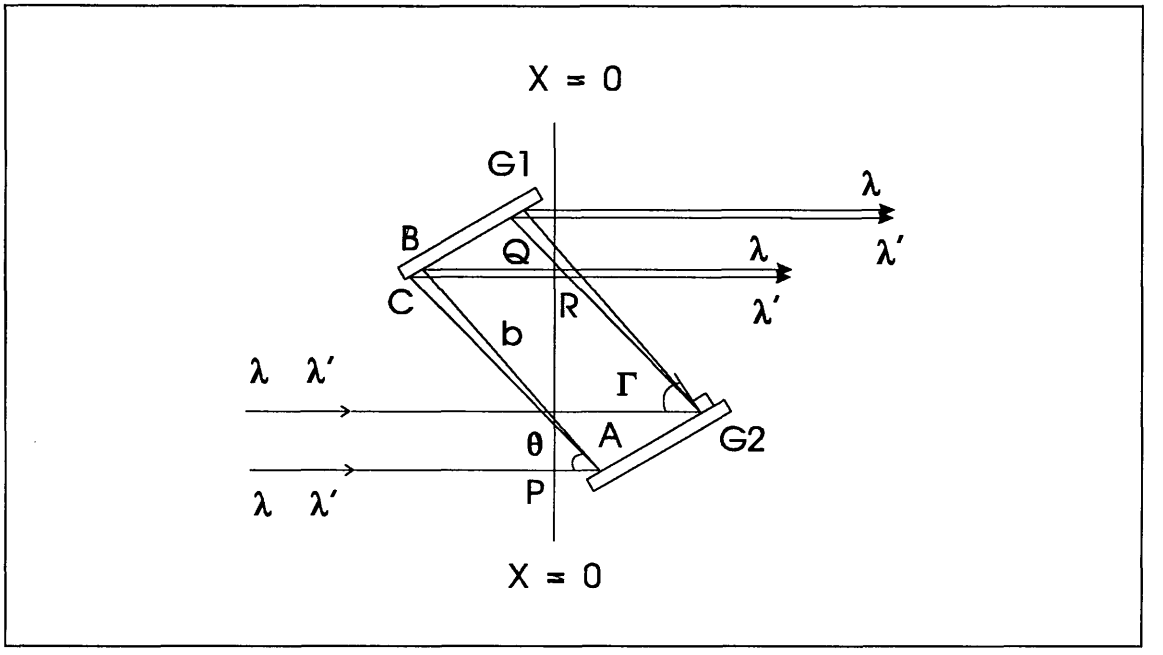

Fig.(3.6) - The grating pair used as a negative GVD dispersive line. G1 and G2 are the two gratings. The angle of incidence is Γ and θ is the angle between the incident and diffracted rays. The distance PABQ is shorter than PACR, which leads to dispersion.

The slant separation AB (or b) between the gratings is given by:

$$b = G \,.\, \sec(\Gamma - \theta) \qquad (3.12)$$

Where G is the perpendicular distance between the gratings. The path length PABQ for λ, being shorter than PACR or λ', leads to GVD. PABQ can be calculated by:

$$b \,.\, (1 + \cos\theta) = c \,.\, \tau \qquad (3.13)$$

Where τ is the delay introduced in the laser beam by the propagation through the grating pair. τ is clearly a function of the wavelength λ both through θ and b, which is also a function of θ. Taking a derivative of eq.(3.13) with respect to λ:

$$\frac{d\tau}{d\lambda} = \frac{1}{c} \cdot \left[\frac{db}{d\lambda} (1 + \cos\theta) - b \sin\theta \frac{d\theta}{d\lambda} \right] \tag{3.14}$$

$\frac{db}{d\lambda}$ is readily obtained from eq. (3.12):

$$\frac{db}{d\lambda} = G \cdot \frac{\sin(\Gamma - \theta)}{\cos^2(\Gamma - \theta)} \cdot \left(-\frac{d\theta}{d\lambda}\right) \tag{3.15}$$

And, from the grating equation, $\frac{d\theta}{d\lambda}$ can be obtained:

$$d \, . \, [\sin\Gamma + \sin(\Gamma - \theta)] = \lambda \tag{3.16}$$

Where in this case d is the grating groove spacing, i.e., d^{-1} is in units of lines/mm.

$$\frac{d\theta}{d\lambda} = -\frac{1}{d \cos(\Gamma - \theta)} \tag{3.17}$$

Substituting eqs. (3.15) to (3.17) into (3.14) and doing some algebra, one gets:

$$\frac{d\tau}{d\lambda} = \frac{b(\lambda/d)}{c \, d \, [1 - (\lambda/d - \sin\Gamma)^2]} \tag{3.18}$$

Equation (3.18) can be integrated to give the delay time τ as a function of the wavelength λ:

$$\tau(\lambda) = \int_{\lambda_o}^{\lambda} \frac{b(\lambda'/d)}{c \, d \, [1 - (\lambda'/d - \sin\Gamma)^2]} \, d\lambda' \tag{3.19}$$

If $\lambda = \lambda_{max} = \lambda_o + \Delta\lambda_{max}$ where $\Delta\lambda_{max}$ is given by eq.(3.10), then the total group delay $\Delta\tau$ can be obtained from (3.19).

A good approximation for $\Delta\tau(\Delta\lambda)$ can also be obtained from eq.(3.18), by considering the differentials as "deltas" in that equation, as long as $\Delta\lambda_{max} = \lambda_{max} - \lambda_o$ is such that $\frac{\Delta\lambda_{max}}{\lambda_o} << 1$. The gratings used in this project have $d^{-1} = 1800$ lines/mm. The

wavelength is $\lambda_o = 1.064$ μm and the angle of incidence is $\Gamma = 75°$. Substituting all these values in (3.18) one is left with a very simple equation for $\Delta\tau$ as a function of $\Delta\lambda$:

$$\Delta\tau = 0.1162 \left[\frac{ps}{\mu m^2}\right] \cdot b \cdot \Delta\lambda \qquad (3.20)$$

A graphical comparison between equations (3.19) and (3.20) is shown below in fig.(3.7). The wavelength λ was made to vary from λ_o to λ_{max} and the value of b was set to b = 80 cm in both equations. The largest difference of 1.7 ps occurs for $\lambda = \lambda_{max}$ where the total delay is 93 ps, i.e., equation (3.20) is in this case accurate to within 1.8%. For larger bandwidths $\Delta\lambda$ and shorter input pulses, the difference between the exact and approximated group delays can be significantly larger.

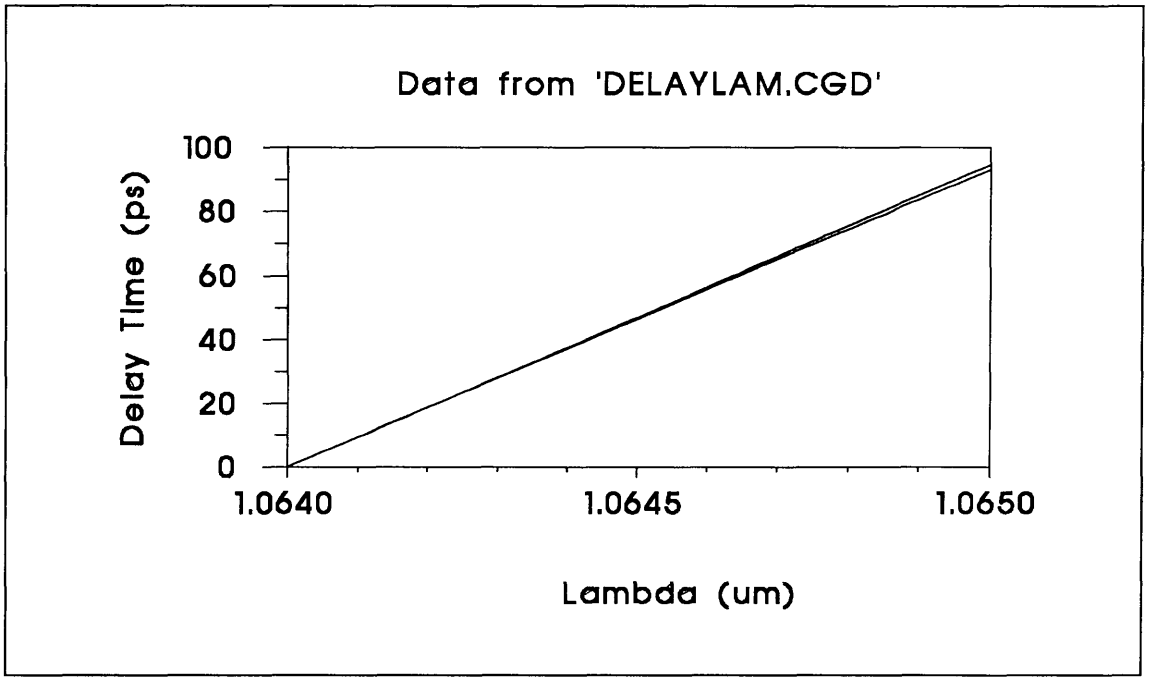

Fig.(3.7) - Graphical comparison between eqs. (3.19) and (3.20). If the bandwidth of the laser pulses is not too large, then the simplified expression in (3.20) can be used to calculate $\Delta\tau$.

The efficiency of coupling light into the fibre was optimised and the average power exiting the optical fibre was measured to be $P_{av} = 1.5$ W, which corresponds to a peak power of $P_{peak} = 150$ W. The bandwidth of these high intensity pulses is very wide due to SPM in the fibre. In fact, the bandwidth exceeded the FSR of the scanning FP

etalon. However, one can use the equation of the straight line fitted to the data in fig.(3.3) to extrapolate the value of $\Delta\lambda$ for this peak power. For P = 150 W, the equation in fig.(3.3) gives $\Delta\lambda$ = 1 nm.

Going back to equation (3.20) one can then make $\Delta\lambda$ = 1 nm (the bandwidth of the laser pulses after the fibre) and leave b as a variable. The following equation is obtained:

$$\Delta\tau = 1.16\ b\ \text{ps/cm} \qquad (3.21)$$

The total time delay $\Delta\tau$ produced by the grating pair can therefore be changed simply by adjusting the separation b, between the gratings. So, if 120 ps pulses are to be compressed, one has to make $\Delta\tau$ = 120 ps in eq.(3.21). The optimum separation between the gratings is then found to be b = 80 cm. This value of b was used to set-up the pulse compressor as shown in fig.(3.8).

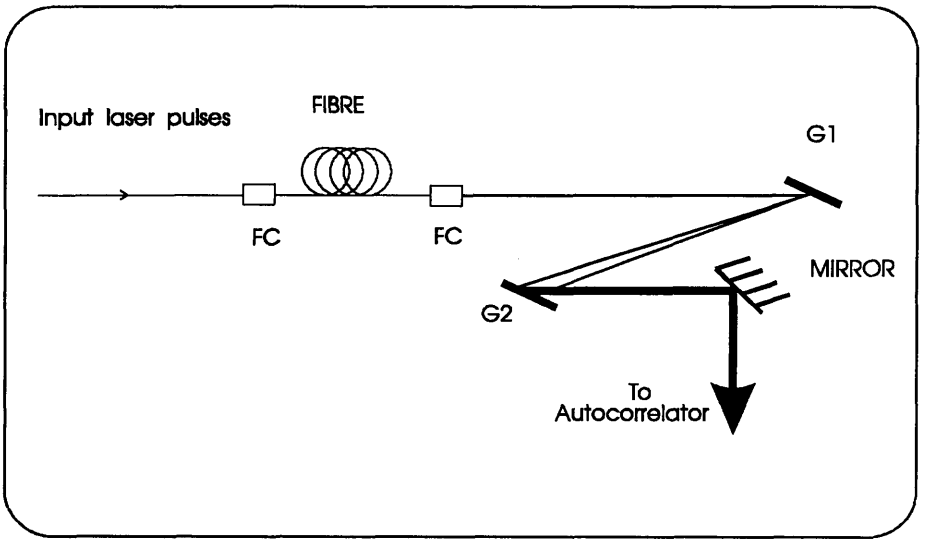

Fig.(3.8) - The fibre-grating pulse compressor. FC stands for fibre coupler and G1 and G2 are the two gratings. The output of the compressor is directed to an autocorrelator by a planar mirror.

Compressed pulses were obtained at the output of the compressor. Fig.(3.9) is an autocorrelation trace of the compressed pulses. The FWHM of the autocorrelation trace is $\Delta t = 4.3$ ps. Assuming that the laser pulses are gaussian, the laser pulsewidth τ_c is given by $\tau_c = 0.707\ \Delta t$. So, the pulsewidth is $\tau_c = 3$ ps. The compression ratio is thus $\tau/\tau_c = 40$.

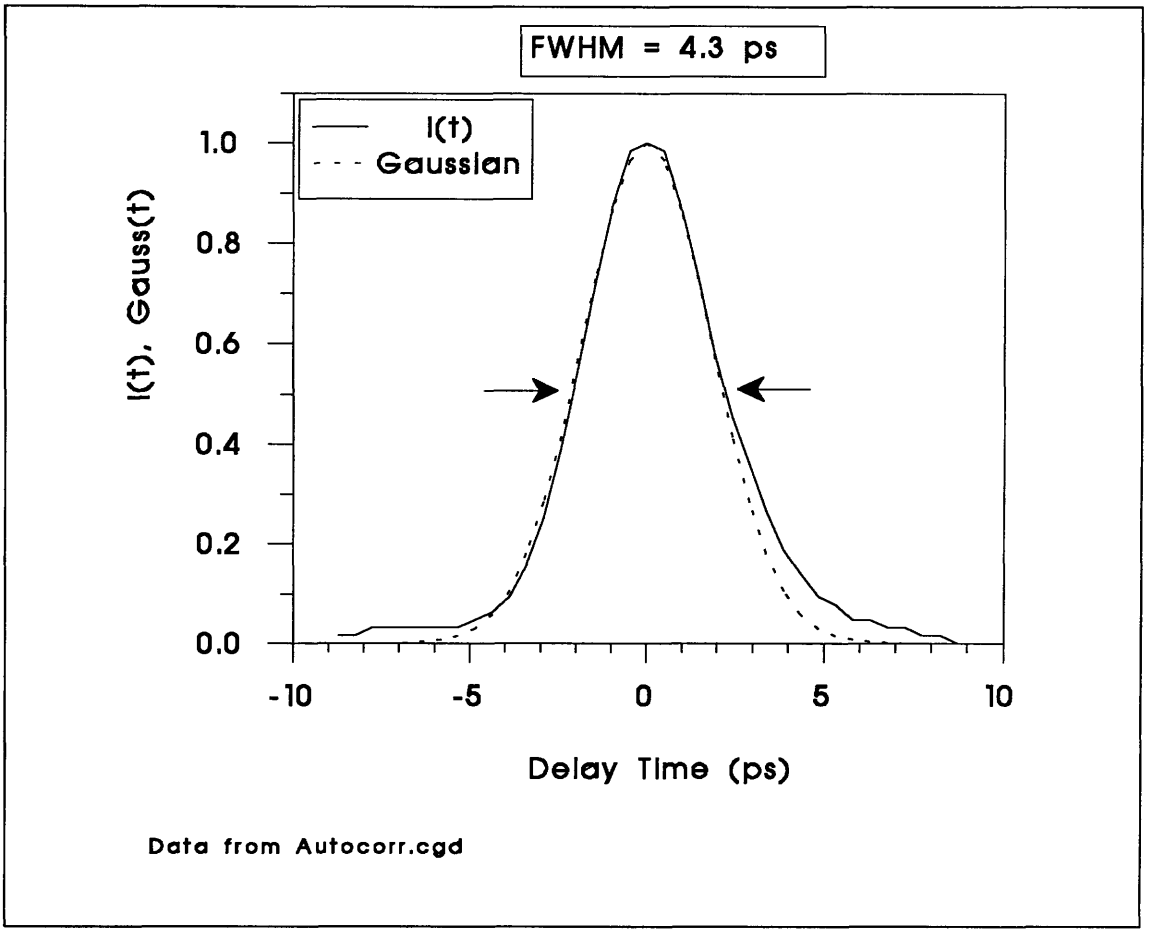

Fig.(3.9) - I(t) is the intensity autocorrelation of the compressed Nd:YAG pulses. The function Gauss(t) is a normalized gaussian function, having the same FWHM as the correlation function. Note that I(t) is slightly asymmetric.

It is important to mention that the compression ratio is still smaller than its theoretical limit. For gaussian, transform-limited pulses, one has

$$\Delta\upsilon \,.\, \Delta t = 0.44 \qquad (3.22)$$

where $\Delta\upsilon$ and Δt are the FWHM of the pulses in frequency and time domain, respectively. The bandwidth $\Delta\lambda$ of the pulse after the fibre can be used to calculate $\Delta\upsilon$ and this in turn, can be substituted into eq. (3.22) to give $\Delta\tau$. The result obtained is then $\Delta\tau$ = 1.3 ps. Therefore, the compressed pulses are still 2.3 times longer than their theoretical limit. Hence, it is likely that part of the chirp ($\Delta\lambda$) still remains in the compressed pulses. It is also interesting to note that the autocorrelation trace of fig.(3.9) is not a true gaussian function, being slightly asymmetric.

Although the compressor achieved its goal of shortening the YAG laser pulses, a number of practical factors affects adversely its performance. The holographic gratings with 1 square inch area are used at grazing incidence angle which produces an elliptically diverging beam. The size of this expanded beam has to be kept smaller than the area of the second grating. This poses an upper limit on the spot size of the beam incident upon the first grating of about 16 mm^2. The power density incident upon the first grating is, in this case, enough to cause optical damage to the grating. Therefore, it was necessary to cut the power after the fibre down to about 500 mW. Roughly 50% of that power appears in the compressed beam after the two gratings.

As the output of the pulse compressor is still infrared light, it would have to be frequency doubled to be used as excitation for photoconductive switches. That proved to be difficult for two reasons. Firstly, the frequency doubled output $P^{2\omega}$ depends on the square of the input power density P^{ω}, which in this case is small. Another fundamental problem arises with the relaxation oscillations in the YAG laser. Any intensity fluctuation in the infrared laser beam affects the SPM in the fibre and the output of the compressor becomes very noisy, producing optical damage in the frequency doubling crystal. This noise can in principle be reduced by a feedback loop between the output of the pulse compressor and the rf mode-locker driver in the YAG laser. This is however, a major area of research in lasers[8,9] and it was not tried in this project.

3.3) - Synchronously pumped dye laser

Without short pulses above and below the bandgap of GaAs, the electrooptic sampling scheme presented in chapter II becomes impossible. For this reason, efforts were concentrated in producing short and visible (above bandgap) pulses to be used in optoelectronic sampling. The output of the Nd:YAG laser was frequency doubled and used to synchronously pump a dye laser with rhodamine 6G. Because the lasing

bandwidth of this dye is very broad, pulses of a few picoseconds can, in principle, be produced. The synchronous pumping scheme implies that for every pulse from the master laser, one pulse is produced by the dye laser. In order to have a stable output, the two laser cavities must be kept at the same length to within a few microns. It was found experimentally that changing the cavity length of the mode-locked Nd:YAG laser by ~ 2 μm would cause it to produce large pulse-to-pulse instabilities and eventually very broad (ns range) Q-switched pulses. Under such conditions the laser can not be frequency doubled by Second Harmonic Generation (SHG) because the SHG crystal can suffer optical damage.

The output of the Nd:YAG laser is continuously monitored, so that when instabilities arise, the laser shutter is closed. The stability monitor picks-up a small amount of light transmitted by the rear mirror of the laser (opposite to the output coupler). The monitor consists of a microscope objective, a high speed , 200 GHz gain-bandwidth-product avalanche photodiode[10] and an oscilloscope. The diode is reversed biased to -135 V and its output is connected to a 500 MHz analogue oscilloscope. Neither the diode nor the oscilloscope are fast enough to show the true laser pulsewidth. The laser pulses appear on the screen of the scope broadened to about 600 ps. Even so, it is still possible to see changes in the laser pulsewidth when the mode-locker is adjusted. Two laser pulses are shown in fig. (3.10.a), separated by roughly 13 ns, which gives the laser repetition rate of ≈ 76 MHz. The stability monitor is effectively used by turning the oscilloscope to very long time basis as shown in fig. (3.10.b), where 100 μs/cm is used. In this case, one has 7600 pulses/division in the picture. If the laser is stable, i.e., if the intensity does not change from pulse to pulse in long time scales, then one should see a bright band on the oscilloscope screen, representing all pulses packed together with the same amplitude. This is what is shown in fig. (3.10.b). On the other hand, when cavity length fluctuations or relaxation oscillations[11] occur, this continuous band breaks up and one can actually "see" the instabilities on the oscilloscope screen.

Despite all the instabilities in the Nd:YAG laser, it can be frequency doubled successfully. The crystal conventionally used for SHG with YAG lasers at $\lambda = 1.064$ μm is the KTP crystal in a type II phase matching configuration.[12,13] In this case, two input waves of orthogonal polarizations are mixed inside the crystal, to produce a second harmonic wave at 45 degrees to both of the input waves. For 7W, $\lambda = 1.064$ μm, 120 ps input pulses, the KTP crystal produces up to 1W, $\lambda = 0.532$ μm (green light) of output.

This green light is then used to pump the rhodamine 6G dye laser. The pump power threshold for lasing in the dye laser is about 500 mW, depending on dye concentration and "age". Therefore, the higher pump power is available for operation far above the threshold, the more stable the output of the dye laser will be. For 1W average

pump power at λ = 0.532 mm, the dye laser produces up to 100 mW average output power, but normally the output is lower, at about 80 mW.

When intensity fluctuations occur in the Nd:YAG laser, the second harmonic power also fluctuates and that causes the output of the dye laser to fluctuate as well. It is common to see the output of the dye laser flickering, due to instabilities in the YAG laser. Sometimes, the fluctuations in intensity can be so high that they optically damage the SHG crystal.

The processes behind laser damage are not well understood but three mechanisms have been identified with this phenomenon[14],[15] : acoustic damage caused by stimulated Brillouin scattering, simple heating caused by absorption and electron avalanche. The first process, is regarded as rare and unimportant, whereas the other two can be very important. Heating caused by bulk absorption of the laser light or by absorption at defect sites such as inclusions can cause internal optical damage in a crystal. This process can also occur (and often does) on surfaces of optical components contaminated with dust particles, which can be burnt by the laser beam. It may also follow from cleanliness problems associated with deposition of multilayer films on the surfaces of components. Electron avalanche is closely related to the heating process, but the damage occurs due to high internal electric currents. These currents can be generated by the laser beam if it excites electrons or even ions to the conduction band of the crystal.

KTP crystals have a large nonlinear Second Harmonic Generation (SHG) coefficient which leads to good SHG conversion efficiencies. In this work, typical conversion efficiency was about 10-20%. On the other hand, it is known that KTP crystals may have micrometer size liquid inclusions, sub-micrometer filamentary inclusions, "small" amounts (10-50 ppm) of OH^- and other defects which can easily produce absorption and/or avalanche breakdown. For this reason, its critical power density for optical damage is not known precisely, but seems to fall in a very wide range, from[16] 50 MW/cm^2 to[17] 5 GW/cm^2. This figures will be compared later in this chapter with the damage threshold for a recently introduced nonlinear crystal from China.

The synchronously pumped dye laser was successfully pumped by the Nd:YAG, but its output is again very noisy. Despite that, optoelectronic sampling experiments were performed with it. The details and results of these experiments will be presented later and compared with results obtained with a mode-locked Ti:Sapphire laser.

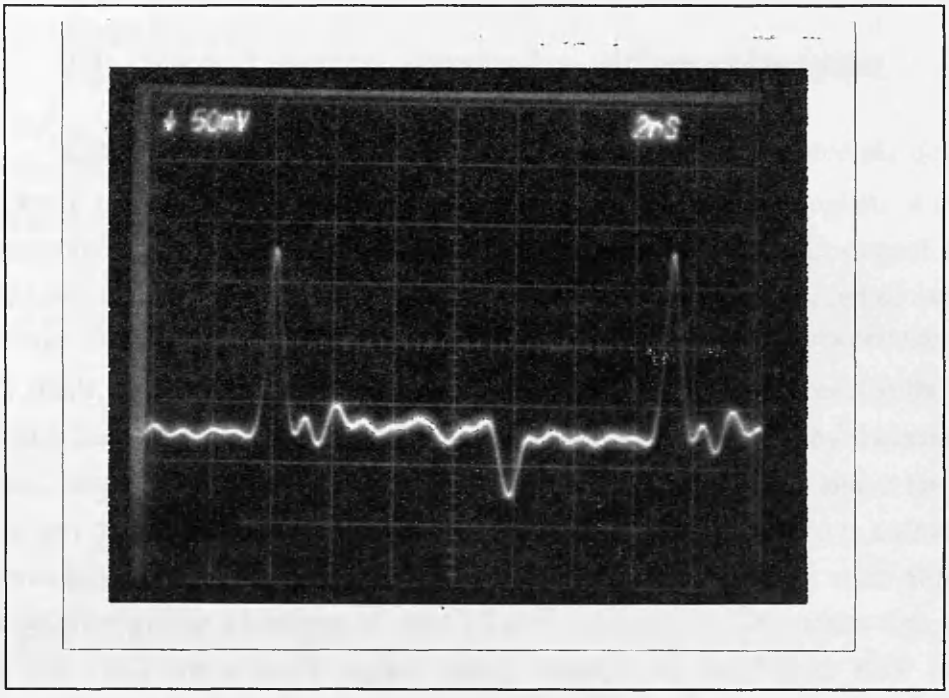

(A)

Fig.(3.10) - Oscilloscope screen picture of the Nd:YAG laser pulses. In (A) two pulses are shown, separated by about 13 ns. The pulsewidth is broadened by the photodiode and the oscilloscope. In (B) a much longer time base is used to show thousands of pulses together, so that the pulse to pulse stability can be monitored.

(B)

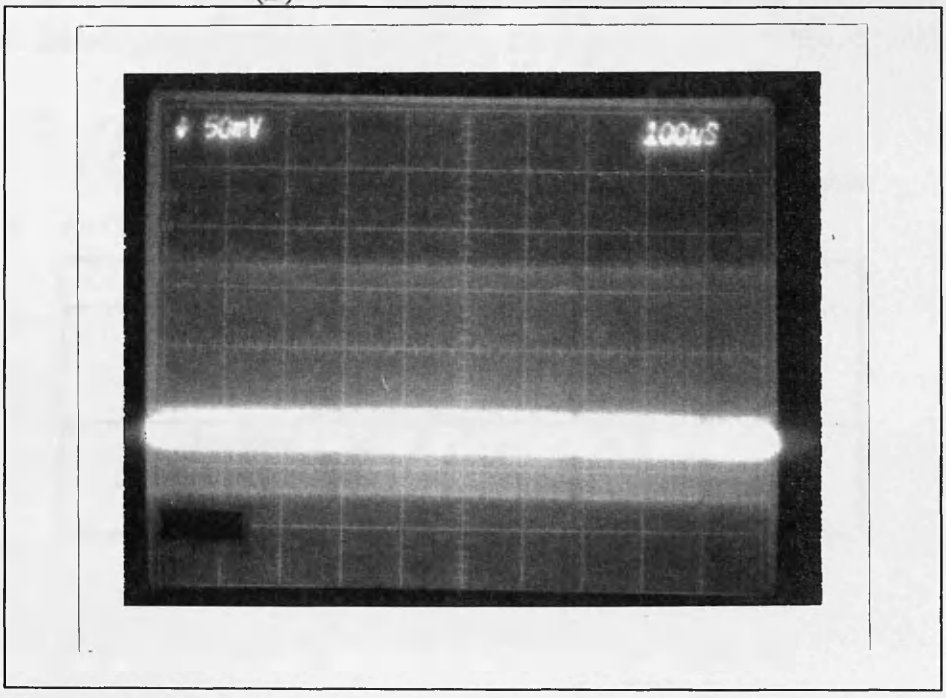

3.4) - Second Harmonic Generation with an LBO crystal.

Lithium Triborate ($Li\ B_3\ O_5$ or LBO) is a new crystal recently developed and marketed by Cashitech, a Chinese company involved in a major program of research and development of crystals.[18] This crystal offers a great advantage in optical damage threshold, when compared with KTP. The lattice of this crystal is composed of extremely long helixes, made up of a spiralling chain of (B_3O_7). The interstices between the helixes are very small, so that only the Li^+ cation can enter them.[19] This ensures that the crystal is inclusion free, which drastically reduces heating due to absorption by inclusions and impurities. Moreover, the bandgap of LBO is very wide, being 7.75 eV and as the crystal lattice is very compact, the production and transport of electrons and ions in an avalanche breakdown process is strongly reduced. As a comparison, KTP has its main absorption edge at 380 nm, giving a bandgap of only 3.3 eV.[12] All this features taken into account suggest that LBO has a much higher optical damage threshold than KTP or other nonlinear crystals. In fact, the measured critical power density for optical damage in LBO is in the range from[20] 10 GW/cm^2 to[19] 25 GW/cm^2. Thus, even in the worst case, the critical power density for optical damage in LBO is twice the highest measured critical power density for KTP.

The disadvantage of LBO in respect to KTP is that the former has an effective nonlinear coefficient about 5 times lower than the latter. The SHG coefficient is normally measured in terms of d_{36} for KDP, where $d_{36}^{(KDP)} = 1.1 \times 10^{-9}$ esu. The comparison between KTP and LBO is summarized in the table (3.1) below, from ref. 20.

Table (3.1) - Comparison between LBO and KTP crystals:

Crystals	LBO	KTP
d_{eff}(SHG) x d_{36}(KDP)	2.7	15.8
Damage threshold (GW/Cm^2)	10	1

Despite the low nonlinear coefficient of LBO, it seemed worth it to investigate its use as the SHG crystal with the Nd:YAG laser.

The refractive indices of LBO have been measured for 16 wavelengths, from 0.2537 μm to 1.0642 μm and Sellmeir equations were fitted to the data.[19] The refractive indices for the wavelengths relevant to this work, $\lambda = 1.0642$ μm and $\lambda = 0.532$ μm are given below:

Table (3.2) - The refractive indices of LBO at $\lambda = 1.064$ μm and $\lambda = 0.532$ μm

	n_x	n_y	n_z
ω ($\lambda = 1.064$ μm)	1.5656	1.5905	1.6055
2ω ($\lambda = 0.532$ μm)	1.5785	1.6065	1.6212

From the table above it is evident that $n_z^{2\omega} > n_y^{2\omega} > n_z^{\omega} > n_y^{\omega} > n_x^{2\omega} > n_x^{\omega}$. It is also true that $n_x^{2\omega} > \frac{1}{2} \cdot (n_x^{\omega} + n_y^{\omega})$ and $n_x^{2\omega} > \frac{1}{2} \cdot (n_x^{\omega} + n_z^{\omega})$. These relationships between the refractive indices mean that the LBO crystal belong to class 10 in Hobden's classification of biaxial crystals.[21]

3.5) - Theory of Second Harmonic Generation

LBO is a negative biaxial (three different refractive indices) crystal[19] of orthorombic group with point symmetry mm2 and its nonlinear optical polarization is given by:[22]

$$\begin{bmatrix} P_x \\ P_y \\ P_z \end{bmatrix} = \varepsilon_0 \begin{bmatrix} 0 & 0 & 0 & 0 & d_{15} & 0 \\ 0 & 0 & 0 & d_{24} & 0 & 0 \\ d_{31} & d_{32} & d_{33} & 0 & 0 & 0 \end{bmatrix} \cdot \begin{bmatrix} E_x^2 \\ E_y^2 \\ E_z^2 \\ 2E_yE_z \\ 2E_xE_z \\ 2E_xE_y \end{bmatrix} \qquad (3.23)$$

where P_i is the ith component of the nonlinear polarization vector, d_{ij} is the ijth nonzero component of the SHG tensor and E_i is the electric field of the input optical waves.

The z component of the nonlinear polarization vector created by a laser beam of components E_x, E_y and E_z is, according to (3.23):

$$P_z = \varepsilon_0 . [d_{31} E_x^2 + d_{32} E_y^2 + d_{33} E_z^2] \qquad (3.24)$$

Therefore a type I phase matching in which two waves of the same polarization E_x ,E_y or E_z combine to produce a second harmonic light beam through the polarization wave P_z, should be chosen for efficient SHG.

3.5.1) - Second Harmonic Power and Coherence Length

The second harmonic power $P^{2\omega}$ generated by a single mode gaussian beam of angular frequency ω and power P^{ω} incident along a principal axis of a crystal of thickness l is given by:[23]

$$P^{2\omega} = \frac{2 \mu_0^{3/2} \varepsilon_0^{1/2} \omega^2 d_{ij}^2 (P^{\omega})^2 l^2}{\pi W_0^2 n^{2\omega} (n^{\omega})^2} \cdot \left[\frac{\sin(l \Delta k/2)}{(l \Delta k/2)}\right]^2 \qquad (3.25)$$

where:

ω = frequency of the input light
W_0 = spot radius of the fundamental beam
n^{ω} = pertinent refractive index of the crystal at ω
$n^{2\omega}$ = pertinent refractive index of the crystal at 2ω
dij = pertinent SHG coefficient
$\mu_0 = 4 \pi \times 10^{-7}$ H/m
$\varepsilon_0 = 8.85 \times 10^{-12}$ F/m
l = Crystal length
$\Delta k = k^{2\omega} - 2k^{\omega}$ is the wavevector mismatch between the fundamental and harmonic waves.

One can estimate the efficiency of the Second Harmonic Generation (SHG) based on equation (3.25). The following values for the parameters will be used:

$\Delta k = 0$	$\lambda = 1.064$ μm
$d_{ij} = d_{32} = 1.62 \times 10^{-12}$ m/V	$\omega = 1.78 \times 10^{15}$ Hz
$n^{2\omega} = 1.6212$	$n^{\omega} = 1.5905$
$W_0 = 50$ μm	$P^{\omega}_{peak} = 700$ W

These numbers, together with eq.(3.25) produce:

$$\frac{P^{2\omega}}{P^{\omega}} = \eta = 22\ \%$$

It is seen from eq.(3.25) that the SHG power depends on the **square** of the pump power density, which makes it critical. Therefore, for a fixed crystal length l and laser wavelength, the critical parameters are the spot size ω_0 of the input laser beam and its peak power.

Because of dispersion in the crystalline medium, $\Delta k \neq 0$ and the SHG power is proportional to the sinc function in the right of eq. (3.25). The period of oscillation of $P^{2\omega}$ through the sinc function, gives rise to the important parameter of coherence length $L_c = \pi/\Delta k$. In terms of refractive indices:

$$L_c = \frac{\lambda_0}{4\,(n^{2\omega} - n^{\omega})} \qquad (3.26)$$

It is possible to choose special directions inside the crystal which make $\Delta k = 0$. This condition is equivalent to $n^{\omega} = n^{2\omega}$. In such special directions, the fundamental and harmonic waves are *critically* phase matched. Along the principal axes, the mismatch can also be reduced to zero by changing the pertinent refractive index of the crystal through a change in temperature. This situation produces non-critical phase matching (NCPM) explained below.

3.5.2) - Phase Matching

Phase matching is the process by which the wavevector mismatch Δk is reduced to zero. This can be accomplished in a number of ways, leading to Critical or Noncritical phase matching. In order to explain this process, some understanding of wave propagation in anisotropic media is needed.

The refractive index n "seen" by a wave propagating inside a crystal with three different refractive indices is given by Fresnel's equation:[24]

$$\frac{\sin^2(\theta)\,.\,\cos^2(\phi)}{n^{-2} - n_x^{-2}} + \frac{\sin^2(\theta)\,.\,\sin^2(\phi)}{n^{-2} - n_y^{-2}} + \frac{\cos^2(\theta)}{n^{-2} - n_z^{-2}} = 0 \qquad (3.27)$$

Where θ and ϕ define the propagation direction and are measured from the z and x axes respectively.

Equation (3.27) is a quadratic equation in n^{-2}, i.e., for every direction (θ,ϕ) there will be two different refractive indices corresponding to two (orthogonal) directions of polarization for the propagating wave.

If θ is set to $\theta = 90^{o}$ so that the light propagation takes place in the X,Y plane, (3.27) can be solved for n^{-2}, producing:

$$n = n_z \quad \text{or}$$

$$\frac{1}{n^2} = \frac{1}{n_x^2} \cdot \sin^2(\phi) + \frac{1}{n_y^2} \cdot \cos^2(\phi) \tag{3.28}$$

Incidentally, if n_x and n_y in this last equation are replaced with n_e and n_0, respectively and ϕ is replaced with θ, one gets the equation governing the propagation of light through a uniaxial crystal, obtained from the index ellipsoid.

Due to dispersion, the equations above are functions of the light wavelength being propagated. Therefore, one has two equations for the fundamental and two for the second harmonic beams:

$$n(\omega) = n_z(\omega) \qquad \text{or}$$

$$\frac{1}{[n(\omega,\phi)]^2} = \frac{1}{n_x^2(\omega)} \cdot \sin^2(\phi) + \frac{1}{n_y^2(\omega)} \cdot \cos^2(\phi) \tag{3.29}$$

$$n(2\omega) = n_z(2\omega) \qquad \text{or}$$

$$\frac{1}{[n(2\omega,\phi)]^2} = \frac{1}{n_x^2(2\omega)} \cdot \sin^2(\phi) + \frac{1}{n_y^2(2\omega)} \cdot \cos^2(\phi)$$

Now, to satisfy the phase matching condition $\Delta k = 0$, we need $n^{2\omega}(\phi) = n^{\omega}(\phi)$. In order to use the coefficient d_{32} in SHG, the fundamental beam has to be polarized in the Y direction (see eq.3.24). Thus, $n^{\omega}(\phi) = n^{\omega}_y$ and $n^{2\omega}(\phi) = n^{\omega}_y$. Using this equations and (3.29), one gets:

$$\sin^2(\phi) = \frac{(n_y^{\omega})^{-2} - (n_y^{2\omega})^{-2}}{(n_x^{2\omega})^{-2} - (n_y^{2\omega})^{-2}} \tag{3.30}$$

If the refractive indices of LBO given in table (3.2) are inserted into this equation, ϕ is found to be $\phi_{32} = 48.7°$.

It is also possible to phase match the SHG due to the coefficient d_{33}. In that case, the input light has to be polarized in the z direction. Thus, $n^{\omega}(\phi) = n^{\omega}{}_z$ and $n^{2\omega}(\phi) = n^{\omega}{}_z$. Again, using (3.29):

$$\sin^2(\phi) = \frac{(n_z^{\omega})^{-2} - (n_y^{2\omega})^{-2}}{(n_x^{2\omega})^{-2} - (n_y^{2\omega})^{-2}} \tag{3.31}$$

When the refractive indices of LBO are used with this equation, a rather small angle is found: $\phi_{33} = 10.75°$. This is the angle for critical phase matching cited by Chen et. al.[19]. If critical phase matching must be used with LBO, it seems advantageous to use the scheme for matching d_{32}, as it is roughly five times larger than d_{33}.

Fig. (3.11) shows a plot of equations (3.29) using the LBO refractive indices. The two phase matching angles obtained above are marked in the graph.

The phase matching discussed so far is termed critical phase matching because $P^{2\omega}$ is a very sensitive function of any mismatch $\Delta\theta$ and $\Delta\phi$. As gaussian (laser) beams are used and not plane waves, mismatch is always present.

A noncritical phase matching (NCPM) condition is achieved if it is possible to make $n^{\omega}{}_y = n^{2\omega}{}_y$ in (3.30) or $n^{\omega}{}_z = n^{2\omega}{}_y$ in (3.31). This can be done by adjusting the temperature of the crystal which in turn changes the refractive indices. In that case a much wider acceptance angle is possible, because Δk now grows much more slowly with $\Delta\theta$ and $\Delta\phi$, which are small deviations from the matched direction (θ,ϕ).[21] Thus, a much wider cone of input light can contribute to SHG. The direction of light propagation in NCPM is along one of the principal axes and in the LBO case it is along the X axis. This can be seen from eq. (3.30) or (3.31), where for NCPM one has $\phi = 0$. Propagation along one of the principal axis avoids problems connected with double refraction and the walk-off angle $\rho = 0$, i. e., the direction of energy flow (Poynting vector) of the fundamental and second harmonic beams is collinear. That ensures efficient energy transfer to the second harmonic beam. The experimentally observed FWHM acceptance bandwidths for LBO in a NCPM arrangement are[19] $\Delta\theta\, l^{1/2} = 71.9$ mrad.cm$^{1/2}$ and $\Delta\phi = 99.1$ mrad.cm$^{1/2}$.

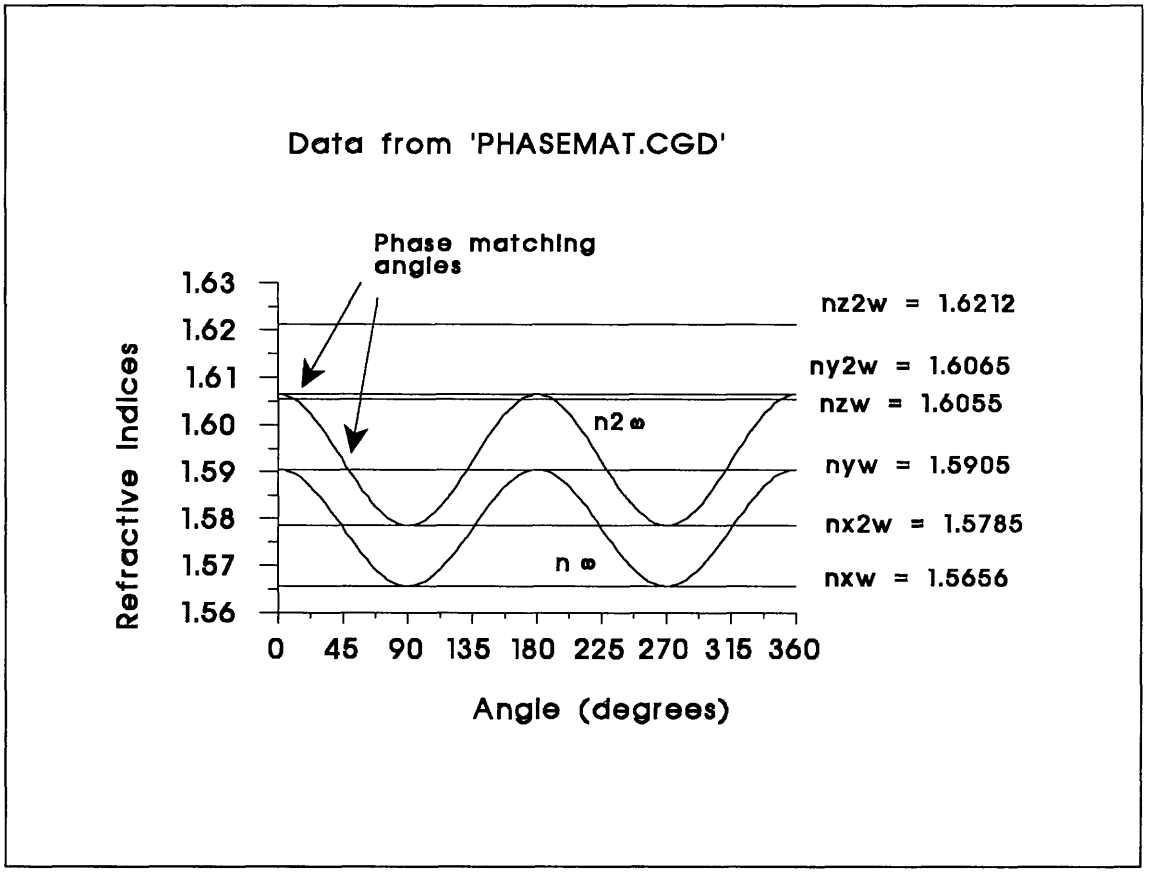

Fig.(3.11) - Graphical representation of equations (3.29). The phase matching angles are shown by the arrows. In NCPM two of the refractive indices (horizontal lines) coincide, making the phase matching angle equal to zero.

3.6) - Experiments in SHG With LBO

The Second Harmonic Generation (SHG) unit of the YAG laser was modified in two important ways for the experiments with the LBO crystal. Firstly, a new support frame was made so that now the SHG crystal can be removed from its fixed position near the laser front mirror and placed at any point on the optical bench. Secondly, a temperature controlled oven with optical access and angle adjustments was built to house the crystal. A CAL9000 PID temperature controller was adapted to drive a low-power power supply connected to a heating element. The heater is kept inside a copper block which works as the crystal holder & heater and the copper block is mounted

inside the small oven with thermally insulating walls. The warm-up characteristics of the oven driven by the temperature controller are shown in Fig.(3.12). The accuracy of the temperature control is very good: the temperature stays within ±0.5° C of the preset value of 150°C. It takes about half an hour to go from room temperature to 150°C. This long warming-up time avoids any temperature gradients inside the crystal.

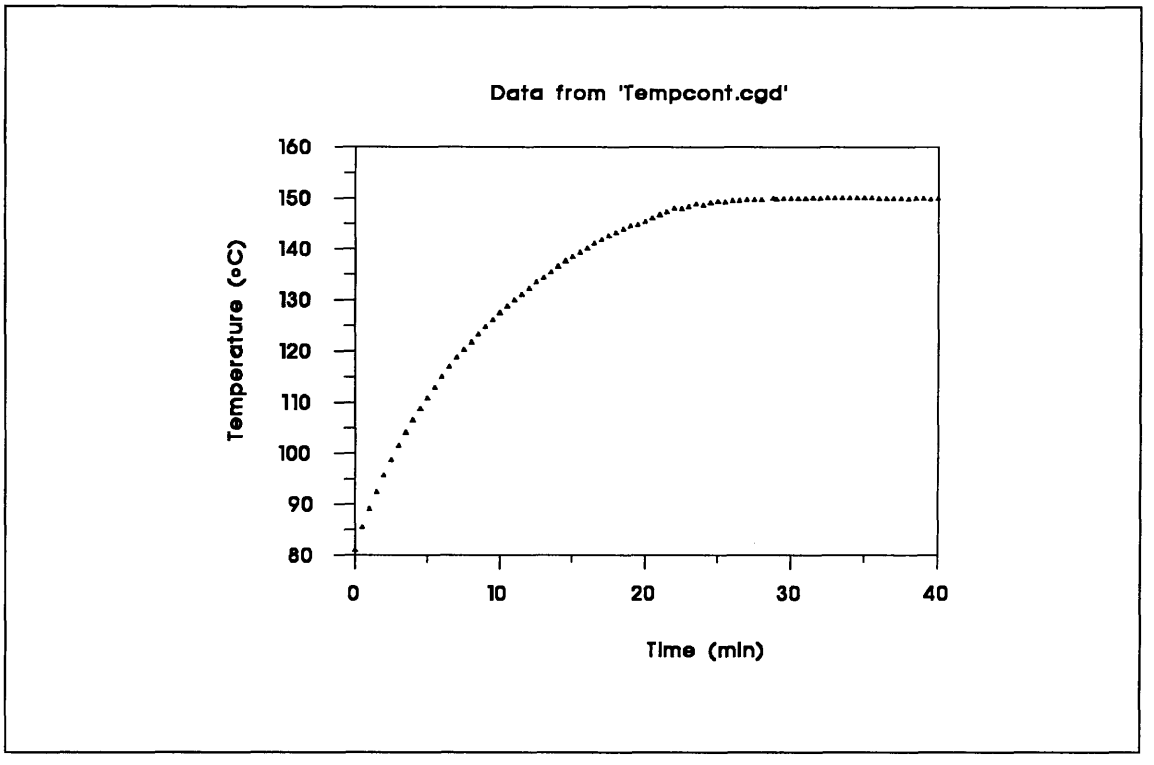

Fig.(3.12) - Warm-up curve for the oven, driven by the temperature controller. It takes about 1/2 hour to reach the temperature of 150°C. The long-term temperature stability is ± 0.5 °C.

The temperature tuning curve of the LBO crystal was measured by heating the oven up to 165° C and then letting it cool down to about 80° C. During the cooling cycle, the mode-locked pulses from the Nd:YAG laser were fired through the crystal and the second harmonic power produced was measured as a function of the temperature. The laser beam was vertically polarized and propagating in the X direction. The crystal was aligned to phase-match d_{32}.The plot in fig.(3.13) shows the distinctive sinc function behaviour as predicted by eq.(3.25).

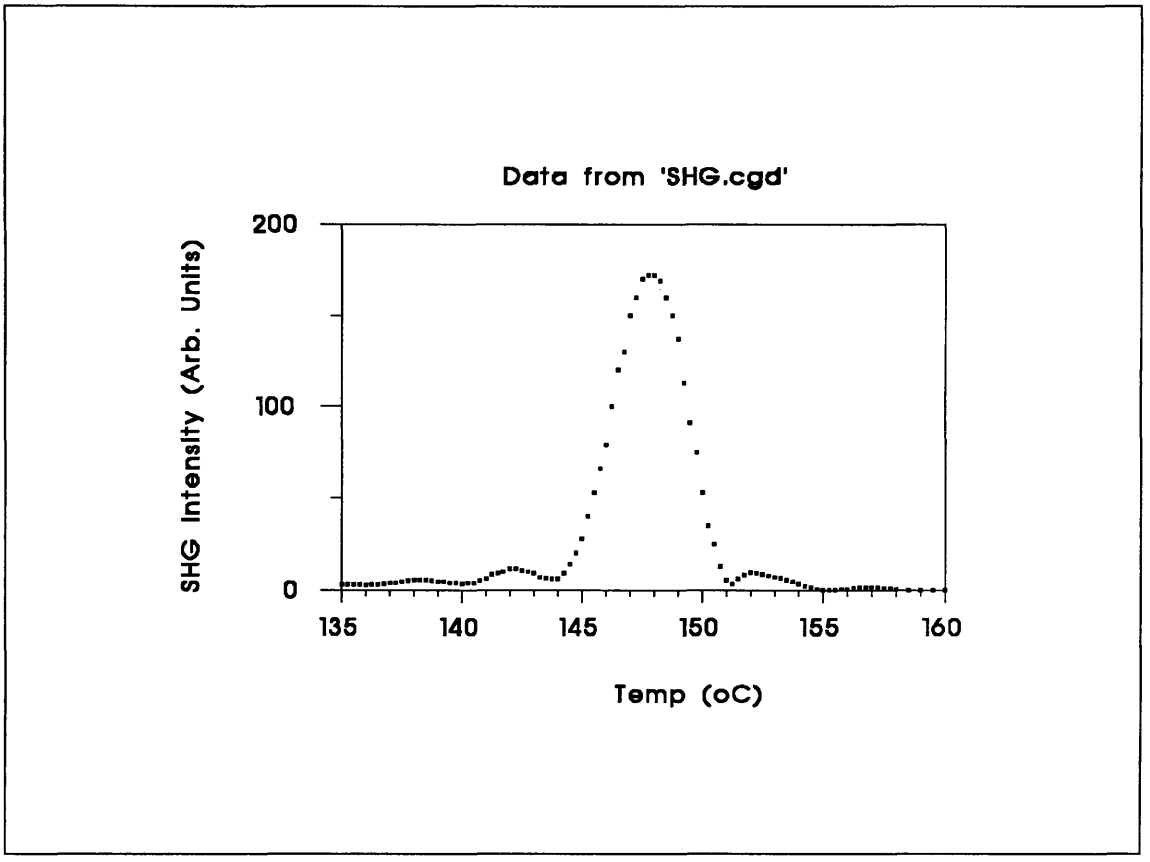

Fig.(3.13) - Measured SHG intensity as a function of the temperature of the LBO crystal.

The phase matching temperature T_m and temperature bandwidth ΔT obtained from fig. (3.13) are $T_m = 148^oC$ and $\Delta T = 3.5^oC$. By rotating the crystal through 90^o around the X axis, the input light is made to interact with a different component of the SHG tensor and so, d_{33} can be measured. The matching temperature is slightly higher, being $T_m = 150^oC$. This is expected, as $(n^{2\omega}_y - n^{\omega}_y) > (n^{2\omega}_y - n^{\omega}_z)$. The temperature bandwidth is unaltered by the rotation.

Various different positions for the SHG unit were tried to see if $P^{2\omega}$ could be maximized. The best position seems to be 65 cm away from the laser front mirror. At this point, the laser spot size is 3 mm.

The best result obtained was $P^{2\omega} = 500$ mW for an input power of $P^{\omega}_{av} = 7$W. That gives a low conversion efficiency of 7%. The reasons for this are not completely understood, but two reasons can be suggested. The spot size might not have been as small as one would expect it to be. Although the lens (f = 35 mm) should have focussed the beam down to well below 50 μm, this might not have happened, because the Nd:YAG laser output is strongly diverging. It was measured to be roughly 2 mrad,

which is one thousand times above the laser specifications. Another source of problems is the fact that the LBO crystal is not AR coated. Part of the input light is wasted in reflections and so is part of the second harmonic light produced, which was seen propagating in the opposite direction, i.e., towards the YAG laser. If the spot size could be reduced inside the crystal and the laser power increased, large improvements in the conversion efficiency could be gained. It is important to mention that the LBO crystal has been used with Q-switched lasers and also as an intracavity second harmonic generator.[20,19] In such cases, very high conversion efficiencies can be obtained. Conversion efficiencies over 70% have been achieved using a power density of 400 MW/cm^2 in a 14 mm long LBO crystal.[20]

3.7) - The picosecond Ti:Sapphire Laser

The mode-locked Ti:Sapphire laser pumped by an Ar^+ ion cw laser seems to be one of the best laser systems for optoelectronic sampling.

In this project, a 2045 (Spectra Physics) cw Argon ion laser was used as the pump source, in power mode, "all lines", producing 9.5 W. The Ti:Sapphire laser used was the (mode-locked) Tsunami laser, manufactured by Spectra Physics. It features an intracavity Gires-Tournois Interferometer[25] as the rear cavity mirror. This is simply a lossless etalon with a partially reflecting front mirror and a 100% reflecting back surface. Interference between the two surfaces produce a periodic phase-versus-frequency curve for the light reflected back into the laser cavity. Portions of this curve can then have the right dispersion to be used as a group velocity dispersion controller for the optical resonator. The separation between the two reflecting surfaces is voltage controlled, so that the GVD control is done by the turn of a single knob.

The laser can be wavelength tuned, from about 720 nm to 840nm. At 790 nm, the peak wavelength, the average output power is 1.6 W. The laser was tuned to $\lambda = 740$ nm and used to pump the photoconductors in the optoelectronic sampling experiments. The laser average output power at this wavelength is about 700 mW. The laser operates at 82 MHz repetition rate and the pulsewidth is very short, being 1.7 ps, as shown by fig. (3.14).

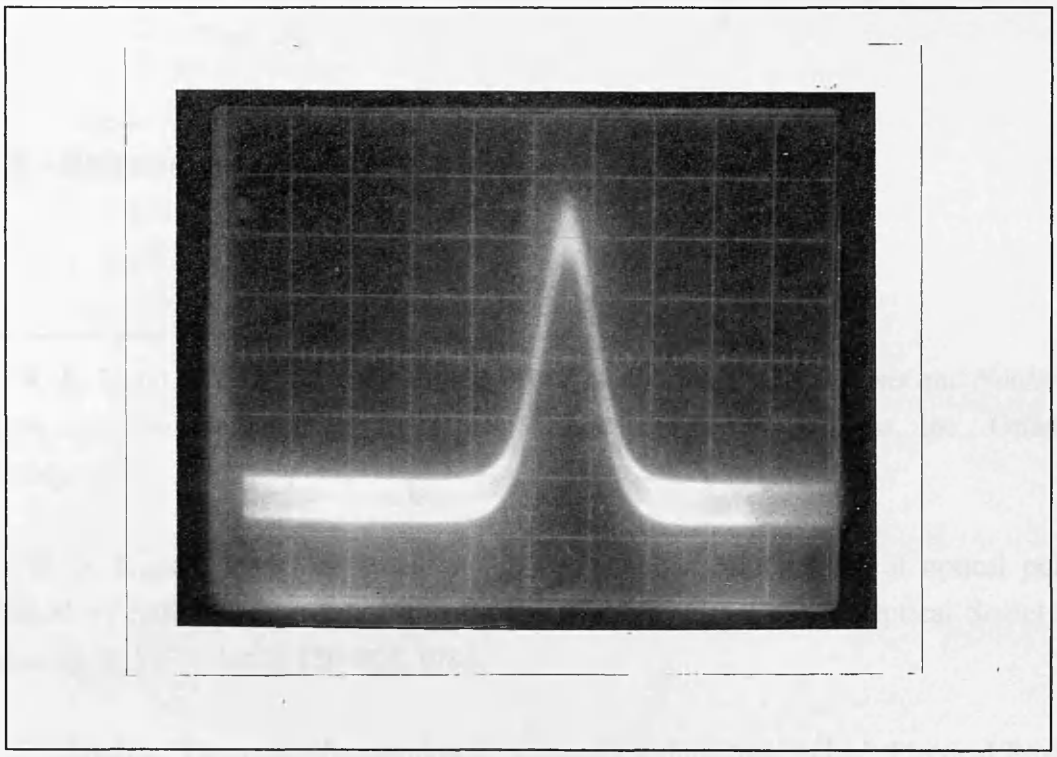

Fig.(3.14) - The autocorrelation trace of the mode-locked Ti:Sapphire laser pulses. The horizontal scale is 2.6 ps/division. Assuming that the pulses have a $[\text{sech}(t)]^2$ shape, the laser pulsewidth is obtained by multiplying the FWHM of the curve above by a factor of 0.6.

Optoelectronic sampling experiments were performed with this laser and the results will be presented later and compared with results from measurements with the dye laser. It is important to notice that this system avoids all the problems with SHG for pumping the dye laser and also that the Ar^+ laser is a much more stable and reliable pump than the Nd:YAG laser.

An enhanced version of the Tsunami laser will soon become commercially available, with tunability from 0.720 μm to 1.06 μm. The pulsewidth will be less than 100 fs and the average power will be roughly the same as the present version.[26] With such a laser system, electrooptic sampling in the manner described in chapter II might come to age. It is also worth mentioning that there is already a Ti:Sapphire mode-locked laser commercially available, with characteristics similar to the above ones, marketed by Coherent Laser Group.

There is, in the conclusions of the present work in chapter VIII, a section devoted to the merits and deficiencies of lasers used in electrooptic and optoelectronic sampling.

3.8) - References to chapter III

[1] - R. K. Dodd, J. C. Eilbeck, J. D. Gibbon and H. C. Morris, in "*Solitons and Nonlinear Wave equations*", Chapter 1, page 19 and chapter 8, Academic Press, Inc., Orlando, Florida, 1984.

[2] - W. J. Tomlinson, R. H. Stolen and C. V. Shank, "Compression of optical pulses chirped by Self-Phase modulation in optical fibers", Journal of the Optical Society of America B, Vol.1, No.2, 139-149, 1984.

[3] - F. Shimizu, "Frequency broadening in liquids by a short light pulse", Physical Review Letters, vol.19, No.19, 1097-1100, 1967.

[4] - A. Siegman, in " *Lasers* ", chapters 9 and 10, Oxford University Press, 1986.

[5] - R. H. Stolen and C. Lin, " Self-Phase modulation in silica optical fibers", Physical Review A, Vol. 17, No.4, 1448-1453,1978.

[6] - A. S. L. Gomes, A. S. Gouveia-Neto, J. R. Taylor, "Optical fibre-grating pulse compressors", Optical and Quantum Electronics, 20, 95-112, 1988.

[7] - E. B. Treacy, "Optical pulse compression with diffraction gratings", IEEE Journal of Quantum Electronics, Vol. QE-5, No.9, 454-458, 1969.

[8] - P. Kean, K. Smith and W. Sibbett, "Modulator frequency detuning effects in a cw mode-locked Nd:YAG laser with active stabilization", Optics Communications, Vol.61, No.2, 129-133, 1987.

[9] - M. J. W. Rodwell, D. M. Bloom and K. J. Weingarten, "Subpicosecond laser timing stabilization", IEEE Journal of Quantum Electronics, Vol. 25, No. 4, 817-827, 1987.

[10] - BPW28 Silicon avalanche photodiode manufactured by Telefunken. See "Data sheets collection IR-components", pages 49-51, by Telefunken Electronic GmbH.

[11] - A. Yariv, "*Optical Electronics*", third edition, chapter 6, section 6.9, Holt-Saunders, N Y, 1985.

[12] - R. F. Belt, G. Gashurov and Y. S. Liu, "KTP as a harmonic generator for Nd:YAG lasers", Laser Focus/Electro-optics, 110-124, October, 185.

[13] - J. Q. Yao, T. S. Gahlen, "Calculations of Optimum phase match parameters for the biaxial crystal $KTiOPO_4$", Journal of Applied Physics, 55 (1), 65-68, 1984.

[14] - "Laser induced damage" in Melles Griot Optics Guide 4, pages 14-2 and 14-3, 1988.

[15] - "Laser induced damage in optical materials", a series of NBS special publications, Vols. 1970 -1987.

[16] - Personal communication from Quantronix Corporation.

[17] - Technical note from Cashitech "LBO, New", Fuzhou, Fujian, China.

[18] - "Chinese researchers develop nonlinear and other crystals", in Laser Focus World, Vol.27, No.12, 46-50, Dec. 1991.

[19] - C. Chen, Y. Wu, A. Jiang, B. Wu, G. You, R. Li and S. Liu, "New nonlinear optical crystal: Li B_3 O_5 ", Journal of the Optical Society of America B, 616-621, 1989.

[20] - Technical note from Cashitech, "Recent developments of LBO crystals", Fuzhou, Fujian, China.

[21] - M. V. Hobden, "Phase-Matched Second-Harmonic Generation in Biaxial Crystals", Journal of Applied Physics, Vol. 38, No. 11, 4365-4372, 1967.

[22] - S. Singh, D. A. Draegert and J. E. Gensic, "Optical and Ferroelectric properties of Barium Sodium Niobate", Physical Review B, Vol.2, No. 7, 2709-2724, 1970.

[23] - S. Singh, "Non-linear optical materials", in *Handbook of Lasers*, Chapter 18, 489-507, CRC Press, USA, 1971.

[24] - M. Born and E. Wolf, "*Principles of Optics*", Chapter 14, section 14.3, 678-684, Sixth edition, Pergamon Press, 1986.

[25] - A. E. Siegman, in "*Lasers*", pages 348-350, Oxford University Press, 1986.

[26] - Spectra Physics - Private communication.

Chapter IV - Modelling of Coplanar Waveguides and Photoconductors.

4.1) - Basic Transmission Line Theory

In the interest of clarification, the basics of the transmission line theory and mode guiding will be presented here. This section is mainly concerned with the definition of terms and parameters which are important for the modelling of the Coplanar Waveguide (CPW).

The rigourous way of analysing transmission lines (TLs) is by writing Maxwell's equations and imposing the appropriate boundary conditions. After some algebraic manipulations, one obtains the wave equation for the problem in question. A more mnemonic approach will be taken here, namely the circuit approach. The advantage of having an equivalent circuit for the TL is that all important terms can be easily defined and essentially the same results are obtained.

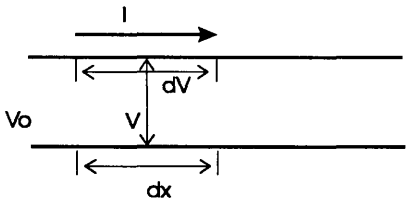

a) - A small piece dx of a TL has voltage drop dV.

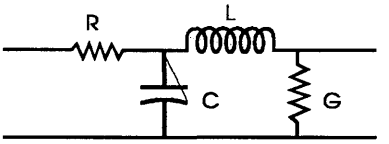

b) - The equivalent circuit for the length dx of the transmission line

Fig.(4.1) - The equivalent circuit for a section of a transmission line.

The equivalent circuit for a small section of a TL is shown in fig. (4.1). The circuit elements are represented as lumped, but in fact they have to be understood as distributed circuit elements. Therefore the series resistance R is a resistance per unit length (Ω/m), the shunt capacitance C is given in F/m and so on. Applying Ohm's law to the TL, the voltage drop dV per length dx of the line is given by the current flowing times the series impedance:

$$\frac{dV}{dx} = -(R + j\omega L) \cdot I \qquad (4.01)$$

The current flowing along the same length dx is:

$$\frac{dI}{dx} = -(G + j\omega C) \cdot V \qquad (4.02)$$

Differentiating (4.01) in x and using (4.02), one gets:

$$\frac{d^2V}{dx^2} = -(R + j\omega L) \cdot \frac{dI}{dx} = (R + j\omega L) \cdot (G + j\omega C) \cdot V = ZYV \qquad (4.03)$$

where

$Z = R + j\omega L$ is the series reactance per unit length, in Ωm^{-1}.
$Y = G + j\omega C$ is the shunt admittance in $\Omega^{-1}\ m^{-1}$

Equation (4.03) is the voltage wave equation for the transmission line. By differentiating (4.02) and using (4.01), the current wave equation is obtained:

$$\frac{d^2I}{dx^2} = ZYI \tag{4.04}$$

The solution of the equations (4.03) and (4.04) can be written as:

$$V(x) = V_1 \cdot e^{-\alpha x} \cdot e^{j(\omega t - \beta x)} + V_2 \cdot e^{\alpha x} \cdot e^{j(\omega t + \beta x)} \tag{4.05}$$

$$I(x) = \frac{V_1}{\sqrt{Z/Y}} \cdot e^{-\alpha x} \cdot e^{j(\omega t - \beta x)} - \frac{V_2}{\sqrt{Z/Y}} \cdot e^{\alpha x} \cdot e^{j(\omega t + \beta x)} \tag{4.06}$$

Where $\alpha = \mathrm{Re}\sqrt{ZY}$ is the attenuation constant and $\beta = \mathrm{Im}\sqrt{ZY}$ is the propagation constant.

The characteristic impedance experienced by a wave travelling in the positive direction is defined as the ratio V/I:

$$Z_0 = \sqrt{\frac{Z}{Y}} = \sqrt{\frac{R + j\omega L}{G + j\omega C}} \tag{4.07}$$

If the line is lossless, i.e., R = 0 and G = 0 or if the frequency is high so that $\omega L >> R$ and $\omega C >> G$, then (4.07) simplifies to:

$$Z_0 = \sqrt{\frac{L}{C}} \tag{4.08}$$

The phase velocity of a wave travelling in the transmission line is given by ω/β. Again, assuming the lossless approximation:

$$v_{ph} = \omega/\beta = \frac{\omega}{\mathrm{Im}(\sqrt{ZY})} = \frac{\omega}{\omega\sqrt{LC}} = \frac{1}{\sqrt{LC}} \tag{4.09}$$

Hence, the phase velocity of a wave and the transmission line characteristic impedance are related, in the lossless case, by:

$$Z_0 = \frac{1}{C\, v_{ph}} \tag{4.10}$$

Where C is the capacitance per unit Length.

4.2) - Types of Transmission Lines used in MMICs

When the characteristics of a transmission line structure can be determined by its dimensions in a single plane, the structure is said to be planar. This is important because it facilitates the design of such circuit elements and its fabrication by lithographic techniques. The most popular transmission line used in MMICs is the microstrip. Other common choices are slotlines and coplanar waveguides. Fig. (4.2) shows diagrams of their cross sections.

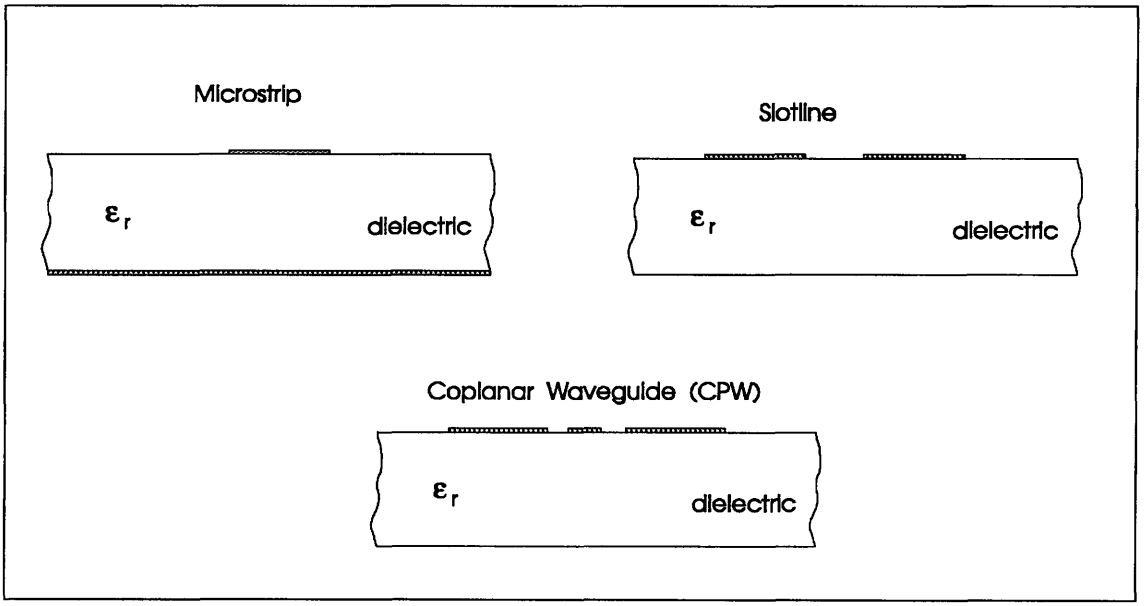

Fig.(4.2) - Cross-sections of common planar transmission lines used in MMICs.

One important feature of these transmission structures is that the dielectric medium in all of them is inhomogeneous. A wave propagating in one of these structures will travel partly in the dielectric of permittivity ε_r and partly in air. This leads to many problems in modelling those structures. In particular it can be shown that the microstrip, CPW and the others can not support a pure TEM wave.[1] The boundary conditions at the air dielectric interface are used to show the existence of axial field components. The departure from pure TEM behaviour is small for the microstrip and even smaller for the CPW. One then talks of quasi-TEM modes for these structures.

The cut-off frequency of the lowest order TE mode of the microstrip line is given by:[1]

$$F_{TE} = \frac{c}{4d\sqrt{\varepsilon_r - 1}} \qquad (4.11)$$

Where c is the speed of light and d is the thickness of the dielectric. Thus, for a microstrip made on a GaAs chip 0.5 mm thick, the frequency below which the mode TE_{10} can not propagate is about 43 GHz. It would seem at first that it would not be possible to propagate low frequency signals along these lines. However, microstrips have been used for years to transmit signals from dc up to the microwave region. This is possible due to the quasi-TEM modes. In fact, the lowest order quasi-TEM mode does not have a cut-off frequency, i.e., dc signals also propagate in the microstrip.

4.3) - The coplanar waveguide transmission line.

The Coplanar Waveguide Transmission Line (CPW) was proposed in 1969, by C. P. Wen.[2] Since then, it has been used in many circuit applications as in a 2-18 GHz distributed amplifier.[3,4] It is a transmission line composed of a central conductor strip of width S, surrounded by two ground planes placed at a distance w. Fig. (4.3.a) shows the basic structure and (4.3.b) a possible field distribution in the CPW. For this simple mode of propagation (normally called the CPW mode), only the lines of the magnetic field cross the discontinuity between the two dielectrics. This suggests that the CPW suffers less departure from the TEM behaviour than the microstrip, at least at low frequencies. Complications arise if the dielectric substrate thickness is not much larger than the gaps in the CPW structure. Another source of potential problems is the finite width of the ground planes, which can lead to dispersion, due to the excitation of higher order modes,

like the slot line mode shown in fig.(4.4) below. The effects of these higher order modes will be briefly discussed later in this chapter.

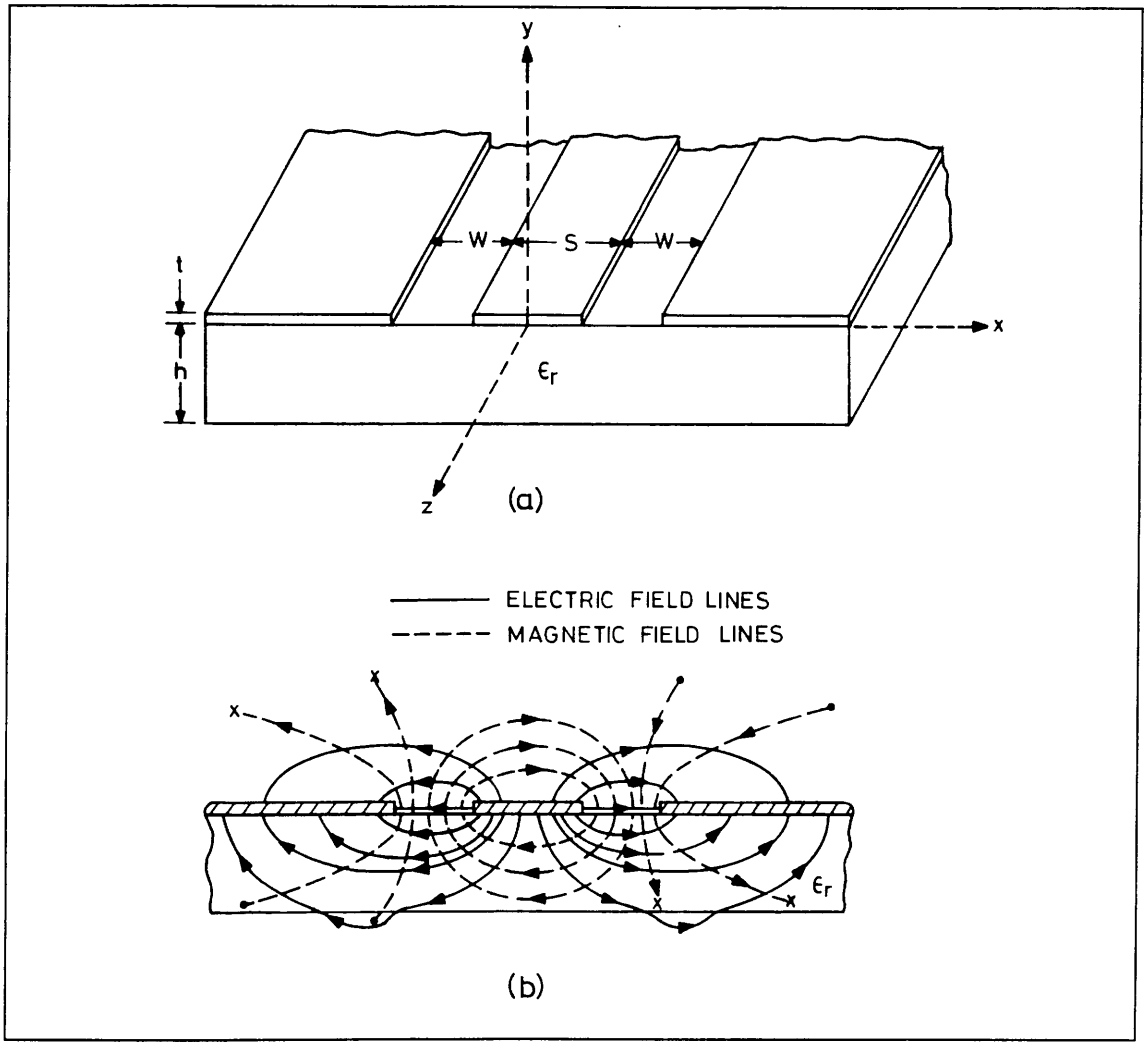

Fig.(4.3) - (a) - The coplanar waveguide structure. (b) - The coplanar waveguide mode.

The exact modes propagating in the CPW, specially at high frequencies (many tens of GHz) are not well understood. The same could be said about the microstrip. In recent years however, the CPW has gained popularity because it offers

some advantages over the microstrip configuration. Most of them stem from the fact that the two grounds are placed at the same plane as the central conductor. This means that no via holes have to be etched in the substrate for ground connections in an MMIC as is the case with microstrips. Much more effective grounding using air bridges can be made in the CPW. Ground connections in microstrips can suffer from parasitic inductances which are difficult to control. It is also common and normally imperative to thin the dielectric substrates of microstrips. This is done to suppress the TE modes by increasing their cut-off frequency (eq. 4.11). In materials such as GaAs, this operation coupled with via holes makes the substrate very brittle and can decrease the yield considerably.

Another important advantage of CPW over microstrips appears when discontinuities in the lines are taken into account. Numerical calculations show that a Tee junction has little effect in the propagating modes of the CPW. For the microstrip, a number of new lossy modes are excited in such a discontinuity.[5]

Finally, It is easy to design Mesfets in a CPW geometry, which allows probing with CPW probes for S-parameter measurements. It seems therefore natural to extend the Mesfets pad structure so as to make the CPWs, pulse generators and sampling gates, as shown in chapter II, fig.(2.8).

4.4) CPW modelling

The analysis of CPW, i.e., the calculation of its dimensions to produce a specific characteristic impedance and mode structure can be done in a number of ways. The simplest approaches assume that the modes of propagation are pure TEM. These are quasi-static methods and the characteristic impedance of the line is calculated from the electrostatic capacitance of the structure.

Dispersive models can also be used, where the deviation from TEM modes is accounted for by empirical means. The non-TEM behaviour causes the effective dielectric constant ε_{eff} (to be defined later) and the characteristic impedance Z_0 to change with frequency.

Propagation modes and dispersion in CPW have been investigated analytically and by numerical techniques.[6,7,8] Loss has also been modelled numerically.[9] Riaziat et. al. studied loss and dispersion in the coplanar waveguide structure in five different cases, based on substrate thickness, backside metallization and ground plane width.[6] An idealized CPW is described in their work as a pair of coupled slotlines, having odd and even modes. These modes are referred to as the CPW mode and the slot

line mode respectively. The field distribution of the CPW mode was shown in fig. (4.3.b) and that for the slotline mode is shown below in fig. (4.4). This is an almost TE mode[1].

The devices made in this work have finite substrate without backside metallization. When the substrate thickness is comparable to the dielectric wavelength (λ inside the dielectric) reflections from the back-plane air-dielectric interface become important. The structure can in this case support dielectric slab waveguide modes. In general, the CPW modes interact very weakly with the above modes. However, in the frequency ranges where the propagation constants of the dielectric slab modes approach that of the CPW and phase matching occur, considerable dispersion and radiation losses can take place.[6]

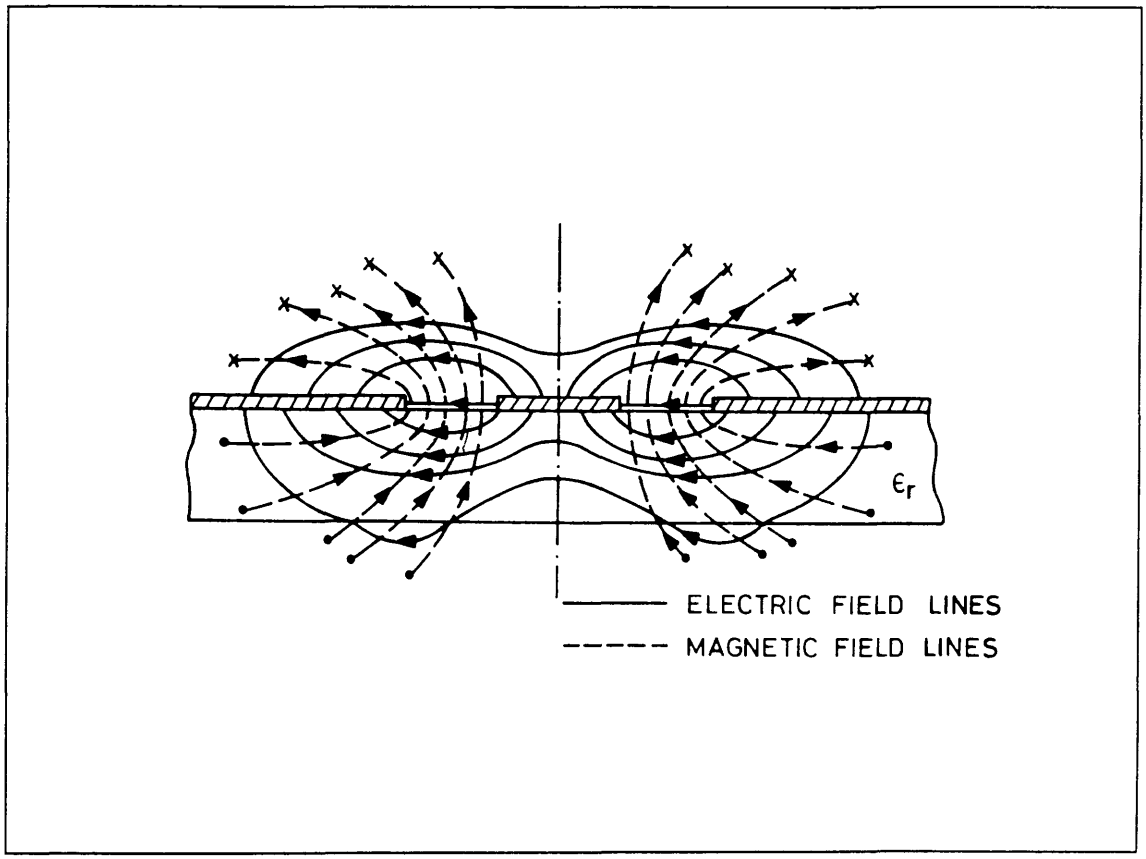

Fig.(4.4) - The slotline mode excited in the Coplanar Waveguide.

It is therefore fair to say that the moding behaviour of these transmission structures (specially when there are discontinuities involved) is still an open area of research. The requirements of computing power and time for the calculations involved

are very demanding. To cite an example, the HP85180 high frequency structure simulator program running in an Apollo workstation, has been used in this department for modelling Tee junctions in CPWs.[5] This is a finite element vector wave equation solver. It can calculate S-parameters of arbitrary lossless 3-dimensional structures, field profiles, characteristic impedances, etc. The program automatically generates a tetrahedral mesh of points and calculates the field inside each cell. The mesh is then refined and the calculations are repeated until the fields converge to a solution. Due to this technique, a minimum of 64 MBytes of memory is necessary. The calculations of a full frequency sweep (up to about 100 GHz) of a CPW Tee junction take approximately three days! The field distributions of a simple piece of CPW without any discontinuity or airbridges take about three hours to be calculated. It is therefore very desirable to have approximated expressions for the estimation of the behaviour of these structures.

4.4.1) - Quasi-static analysis of the Coplanar Waveguide Transmission Line

Wen[2] proposed the CPW structure as a transmission medium and put forward its first theoretical analysis. It was a quasi-static approximation where the modes of propagation were considered to be pure TEM. This is an interesting approximation, because it gives helpful insights into the behaviour of the CPW. In his model, the dielectric substrate has a very large thickness so that it can be considered infinite. The metallization thickness is considered negligible and the width of the ground planes is also considered to be infinite. The assumptions above are reasonable if the substrate thickness is greater than twice the slot width,[1] which is the case here. Finite substrate thickness corrections of this model can be found in M. E. Davis[10] et. al..

The mathematical derivations that lead to the calculation of the characteristic impedance will be presented in detail in the appendix 4.A of this chapter. As the calculation itself is lengthy and not essential here, it is left to the appendix. Only the main results are quoted below. It is necessary to use complex function techniques to obtain an analytic expression for the capacitance of the CPW structure.

Fig. (A.1.a) in appendix 4.A shows a cross section of the device. By using the Schwarz-Christoffel conformal transformation, the X axis and the half complex plane below it can be mapped onto the rectangle shown in fig. (A.1.b), in appendix 4.A. The location of the four vertices of the rectangle is then determined by two numbers a and b (fig. A.1.b), whose ratio is:

$$\frac{a}{b} = \frac{K(k)}{K'(k)} \qquad (4.12)$$

Where K(k) is the complete elliptic integral of first kind and

$$K'(k) = K(k'),$$

with

$$k = \frac{a_1}{b_1} = \frac{S}{S + 2w}$$

and (4.13)

$$k^2 + k'^2 = 1$$

S is the central conductor (strip) width and w is the gap width.

It is easy to analyse the CPW in the transformed complex plane, where it is represented by the rectangle in fig. (A.1.b). Using eqs. (A.11), (A.12) and (A.13), which give the vertices of the rectangle, the capacitance per unit length associated with the half space filled by the dielectric substrate can be evaluated as:

$$C_d = \varepsilon_0 \varepsilon_r \frac{2a}{b} \tag{4.14}$$

And the capacitance of the empty half-plane is:

$$C_{air} = \varepsilon_0 \frac{2a}{b} \tag{4.15}$$

Hence, the total capacitance per unit length is:

$$C_T = C_d + C_{air} = (\varepsilon_r + 1)\, \varepsilon_0 \frac{2a}{b} \tag{4.16}$$

The useful concept of effective dielectric constant has to be introduced now. It is important because it gives a measure of the proportion of field travelling in the air to that in the substrate. From eq. (4.09) the phase velocity along the CPW made on the GaAs substrate is:

$$v_{ph} = [\, L\, C_T \,]^{-1/2} \tag{4.17}$$

And the field travelling along the line with the substrate replaced by air has a phase velocity equal to c, the speed of light in vacuum:

$$c = [\, L\, C_{Tair}\,]^{-1/2} \tag{4.18}$$

Where $C_{Tair} = 2\, C_{air}$ from eq. (4.15).

The effective dielectric constant, or effective permittivity, is defined as the ratio of the squares of the two equations above:

$$\varepsilon_{eff} = \frac{c^2}{v_{ph}^{\,2}} = \frac{C_T}{C_{Tair}} = \frac{\varepsilon_r + 1}{2} \tag{4.19}$$

It is important to mention that this expression is an approximation as the expression for v_{ph} itself is also approximated. Many correction expressions to eq.(4.19) exist and one of them will be presented later. ε_{eff} is frequency dependent and this fact is not taken into account in (4.19). The geometrical shape of the line is also important, specially the ratio (w/d) of the gap width w to the substrate thickness d. Nevertheless, a good estimation of the characteristic impedance can be obtained from (4.19), which holds at least up to about 10GHz (the X band), according to Gupta.[1]

$$Z_0 = \frac{1}{C\, v_{ph}} = \frac{1}{C_T} \cdot \frac{\sqrt{\varepsilon_{eff}}}{c} \tag{4.20}$$

Hence

$$Z_0 = \frac{1}{4\, c\, \varepsilon_0} \cdot \frac{1}{\sqrt{\dfrac{\varepsilon_r + 1}{2}}} \cdot \frac{K'(k)}{K(k)} \quad (\Omega) \tag{4.21}$$

Where equations (4.10), (4.12), (4.14)-(4.16) were used to obtain (4.21), and

c = speed of light in vacuum

ε_0 = electric permittivity of vacuum

ε_r = relative dielectric constant of the substrate material

K,K' = complete elliptic integrals of first kind.

The ratio between the two elliptic integrals in the expression above can be approximated by elementary functions. The algorithm developed by W. Hilberg can produce results with any degree of accuracy.[11] In particular:

$$\frac{K}{K'} = \frac{1}{\pi} \cdot \ln\left(2\frac{1+\sqrt{k}}{1-\sqrt{k}}\right) \qquad \text{for} \quad \frac{1}{\sqrt{2}} < k < 1$$

and (4.22)

$$\frac{K}{K'} = \frac{\pi}{\ln\left(2\frac{1+\sqrt{k'}}{1-\sqrt{k'}}\right)} \qquad \text{for} \quad 0 < k < \frac{1}{\sqrt{2}}$$

These expressions have an error lower than 3×10^{-6}.

Using equations (4.21) and (4.22) and fixing the central conductor strip width to s = 43 μm, Z_0 was calculated for w varying from 430 μm to 4.3 μm. The plot below in fig. (4.5) shows Z_0 as a function of the ratio s/w. The GaAs dielectric constant ($\varepsilon_r = 13$) was used in the calculations.

Coplanar waveguides of characteristic impedance $Z_0 = 50\Omega$ were made in this work. This choice of impedance avoids any electrical mismatch between the CPW structure and the MESFET gate and drain contacts. Following previous work done in this department, the FETs are also designed to have an impedance of 50Ω in their pads, which allows them to be probed by 50Ω Cascade Microtech CPW probes.[12] From the data shown in fig. (4.5), the ratio s/w = 1.43 gives an impedance of 50Ω. For the strip width s considered before, this gives a gap width w = 30μm.

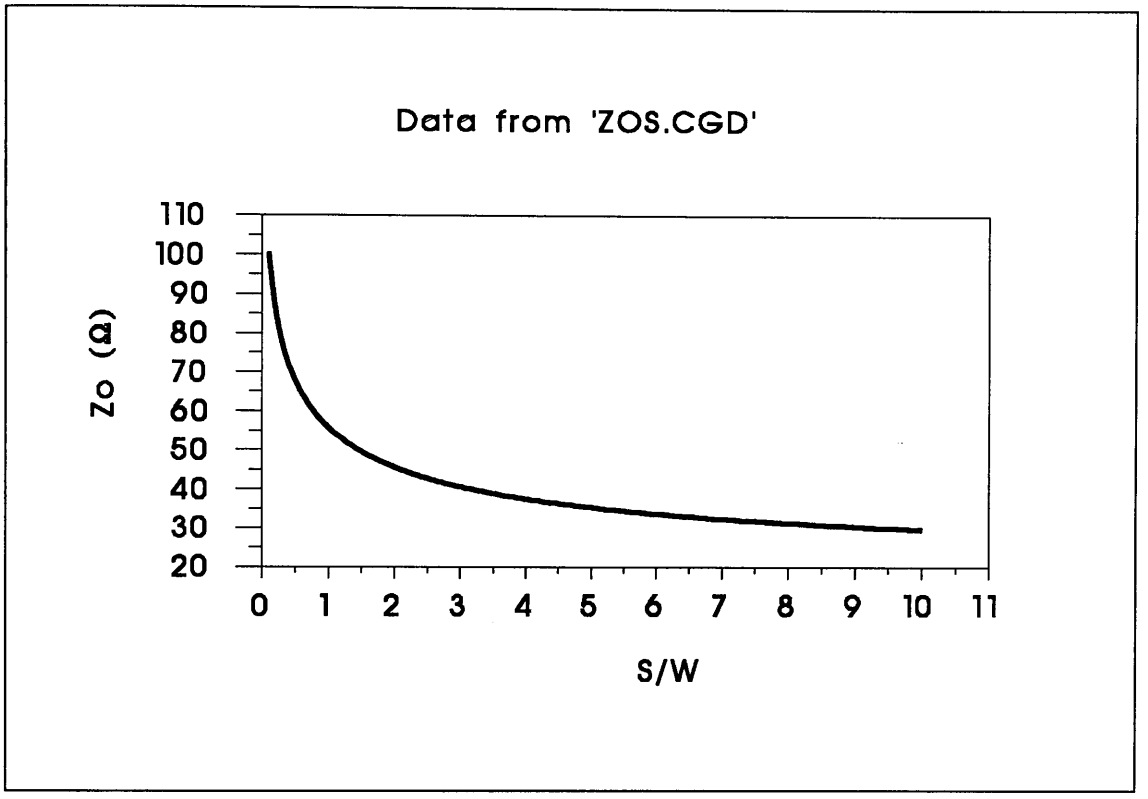

Fig.(4.5) - Variation of the Characteristic impedance Zo with the ratio of the CPW dimensions. s is the central strip width and w is the gap width.

4.4.2) - Dispersion relations for the Coplanar Waveguide Transmission Lines.

The situation where ultra-short electric pulses propagate in the coplanar waveguide is considerably more complicated than cw propagation. An ultra-short pulse will have a wide bandwidth and different frequencies composing the pulse will have different group velocities. Li, Arjavalingam and others[13] have shown that gaussian pulses of FWHM = 0.5 ps have their low and high frequencies split after propagating 10 mm in a microstrip.

The propagation of short electric pulses through CPWs has some aspects in common with the propagation of short light pulses through optical fibres (chapter III) having group velocity dispersion, but with negligible self-phase modulation. In particular, if the frequencies present in the pulse are not higher than about 700 GHz, then the CPW has a *positive* group velocity dispersion behaviour, i.e., $dv_g/d\omega < 0$. In the case of pulses generated by photoconductive switches, this leads to pulse re-shaping, because the high frequency components move to the trailing edge of the pulse.

If the frequency of the electrical waveform being propagated is sufficiently high, the wavelength becomes comparable to the cross section of the line. In this situation, the wave velocity becomes frequency dependent. This phenomenon of dispersion can be conveniently described by an effective dielectric constant.

Yamashita[14] et. al. found a simple analytical expression that fits well to calculations of dispersion, by solving Maxwell equations for the microstrip. These approximate dispersion relations were extended to coplanar-type transmission lines up to the terahertz regime and used to compute the distortion of picosecond pulses propagating in such lines.[15] The effective dielectric constant ε_{eff} for the CPW, as a function of frequency, is given by the following set of equations:[15]

$$\sqrt{\varepsilon_{eff}(f)} = \sqrt{\varepsilon_{eff}(0)} + \frac{\sqrt{\varepsilon_r} - \sqrt{\varepsilon_{eff}(0)}}{1 + a F^{-b}} \qquad (4.23)$$

Where

$$\varepsilon_{eff}(0) = \frac{\varepsilon_r + 1}{2} \cdot \{ \tanh\left[1.785 \log\left[\frac{d}{w}\right] + 1.75\right] + + \left[\frac{k\,w}{d}\right] \cdot [\, 0.04 - 0.7\,k + 0.01\,(1 - 0.1\,\varepsilon_r)\,.\,(0.25 + k)\,]\} \qquad (4.24)$$

In the last equation ε_r is the relative dielectric constant of the substrate material, d and w were defined in fig. (4.3.a) and $k = a_1/b_1$ was defined in eq. (4.13).

The normalized frequency F appearing in (4.23) is given by:

$$F = \frac{f}{F_{TE}} \qquad (4.25)$$

Where f is the frequency and F_{TE} is the cut-off frequency of the lowest order TE mode given in eq.(4.11).

The constants a and b in (4.23) depend in general on the line geometry. For CPWs, $b \approx 1.8$, being almost independent of the dimensions, while a is obtained from:

$$\log(a) = u \,.\, \log\left[\frac{s}{w}\right] + v \qquad (4.26)$$

and

$$u = 0.54 - 0.64\,q + 0.015\,q^2$$
$$v = 0.43 - 0.86\,q + 0.540\,q^2 \qquad (4.27)$$

Where

$$q = \left[\frac{s}{d}\right] \qquad (4.28)$$

The set of equations above were derived based on a full wave analysis in the spectral domain.[16,17] It was found that the results obtained from this set of equations agree within 5% with the full wave analysis for the following range of parameters:

$$0.1 \leq s/w \leq 5 \qquad 0.1 \leq s/d \leq 5$$
$$1.5 \leq \varepsilon_r \leq 50 \qquad 0 \leq f/F_{TE} \leq 10 \qquad (4.29)$$

When these formulas were proposed, their validity was not tested outside this range of parameters, due to computational limitations to perform the full wave analysis. Recently they were combined with expressions for attenuation and shown to be in excellent agreement with *experimental* results for frequencies up to 1 THz![18]

There are also other experimental results validating these equations. Measurements of dispersion were made on coplanar waveguides fabricated on Lithium Tantalate substrates.[19] The prediction of dispersion obtained from equations (4.23) - (4.28) agrees remarkably well with those experimental results, from dc up to 150 GHz. In another experiment with superconducting transmission lines, these equations were used with other analytical expressions for superconducting loss and dispersion, to predict the pulse shapes after propagation.[20] Ultrafast optical switches were used to launch fast electrical pulses on the superconducting lines. These pulses were then measured by electro-optic sampling after propagating 0, 0.15, 0.3, 0.9 and 1.5 mm down the line. It was found that severe pulse reshaping takes place, even for these short propagation distances. The measurements were compared with a theoretical model which includes

eqs. (4.23) - (4.28) to account for modal dispersion. The agreement between theory and experiment is remarkable in this case.

The fabrication of the coplanar waveguides will be fully described in the next chapter. For the purpose of modelling, the CPW dimensions are:

strip s = 43 μm w = 30 μm

d = 500 μm

Using the values for the parameters above and the equations (4.23) - (4.28), the effective permittivity as a function of frequency was calculated and it is shown in fig.(4.6), below. For simplicity, ε_r was considered constant over the whole frequency range.

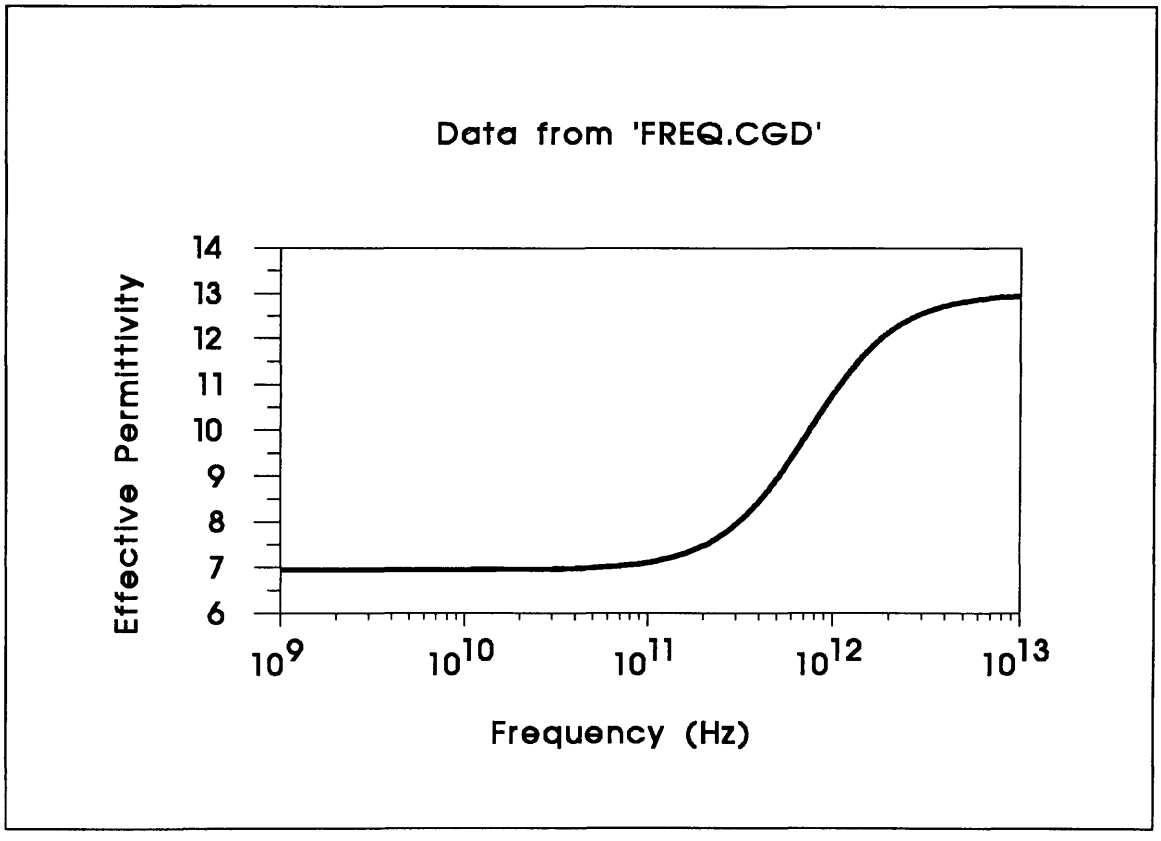

Fig.(4.6) - The effective permittivity for the 50Ω coplanar waveguide, from 1GHz up to 10THz. Note that up to about 700GHz, $\frac{d^2n}{dv^2} > 0$, which leads to $\beta'' > 0$.

It is important to mention that, in general, ε_r is also a function of frequency. However, for GaAs, the change in ε_r is very small for frequencies up to 1THz.[21] In this frequency range, ε_r increases from 13.0 to 13.028 and thus its effect is negligible. At frequencies of about 7 THz, on the other hand, the TO phonon resonance comes into play and ε_r increases sharply. Thus, the curve in fig.(4.6) does not describe ε_{eff} correctly for frequencies of many THz.

If the effective permittivity above is used together with equation (4.20) for the characteristic impedance, one gets Zo as a function of the frequency. Fig. (4.7) below shows Zo x ν for s/w = 1.43.

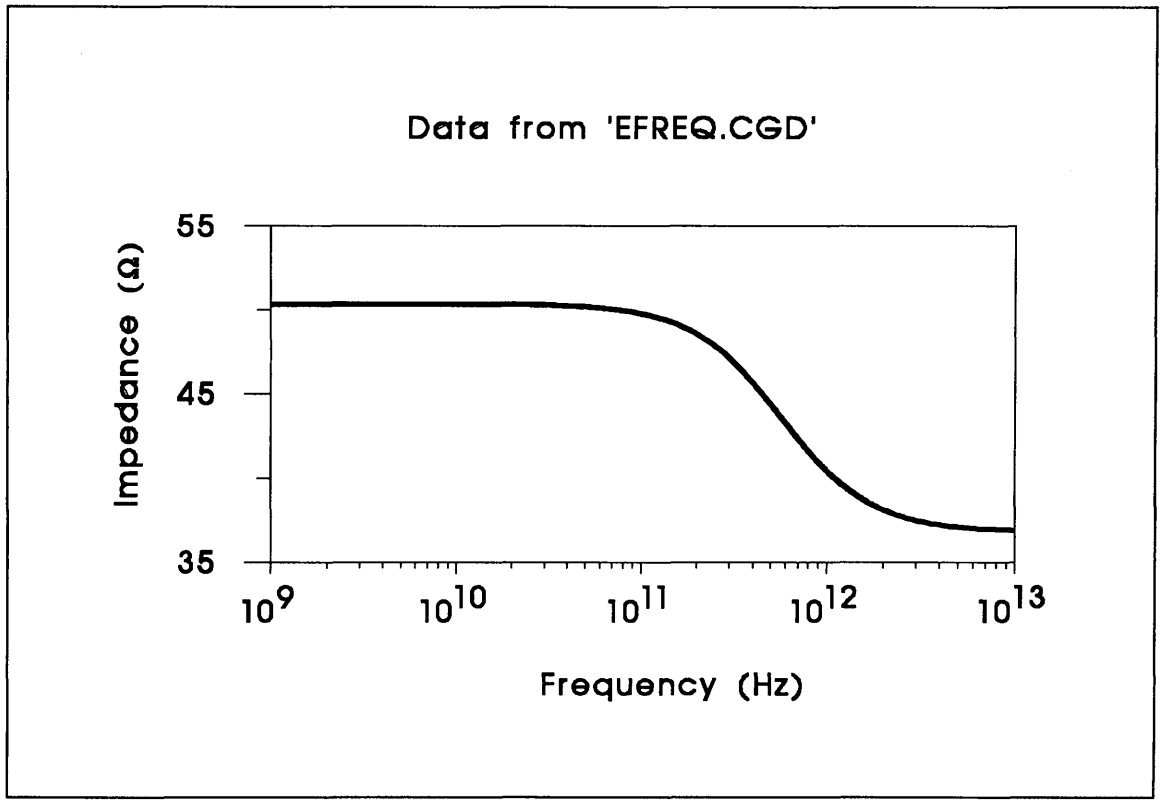

Fig.(4.7) - The variation of characteristic impedance Zo with frequency for the coplanar waveguide with dimensions s = 43 μm and w = 30 μm. ε_r was assumed to be constant for the whole frequency range considered in the graph.

4.4.3) - Pulse propagation and distortion in CPWs.

The propagation of short electric pulses in microstrips was investigated by Li, Arjavalingam and others.[13] Dispersion models for conventional and superconducting coplanar waveguides were developed by Hasnain[15] and Whitaker[22] respectively. The propagation of short pulses in the CPWs fabricated in this work will now be considered.

A gaussian pulse of FWHM τ and amplitude V_0 has the following form:

$$V(0,t) = V_0 \cdot e^{-(4 \ln 2)\, t^2/\tau^2} \tag{4.30}$$

Its Fourier transform is given by:

$$V(0,\omega) = \sqrt{\frac{\pi}{4 \ln 2}} \cdot V_0 \cdot \tau \cdot e^{-\omega^2\tau^2/(16 \ln 2)} \tag{4.31}$$

If the pulse in equation (4.30) propagates a distance L in a CPW, its different frequencies will have different propagation constants. This leads to dispersion and pulse distortion. In frequency domain, this can be accounted for by multiplying each frequency by the appropriate phase factor:

$$V(L,\omega) = e^{-j\beta(\omega)L} \cdot V(0,\omega) \tag{4.32}$$

The propagation function $\beta(\omega)$ is given by:

$$\beta(\omega) = \frac{\omega}{c} \cdot \sqrt{\varepsilon_{eff}(\omega)} \tag{4.33}$$

and $\varepsilon_{eff}(\omega)$ is obtained from eqs.(4.23) - (4.28).

The pulse in time domain at a distance L can then be obtained by taking the inverse Fourier transform of eq. (4.32).

A computer program was written to perform these calculations. The FFT algorithm was used to calculate the Fourier transforms.[23,24] The gaussian pulse was generated with $V_0 = 1$ and $\tau = 0.5$ ps. A time interval T from - 32 ps to + 32 ps was sampled at 512 points to obtain the pulse in time domain. Thus, the interval between two successive points is $\Delta t = 0.125$ ps. This translates into a total bandwidth of $\Delta t^{-1} = 8$ THz, with a frequency resolution of $T^{-1} = 15.625$ GHz. The pulse was Fourier inverted by FFT and the different frequencies were propagated by a distance L = 500 μm

according to equation (4.32). The resulting V(L,ω) was then inverted back to time domain. The input pulse V(0,t) and the output pulse V(L,t) are shown together in fig.(4.8) for comparison. It is clearly seen that dispersion during propagation in the CPW severely changes the pulse shape, resulting in pulse break-up as mentioned by Li et. al..[13]

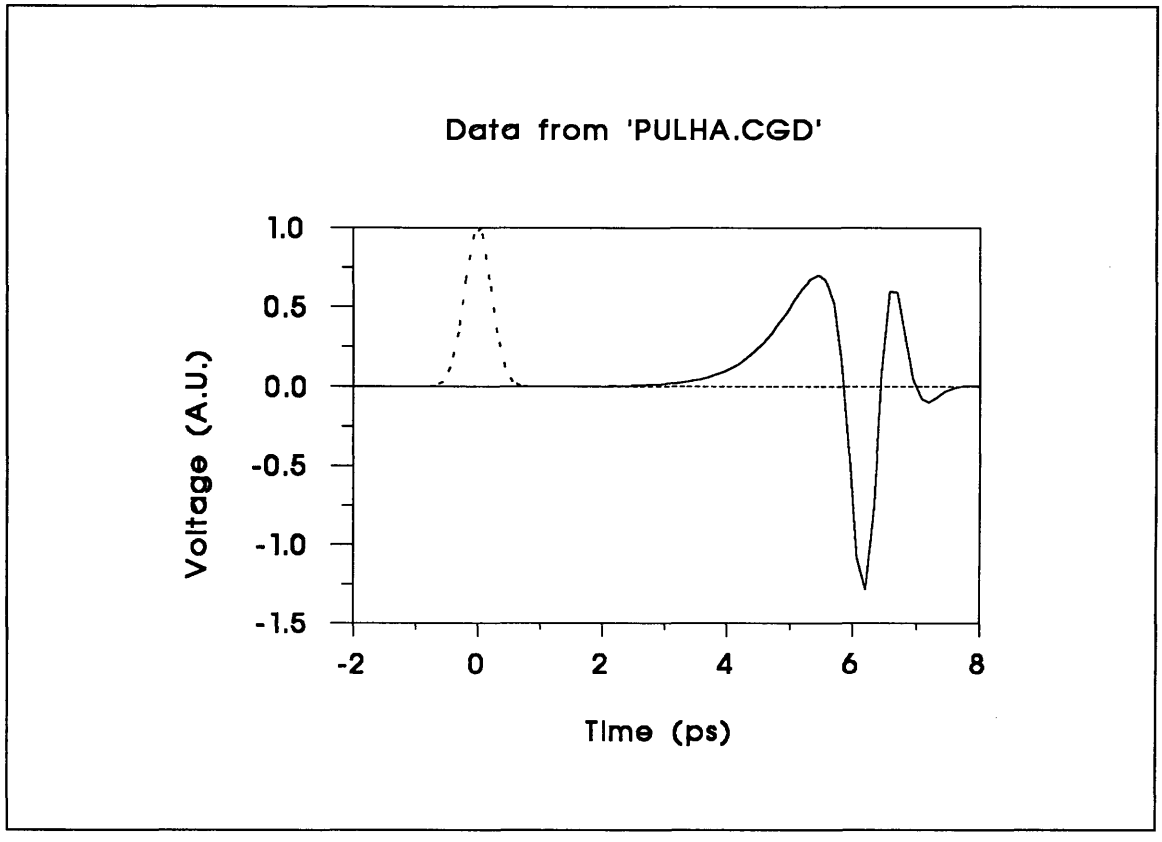

Fig.(4.8) - Ultra-short pulse propagation in the 50Ω CPW. The pulse centred at t = 0 is a 0.5 ps FWHM gaussian pulse. Its 3dB bandwidth is 882 GHz. As the CPW is strongly dispersive at these very high frequencies, pulse distortion takes place even for short propagation distances. This is shown by the second curve in the figure above, which depicts the pulse shape after propagating 500 μm in the CPW. The pulse is severely distorted and broadened.

The same calculations were repeated for a gaussian pulse of $\tau = 5$ ps. As this longer pulse has a narrower bandwidth (88.2GHz), it is much less affected by dispersion. For the same propagation distance (0.5mm), the input and output pulses are indistinguishable. After propagating 7mm, the distorted pulse shown in fig.(4.9) is obtained.

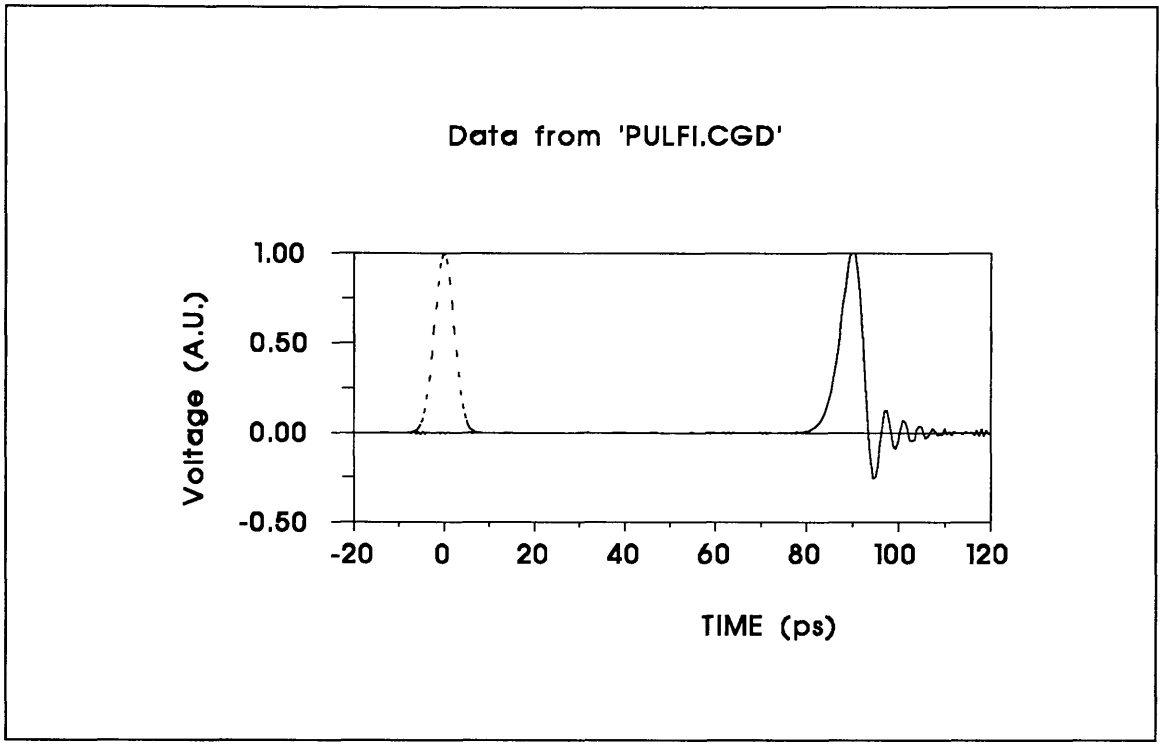

Fig.(4.9) - The propagation of a 5 ps gaussian pulse through the 50Ω CPW. The dashed curve is the input pulse and the other one is the pulse after propagating 7mm in the CPW. The high frequencies move to the trailing edge of the pulse, causing the oscillations.

A more interesting and relevant situation for this project concerns the propagation of electrical pulses generated by photoconductive switches. It will be seen later in this chapter that photoconductive switches generate time asymmetrical pulses. In general, these pulses have a very fast gaussian risetime, followed by a much slower decay, which can, in some circumstances, be considered as exponential. The same computer program was used to study the propagation of a pulse where the gaussian rise time and the exponential decay time are equal to τ_d = 3ps. The input (dashed curve) V(0,t) and output V(L,t) pulses are shown in fig. (4.10). The coplanar waveguide acts as a dispersive line with *positive* group velocity dispersion (chapter III), for frequencies below about 700 GHz. Therefore, the higher frequencies at the leading edge of the pulse travel slower than the lower frequencies at the trailing edge. This leads to the pulse reshaping effect seen in V(L,t), where the high frequencies are "left behind", at the trailing edge of the pulse.

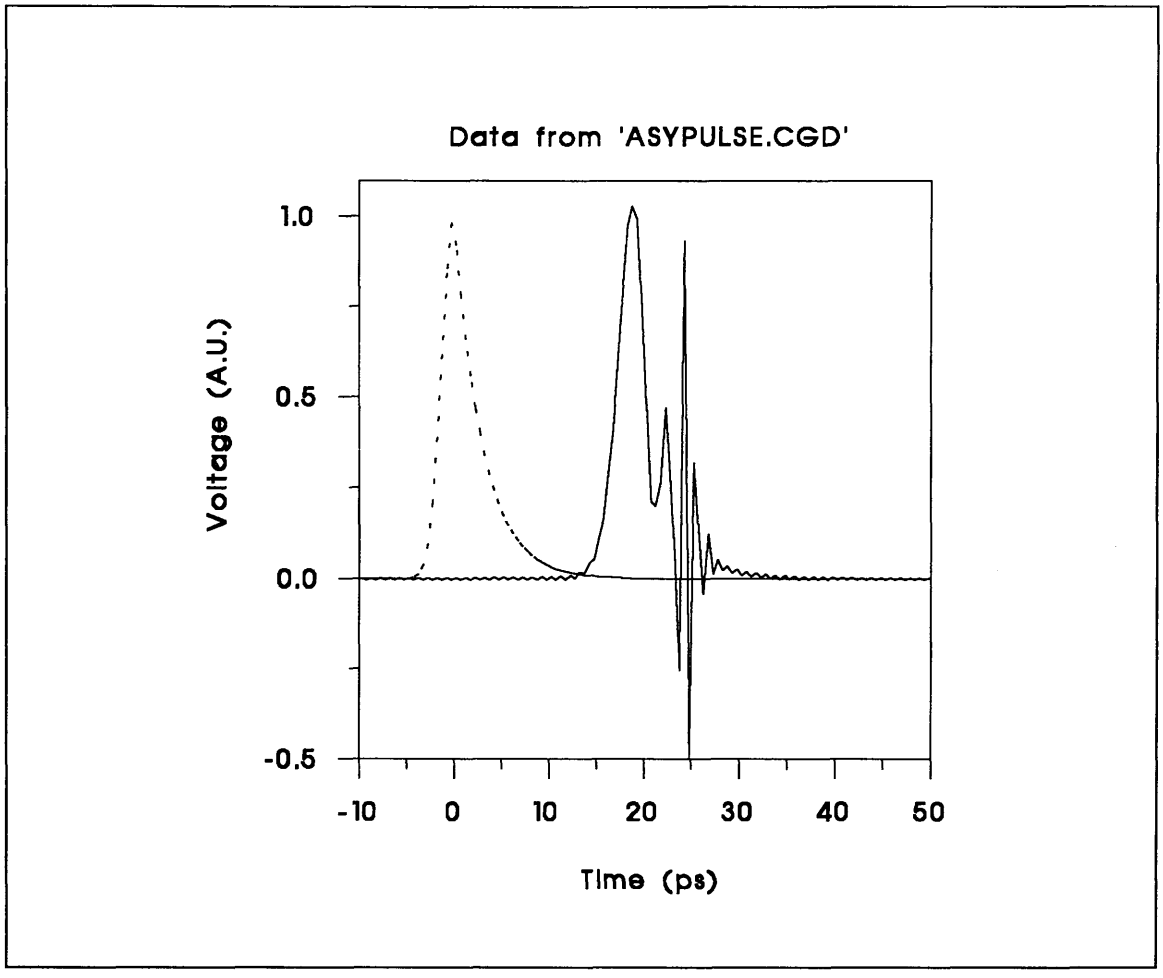

Fig. (4.10) - The asymmetric pulse centred at t = 0 has a gaussian rise time and an exponential decay time equal to τ_d = 3 ps. After propagating 2 mm in the CPW, the high frequencies of the leading edge are left behind, creating the oscillations at the trailing edge.

In all modelling presented in this section, no attempt has been made to model the attenuation. Radiative losses have been shown to be proportional to ν^r, where r is between two and three.[18] Dielectric and conductor losses should also be taken into account. The net effect of attenuation is to reduce the high frequency components in a propagating pulse. Thus, the high frequency oscillations to the right of the pulse at L = 2mm in fig.(4.10) are damped much more than the main peak. The asymmetric starting pulse is then expected to be sharpened by the interplay of dispersion and frequency dependent attenuation in the CPW.

4.5) - Response of Photoconductors in transmission lines

A full wave analysis of a photoconductor in a transmission line involves the solution of Maxwell equations in three dimensions, coupled with current continuity equations including generation, diffusion and carrier recombination. This is a computer intensive calculation but it has been done by Sano and Shibata, using a finite difference scheme.[25] Assuming that the photoconductors are triggered by 100 fs laser pulses, ultrashort electrical pulses with minimum pulsewidth of 200 fs are predicted for pulse forming networks in CPWs. Their results also indicate that the propagation of non-quasi-TEM modes on CPW can be inhibited by decreasing the strip width s. For microstrips, the same effect can be achieved by thinning the substrate, which is not desirable in most cases.

It is also possible to model a photoconductor by lumped circuit elements. An equivalent circuit developed by Auston is used here. This model has been widely tested and shown to agree with experimental results.[26,27]

Auston studied the effect of photoconductors in transmission lines. A single photoconductor gap or photoconductive switch is modelled as a capacitor C_s in parallel with a time varying conductance g(t). Because of the travelling wave nature of the electrical pulses generated, the response of the photoconductors has to be analysed in terms of incident, reflected and transmitted waves. The simplest configuration is when a photoconductor is in series with a transmission line as shown in fig.(4.11), which also shows its equivalent circuit.

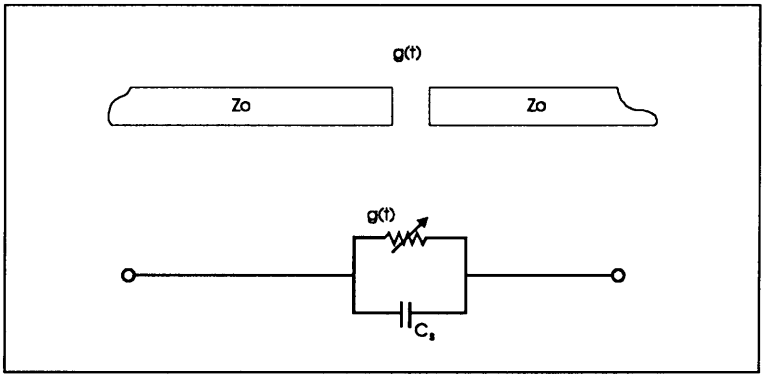

Fig.(4.11) - A single gap in a transmission line, acting as a series photoconductive switch. In the equivalent circuit, the photoconductive switch is modelled as a capacitor C_s in parallel with a time varying photoconductance g(t).

The circuit laws can be applied to the equivalent circuit and a differential equation is obtained for the charge in the capacitor. This equation can be integrated producing an expression for the charge q(t) as a function of time.

The photoconductive gap can also be placed in parallel with the transmission line. The charge transfer across the gap can be written as a convolution of the incident voltage with a sampling function, which describes the switch behaviour. This situation is described in fig.(4.12).

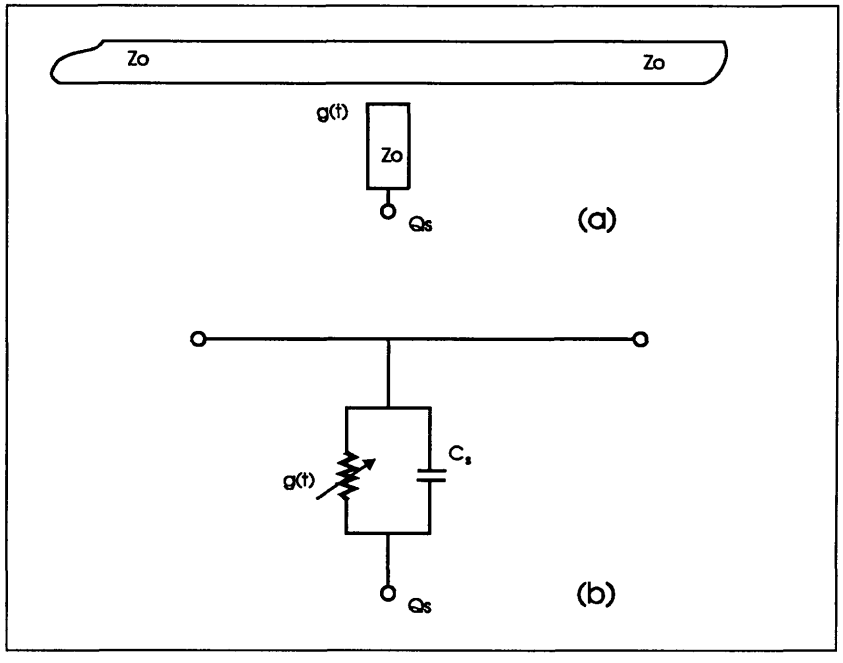

Fig.(4.12) - The photoconductive switch is now formed by the side line and the central conductor of the CPW as shown in (a). The circuit model in (b) shows the circuit elements in parallel with the main CPW.

The two gaps geometry of fig.(4.13.a) is an extension of the previous configuration, which shows the pulse generator and sampling gap photoconductive switches. Each photoconductor is modelled as a capacitor C_s and a conductance g(t). When the transmission line impedance and the impedance of the two side lines are included in the circuit model, one obtains the equivalent circuit shown in fig.(4.13.b).

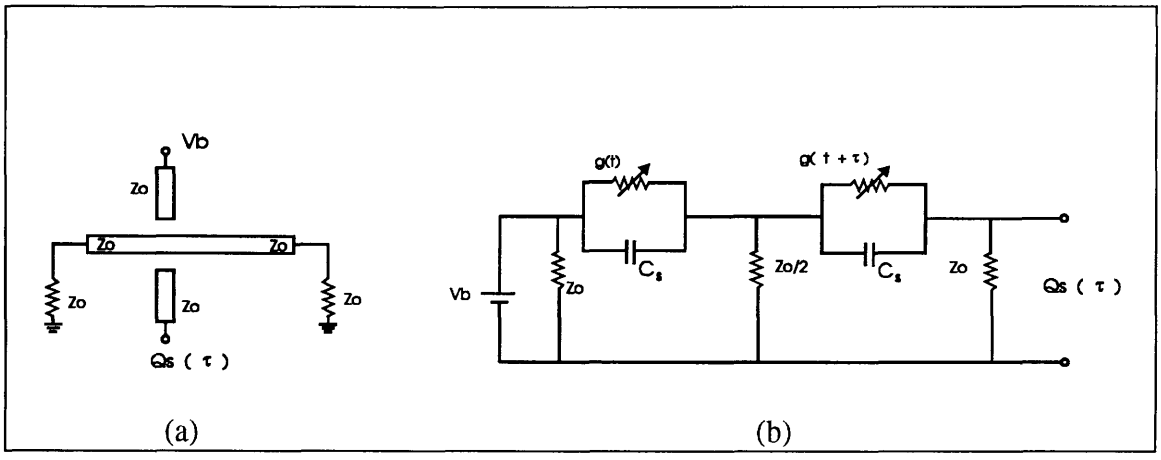

Fig.(4.13) - The double gap geometry with two photoconductors in parallel with the central conductor of a CPW. The schematic diagram of the device is shown in (a), where for clarity the ground planes of the CPWs were not drawn. The equivalent circuit for this device, including the impedance of the central conductor and of the two side lines is shown in (b).

The sampled charge $Q_s(\tau)$ can be written in the general form:[26]

$$Q_s(\tau) = A\,V_b Z_0 \{G_2 \int_{-\infty}^{+\infty} g_1(t)\,dt + G_1 \int_{-\infty}^{+\infty} g_2(t)\,dt + \int_{-\infty}^{+\infty} [\int_{-\infty}^{t} g_2(t) \cdot g_1(t' + \tau) \cdot K(t - t')\,dt']\,dt\} \qquad (4.34)$$

Where K(t) is the circuit response function, given by:

$$K(t) = \begin{cases} \Gamma_1 \Gamma_2 \cdot \dfrac{e^{-\Gamma_1 t} - e^{-\Gamma_2 t}}{\Gamma_1 - \Gamma_2} & t \geq 0 \\ 0 & t < 0 \end{cases} \qquad (4.35)$$

G_1 , G_2 , $g_1(t)$ and $g_2(t)$ are the dark conductances and photoconductances of the two gaps respectively.

τ is the optical delay time, i.e., the time delay between the activation of the two photoconductances.

A is a constant factor

V_b is the dc bias voltage on the pulse generator gap and

Z_0 is the transmission line impedance, C_s is the gap capacitance and

$$\Gamma_1 = \frac{1}{2Z_0C_s} \qquad \text{and} \qquad \Gamma_2 = \frac{1}{Z_0C_s} \tag{4.36}$$

The right hand side of (4.34) can be integrated analytically, provided that the photoconductances $g_1(t)$ and $g_2(t)$ are modelled by suitable functions. Assuming that the photoconductivity rises instantaneously and that its decay follows a single exponential, with a time constant t_0, then

$$g_1(t) = \begin{cases} e^{-t/t_0} & t \geq 0 \\ 0 & t < 0 \end{cases} \tag{4.37}$$

and

$g_2(t) = g_1(t - \tau)$, if the two photoconductors are identical.

The first two terms to the right of equation (4.34) do not depend on τ and contribute only with a constant background to the average current flowing through the two switches.

Hence, neglecting the first two terms and constant factors in (4.34), the sampled charge can be written as:

$$Q_s(\tau) = \int_{-\infty}^{+\infty} g_1(t - \tau) \cdot \left[\int_{-\infty}^{t} g_1(t' + \tau) \cdot K(t - t')\, dt' \right] dt \tag{4.38}$$

The equation above can be integrated easily, using the expressions for $g_1(t)$ and K(t) given previously. The integrations are straightforward but tedious and thus, they will not be carried out here. The resulting expression for the sampled charge is:

$$Q_s(\tau) = \frac{t_0}{1 - \Gamma_1 t_0} \cdot \left[\frac{t_0}{1 + \Gamma_1 t_0} \cdot e^{-\Gamma_1 \tau} - \frac{t_0}{2} \cdot e^{-\tau/t_0} \right] - \qquad (4.39)$$

$$\frac{t_0}{1 - \Gamma_2 t_0} \cdot \left[\frac{t_0}{1 + \Gamma_2 t_0} \cdot e^{-\Gamma_2 \tau} - \frac{t_0}{2} \cdot e^{-\tau/t_0} \right] \qquad \tau \geq 0$$

$$Q_s(\tau) = \left\{ \frac{t_0}{1 - \Gamma_2 t_0} \cdot \left[\frac{t_0}{2} - \frac{t_0}{1 + \Gamma_2 t_0} \right] - \frac{t_0}{1 - \Gamma_1 t_0} \cdot \left[\frac{t_0}{2} - \frac{t_0}{1 + \Gamma_1 t_0} \right] \right\} \cdot e^{\tau/t_0} \quad \tau \leq 0 \qquad (4.40)$$

Assuming that the gap capacitance is C_s = 30 fF, the circuit time constant $Z_0 C_s$ is 1.5 ps for $Z_0 = 50\Omega$. Using these parameters, Γ_1 and Γ_2 are obtained immediately and the sampled charge $Q_s(\tau)$ can be calculated as a function of τ for a given photoconductivity decay t_0. These values are interesting because they correspond to the characteristics of the simplified optoelectronic sampling device, to be described in chapter V. The function $Q_s(\tau)$ was plotted in fig.(4.14) using this circuit time constant for t_0 = 20 ps, 10 ps, 5 ps and 1.5 ps. The function describing the circuit response, K(t) in eq. (4.35) is also plotted for comparison. When the photoconductivity decay is very short, the autocorrelation function approaches the circuit response limit. On the other hand, when t_0 is very long, it will be necessary to sample a much wider time window to obtain the correlation function, as it becomes very broad.

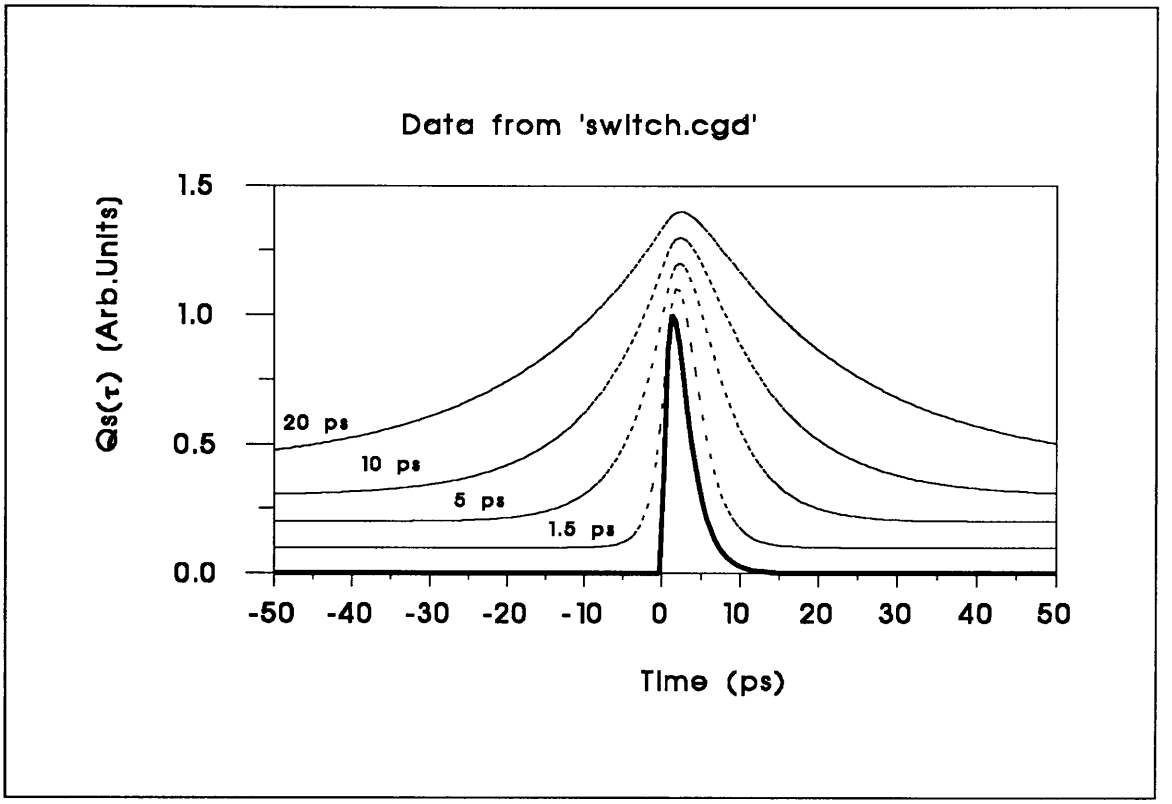

Fig.(4.14) - Correlation of a pair of photoconductors. The sampled charge $Q_s(\tau)$ is plotted as a function of the delay time between the two laser pulses, for a number of photoconductive decay times. The curve in bold is the function K(t), which represents the circuit response time. This is the time taken for discharging the first gap capacitance and charging the second one where the charge is sampled. The curves representing $Q_s(\tau)$ were displaced upwards for clarity.

As a summary, it was developed in this chapter, a model for the variation of the effective dielectric constant of the CPW with frequency. This was then used to investigate pulse propagation and pulse distortion in coplanar waveguides.

A circuit approach was used for the modelling of pairs of photoconductors in coplanar waveguides. Assuming that the gap photoconductance after illumination by an infinitesimally short laser pulse can be described by a single exponential, an analytical expression for the sampled charge was obtained. This is useful because it gives an insight into the measurement technique and it shows which are the critical parameters in a practical device. In particular, it can be seen from fig. (4.14) that the photoconductor capacitance should be kept to a few tens of fF to avoid circuit response time limitations. The model also predicts that the photoconductance decay time, t_0 is a critical parameter.

When the decay time is long, a much wider time window has to be sampled in order to show the voltage (charge) pulse switched across the two photoconductors.

4.6) - References to Chapter IV

[1] - K. C. Gupta, R. Garg and I. J. Bahl, in "*Microstrip Lines and Slotlines*", Artech House, Dedham, Massachusetts, 1979.

[2] - C. P. Wen, "Coplanar Waveguide: a surface strip transmission line suitable for nonreciprocal gyromagnetic device applications", IEEE Transactions on Microwave Theory and Techniques, Vol. MTT17, No.12, 1087-1090, 1969.

[3] - M. Riaziat, I. Zubeck, S. Bandy and G. Zdasiuk, "Coplanar waveguides used in 2-18 GHz distributed amplifier", in "1986 IEEE MTT-S International Microwave Symp. Dig., June, 1986.

[4] - M. Riaziat, E. Par, G. Zdasiuk, S. Bandy and S. Glenn, " monolithic millimeter wave CPW circuits", in "1989 MTT-S International Microwave Simp. Dig., 525-528, June, 1989.

[5] - M. Taylor - private communication.

[6] - M. Riaziat, R. M. Ahy and I. J. Feng, "Propagation modes and dispersion characteristics of coplanar waveguides", IEEE Transactions on Microwave Theory and Teechniques, Vol. 38, No. 3, 245-250, 1990.

[7] - Y. C. Shih and T. Itoh, "Analysis of conductor backed coplanar waveguide", Electronics Letters, Vol. 18, No.12, 538-540, 1982.

[8] - R. W. Jackson, "Mode conversion at discontinuities in finite width conductor backed coplanar waveguide", IEEE Transactions on Microwave Theory and Techniques, Vol. 37, No.10, 1582-1589, 1989.

[9] - R. W. Jackson, "Considerations in the use of coplanar waveguide for millimeter wave integrated circuits", IEEE Transactions on Microwave Theory and Techniques, Vol. MTT-34, 1450-1456, 1986.

[10] - M. E. Davis, E. W. Willimas and A. C. Celestini, "Finite-boundary corrections to the coplanar waveguide analysis", IEEE Transactions on Microwave Theory and Techniques, Vol. 21, 594-597, 1973.

[11] - W. Hilberg, "From approximations to exact relations for characteristic impedances", IEEE Transactions on Microwave Theory and Techniques, Vol. MTT-17, No. 5, 259 - 265, 1969.

[12] - See application note: "Layout rules for GHz probing", from Cascade Microtech.

[13] - K. K. Li, G. Arjavalingam, A. Dienes and J. R. Whinnery, "Propagation of picosecond pulses on microwave striplines", IEEE Transactions on Microwave Theory and Techniques, Vol. MTT30, No.8, 1270-1273, 1982.

[14] - E. Yamashita, K. Atsuki and T. Ueda, "An approximate dispersion formula of microstrip lines for computer-aided design of microwave integrated circuits", IEEE Transactions on Microwave Theory and Techniques, Vol. MTT27, No.12, 1036-1038, 1979.

[15] - G. Hasnain, A. Dienes and J. R. Whinnery, "Dispersion of picosecond pulses in coplanar transmission lines", IEEE Transactions on Microwave Theory and Thecniques, Vol. MTT34, No.6, 738-741, 1986.

[16] - T. Itoh and R. Mitra, "Dispersion of picosecond pulses on microstrip transmission lines", SPIE Proceedings, Vol. 439, 159-163, 1983.

[17] - J. B. Knorr and K. D. Kuchler, "Analysis of coupled slots and coplanar strips on dielectric substrate.", IEEE Transactions on Microwave Theory and Techniques, Vol. MTT-23, 541-548, 1975.

[18] - M. Frankel, S. Gupta, J. A. Valdmanis and G. A. Mourou, "Terahertz attenuation and dispersion characteristics of coplanar transmission lines", IEEE Transactions on Microwave Theory and Techniques, Vol. 39, No. 6, 910-916, 1991.

[19] - G. A. Mourou and K. E. Meyer, "Subpicosecond electro-optic sampling using coplanar strip transmission lines", Applied Physics Letters, 45(5), 492-494,1984.

[20] - J. F. Whitaker, R. Sobolewski, D. R. Dykaar, T. Y. Hsiang and G. A. Mourou, "Propagation model for ultrafast signals on superconducting dispersive striplines", IEEE Transactions on Microwave Theory and Techniques, Vol. 36, No.2, 277-285, 1988.

[21] - See "*Properties of Gallium Arsenide*", Chapter8, "Optical functions of Gallium Arsenide", Emis Data reviews series, No. 2, published by INSPEC, The Institution of Electrical Engineers, London, 1986.

[22] - J. F. Whitaker, R. Sobolewski, D. R. Dykaar, T. Y. Hsiang and G. A. Mourou, "Propagation model for ultrafast signals on superconducting dispersive striplines", IEEE Transactions on Microwave Theory and Techniques, Vol. 36, No.2, 277-285, 1988.

[23] - G. D. Bergland, "A guided tour of the Fast Fourier Transform.", IEEE Spectrum, 41-52, 1969.

[24] - R. J. Higgins, " Fast Fourier Transform: an introduction with some minicomputer experiments", American Journal of Physics, Vol. 44, No.8, 766-773, 1976.

[25] - E. Sano and T. Shibata, "Full wave analysis of picosecond photoconductive switches", IEEE Journal of Quantum Electronics, Vol. 26, No. 2, 372-377, 1990.

[26] - D. H. Auston, "Picosecond Photoconductors: Physical properties and applications", in *Picosecond Optoelectronic Devices*, Chapter 4, Academic Press, Orlando, 1984.

[27] - M. B. Ketchen, D. Grischkowsky, T. C. Chen, C-C. Li, I. N. Duling, III, N. J. Halas, J. M. Halbot, J. A. Kash and G. P. Li, "Generation of subpicosecond electrical pulses on coplanar transmission lines", Applied Physics Letters, 48 (12), 751-753, 1986.

Appendix 4.A

A.1) - Conformal mapping and the Schwarz-Christoffel Transformation

A mapping of the complex Z plane onto the complex W plane is called conformal when it is done by an analytic function.[1] The conformal mapping technique can be very useful in problem solving when it is possible to transform a complicated problem in a certain domain in the complex Z plane onto a new domain in the W plane where the problem is easily solved. One of its main features is that Dirichlet and Neumann boundary conditions remain constant under such transformation.

The Schwarz-Christoffel transformation is used to do a conformal mapping of the X axis and the half plane below it onto the boundary and interior of a polygon with n sides. If the polygon is chosen to be a rectangle, then the Schwarz-Christoffel transformation is given by:

$$w = \int_0^z g(s)\ ds \qquad (A.01)$$

Where

$$g(z) = (z + a_1)^{-1/2} \cdot (z + b_1)^{-1/2} \cdot (z - a_1)^{-1/2} \cdot (z - b_1)^{-1/2} \qquad (A.02)$$

and $-\pi \leq \arg(z - x_i) \leq 0; \quad x_i = \pm a_1, \pm b_1.$

This conformal transformation is depicted in fig. (A.1), below.

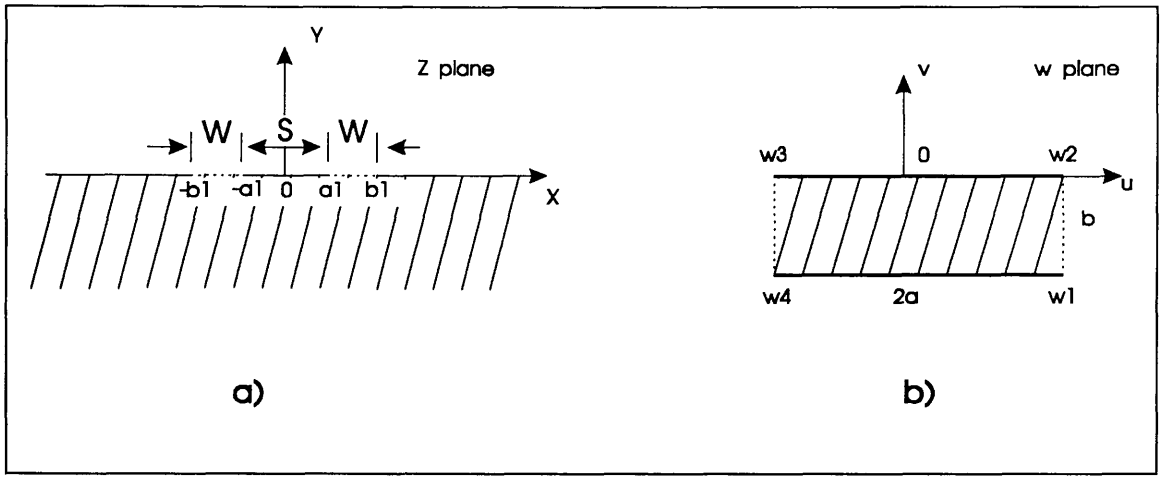

Fig.(A.1) - The Schwarz-Christoffel transformation maps the lower half and the X axis of the Z complex plane in (a) onto the interior and boundary of the rectangle in the W plane shown in (b).

The points $\pm a_1$ and $\pm b_1$ are the folding points of the transformation, i.e., they are the points in the X axis, whose images are to be the vertices of the rectangle in the w plane.

Combining equations (A.01) and (A.02):

$$w = \int_0^z \frac{ds}{\sqrt{(s^2 - a_1^2) \cdot (s^2 - b_1^2)}} \qquad (A.03)$$

This last equation can be evaluated in terms of elliptic integrals.

The four vertices in the w plane can be described by two numbers a and b, defined in terms of the two elliptic integrals:[2,3]

$$K(k) = \int_0^1 \frac{dt}{\sqrt{(1 - t^2) \cdot (1 - k^2 t^2)}} \qquad (A.04)$$

$$K'(k) = K(k') = \int_0^1 \frac{dt}{\sqrt{(1 - t^2) \cdot (1 - k'^2 t^2)}} = \int_1^{1/k} \frac{dt}{\sqrt{(t^2 - 1) \cdot (1 - k^2 t^2)}} \qquad (A.05)$$

and

$$k^2 + k'^2 = 1 \qquad \text{(A.06)}$$

K(k) and K'(k) = K(k') are the complete elliptic integrals of first kind of modulus k and k' respectively. k' is called the complementary modulus.

A.2) - Location of the vertices of the rectangle

The vertices of the rectangle are located in terms of the two numbers a and b, defined by:[1]

$$a = \int_0^{a_1} |g(s)|\ ds = \int_0^{a_1} \frac{ds}{\sqrt{(s^2 - a_1^2)\,.\,(s^2 - b_1^2)}} \qquad \text{(A.07)}$$

and

$$b = \int_{a_1}^{b_1} |g(s)|\ ds = \int_{a_1}^{b_1} \frac{ds}{\sqrt{(s^2 - a_1^2)\,.\,(b_1^2 - s^2)}} \qquad \text{(A.08)}$$

A.2.1) - Location of the vertices in terms of 'a' and 'b'.

Let w_1, w_2, w_3 and w_4 be the images of the points $-b_1$, $-a_1$, a_1 and b_1 respectively. The point w_1 can be located by the following considerations:

If $-b_1 < s < -a_1$, then

$$(s + a_1)^{-1/2} = |s + a_1|^{-1/2}\,.\,e^{-j\pi/2}$$

$$(s + b_1)^{-1/2} = |s + b_1|^{-1/2}$$

$$(s - a_1)^{-1/2} = |s - a_1|^{-1/2}\,.\,e^{-j\pi/2}$$

$$(s - b_1)^{-1/2} = |s - b_1|^{-1/2} \cdot e^{-j\pi/2}$$

Hence, in this interval, $g(s) = |g(s)| \cdot e^{-j3\pi/2} = +j\,|g(s)|$ (A.09)

When $-a_1 < s < 0$, one can easily see that $\arg(s + a_1) = \arg(s + b_1) = 0$ and $\arg(s - a_1) = \arg(s - b_1) = \pi$, where arg(z) is the argument of the complex number z. Thus, for this interval,

$$g(s) = |g(s)| \cdot e^{-j\pi} = -|g(s)| \quad \text{(A.10)}$$

Therefore

$$w_1 = \int_0^{-b_1} g(s)\,ds = \int_0^{-a_1} g(s)\,ds + \int_{-a_1}^{-b_1} g(s)\,ds$$

or using equations (A.09) and (A.10):

$$w_1 = -\int_0^{-a_1} |g(s)|\,ds + j \cdot \int_{-a_1}^{-b_1} |g(s)|\,ds$$

finally, from (A.07) and (A.08):

$$w_1 = a - j\,b \quad \text{(A.11)}$$

The second vertex, w_2, is obtained by the integral of g(s) in the interval $-a_1 < s < 0$. In this case, as seen before in (A.10), $g(s) = -|g(s)|$.
Thus, the second vertex is given by:

$$w_2 = \int_0^{-a_1} g(s)\,ds = -\int_0^{-a_1} |g(s)|\,ds = a \quad \text{(A.12)}$$

The other two vertices w_3 and w_3 are obtained by similar transformations. In the interval $0 < s < a_1$, $g(s) = -|g(s)|$ and when $a_1 < s < b_1$, one has $g(s) = -j|g(s)|$. The remaining two vertices are then found to be equal to:

$$W_3 = -a \qquad \text{and} \qquad w_4 = -a - j\,b \tag{A.13}$$

A.3) - Calculation of the integrals 'a' and 'b'.

The two numbers a and b (equations A.07 and A.08) can be expressed in terms of the elliptic integrals K(k) and K'(k). To do that, some changes of variables are necessary.

A.3.1) - Calculation of the integral 'a'.

$$k = \frac{a_1}{b_1} \qquad \text{and} \qquad u = \frac{s}{b_1} \tag{A.14}$$

then

$$(s^2 - a_1^2) \,.\, (s^2 - b_1^2) = b_1^4\,(k^2 - u^2) \,.\, (1 - u^2) \tag{A.15}$$

so that

$$a = \int_0^k \frac{du}{b_1\, k \,.\, \sqrt{(1 - \frac{u^2}{k^2}) \,.\, (1 - u^2)}} \tag{A.16}$$

A new change of variables is now performed:

$$\frac{u}{k} = t \text{ so that}$$

$$u \rightarrow k \quad \Rightarrow \quad t \rightarrow 1$$

$$u \rightarrow 0 \quad \Rightarrow \quad t \rightarrow 0$$

and then

$$a = \frac{1}{b_1} \cdot \int_0^1 \frac{dt}{\sqrt{(1 - t^2) \,.\, (1 - k^2\, t^2)}} \tag{A.17}$$

Comparing (A.17) with (A.04), one gets:

$$a = \frac{1}{b_1} \cdot K(k) \tag{A.18}$$

A.3.2) - Calculation of the integral 'b'.

The integral defining b can also be evaluated by similar transformations:

$$u = \frac{s}{a_1} \tag{A.19}$$

then

$$(s^2 - a_1^2) \,.\, (b_1^2 - s^2) = \frac{a_1^4}{k^2} \cdot (u^2 - 1) \cdot (1 - k^2.u^2) \tag{A.20}$$

It is important to note that:

$$s \rightarrow a_1 \quad \Rightarrow \quad u \rightarrow 1$$

$$s \rightarrow b_1 \quad \Rightarrow \quad u \rightarrow 1/k$$

therefore

$$b = \int_{1}^{1/k} \frac{du}{\frac{a_1}{k} \cdot \sqrt{(u^2 - 1) \cdot (1 - k^2.u^2)}} = \frac{k}{a_1} \cdot K'(k) \qquad (A.21)$$

Equation (A.05) was used to establish the last equality in (A.21).

The ratio between a and b is very important for the calculation of the characteristic impedance of coplanar waveguides. From equations (A.18) and (A.21), it is given by:

$$\frac{a}{b} = \frac{K(k)}{K'(k)} \qquad (A.17)$$

A.4) - References to Appendix 4.A.

[1] - R. V. Churchill, J. W. Brown and R. F. Verhey, in "*Complex Variables and applications*", Third edition, chapters 9 and 10, McGraw-Hill Inc., USA, 1974.

[2] - W. J. Gibbs, "*Conformal Transformations in Electrical Engineering*", page 133, Chapman & Hall Ltd., London, 1958.

[3] - " *Handbook of mathematical functions*", section 17.3, page 590, edited by M. Abramowitz and I. A. Stegun, Dover Publications, Inc., NY, 1970.

Chapter V - Design and Fabrication

5.1) - Introduction

Lithography is the process used to transfer a geometric shape to a radiation sensitive substrate. In semiconductor processing various lithographic methods are used. Virtually all patterning methods employ resists, which are chemical compounds sensitive to some sort of radiation. A thin film of resist is deposited onto the semiconductor substrate and then selectively exposed to radiation. The exposure can be done by light, electron beams, X-rays or ion beams. The minimum feature size and maximum area to be patterned determine the lithographic technique to be used.

5.1.1) - Optical Lithography

Optical or photolithography is by far the most used technique for transferring a geometric shape onto a semiconductor substrate. The pattern to be transferred is first produced in a mask by, perhaps, a photographic or electron beam lithography technique. A bright (transparent) pattern in a dark field is most used, although the reverse situation is also common. Both types of mask were used in this project. The mask is used together with a (ultraviolet) light source, to illuminate selectively certain areas of a semiconductor substrate previously coated with a layer of photosensitive resist. The rate of dissolution (in the appropriate solvent) of the exposed areas of the resist, as compared

with the unexposed ones, is greatly changed by the photochemical reaction. Therefore, the pattern in the mask can be transferred to the resist profile after selective resist removal in the right solvent (called developer in this contest).

The resists used in photolithography come in two different types: positive and negative resists. For positive resists the exposed areas are removed by the developer and the unexposed areas remain on the substrate. In negative resists the reverse happens, so that the exposed areas stay on the substrate. The diagrams in fig.(5.1) summarize the photolithographic processing with positive and negative resists, followed by a (additive) metal lift-off step.

In an additive process, metal is evaporated over the substrate and resist after resist exposure and development. In the large majority of cases the resist is used only as a transfer medium and it is removed after the metallization step by immersing the whole substrate in a solvent such as acetone. The resist is then dissolved and the metal over it is lifted-off, leaving only the metallic pattern defined on the substrate.

In subtracting processes, metal is first deposited onto the whole surface of the substrate and then the resist is applied by spin coating. After the lithographic step and resist development, it is used as a mask in an etching step which removes the un-wanted metal, not covered by the resist. The resist is then dissolved, leaving the metallic pattern which it was covering, on the substrate.

Device Processing in Photolithography.

Before any lithographic step is done, the samples have to be thoroughly cleaned. In this project the samples were cleaned using the organic solvents: trichloroethylene, methanol, acetone and IPA (Isopropyl alcohol). The samples were immersed in beakers containing one of the above solvents at a time and then placed in an ultrasonic bath for five minutes. At the end of the cleaning process, the samples were rinsed in IPA and blown dry.

The photoresist used was the Microposit S1400-31, supplied by Shipley Europe Ltd.[1] When spun at 7000 rpm for 40s, this resist produces a film about 1.4 μm thick. At 5000 rpm, the film thickness increases to approximately 1.6 μm. A chlorobenzene process[2,3] was used to ensure successful lift-off by producing an overhang top layer during the development step. Hence, after spinning the samples were baked for 15 min, soaked in chlorobenzene for 15 min, blown dry and baked again for 5 more minutes.

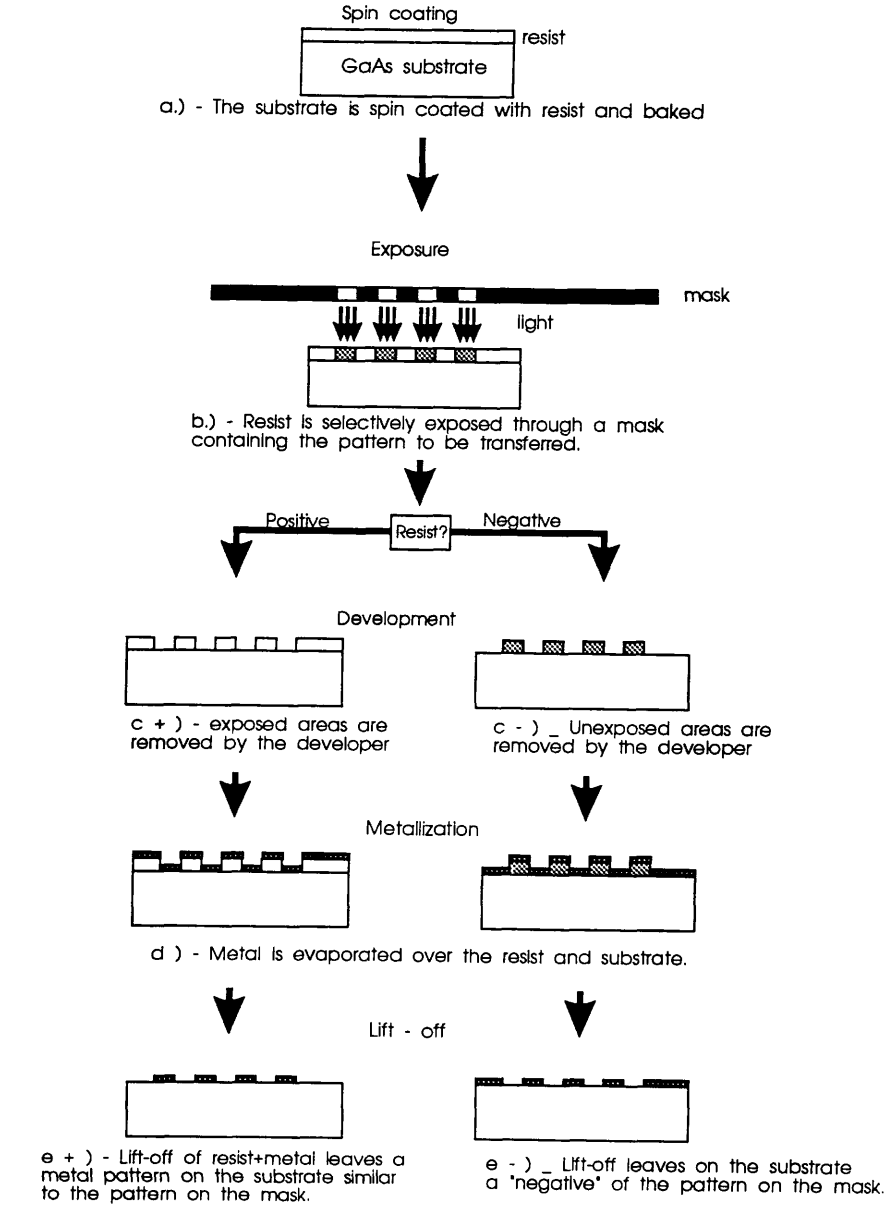

Fig.(5.1) - Lithography in semiconductor processing. The figure exemplifies the lithographic process with positive and negative resists, followed by metal evaporation and lift-off.

The exposure was done in a mask aligner fitted with a mercury lamp whose output wavelength is 356 nm (i line). The exposure time varied between 10 and 15 s, depending on the thickness of the resist being exposed.

The development step proceeded by immersing the sample in a beaker with 1:1 Microposit Developer : H_2O, for 45s. The sample was then rinsed in H_2O and blown dry. Process data sheets will be presented later in this chapter for each photolithographic step.

Perhaps one of the main advantages of photolithography is its ability to expose all patterns in a mask at once, i.e., the exposure is in parallel and it takes only a few seconds. Thus, the exposure time does not depend on the size of the patterns in a particular mask. The major problem with photolithography on the other hand, is its limit of resolution due to diffraction. The theoretical limit of resolution is around 0.25 μm but it seems difficult to have reliable commercial processes working below about 0.5 μm. If very high speed devices such as Mesfets with gate lengths on the order of 100 nm are to be made, other lithographic techniques have to be employed.

5.1.2) - Electron beam lithography

Electron beam lithography (EBL) is the dominant nonoptical lithographic method used in GaAs processing.[4] It can be used either to write patterns in masks for photolithography or for direct writing of patterns on wafers.

EBL uses a focussed beam of electrons to draw, under computer control, a pattern on a substrate covered by a resist layer. The electron beam is accelerated to a high energy (50-100 KV are common accelerating voltages) and focussed before impinging upon the resist and substrate. The processes through which the beam of electrons loses its energy in the resist cause physical and chemical changes in the resist layer. This exposure process produces secondary electrons which break up the molecular chains of positive resists into low molecular weight fragments, or cause cross-linking in negative resists.[5] The sample is then developed to remove the exposed areas (if the resist is positive) or the unexposed ones (if the resist is negative).

The basic elements of an electron beam column are an electron gun that produces high energy electrons, condenser lenses to collect them and an objective lens to focus the electrons on the substrate.[5] There are also deflection coils which enable the e-beam to be scanned over the specimen and a system of switching (beam blanking) the e-beam on and off. The beam blanking and deflection coils are computer controlled through a scan generator unit.[6] Geometrical patterns in the computer are converted into instructions and sent via the scan generator to the deflection coils. The instructions are

used to scan the e-beam on the resist, reproducing the original geometrical patterns. A great advantage is that no mask is needed in such a lithographic equipment as the patterns are directly written on the resist.

Other advantages of e-beam lithography are its improved resolution, excellent level-to-level alignment and easy pattern modification. The limit of resolution of EBL is roughly 10 nm, a factor of at least 25 below the (theoretical) resolution of photolithography.

The major disadvantages of EBL include price and complexity of the equipment and writing speed. The many millions of pixels composing a pattern have to be scanned in series, i.e., one after the other. Even very high exposure rates, in the hundreds of MHz, can not approach the exposure times of photolithography, specially when large areas are involved.

EBL Machine

The equipment used in this project was a Philips PSEM500 scanning electron microscope, modified for lithography. The modifications to the original microscope include among others:

* Computer control of the beam deflection coils and beam blanking.

* Automatic detection of contrast in the secondary electron detector signal, enabling edge detection and automatic alignment.

*Automatic beam focussing.

The detailed description of the lithography machine can be found in Mackie[7] and Adams[6].

Some features of the original SEM include a spot size variable from 1 μm down to 8 nm, accelerating voltages up to 50KV and selectable magnifications from 20x up to 80000x. The modified EBL machine is capable of very high resolution as demonstrated by Lee et. al., who wrote 16 nm lines separated by 8nm gaps on silicon nitride membranes.[8]

Resists

The most common positive e-beam resist is Polymethylmethacrylate (PMMA). This is an organic polymer with long molecular chains of $[CH_2CCH_3COOCH_3]_n$. A bilayer resist process was used in all EBL steps in this project. The use of two layers of PMMA with different molecular weights has been shown to: produce a desirable undercut profile, increase development latitude (tolerance to over-development), reduce the proximity effect and produce higher resolution than a single layer.[9,10,11] The bilayer resist consists of a high molecular weight (low sensitivity) layer on top of a low molecular weight (high sensitivity) layer. PMMA of 85000 molecular weight (from BDH Chemicals Ltd.) and 350000 molecular weight ("Elvacite" from Dupont) were used in this work. Following a popular convention in use in the laboratory, these resists will be referred to as "BDH" and "Elvacite" in the text.[6] The details of resist solubility and resist characterization can be found in Binnie[12] and Adams.[6] It suffices to say here that the resists were dissolved in o-xylene in concentrations of 8% and 4% by weight respectively, for spin coating. The process data sheets for each type of device made will be given later in this chapter.

5.2) - Design and Fabrication of individual IC components

5.2.1) - Resistors

Design

In order to test the fabrication process and accuracy of the design, some individual resistors were made in a small (5x5 mm) GaAs chip. The resistivity of bulk semi-insulating GaAs is too high (typically 3.7×10^8 $\Omega.cm$) for making the 50Ω load resistors for the CPW transmission lines. Metal alloys on the other hand offer a simple and practical way of producing integrated resistors.

An alloy of NiCr with 90%Ni : 10%Cr whose resistivity is $\rho = 70.6$ $\mu\Omega.cm$ was chosen as the resistor material. The resistor length and width were set in the design

of the CPW (given later in this chapter) to be ℓ = 100μm and ω = 43μm, so that ℓ/ω = 2.33. The resistor thickness is then obtained from:

$$t = \rho \frac{\ell}{\omega} \cdot \frac{1}{R} \qquad (5.01)$$

where t,ℓ and ω are the resistor thickness, length and width respectively, R is the resistance and ρ is the resistivity of the material making the resistor. For a 50Ω resistor and assuming the other parameters to be as above, eq.(5.01) gives t = 33 nm.

Fabrication

Resists

A two layer resist technology was used. They were spun according to:

8 % BDH in o-xylene, 5000 rpm, 40s
bake 1 hour at 180°C

4 % Elvacite in o-xylene, 5000 rpm, 40s
bake 2 hours at 180°C

The thickness of this resist bilayer was measured in a Talystep thickness monitor to be about 300 nm. This ensures that the lift-off process will be easily done as the resist is almost an order of magnitude thicker than the metal layer deposited.

Exposure

The resist was exposed to the focussed e-beam of the modified PSEM500 Philips electron microscope. For the resistor patterns the electron dose was 350 μC/cm^2. Apart from the resistor patterns, there are also 4 alignment marks defined in this level. These marks are used later to align pads to the resistors in a second lithographic run. The dose for the alignment marks is higher, being 400 μC/cm^2. As the marks are much smaller than the other patterns, much less proximity effect[13] takes place inside each alignment mark. Thus, the electron dose has to be increased to produce the same exposure.

Development

The development of the exposed resist was done by immersing in 2.5:1 IPA :MIBK (Isopropyl alcohol : Methylisobutylketone) for 30s at 23°C. At the end the sample is immersed for a further 30s period in a beaker containing pure IPA to stop the development process and then it is dried with nitrogen gas.

Metallization & Lift-off

Prior to the actual evaporation of metal, the sample was de-oxidized in 1:4 $HCl:H_2O$ for 60s, rinsed in de-ionized water and dried again with nitrogen.

The metal deposition was done in a home made vacuum system at pressures below 5×10^{-6} torr. The Ni:Cr alloyed wires are put in a tungsten boat through which a high current is passed. The metal being evaporated is measured by a metal thickness monitor. This system comprises a quartz crystal oscillating at about 6 MHz, placed inside the evaporation chamber and a frequency meter. The metal deposited upon the chip and the crystal reduces the frequency of oscillation of the latter. The thickness of the metal deposited is obtained from calibration curves of change in frequency of the crystal oscillator versus metal thickness. The measured calibration curve for Ni:Cr gives 3KHz for a thickness of 30nm.

After evaporation the resist was removed in the lift-off process by immersing the chip in a beaker with acetone.

Resistor Pads

Rectangular metallic pads were made in a second lithographic level, to allow probing of the resistors. The same resists were used and the pads exposure was 350 $\mu C/cm^2$. Again, the development process and de-oxidation were performed. The metals evaporated in this level are:

Ti	30 nm
Au	100 nm

Fig.(5.2) shows a micrograph of a completed resistor, after the two fabrication steps. The I-V characteristics and resistance of the resistors were measured in an HP4145B semiconductor parameter analyser. Fig.(5.3) shows one such measurement,

where the gradient of the I-V curve produces a resistance of R = 47Ω. For all the 25 resistors in the chip, the resistance varied from 47Ω to 52Ω, showing that it is possible to have the resistance within ±5% of the design value.

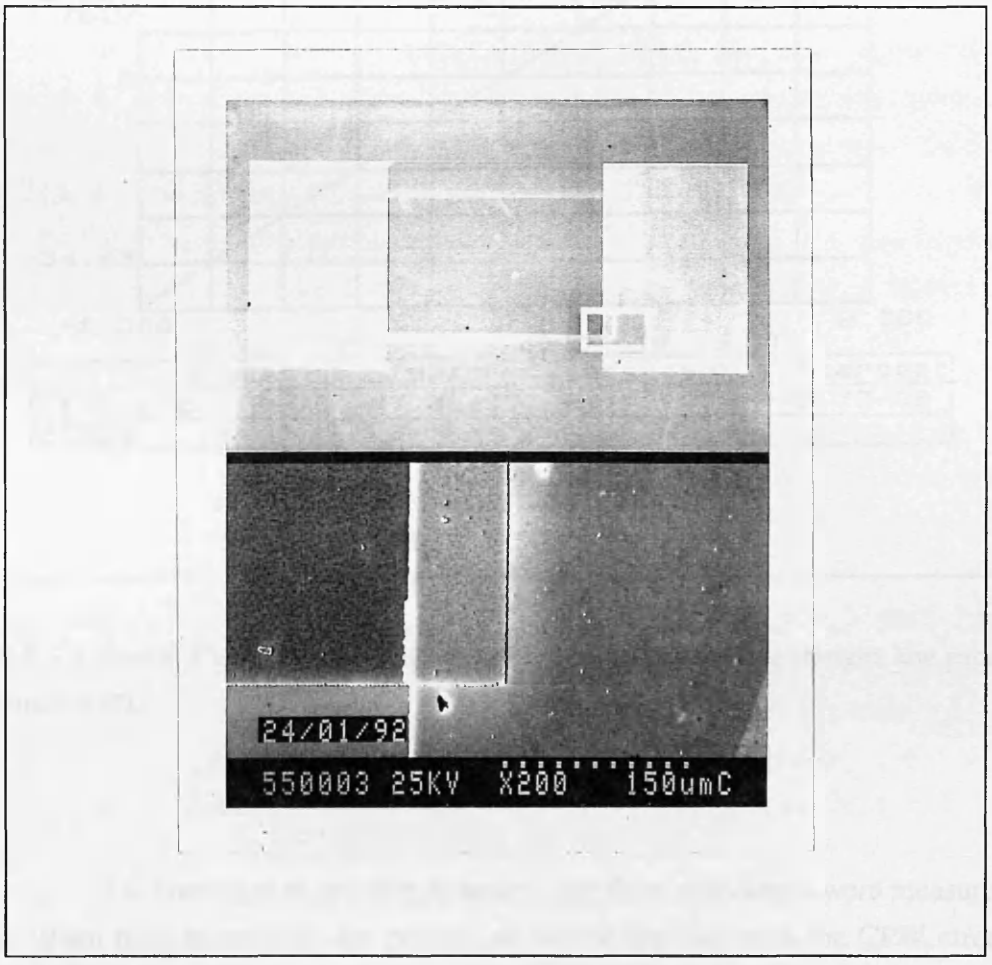

Fig.(5.2) - The picture above is a micrograph of a completed NiCr resistor connected to two TiAu contact pads.

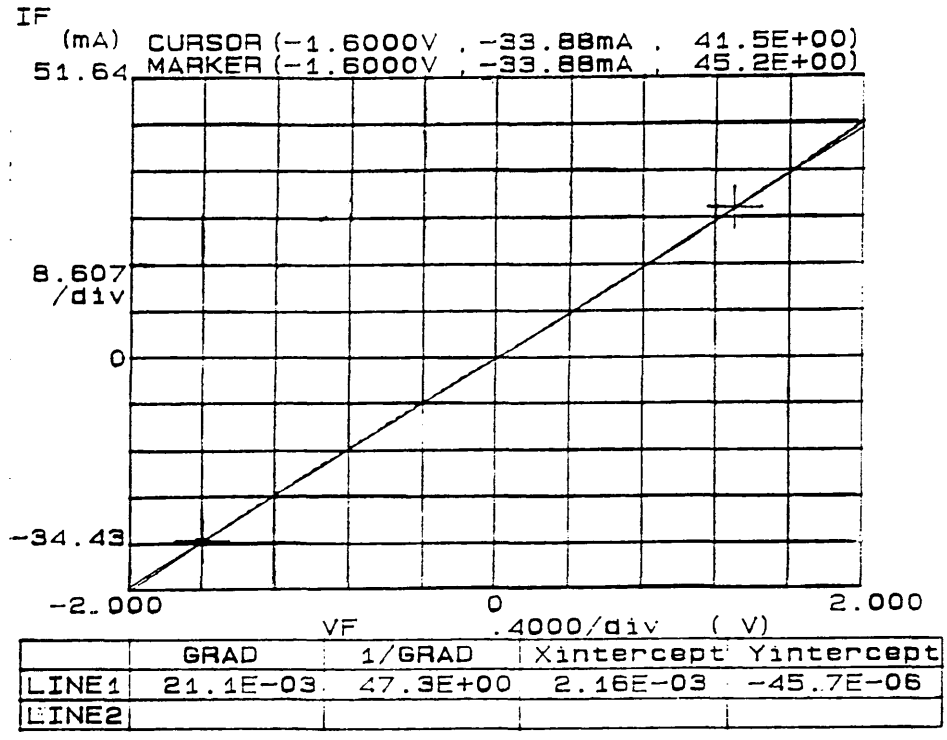

Fig.(5.3) - A typical I-V curve of a NiCr resistor. The gradient of the straight line produces a resistance of 47Ω.

It is important to mention however, that these resistances were measured only at dc. When high frequencies are present, as will be the case with the CPW circuit, the resistor characteristics can change drastically. At high frequencies, a physically large resistor will become a distributed element, having series resistance and shunt capacitance and acting as a lossy transmission line.

5.2.2) - Capacitors for the Optoelectronic Sampling Device

Design

Two types of capacitors are used in monolithic microwave integrated circuits. Interdigitated capacitors are normally used when the required capacitance is a few picofarads or less. For larger capacitances metal-insulator-metal (MIM) capacitors are preferred. In this project, MIM capacitors were made connected to the pulse generator and sampling gate photoconductors.

The design of the capacitors for this project is dictated by the design of the optoelectronic sampling device (OSD). Four capacitors were included in each device, connected to the four photoconductors. It is therefore necessary to address some of the issues involved in the design of the OSD here.

In fig. (5.4) a drawing of the OSD is presented. This is an improvement over the device design in fig.(2.8) where it was necessary to split the ground plane in four different places to make the side lines. A better solution would be to make the four side lines first, with an appropriate size. A dielectric layer can then be used to cover part of them and the top ground plane is finally made with holes where the side lines are not covered by the dielectric. This design allows the side lines to be biased or probed through the holes in the ground plane. Moreover, the dielectric between the two metal layers will form a MIM capacitor that will act as a voltage power supply for the photoconductor pulse generator. As for the other photoconductor that acts as a sampling gate through which the measured charge is transferred, the addition of a 5 pF capacitance will have essentially no effect. The capacitance of the coaxial cable that extracts the signal is about 200 pF. Thus, the addition of a 5 pF parallel capacitor to this, makes the RC time constant only 2.5% larger. As mentioned before in chapter II, the highest frequency involved in the detection circuit is the laser chopping frequency, which is below 1 KHz. More will be said about the optoelectronic sampling device (OSD) in section 5.3.

The capacitance required in each of the four capacitors can be crudely estimated by considering how much charge should be stored and available in the biasing circuit when the laser beam is fired upon the photoconductor. Fig.(5.5) presents a circuit model for the bias circuit and the pulse generator photoconductor. The laser pulses are taken to be rectangular in shape, with a width of 10 ps. Assuming that when the laser pulse strikes the photoconductor biased with V = 10 Vdc, its resistance is lowered down to say, R = 50Ω, then the current would be i = V/R = 10V/100Ω = 0.1A. The charge needed to provide this current over the duration of the laser pulse is $\Delta Q = i\,\Delta t = 0.1A \times 10^{-11}\ s = 10^{-12}$ C. The smallest capacitor that would hold this charge, biased at 10 Vdc, would have a capacitance given by:

$$C = \frac{\Delta Q}{V_{dc}} = \frac{\Delta t}{R} = \frac{10^{-11}\ s}{100\ \Omega} = 0.1\ pF$$

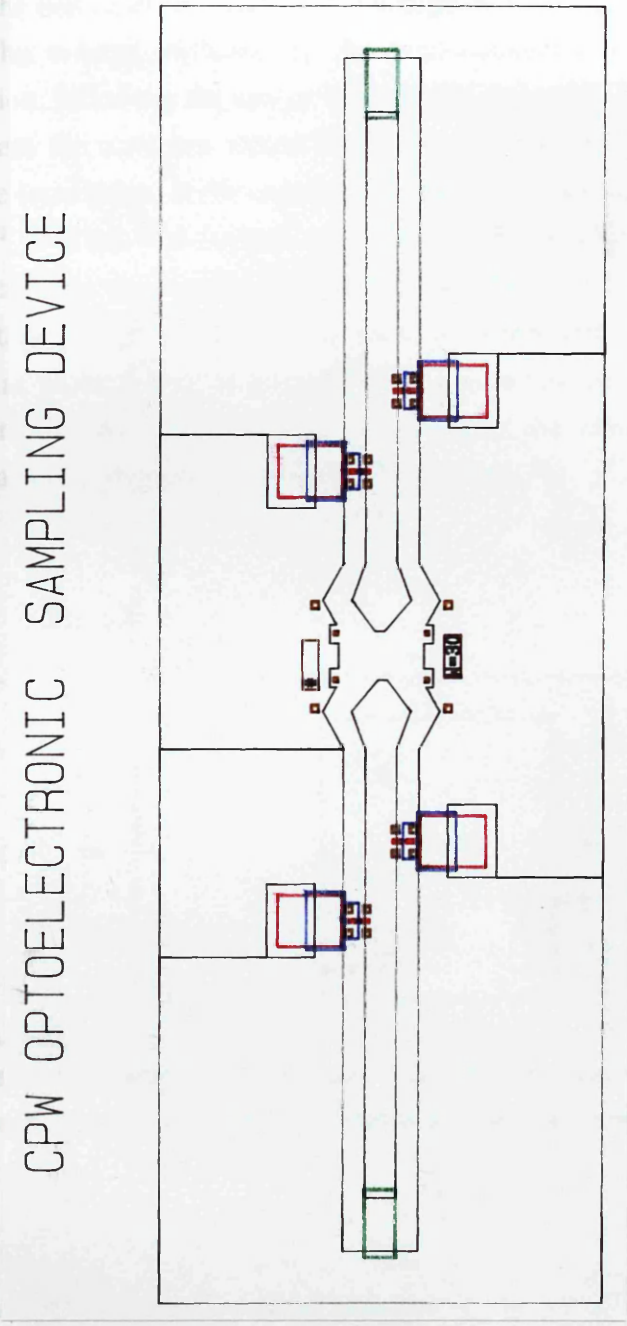

Fig.(5.4) - A diagram of the optoelectronic sampling device, containing 4 capacitors, 2 resistors, CPW transmission lines and 4 photoconductive gap switches.

Such a capacitor discharging over the 100Ω photoconductor resistance in series with the 50Ω CPW transmission line would have a time constant RC = 10 ps. This means that at the end of every laser pulse the capacitor has discharged to one half of its full charge. The voltage switched by the photoconductor will be an exponentially decaying function, following the charge decay in the capacitor. The ideal situation would be the one where the capacitor would be large enough so that it would discharge very little during the laser pulse. If the capacitor is made 50 times bigger than the one above, i.e., if C = 5 pF, than the time constant would now be RC = 150Ω x 5pF = 750 ps. At the end of one laser pulse, the capacitor would still have 98.7% of its full charge. Therefore it acts as a voltage power supply, holding the bias voltage at a constant value during the pulse. If the bias probe is kept in contact with the capacitor all the time, then it will not discharge, even in a long time scale. This is roughly the same procedure adopted for biasing fast avalanche photodiodes and photomultipliers.[14]

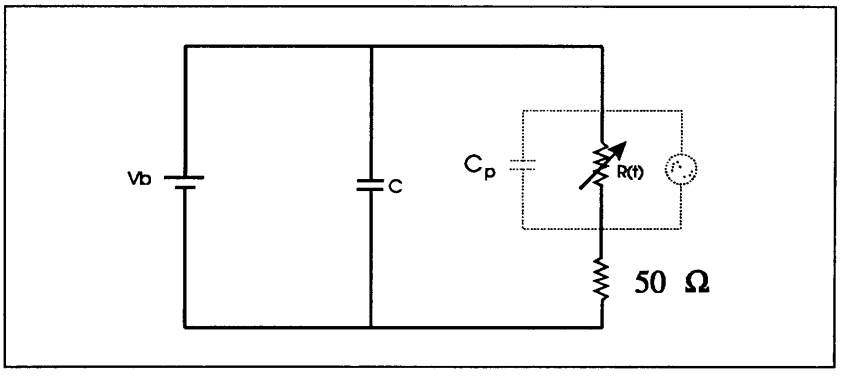

Fig.(5.5) - Model for the pulse generator circuit. The photoconductor is represented here by the variable resistor R(t) and the dotted components including a current source and a parasitic capacitance.

The photoconductors were assumed to be purely resistive devices in the analysis above. Their capacitances, being in the fF range have little or no effect here, but they also have an internal current source, due to the electron-hole plasma generated by the laser pulse. Thus, following the argument used to estimate the necessary capacitance, the 5pF capacitor above will be overdimensioned, as it is not the only source of charge carriers in the circuit, but that only increases the time constant of the biasing, which is desirable. Again, if the photoconductor resistance R is not lowered down to 100Ω during

the laser pulse, which is probably the case, then the time constant will be correspondingly larger. For R = 1 KΩ, for example, RC = 5 ns. This ensures that the capacitor works as a constant voltage source.

Fabrication

The capacitors are to be made of one layer of Si_3N_4, 200 nm thick sandwiched between two layers of metals. The bottom layer is made of ohmic contacts to the GaAs substrate. The materials and layer thicknesses are the following:

Metal	Thickness (nm)
Ge	85
Au	65
Ni	18
Au	20

Hence, the total thickness is 188 nm. The two dielectric materials mostly used in MMIC's are SiO_2 and Si_3N_4, whose dielectric constants are 5 and 7.5 respectively. When the dielectric layer is used as an interlevel spacer to separate metal cross-overs with minimum parasitic capacitances, SiO_2 is preferred due to its lower dielectric constant. On the other hand, the higher dielectric constant of Si_3N_4 makes it the dielectric of choice for integrated MIM capacitors.

This dielectric is normally formed in a Plasma Enhanced Chemical Vapour Deposition (PECVD) equipment at temperatures low compared to CVD processes. The gases normally used are silane (SiH_4), ammonia (NH_3) and Nitrogen (N_2). The desired chemical reactions are:

$$3SiH_4 + 4NH_3 \rightarrow Si_3N_4 + 12H_2$$

and

$$3SiH_4 + 2N_2 \rightarrow Si_3N_4 + 6H_2$$

but there are a large number of possible intermediate steps. The growth conditions used in this project are:

Gas	Flow rate

	(ccm/min)
SiH_4	10
NH_3	40
N_2	100

Temperature: 300 °C
Pressure: 350 mtorr
rf power: 20 W

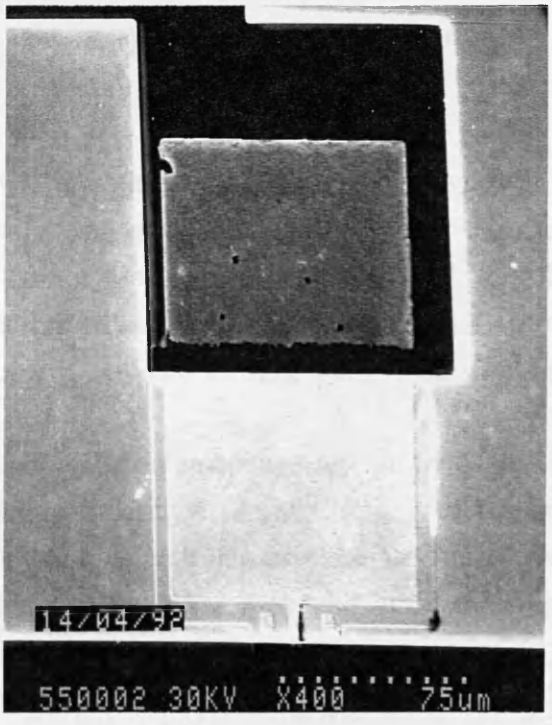

Fig.(5.6) - SEM micrograph of a completed Metal-Insulator-Metal capacitor in an Optoelectronic Sampling Device.

After deposition the samples are inspected and spun with photoresist, which is then exposed and developed. The photoresist patterns left on the samples cover only the capacitors areas and are used as an etch mask to remove the unwanted Si_3N_4. This is done by dry etching in C_2F_6. The dry etching conditions as well as other details of the

fabrication procedure are summarized in the process sheet that follows. Finally, the third and last lithographic level is done, completing the capacitors. The metal layers used in this level are 100nm of Ti and 500nm of Au. Fig.(5.6) shows a completed MIM capacitor.

The capacitors were tested using an LCR meter, in the frequency range of 10KHz to 10MHz. The capacitance is constant over this range, being 4pF, which is 1 pF less than the design value. This is attributed to a dielectric layer thicker than the intended value of 200nm. The parallel resistance was also measured and typical values obtained are about 0.5 MΩ. The maximum value obtained for the parallel resistance was 2MΩ. Therefore, capacitors with very low leakage currents were demonstrated. Their integration in the OSD is straightforward as the process used in their fabrication is compatible with the fabrication and operation of the other devices in the circuit.

5.3) - Fabrication of Mesfets

Discrete short-gate-length Mesfets were made using electron beam lithography. These devices are made in 5 lithographic levels, in a CPW structure, which enables direct on-wafer probing and electrical S-parameter measurements. The fabrication procedure for the Mesfets was developed by J. A. Adams[6] in this department and it is thoroughly described in ref. 6. Thus, the fabrication procedure is not discussed in full detail here, but it is outlined in the process data sheets given at the end of this chapter.

Mesfets were made on an epilayer grown by Molecular Beam Epitaxy. The layer, grown on the semi-insulating GaAs substrate, is 70 nm thick and doped with 3 x 10^{18} Silicon atoms/cm^3. Simple Van der Paw test structures were made and the carrier concentration and Hall mobility were measured at room temperature. A mobility of around 1600 cm^2/V.s is expected at this carrier concentration at room temperature. Hall measurements of carrier concentration and mobility give n = 3 x 10^{18} cm^{-3} and μ = 1590 cm^2/V.s.

Chips of 5 x 5 mm were cleaved from the wafer and used in the fabrication. As the Mesfets are small ($\simeq$250 x 300 μm), it is possible to have 100 sites in a single chip. Some of these sites contain process control devices such as devices to measure the contact resistance of the ohmic contacts. Again, the Mesfets fabrication procedure is the same as the one described in ref. 6. Fig. (5.7.a) is a micrograph of a mesa-isolated, short-gate Mesfet made in this project. The source-drain gap in this device is 1 μm wide and the gate-length is only 70 nm. The gate-length can be easily measured in fig.(5.7.b), which is a very high resolution SEM picture.

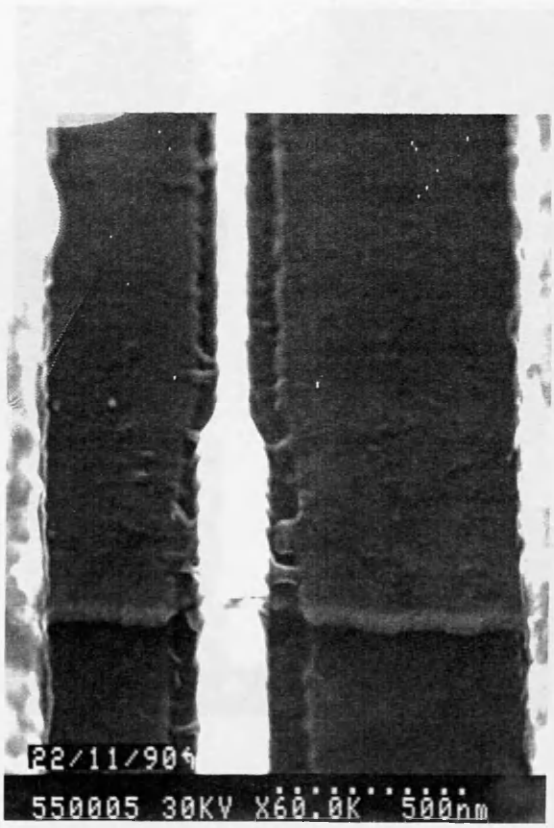

Fig.(5.7.a) - Scanning Electron Microscope micrograph of a mesa-isolated short-gate Mesfet, made by electron beam lithography.

The I-V characteristics of the Mesfets were measured with an HP4145B semiconductor parameter analyser. A result is shown in fig. (5.8), where the source drain

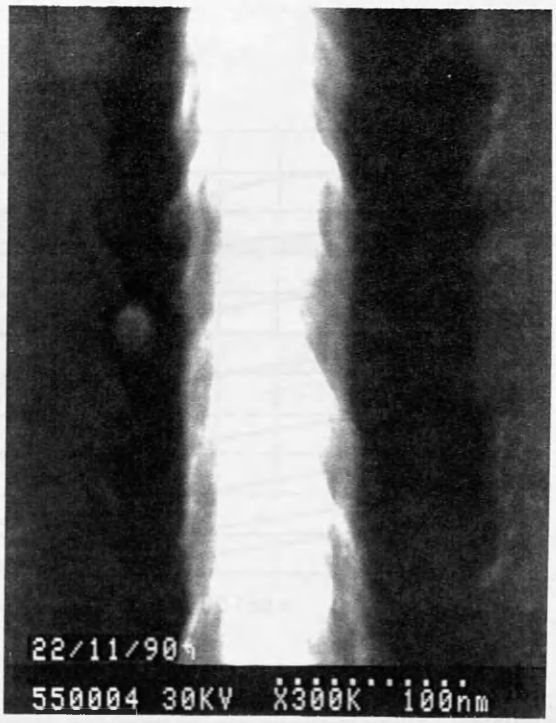

Fig.(5.7.b) - A 70 nm TiAu gate in a Mesfet.

bias was varied from 0 to 2.5Vdc and the gate bias was varied from 0 to -3.5Vdc, in steps of 0.5Vdc, resulting in the 8 curves in fig. (5.8). The Mesfets can not be pinched-off completely for drain bias above $\approx$0.5V. This is caused by the short channel effect of electrons "punching through" the potential barrier of the gate, as demonstrated by Adams.[6]

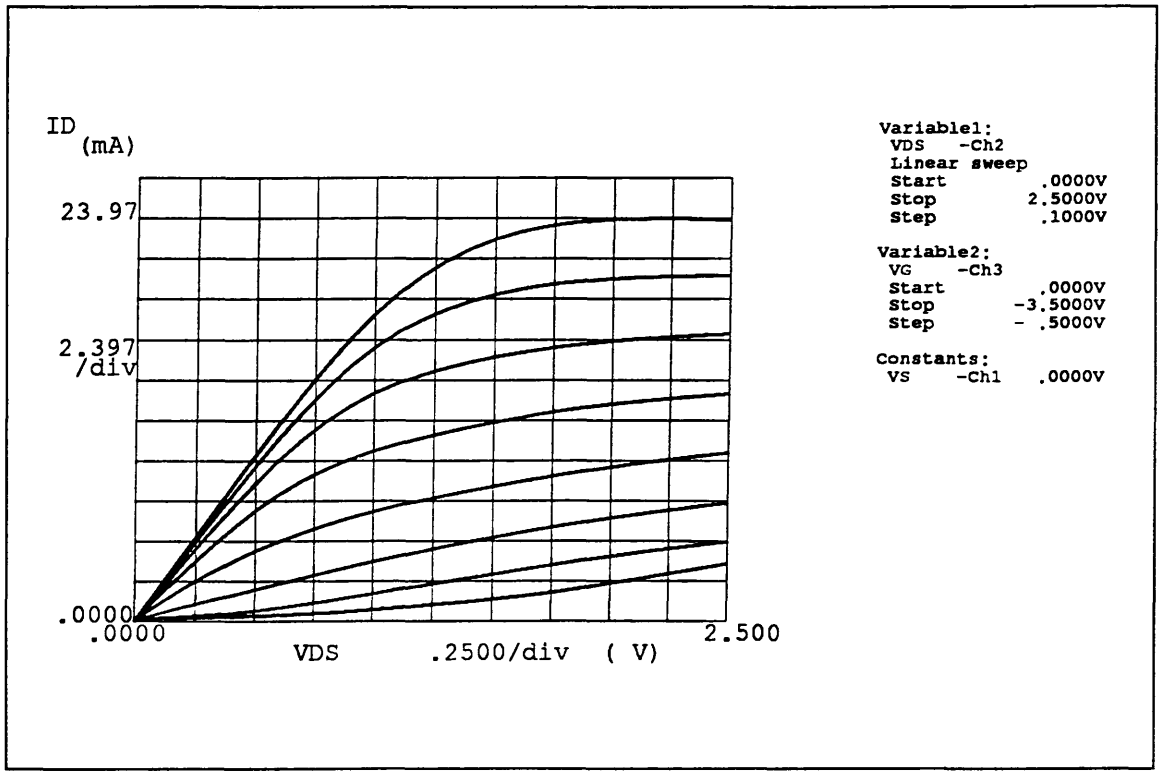

Fig.(5.7) - I-V characteristics of a short gate length Mesfet. Electrons punching through the gate barrier prevent pinch-off above $\approx$ 0.5Vds

5.4) - Design and fabrication of the optoelectronic sampling device.

The diagram of an individual optoelectronic sampling device was shown in fig.(5.4). This circuit includes all the individual devices treated before. Capacitors, resistors, CPW's, photoconductors and a Mesfet are integrated in this single device. The ends of the two coplanar waveguides (CPW) are terminated by 50Ω resistors. In the figure there is no central device so that the two CPWs have open circuits at the centre. The central part of the circuit is where the dual source Mesfet is made, connected to the CPW. The two sources of the FET are connected to the ground plane of the CPW and the gate and drain are connected to the central conductors of the two CPW's.

marks for the fabrication of the Mesfet by e-beam lithography are provided at the centre of the device.

There are also four 5pF MIM capacitors, connected to four photoconductors for the transmission of a voltage pulse to the central conductor of the CPW and its later detection. As discussed previously one of the capacitors will have a probe needle connected to it and to a voltage power supply during the experiment. This ensures the capacitor will always be charged, keeping a constant voltage bias V_b.

The width s of the central strip and the gaps ω were chosen to be $s = 43\ \mu m$ and $\omega = 30\ \mu m$, so that $s/\omega = 1.43$. These dimensions of the CPW were chosen so that its characteristic impedance is $Zo = 50\Omega$, according to the model of chapter IV.

Fabrication

Six masks were designed using a CAD program. They correspond to the six photolithographic levels in the coplanar waveguide device:

- Alignment marks for later photolithographic levels and for electron beam levels.
- Mesa isolation for the Mesfets and process control devices (MESA).
- Photoconductors and bottom plate of the capacitors (CAPS).
- Silicon Nitride pattern (Si3N4).
- Resistors (RESISTOR).
- CPW top layer (CPW).

Figs. (5.9) shows the CPW top layer mask, designed with the CAD program. The other masks have very small details and therefore they will not be shown here. The masks were manufactured at Rutherford & Appleton Laboratory, by e-beam lithography, using the drawing files generated by the CAD program.

The fabrication procedure for the optoelectronic sampling device will be outlined now:

* Firstly, alignment marks for photo and electron beam lithography are patterned and formed on the substrate.
* If an active device is to be made at the centre of the circuit, a mesa isolation lithographic step now follows. When simple test structures on SI GaAs are to be made, this lithographic level is skipped.

* The bottom plate of the capacitors and the connections of the photoconductors are patterned and ohmic contacts are formed.
* Si_3N_4 is deposited by PECVD and patterned to form the dielectric layers of the capacitors.
* NiCr resistors are made to act as matched terminations for the CPWs.
* If an active device such as a Mesfet is to be made at the centre of the device, the e-beam lithographic levels are done now, using the alignment marks for registration made previously. Otherwise, the central part of the sampling device can be left empty, being an open circuit. Alternatively, simple straight-through connections or short circuits can be made.
* The top CPW layer is now patterned and a thick layer of metal (100nm Ti, 500nm Au) is evaporated. This thick layer is necessary to reduce losses in the coplanar waveguide and make it possible for high frequency signals to propagate over distances of many millimetres.
* Finally, proton implantation is performed to reduce the carrier lifetime in the GaAs substrate, producing short turn-off times in the photoconductors. If any active device is made at the centre of the optoelectronic circuit, another photolithographic level is necessary to produce a MOP (metal-on-polymer) mask and protect the device from the beam of protons. When the central part of the circuit is empty or contain only test structures, no mask is needed and protons are implanted over the whole substrate area.

The details of ohmic contacts formation, Si_3N_4 deposition, Mesfets fabrication, etc, can be found in the process data sheets for the discrete devices at the end of this chapter.

Proton implantation

As mentioned previously, the lifetime of charge carriers in GaAs can be reduced by the implantation of protons. CPW devices made on semi-insulating GaAs were implanted with protons at the University of Surrey. The details of the implant are the following:

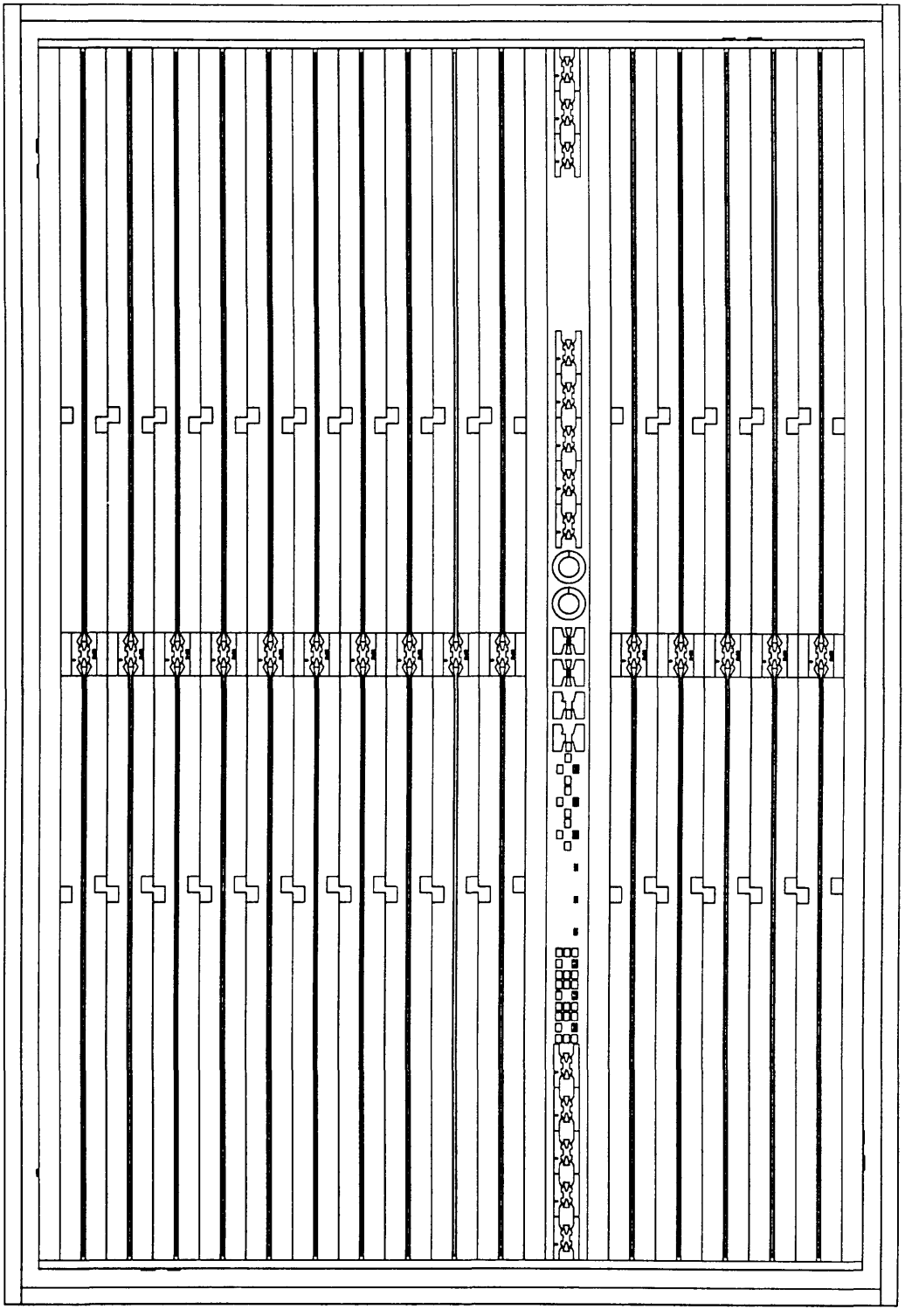

Fig.(5.9) - The coplanar waveguide (CPW) mask for the production of 15 optoelectronic sampling devices in a single chip.

- Ion species: $^{1}H^{+}$
- Dose: 10^{14} cm^{-2} , 2 x 10^{14} cm^{-2} and 4 x 10^{14} cm^{-2}
- Energy: 180 KeV
- Beam current: 0.2 μA
- Ion beam at 7° off normal incidence.

Fig.(5.10) shows the result of a Monte Carlo simulation of the implant process, using the implant parameters above. The average depth of the implanted protons is about 1.2 μm.

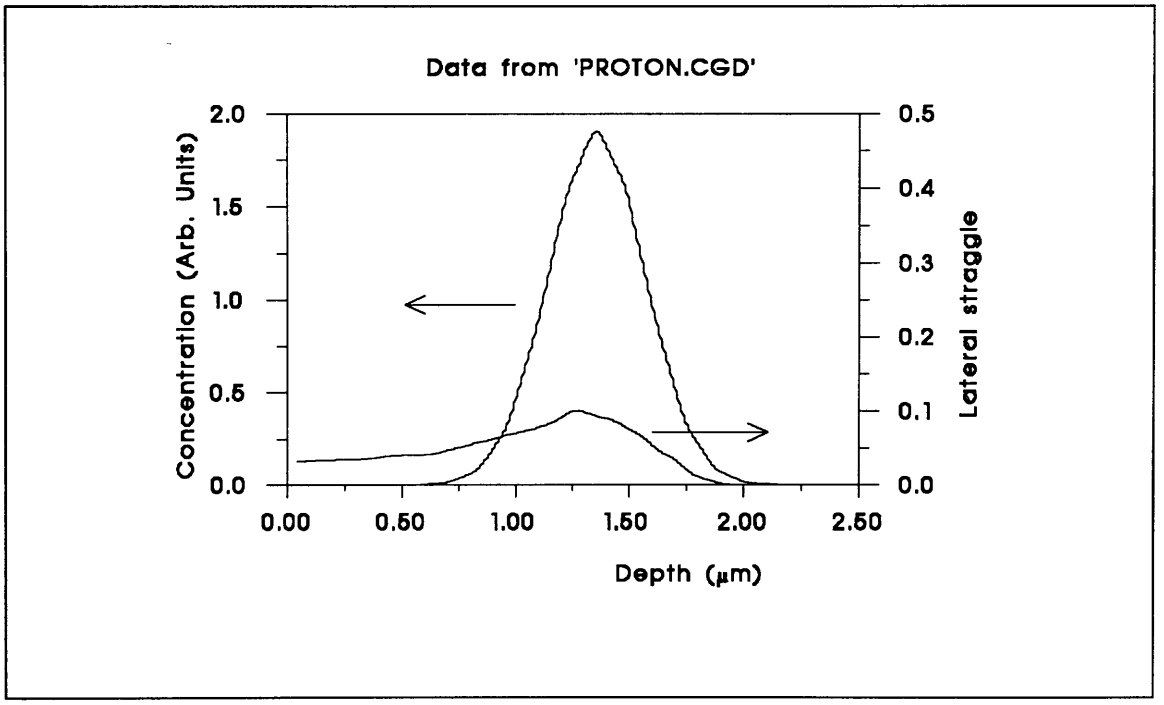

Fig.(5.10) - Monte Carlo simulation of proton implantation. The average depth is ≈ 1.2 μm. The lateral straggle is the statistical fluctuation of the density of implanted protons, in a direction perpendicular to the incident ion beam.

The implants done at Surrey differ from the work done by Paulter[15] et. al. in two important aspects. The beam current is one order of magnitude lower and the samples in this project did not have the benefit of any temperature control. The implants done by Paulter had the substrate temperature carefully controlled and kept down to 8°C. It is known that the temperature of the chip can be, locally, very high during the implant.

This can degrade (anneal) the defects that generate the deep levels in GaAs, responsible for the short lifetime.

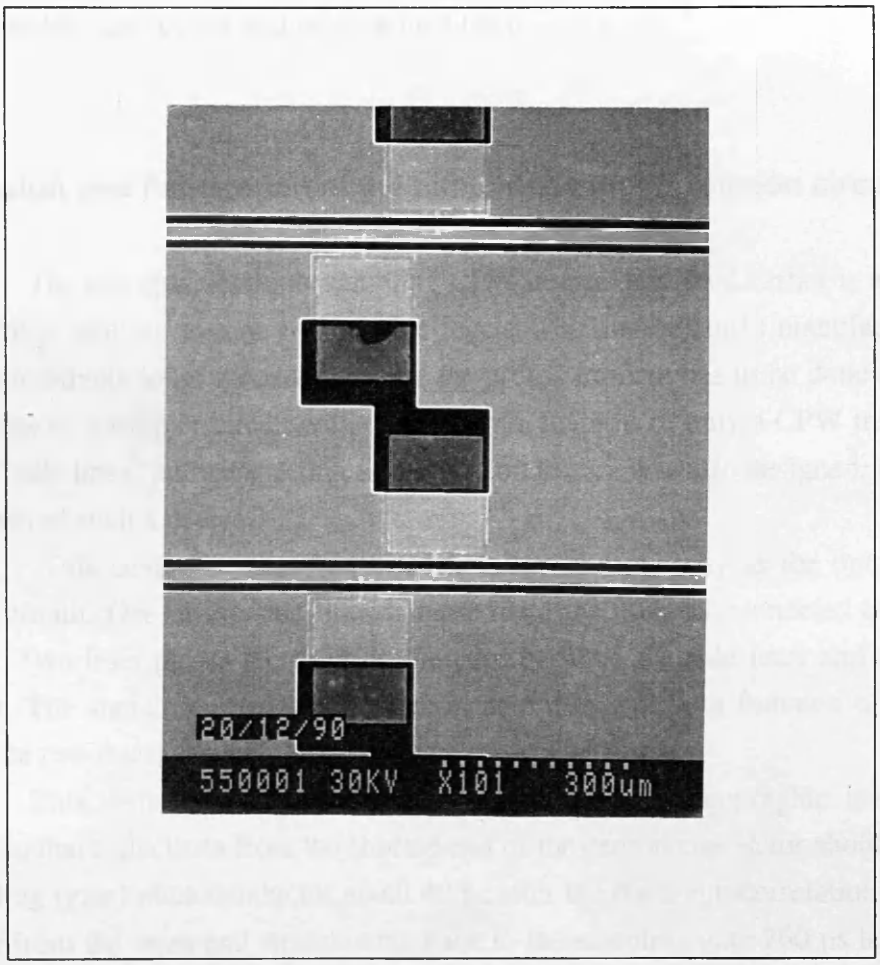

Fig.(5.11) - SEM micrograph of part of a completed chip containing 15 Optoelectronic Sampling Devices. The region near the capacitors and photoconductive gap switches of two OSDs is shown in the picture.

Only test structures, without the Mesfet in the centre were implanted for the preliminary correlation measurements. These samples did not have any type of mask over them, so that the whole surface was implanted with protons. This was the last fabrication step to avoid any high temperatures during resist baking which could degrade the implants.

Fig. (5.11) shows a small region of two sampling devices in a chip. The two horizontal lines in the picture are the central strips of two CPWs. There is a capacitor at each side of the central strip, connected to the photoconductive gap switches. Note that

all ground planes, around the central strips, form a simply connected surface and adjacent devices share the ground plane between them.

Lifetime and photoluminescence measurements were done on these and on control samples. The results will be presented later.

5.4) - Design and Fabrication of the simplified autocorrelation circuit.

The full optoelectronic sampling CPW device described earlier is a relatively complex chip, with up to nine lithographic levels. The time taken to manufacture these devices is relatively long, specially because the proton implant has to be done elsewhere. For this reason, a simpler circuit with the minimum features of only a CPW transmission line, two "side lines" and gaps acting like photoconductors was also designed. Fig. (5.12) is a diagram of such a device.

This device is measured in essentially the same way as the optoelectronic sampling circuit. One of the side lines is biased and the other is connected to a lock-in amplifier. Two laser pulses are fired on the gaps between the side lines and the central conductor. The signal detected by the lock-in amplifier will be a function of the delay between the two laser pulses.

This simplified device can be made in a single lithographic level. It was designed so that reflections from the shorted end of the central conductor should arrive at the sampling (gate) photoconductor about 40 ps after the main autocorrelation peak. The reflection from the open end would come back to the sampling gate 260 ps later, due to its further distance. It is also expected that this reflection will be attenuated by the losses in the CPW. The fabrication procedure is given at the end of the chapter and Fig. (5.13) shows a completed device, where bond wires were used to connect the ground planes across the central strip.

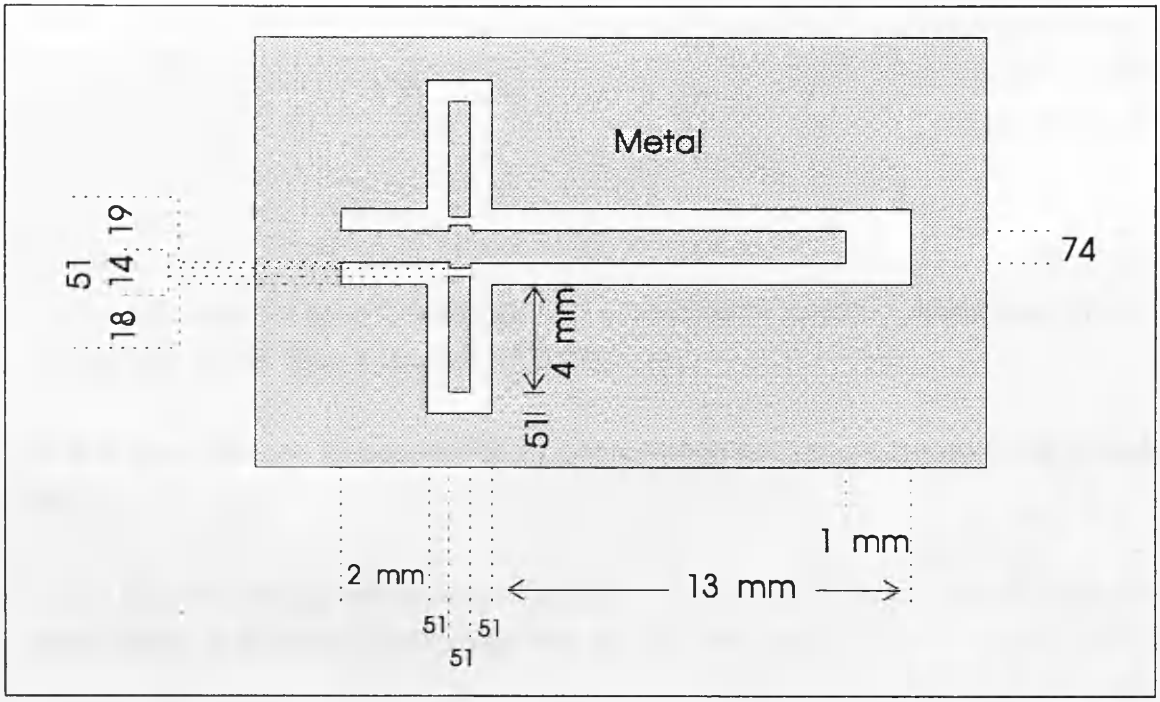

Fig.(5.12) - The simplified optoelectronic sampling device. All dimensions are in μm, unless otherwise stated.

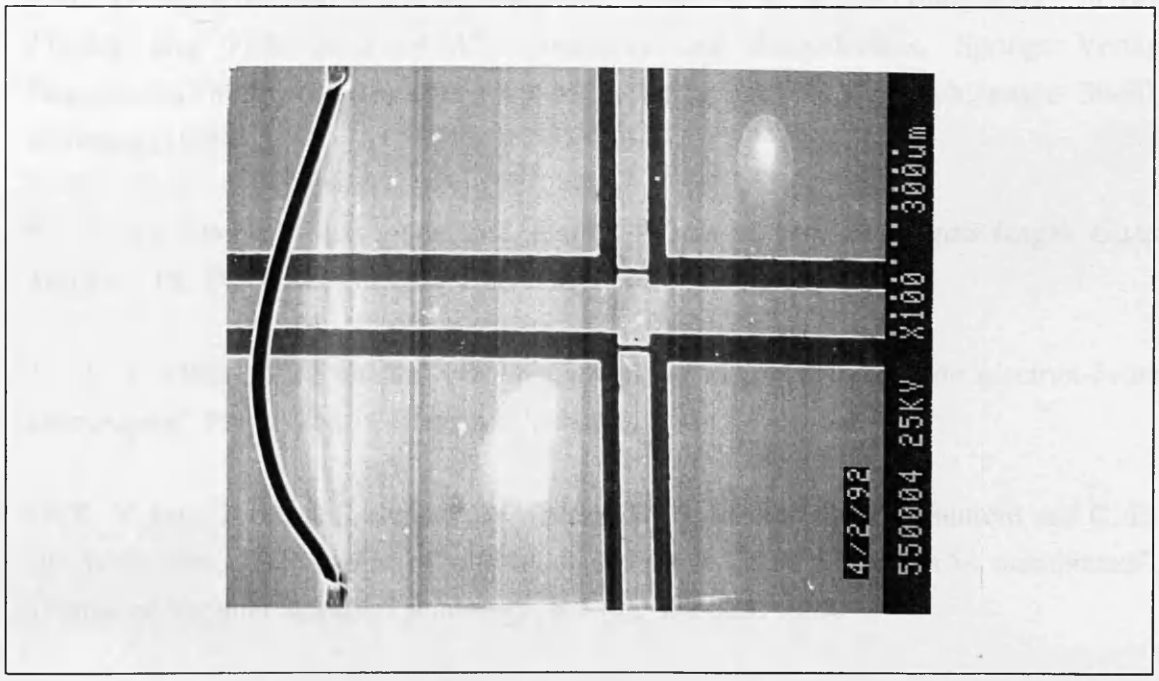

Fig. (5.13) - SEM micrograph of the simplified Optoelectronic sampling device, showing bond wires connecting the ground planes at each side of the central conductor.

5.5) - References to Chapter V

[1] - See the technical note "Microposit S1400 series photoresist", published by Shipley Europe Ltd. Herald Way, Coventry, CV3 2RQ, UK.

[2] - B. J. Canavello, M. Hatzakis and J. M. Shaw, IBM Tech. Disclosure Bull., 19, p.4048, 1977.

[3] - M. Hatzakis, B. J. Canavello and J. M. Shaw, "Single-step optical lift-off process", IBM Journal of Research and Development, 24, 452-460, 1980.

[4] - R. Williams, "*Modern GaAs processing Methods*", Artech House, Norwood, MA, 1990.

[5] - C. D. W. Wilkinson and S. P. Beaumont, "Electron Beam nanolithography", in *The Physics and Fabrication of Microstructures and Microdevices*, Springer-Verlag Proceedings in Physics 13, edited by M. J. Kelly and C. Weisbuch, pages 36-50, Germany, 1986.

[6] - J. A. Adams, "*Fabrication and scaling effects of very short gate-length GaAs Mesfets*", Ph. D. Thesis, Glasgow University, 1990.

[7] - W. S. Mackie, "*Techniques and applications of very high resolution electron-beam lithography*", Ph. D. Thesis, Glasgow University, 1984.

[8] - K. Y. Lee, J. Frost, C. Stanley, W. Patrick W. S. Mackie, S. P. Beaumont and C. D. W. Wilkinson, "Fabrication of ultrasmall devices on thin active GaAs membranes", Journal of Vacuum Science Technology, B 5 (1), 322-325, 1987.

[9] - M. Hatzakis, J. Paraszczak and J. Shaw, "Double layer resist systems for high resolution lithography", in Proceedings of Microcircuit Engineering, 386-396, Delft University Press, Amsterdam, 1981.

[10] - S. P. Beaumont, T. Tamamura and C. D. W. Wilkinson, "A two-layer resist system for efficient lift-off in very high resolution electron beam lithgraphy", in Proceedings of Microcircuit Engineering, 381-385, Delft University Press, Amsterdam, 1981.

[11] - M. J. Rooks, S. Wind, P. McEuen and D. E. Prober, "Fabrication of 30nm-scale structures for electron transport studies using a Polymethylmethcrylate bilayer resist", Journal of Vacuum Science and Technology, B 5 (1), 318-321, 1987.

[12] - C. E. Binnie, "*The Fabrication of samll geometry Mosfets using electron beam lithography*", Ph. D. Thesis, Glasgow University,1986.

[13] - A. N. Broers, "High Resolution Lithography: some comments on limits and future possibilities", in *The Physics and fabrication of Microstructures and Microdevices*,pages 2-14, edited by M. J. Kelly and C. Weisbuch, Springer Proceedings in Physics 13, Springer-Verlag, 1986.

[14] - See thecnical notes published by Hamamatsu Photonics KK, "Photomultiplier Tubes" and "Accessories for Photomultiplier Tubes".

[15] - N. G. Paulter, A. J. Gibbs and D. N. Sinha, "Fabrication of high-speed GaAs photoconductive pulse generators and sampling gates by ion implantation", IEEE Transactions on Electron Devices, Vol. 35, No.12, 2343-2348, 1988.

FABRICATION PROCEDURE FOR: Ni Cr Resistors

Pattern transfer technique: Electron beam lithography

Number of Lithographic levels: two

First Level:	*Ni Cr*	*Resistors &*	*Alignment*	*marks*	
CLEAN: Tric., meth., acetone, IPA Ultrasonic bath 5 min each solvent blow dry in N_2	SPIN: 8% BDH, 5k rpm, 60s bake 1hr 180°C 4% Elvacite 5k rpm 60s bake 2hrs 180°C	EXPOSE: Mag 160x 0.25 µm spot size Beam cur: ~8000 pA	DEVELOP: 2.5 : 1 IPA: MIBK 23°C 30s IPA 30s blow dry	DE - OXIDISE: Wet IPA,H_2O 1:4 HCl:H_2O 30s rinse H_2O blow dry	EVAP.: Ni Cr 30 nm lift-off in acetone

OBS.: Tric = Thrichloroethylene; Meth = Methanol; IPA = Isopropyl alcohol; MIBK = Methylisobutylketone

Second Level:		*PADS*			
CLEAN: rinse acetone, IPA blow dry in N_2	SPIN: 8% BDH, 5k rpm, 60s bake 1hr 180°C 4%Elvacite 5k rpm 60s bake 2hrs 180°C	EXPOSE: Mag 160x 0.25 µm spot size Beam cur: ~8000 pA	DEVELOP: 2.5 : 1 IPA: MIBK 23°C 30s IPA 30s blow dry	DE - OXIDISE: Wet IPA,H_2O 1:4 HCl:H_2O 30s rinse H_2O blow dry	EVAP.: Ti: 30nm Au: 200 nm lift-off in acetone

FABRICATION PROCEDURE FOR: Capacitors

Pattern transfer technique: Photolithography

Number of Lithographic levels: three

First Level:	*Bottom*	*Plate of*	*Capacitors*		
CLEAN: Tric., meth., acetone, IPA Ultrasonic bath 5 min each solvent blow dry in N_2	SPIN: S1400-31 7k rpm 60s bake 15min 90°C Soak in chlorobenzene 15 min bake 5min 90°C	EXPOSE for 11s in mask aligner. mask: CAPS	DEVELOP: 1 : 1 MP:H_2O 45s Stop bath: H_2O blow dry	DE - OXIDISE: Wet H_2O 1:4 HCl:H_2O 30s rinse H_2O blow dry	EVAP.: Metal (nm) Ge 85 Au 65 Ni 18 Au 20 lift-off in acetone anneal 360°C 30s in 95:5 Ar:H_2

OBS.: MP = Microposit Developer; Tric = Thrichloroethylene;
Meth = Methanol; IPA = Isopropyl alcohol.

Second	**Level:**	*Si_3N_4*	*Deposition*	*& patterning*
DEPOSIT: 200nm Si_3N_4 gases ccm SiH_3 10 NH_3 40 N_2 100 Temp:300°C P: 350 mtorr rf: 20 W	SPIN: S1400-31 7k rpm 60s bake 15min 90°C Soak in chlorobenzene 15 min bake 5min 90°C	EXPOSE for 11s in mask aligner. mask: SI_3N_4	DEVELOP: 1 : 1 MP:H_2O 45s Stop bath: H_2O blow dry	SI_3N_4 ETCH gas: C_2F_6, 20 sccm 100W power P: 16 mtorr dc bias: 420V Remove resist etch mask in acetone

Third Level:	*Top*	*Plate of*	*Capacitors*		
CLEAN: Rinse in acetone Rinse in IPA blow dry in N_2	SPIN: S1400-31 7k rpm 60s Repeat step above twice. bake 15min 90°C Soak in chlorobenzene 15 min bake 5min 90°C	EXPOSE for 15s in mask aligner. mask: CPW	DEVELOP: 1 : 1 MP:H_2O 60s Stop bath: H_2O blow dry	DE - OXIDISE: Wet H_2O 1:4 HCl:H_2O 30s rinse H_2O blow dry	EVAP.: metal (nm) Ti 100 Au 500 lift-off in acetone

FABRICATION PROCEDURE FOR: Mesfets

Pattern transfer technique: *e-beam lithography*
Number of levels: *Five*

First level:	*Alignment*	*marks*			
Clean: Tric.,Meth acetone, IPA	Spin: 10%BDH 5k 60s Bake 1hr 180°C 4%Elv 5k 60s Bake 2hr 180°C	Expose: 64nm spot BC 600pA 320 mag	Develop: 2.5:1 IPA:MIBK 30s IPA 30s	De-Oxidise: Wet IPA,H_2O 1:4 HCl:H_2O 30s rinse H_2O blow dry	Evap: Metal (nm) Ni 10 Au 70 lift-off in acetone

Second	***Level:***	*Mesa*	*isolation*			
Clean: Tric.,Meth acetone, IPA	Spin: 6% Polyimide 5k 60s bake 1hr 180°C 10%BDH 5k 60s Bake 1hr 180°C 4%Elv 5k 60s Bake 2hr 180°C	Expose: 0.125μm BC:2000pA 320 Mag	Develop: 1:1 IPA:MIBK 30s rinse IPA	Evap: 500 nm Ge Lift-off	Mesa Etch: Oxygen Polyimide etch 50W 10min Flow 30cc/min methane/H_2 80W 10nm/min Flow 50/25cc	Remove: Actphnone boil 1hr examine utlrasonic Fresh actphnone boil 1/2 hr examine

Actphnone = Acetophenone

Third	***level:***	*Ohmic*	*contacts*			
Clean: Tric.,Meth acetone, IPA	Spin: 10%BDH 5k 60s Bake 1hr 180°C 4%Elv 5k 60s Bake 2hr 180°C	Expose: 64nm spot BC 600pA 640 mag	Develop: 2.5:1 IPA:MIBK 30s IPA 30s	De-Oxidise: Wet IPA,H_2O 1:4 HCl:H_2O 30s rinse H_2O blow dry	Evap: Metal (nm) Au 70 Ge 30 Ni 10 Au 20 lift-off in acetone	Anneal: 360°C 30s in 95:5 Ar:H_2

Fourth	***level:***	*Probing*	*Pads*		
Clean: Tric.,Meth acetone, IPA	Spin: 15%BDH 5k 60s Bake1hr 180°C 4%Elv 5k 60s Bake 2hr 180°C	Expose: 0.25μm spot BC 8000pA 320 mag	Develop: 2.5:1 IPA:MIBK 30s IPA 30s	De-Oxidise: Wet IPA,H_2O 1:4 HCl:H_2O 30s rinse H_2O blow dry	Evap: Metal (nm) Ti 40 Au 300 lift-off in acetone

Fifth	***level:***	*Gates*				
Clean: Tric.,Meth acetone, IPA	Spin: 4%BDH 5k 60s Bake1hr 180°C 4%Elv 5k 30s Bake 2hr 180°C	Expose: 16 nm spot BC: 60pA 1250 mag	Develop: 2.5:1 IPA:MIBK 30s IPA 30s	De-Oxidise: Wet IPA,H_2O 1:4 HCl:H_2O 30s rinse H_2O blow dry	Recess: Wet IPA,H_2O 5:1:200 H_2SO_4:H_2O_2:H_2O	Evap: Metal (nm) Ti 20 Au 65 lift-off in acetone

FABRICATION PROCEDURE FOR:Simplified Optoelectronic Sampling Device

Pattern Transfer Technique: *Photolithography*
Number of levels: *One*

Simplified	*Opto electronic*		*Sampling*	*Device*	
Clean: Tric, Meth Acetone IPA blow dry	Spin: S1400-31 7k rpm 60s three times bake 15min 90°C soak in chlorobenzene 15min bake 5 min 90°C	Expose: for 11s in mask aligner mask: SOSD	Develop: 1:1 MP:H_2O 45s Stop bath: H_2O blow dry	De-Oxidise: Wet H_2O 1:4 HCl:H_2O 30s rinse H_2O blow dry	Evap: Metal (nm) Ti 100 Au 500 Lift-off in acetone Anneal at 320°C in Ar:H_2

Chapter VI - Optoelectronic Measurements

6.1) - Dye laser measurements

The rodhamine 6G synchronously pumped dye laser was used for correlation measurements. The frequency doubled mode-locked Nd:YAG laser described in chapter II was used as the pump laser. The dye laser wavelength was tuned to $\lambda = 590$nm.

The sample to be measured was mounted on a copper plate rig where electric probe needles (for low frequency signals) were used to bias one of the photoconductors and extract the correlation voltage from the other. Ground connections were provided by bond wires from the device to the copper plate.

The signal extracted by the probe is fed, by a coaxial cable, to a low impedance (50Ω) current amplifier with a gain of 1 V/μA. The output of the current amplifier goes to the input of the lock-in amplifier. Figure (2.9) from chapter II shows schematically the experimental set up.

The two fibres f_1 and f_2 have the same length, namely, 80 cm. The distance (in air) l_{a1} between the beamsplitter and fibre f_1 is 175 mm. Therefore, in order for the pulses going through route 1 and 2 (Fig.(2.9), chapter II) to arrive simultaneously at the two photoconductors, l_{a2} must also be 175mm. The two laser beams are coupled into the two fibres using microscope objectives and the average power exiting each fibre is about 5 mW.

The delay line, consisting of the retroreflector mirror mounted onto the computer controlled step motor translation stage, was set-up so that the zero delay point

is roughly in the middle of its total travel of 150mm. The total travel range corresponds to a time window of 1.2 ns. One single step in the translation stage moves the retroreflector by 2.5 μm. Thus the time resolution is 2 x 2.5/(3 x 10^{14}) = 17 fs. Therefore, the time resolution of the whole measurement system is not limited by the step size of the translation stage. It will rather be determined by the laser pulsewidth or the carrier lifetime in the material. The larger of these two parameters will determine the time resolution of the measurement system.

It is essential to align the delay line so that when the retroreflector is moved, the light intensity exiting the fibre does not change. In general, it is difficult to maintain this alignment for the whole travel range of the delay line. On the other hand, for short travel distances, up to about 3 cm, this is easily achieved. Moving the retroreflector by 3 cm corresponds to a time window of 200 ps.

Experiments were performed with the dye laser pumped by 700 mW (average) of 514.5 nm laser pulses. The pump light is obtained by frequency doubling the output of the Nd:YAG laser using a KTP crystal. The alignment of the delay line was checked by scanning it 15 mm from the zero delay position in each direction while monitoring the output of the fibre f_2 with a power meter. After alignment optimization the delay line can be moved more than 20 mm in each direction, without any observable change in the coupling to the fibre f_2.

A typical measurement procedure can be described in the following manner. The device to be measured is biased with V_b = 5 Vdc, the probe to extract the signal was connected to the sampling photoconductor and the fibres are aligned to the photoconductors. The sampling laser beam is chopped at 196 Hz. The lock-in settings are as follows: time constant = 1s and sensitivity of 20 mV. The signal detected by the lock-in at the reference frequency of 196 Hz is 9 mV. Some tests are then performed to ensure that this signal is the actual autocorrelation voltage:

* The signal displayed by the lock-in goes down to zero if either of the two laser beams is blocked.

* The signal increases or decreases if the voltage bias is increased or decreased respectively. Thus it depends on the voltage bias as expected. Accurate measurements of this dependence will be presented later in this chapter.

* If either or both laser beams are blocked and the voltage bias is still on, the signal drops to 0.02 mV, i.e., the dark current is very low. Conversely, if Vb = 0 and the two laser beams are impinging upon the photoconductors, the signal is zero.

The checking procedure above ensures that the signal detected is the autocorrelation voltage. One problem is evident, however. It is sometimes possible to see the dye laser output flickering. This very low frequency noise has a drastic effect on the correlation measurements, as shown by the correlation plots in fig.(6.1). No autocorrelation peak at t = 0 can be found. The data can not be reproduced even in a time scale of a few minutes. All measurements in fig. (6.1) were taken one after the other, i.e., the time elapsed between two measurements is about 5 min. A number of alignment optimization procedures were tried with the Nd:YAG laser, with the KTP crystal and also with the dye laser. They proved unsuccessful. The laser noise seemed to dominate the signal.

The laser noise can be traced back to the Nd:YAG pump laser. A possible way to improve the laser stability was mentioned in chapter II, which involves a feedback loop from the laser output to the rf power supply for the mode-locker. This system was not tried in this project. Hence, despite a great deal of work to optimize the laser performance or to remove the laser noise after measurement, this laser was eventually abandoned. It is important to note that only state of the art lasers have been used so far in this type of measurement. Virtually all of them are home made. It is therefore not a coincidence that optoelectronic high frequency measurements have been made in groups with strong research in short pulse lasers.

6.2) - Measurements with the Ti:Sapphire laser

6.2.1) - Correlations

The Ti:Sapphire laser described in chapter II was used for autocorrelation measurements in the proton implanted and control samples. A vast improvement in the signal to noise ratio as compared to the dye laser measurements was achieved. The experimental set-up is the same, except for the laser. The parameters of the experiment are:

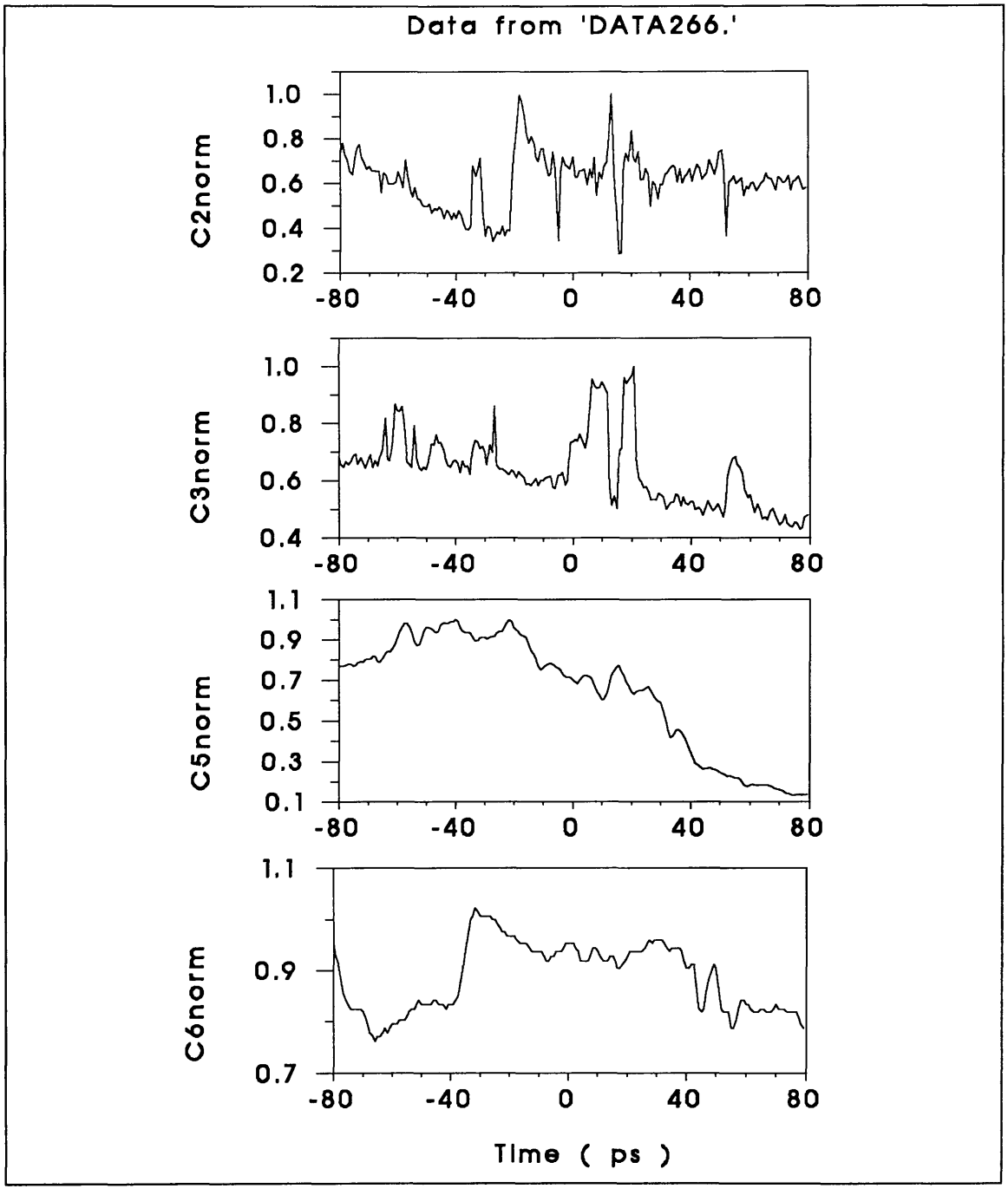

Fig.(6.1) - Autocorrelation curves measured in a proton implanted device ($4x10^{14}$ cm^{-2}) using the dye laser as the source of light pulses. In the first two measurements, the lock-in time constant was set to 1s. In the last two, the time constant was increased to 10s in an attempt to reduce the noise, with limited success. The drift in the laser intensity occurs in a time scale shorter than the time taken to perform one measurement.

V_b = 3.2 Vdc
Chopping frequency : 600 Hz
Lock-in settings:
time constant: 300 ms
sensitivity: 200 mV

Laser settings:
λ = 740 nm
P1 = P2 = 20 mW
τ = 2 ps

The signal goes first to the current amplifier and then to the lock-in. The first measurement taken from the same sample tested with the dye laser is shown in fig.(6.2). The correlation trace is not centred in the time window.

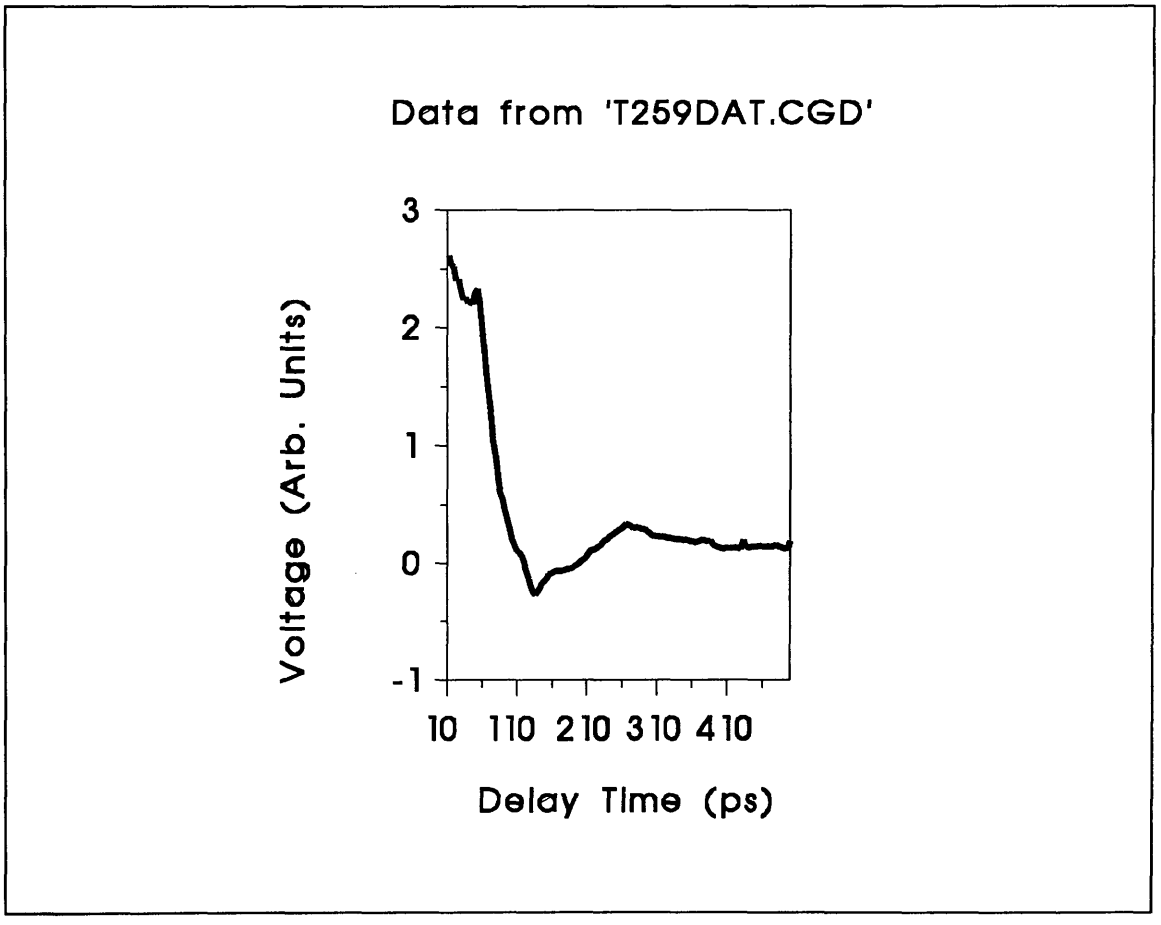

Fig.(6.2) - The first correlation curve measured with the Ti:Sapphire laser. The peak is not centred in the time window because the distance travelled by the two laser beams is not the same. Compare this with the next picture, obtained after adjusting the distances in the experimental set-up.

The "fixed" arm of the measurement set-up (route 1, fig.2.9) was then increased by ≈ 12mm, in order to centre the curve in the time window. Many measurements were then taken and the one shown in fig.(6.3) is the cleanest. The laser is monitored during measurements by a SHG autocorrelator whose output is displayed in an oscilloscope. Any intensity fluctuations in the laser will show up in the oscilloscope display.

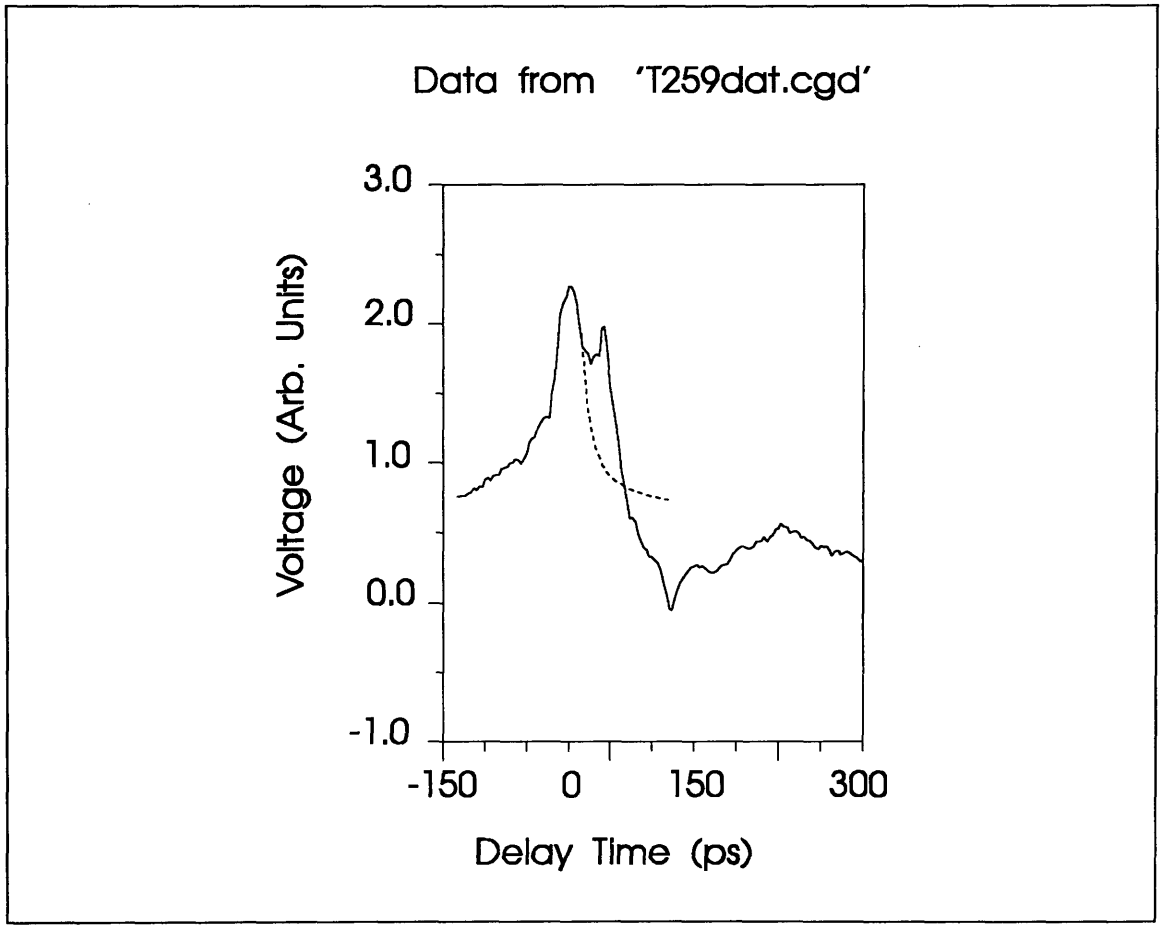

Fig.(6.3) - Correlation measurement of a proton implanted device. The lifetime in the material was not shortened enough by the proton implantation. The main peak and the reflection from the end of the line overlap. The dashed line suggests the possible pulse shape for the main peak and it will be used for pulsewidth estimation in the text.

A preliminary inspection in the curve in fig. (6.3) shows interesting features. It has to be recalled from chapter II that a voltage pulse generated at the photoconductive

switch would take roughly 25 ps to reach the centre of the device where there is an open circuit and so, it would be reflected back and pass the sampling photoconductor ≈ 50 ps after generation. It is assumed in the reasoning above that the signal travels at a speed of $c/n \approx 100$ μm/ps, where n is the refractive index of GaAs. The distance between the two first peaks in fig. (6.3) is 42 ps. These two peaks are interpreted as being the autocorrelation trace of the voltage wave and its reflection from the open circuit at the centre of the device. They merge together because they are much broader than expected.

It is also predicted that the other end of the line, i.e., the end terminated by the integrated resistor, will also produce some reflection which should arrive at the sampling photoconductor 100 ps later. The small, negative going, peak at 120 ps is interpreted as being this reflection.

The correlation measurements were repeated many times and in different devices of the same chip. Small differences in the separation between the two peaks are evident, but the overall shape of the correlation traces is very similar. Some of these measurements are presented in fig. (6.4).

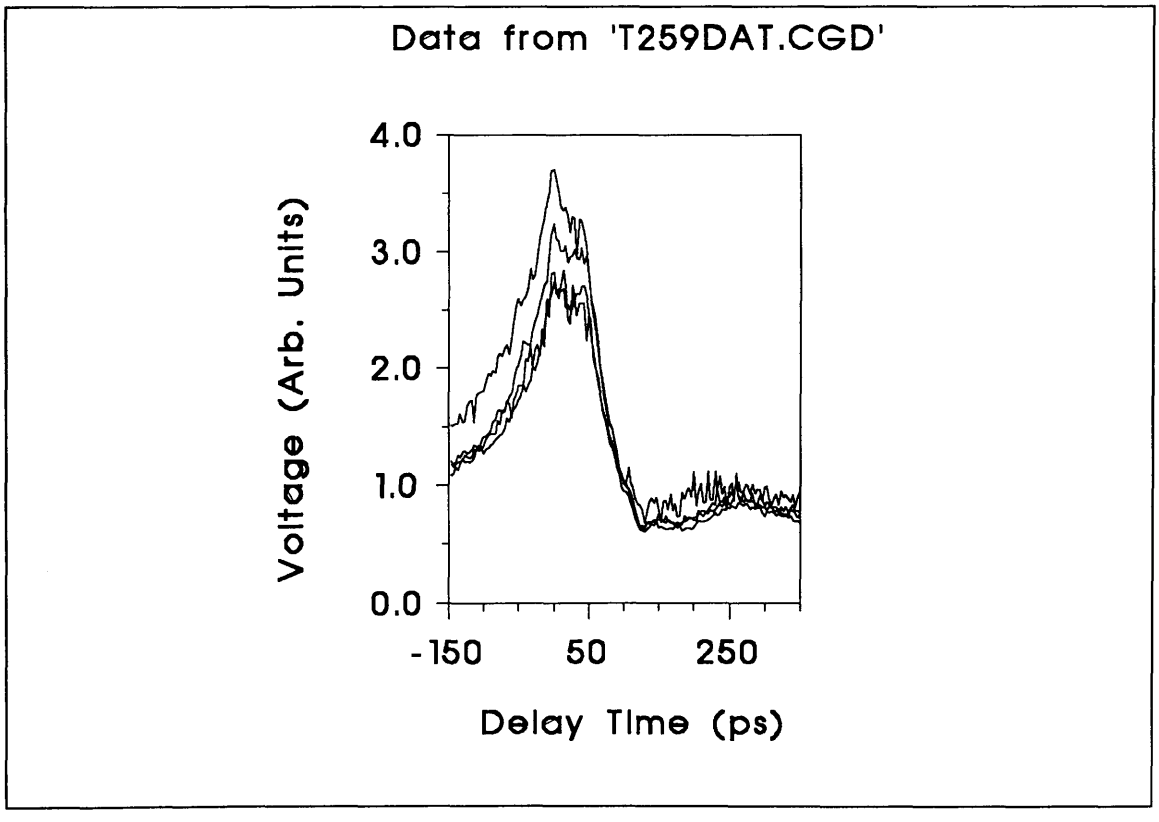

Fig. (6.4) - Some of the measurements taken from different devices in the chip. Some variations in the leading edge of the main peak are evident, but the overall curve shape is the same for all devices measured.

A correlation trace was deliberately measured during intensity fluctuations in the laser. The curve is shown in fig. (6.5). The spurious peaks appearing at the beginning and at the end of this curve were caused by oscillations in the laser. It is therefore essential to have stable and short pulses for this experiment! It is also clear that the curves measured with the dye laser (fig.6.1) were totally swamped by the low frequency fluctuations in that laser.

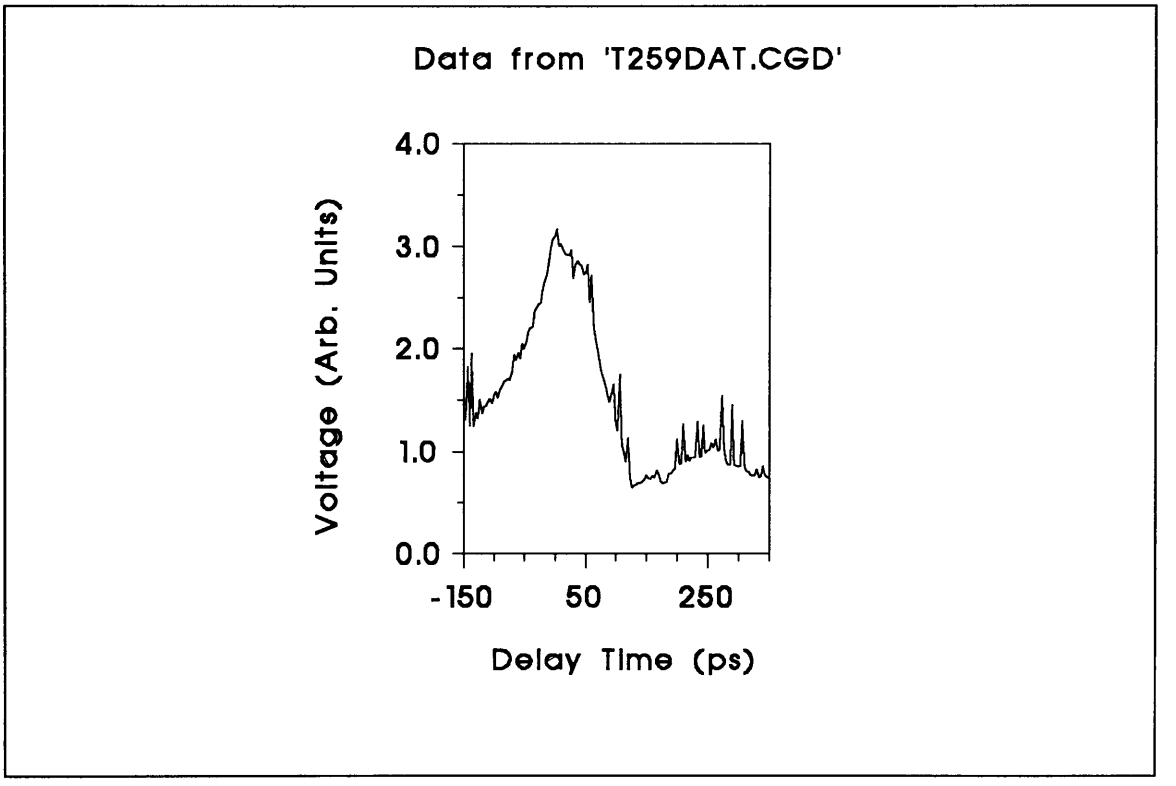

Fig. (6.5) - Measurement done during intensity fluctuations in the Ti:Sapphire laser. It is clear that noise-free measurements are possible only with a stable laser.

The sample used in the experiments above had been implanted with 4 x 10^{14} protons/cm^2. Many measurements were performed in samples with implant doses of 10^{14} and 2 x 10^{14} protons/cm^2. No significant differences were found in the correlation curves for these two different doses and the control (non-implanted) samples. This can be explained by a failure of the proton implantation to produce a high enough density of fast recombination centres. If the number of traps is not high enough, the carriers can not tunnel between them to recombine. When these recombination paths are not provided, the carriers are eventually re-emitted, making the overall lifetime very long.[1] Shallow defects can also cause this type of problem as they tend to have fast re-emission rates.[1]

The density of defects generated in the sample implanted with 4×10^{14} protons/cm^2 can be estimated from:[1]

$$N_t = \frac{1}{\tau_c \sigma_c < v_{th} >}$$

and from fig.(6.3). By extrapolating the trailing edge of the first peak (as suggested by the dotted line in fig.6.3), its FWHM is found to be $\Delta t = 40$ ps. Assuming that the electric pulse generated at the photoconductive switch can be described by a gaussian with FWHM τ_c, then[2] $\tau_c = 0.707\Delta t = 28$ ps. Taking the capture cross section to be 10^{-13} cm^2 and the thermal velocity equal to $< v_{th} > = 10^7$ cm/s, N_t is given by $N_t \approx 3 \times 10^{16}$ cm^{-3}. This is a very low density of capture centres if compared to the 10^{18} or 10^{20} cm^{-3} necessary to produce a lifetime of 1 ps in GaAs.[1]

The possible explanation for the failure of the proton implantation is the lack of temperature control in the implanter. Paulter[3] performed experiments where the temperature of the specimen could be accurately controlled during implant. It was then shown that if the temperature of the specimen is increased above 8°C, a correspondingly higher ion dose had to be used to produce the same lifetime. This dependence of the carrier lifetime on the implant temperature was interpreted as evidence for creation and subsequent annealing of the fast recombination centres. Therefore, according to this picture, a much higher dose of ions would have to be used in implants without the benefit of temperature control. For this reason, the devices made on this work were implanted with 1, 2 and 4 times the ideal dose of 10^{14} cm^{-2} suggested by Paulter.[3] It seems that the dose was still too small to produce the short lifetime required for high speed optoelectronic sampling. A comparative investigation of the luminescence of the proton implanted devices, Low temperature GaAs devices and control samples will be presented later in this chapter.

It is also important to mention that the increase of lifetime with implant temperature is not a widely accepted phenomenon. There are in fact, reports in the literature where an annealing step after implant is used to anneal shallow defects, but retain the deep traps, producing short lifetime.[4] Such conflicting data is a sign of the poor understanding of the fast capture mechanisms produced by the ion damage.

Control devices made on semi-insulating GaAs without proton implantation were also measured by the optoelectronic sampling technique. The result of one such measurement is shown in fig.(6.6) below. This correlation curve shows almost no

features, increasing slowly for negative time delay and decreasing slowly for positive delays. This is what should be expected if the carrier lifetime in the material is very long.

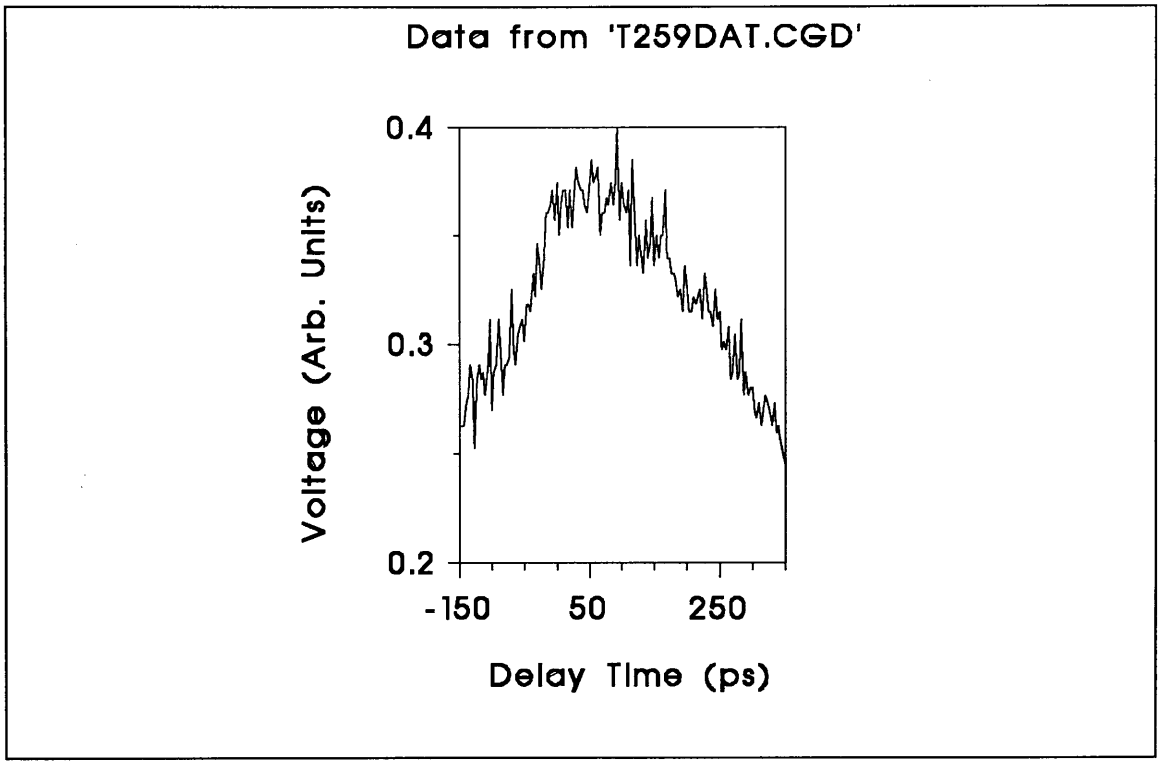

Fig.(6. 6) - Correlation curve measured in a control (i.e., semi-insulating) device. The lifetime is longer than the proton implanted devices.

The above results can be summarized as follows. The semi-insulating, undoped GaAs has a long lifetime (of the order of 200ps) and the incident and reflected pulses can not be resolved. The samples implanted with 1 and 2 x 10^{14} protons/cm^2 have a lifetime very similar to the control samples, which indicate a total failure of the proton implantation in reducing the carrier lifetime. The devices implanted with 4 x 10^{14} protons/cm^2 have a shorter carrier lifetime and the incident and reflected pulses can just be resolved, producing pulses of an estimated FWHM of $\simeq$40ps. The lifetime in these implanted devices is still over one order of magnitude above the desired value.

6.2.2) - Network analyser measurements

Another way of detecting the signal sampled at the second photoconductor is by the use of a spectrum analyser. An HP8553B spectrum analyser with a bandwidth of 110MHz and a frequency resolution of 30Hz was used for some measurements. The experimental set-up is the same as that used before. The only difference is that the preamplifier and lock-in were replaced by the spectrum analyser. As the latter does not have any interface for computer control, data could not be recorded by the computer. However, an interesting graphical representation of the signal is obtained on the screen of this instrument. The pulse generator is biased at 5 V_{dc}, the paths for the two laser pulses are adjusted to make them arrive simultaneously at the photoconductors and a probe needle extracts the signal. Fig. (6.7) below shows the signal detected by the network analyser.

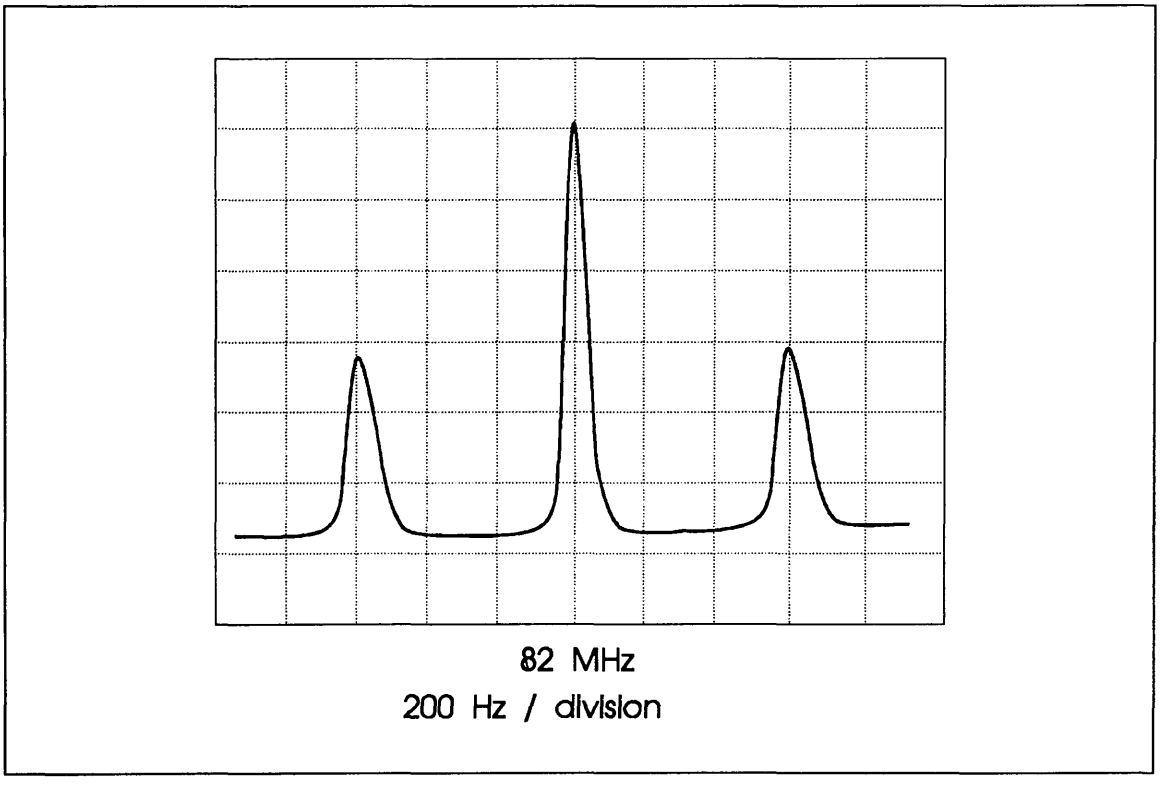

Fig. (6.7) - Signal detected by the Network analyser. The peak centred at 82 MHz is picked-up from the rf power supply for the laser mode-locker. The two side-lobes at ± 600 Hz represent the signal switched across the two photoconductors.

The peak in the middle is centred at 82 MHz. This is in fact a signal picked up from the rf power supply for the mode-locker in the Ti:sapphire laser. If both laser

beams are blocked so that no light reaches the photoconductors, this central peak remains unchanged.

The two side lobes, 600 Hz away from the central peak are the signal detected by the probe. As the mechanical chopper produces an ON-OFF modulation at 600 Hz, the carrier wave i.e., the pulse repetition rate of the laser is totally suppressed. The two side-lobes move away or towards the central peak if the frequency of the chopper is increased or decreased respectively. If either of the laser beams is blocked, the two side-lobes disappear completely, showing that this is in fact the electrical signal switched across the two photoconductors.

Scanning the delay line in a time window of about 400 ps makes the signal vary slowly, decreasing at the extremes of the travel distance. This is not an accurate autocorrelation measurement, but the signal varies in a way similar to the experiments with the lock-in amplifier. Thus, despite the lack of numerical data and accuracy, this test helped to confirm, by a totally independent measurement system, the results obtained with the correlation functions recorded by the computer.

6.2.3) - Sampling oscilloscope measurements

As the electric pulses generated by switching across the photoconductors are long, one should be able to detect them directly, using a fast sampling oscilloscope. In this case, it is not necessary to use a chopper to create a known modulation in the output signal.

A Tektronix 7904A sampling oscilloscope fitted with an S6 sampling head was used. This system has a risetime of about 25 ps.

Firstly, one single photoconductor was tested as shown by the schematic drawing in fig.(6.8). The photoconductor was biased with V_b = 5 Vdc. A cascade Microtech CPW probe (18 GHz) was used to extract the signal from the central conductor of the CPW device, which is fed to the sampling oscilloscope. It was necessary to use this special probe (and microwave cables) because the signal detected by the probe needle is too small to be displayed by the oscilloscope. This is due to the probe high inductance and loss. A trigger signal at 82 MHz was provided by the rf driver for the laser mode-locker. Figs. (6.9.a) and (6.9.b) show two of the pictures obtained. In (6.9.a), two electric pulses are displayed, separated in time by about 11.5 ns, which is the laser pulse repetition time. Fig. (6.9.b) shows a single pulse with $\simeq$200 ps FWHM. The electric pulses displayed by the sampling oscilloscope are longer than the autocorrelation traces, due to the bandwidth limitations of the oscilloscope, probes and high frequency

connecting cables. Note the fast risetime of the pulse in (6.9.b), followed by the much slower decay associated with the long carrier lifetime. Again, the electric signals shown in fig. (6.9) go to zero if the laser beam is blocked or if the voltage bias is reduced to zero. This is the most direct visualization of the electric pulses switched by a photoconductor.

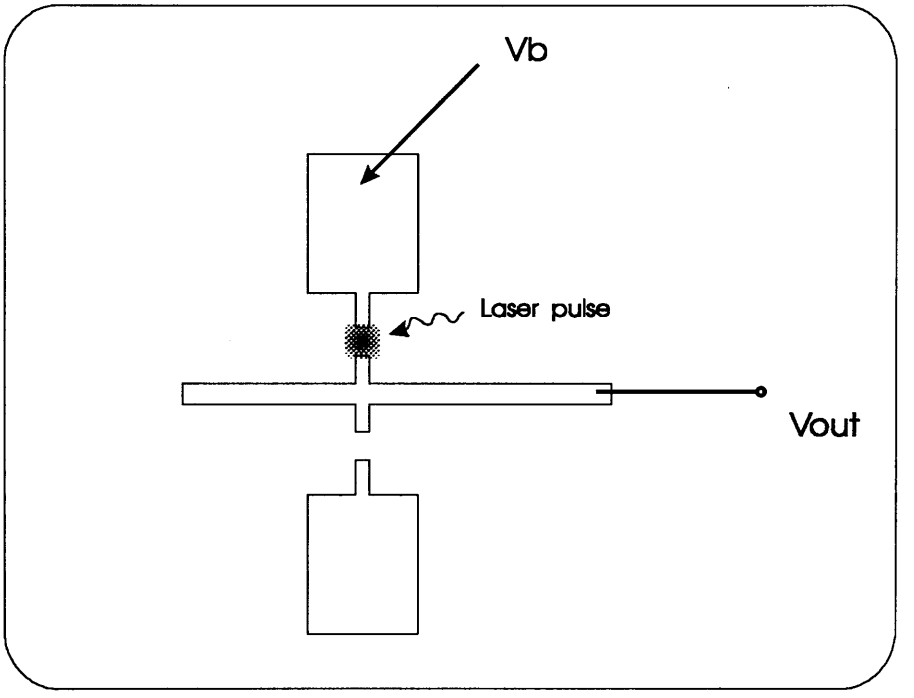

Fig.(6.8) - Schematic drawing of a single photoconductor measurement. The signal Vout is detected by a high frequency coplanar probe and displayed by a sampling oscilloscope.

A double switching scheme, i.e., the use of two laser beams and two photoconductors was also tried. A picture of the signal detected is shown in fig. (6.10). In this case the signal is very weak and the voltage bias has to be increased largely to produce a switched signal strong enough to be displayed by the oscilloscope. This is to be expected as the signal switched by the first photoconductor becomes the voltage bias for the second one. From fig. (6.9), the switching efficiency (V_{out}/V_b) is 2.26 x 10^{-2}. If the system is linear then, the same relation will hold for the second switch. One would then expect the efficiency to be the square of the value above, i.e., 5.1 x 10^{-4}. From fig. (6.10), the peak signal is 12.5 mV for a voltage bias of 25 Vdc. Thus, the ratio of the signal switched across the two photoconductors and the voltage bias is 5 x 10^{-4}. This highlights the linearity of the extracted signal with the voltage bias.

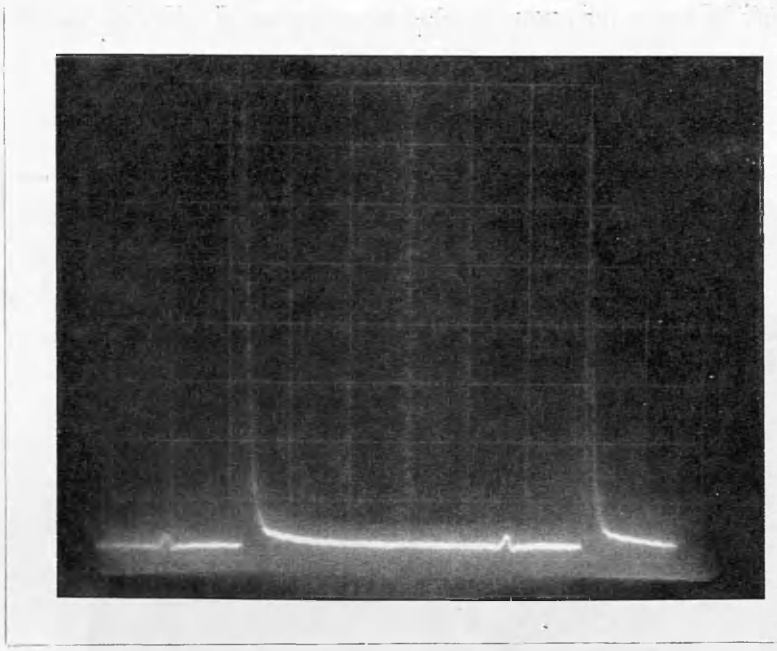

(a)

Fig.(6.9) - Pictures of the electric pulses switched across a single photoconductor. In (a), the horizontal scale is 2ns/division and the vertical scale is 20mV/division. In (b) one has 200ps/division in the horizontal and 20mV/division in the vertical.

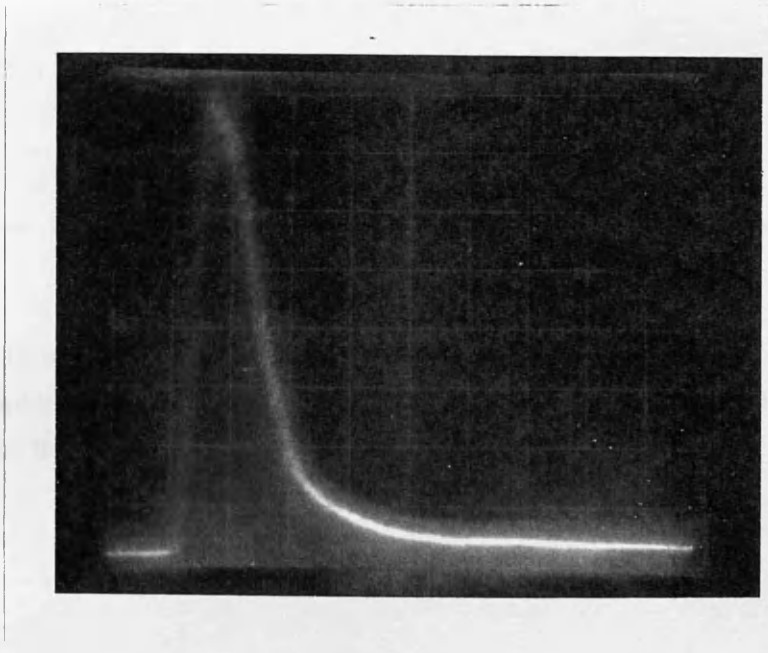

(b)

The sampling oscilloscope technique is the simplest way of detecting the signal and its use in other measurements will be reported again in this and in the next chapter.

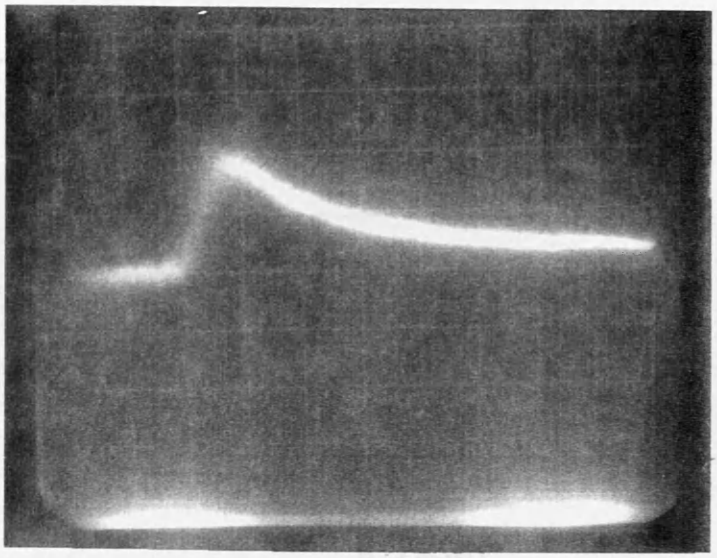

Horizontal: 200ps/division
Vertical: 5mV/division

Fig.(6.10) - Picture of a voltage pulse switched across two photoconductors. The voltage bias in the first photoconductor had to be increased to 25 Vdc to produce a signal large enough to be displayed by the oscilloscope.

6.3) - Sampling Oscilloscope Measurements of the Signal linearity.

The output signal of a single switch (as in fig.6.9) was measured as a function of the voltage bias and laser power. Firstly, the voltage bias was kept fixed at V_b = 5Vdc and the average power in the laser beam was varied. The laser beam is chopped before entering the optical fibre, at a frequency of 470 Hz. The signal at this reference frequency is then detected by the lock-in amplifier. The data obtained is plotted in fig.(6.11), where the linear variation is evident.

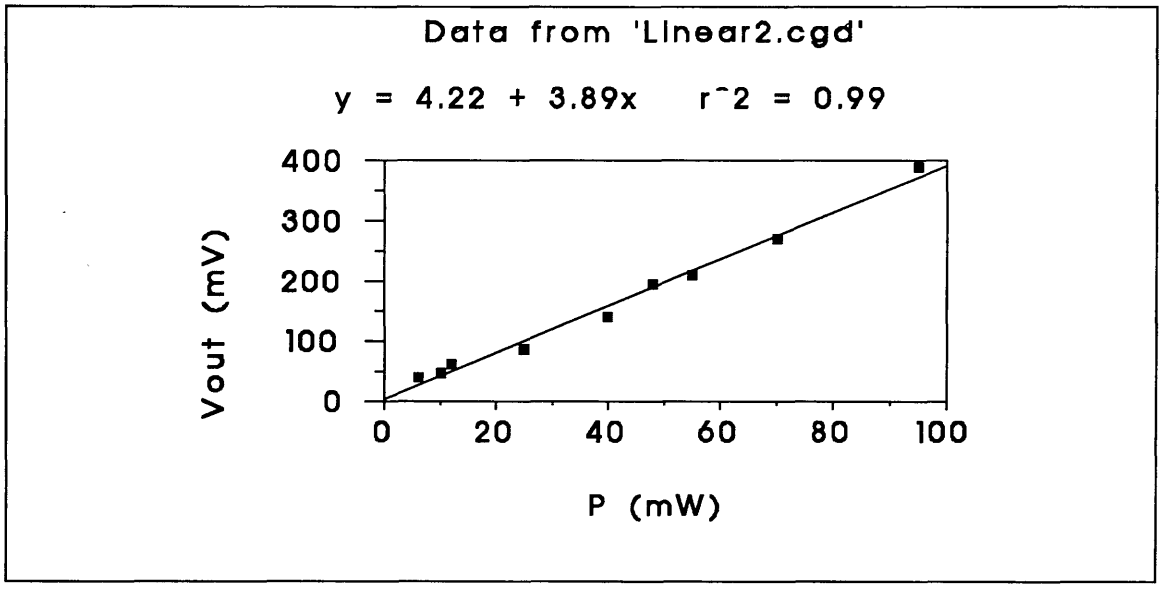

Fig. (6.11) - Output voltage from a photoconductor as a function of the pump laser power, for a fixed voltage bias of V_b = 5 Vdc.

The variation of the extracted signal with the voltage bias was also measured, keeping constant the laser intensity. Fig. (6.12) is a plot of that measurement, where the voltage bias was varied from 0 to 12 V_{dc} and the laser intensity was kept fixed at 10 mW.

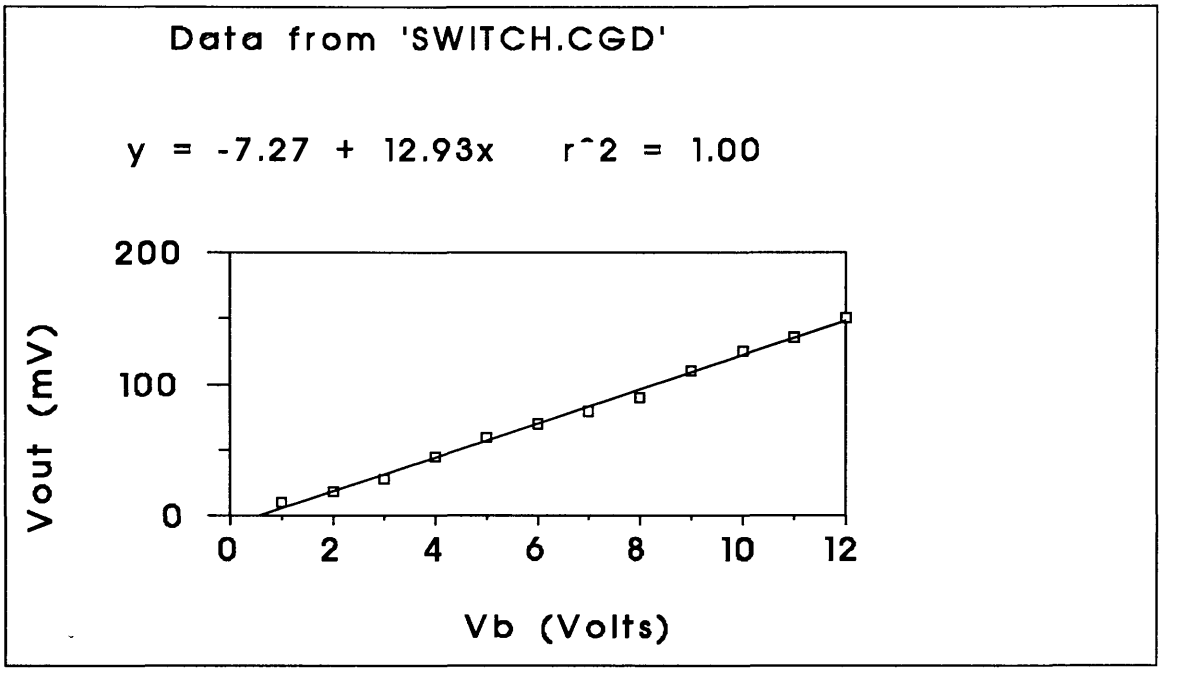

Fig. (6.12) - Measured response of a photoconductor as a function of the voltage bias, for a fixed laser power of 10 mW.

Other optoelectronic measurements were performed on devices made on GaAs grown by MBE at very low temperatures. The properties of this material will be reviewed in the next chapter and its growth procedure, characterization and the performance of devices made on it will be presented.

6.4) - References to Chapter VI

[1] - D. H. Auston, "Picosecond Photoconductors: Physical properties and applications", in *Picosecond Optoelectronic Devices*, edited by Chi H. Lee, 73-117,Academic Press, Inc. Orlando, 1984,

[2] - K. L. Sala, G. A. Kenney-Wallace and G. E. Hall, " CW autocorrelation measurements of picosecond laser pulses", IEEE Journal of Quantum Electronics, Vol. QE16, No.9, 990-996,1980.

[3] - N. G. Paulter, A. J. Gibbs and D. N. Sinha, "Fabrication of high speed GaAs photoconductive pulse generators and sampling gates by ion implantation", IEEE Transactions on Electron Devices, Vol. 35, No. 12, 2343-2348, 1988.

[4] - A. G. Foyt, F. J. Leonberger and R. C. Williamson, "Picosecond InP optoelectronic switches", Applied Physics Letters, Vol.40, 447-449, 1982.

Chapter VII - Low Temperature Buffer Layers

7.1) - Introduction

There are presently two possible ways of producing GaAs material with short carrier lifetime. The first and more conventional way involves the implantation of ions on a GaAs substrate. This was discussed before, in chapter V. In the last four years, a new material, GaAs with excess arsenic (GaAs:As) grown by MBE at low temperatures, was shown to produce very short lifetimes. The initial motivation for the development of this material was a common isolation problem in GaAs Mesfets,[1,2,3] known as backgating or sidegating. This is a reduction in I_{ds}, the drain-source current due to a negative voltage bias applied to the substrate or to an isolated contact pad (the sidegate). Thus, an applied voltage on the substrate or on other devices in the same chip can have an effect on space-charges at the channel-substrate interface. If this interfacial depletion region widens into the channel, the current flowing through the channel of the Mesfet is reduced.[4] This can be particularly detrimental for the operation of GaAs integrated circuits.

An obvious way of trying to reduce or eliminate this problem is the insertion of a buffer layer between the substrate and the active channel. A number of different

materials have been used for such purpose, with limited success, including undoped GaAs, AlGaAs and superlattices (AlGaAs/GaAs) with and without growth interruptions.[5]

A breakthrough happened in 1988, when F. W. Smith et. al. developed a new buffer layer which completely eliminates sidegating in GaAs Mesfets.[6] This new buffer layer is grown by MBE at temperatures between 200 and 300°C. These growth temperatures are much lower than the typical 600°C MBE growth temperature for GaAs. For this reason, this material became known as Low Temperature Buffer Layers, or LTBLs.

7.2) - Growth procedure for Low Temperature Buffer Layers.

A Typical growth procedure can be described as follows:[7]

* A 2" LEC GaAs wafer is degreased in H_2SO_4 and placed in substrate holders for growth.
* It is then outgassed in the entry chamber of the MBE machine for 2h at 200°C and then moved to the growth chamber where it is heated to 615°C for 2 min. This last step removes the surface oxides which desorb at 580°C. The temperature is then lowered to the initial growth temperature of 600°C.
* The growth rate is set to 1 μm/h. Both As_4 and As_2 can be used. For samples grown with As_2 the As/Ga beam equivalent pressure is set to 22. Similar pressures are used for As_4. In general, the beam equivalent pressure is well above 10. This ratio is normally much higher than the normally used ratio during MBE growth of "standard temperature" layers.
* Initially 0.75 μm of GaAs is grown. The temperature is then lowered from 600°C to 250°C during growth of the next 0.25μm of GaAs.
* The low temperature buffer layer (LTBL) is now grown. The thickness is normally 1 or 2 μm.
* The substrate temperature is raised again to 600°C during the growth of the next 50nm of GaAs. Upon reaching 600°C, a 10 nm top layer of undoped GaAs is grown.
* The wafer is then annealed *in situ*, in the As_2 or As_4 flux for 1h at 600°C. This annealing step can also be done at a later stage in a conventional furnace or rapid thermal annealer. A shorter time is used in such cases.
* The substrate is rotated at 5 rpm during the growth and *in situ* annealing.

The measurement of temperature during this growth procedure is not straightforward. At high temperatures, in the neighbourhood of 600°C, the temperature is

measured by a pyrometer. This is a measurement of the temperature at the surface of the wafer, where growth takes place. When the temperature is lowered down to 250°C, this technique can not be used as the wafer is not hot enough to produce any visible glow. A thermocouple embedded in the substrate holder block is used instead. It is immediately evident that this is not the same as the substrate temperature. The calibration between these two methods of temperature measurement normally changes with different substrate holders and the amount of material deposited on the holder[8]. In general, when the pyrometer measures a temperature in the neighbourhood of 600 °C, the thermocouple reading is around 700 °C. Therefore, the absolute temperature of growth of the LTBL is not directly measured, which makes it difficult to establish a growth procedure in a particular MBE machine.

The temperature of 250°C quoted before, in the growth procedure, is a temperature measured by the thermocouple . It should be taken only as a guide-line because this value changes from one substrate holder (or MBE machine) to another.

7.3) - Structural, Electrical and Optical characteristics of Low Temperature Buffer Layers

The low temperature buffer layers have unique electrical and optical properties. The most relevant of them are summarized below, for (non-annealed) "as-grown" and annealed samples.

Non-annealed samples:

* The growth at low temperature with a large As/Ga beam equivalent pressure produces a material containing 1-2% excess arsenic. The excess As increases linearly with decreasing substrate growth temperature. The lattice constant of the buffer layer is larger than that of bulk GaAs. It is directly proportional to the excess arsenic in the layer.[9]

* Electron paramagnetic resonance (EPR) measurements showed that these layers have about 5×10^{18} cm^{-3} As antisite defects. Particle induced X ray emission (PIXE) and ion channelling experiments using 0.5 MeV H^+ reveal that $\approx 4 \times 10^{20}$ excess As atoms/cm^3 are present in these layers. They are located in an interstitial position, close to the substitutional As atoms.[10]

* This excess As, responsible for the increase in lattice parameter, is uniformly dispersed in the layer, since TEM does not show defects, even in high resolution mode.[10]

* There are conflicting reports in the literature regarding the conductivity of these layers. They were found to exhibit large conductivities (10Ωcm) due to hopping between the

large number of defect sites (estimated to be $\approx$ 2 x 10^{19} cm^{-3}) by Puechner[11] and Gupta.[12] Layers with an estimated antisite density of $\approx$ 5 x 10^{18} cm^{-3}, on the other hand, were found to be 'highly resistive'.[10] Therefore, it can be suggested that the density of antisite defects controls the resistivity of the "as-grown" layers. It was also found in this work that the resistivity is not uniform across the wafer. Results will be presented later.

* 4K photoluminescence of the LTBLs show no excitons or acceptor-band carbon transitions. They are almost inactive optically and As_2 and As_4 LTBLs have nearly identical optical characteristics.

Annealed samples.

Upon annealing, either *in situ,* or in an RTA (Rapid Thermal Annealer), structural, electrical and optical properties change.

* The first and most relevant property of the annealed LTBL (for this project) is that it has extremely short carrier lifetime, reaching the subpicosecond range.[12,13] Photoconductive switches made on this material have produced electrical pulses of about 0.6 ps. The FWHM bandwidth of such pulses is above 500 GHz. Thus, this material seems ideally suited for high speed optoelectronic applications.

* Another change produced by annealing is that the strain in the layer is eliminated and the material becomes lattice matched and semi-insulating, with a resistivity of about 10^8 Ωcm.[11]

* No EPR signal can be detected in the LTBLs annealed at 600°C for 1 hour. This means a reduction in the antisite defects by a factor of at least 5. The limit of detection of As antisite defects in thin epitaxial layers is $\approx$ 10^{18} cm^{-3}. So, any defects below this concentration would remain undetected.[14]

* TEM examination of the samples reveals the formation of As precipitates throughout the LTBL.[15] The precipitates have a diameter between 2 and 10 nm with a density of the order of 10^{17} - 10^{18} cm^{-3}. The average precipitate diameter is directly proportional to the annealing temperature. The precipitate density decreases with annealing temperature and annealing time, suggesting that some precipitates grow at the expense of others which disappear. The precipitate density is in general a strong function of growth temperature, annealing time and annealing temperature.[11]

* HEMT (High Electron Mobility Transistor) layers grown on top of a LTBL showed an electron mobility of 2 x 10^6 $cm^2/V.s$ at an electron density of 5 x 10^{11} cm^{-2}. This is comparable to the highest mobilities ever reported at these carrier densities. So, the LTBL has no deleterious electrical effects on active layers grown on it.[16]

The model which explains all the experimental data presently available was proposed by Warren[17] et. al. in 1990. In this model, metallic As clusters are surrounded by spherical depletion regions analogous to the depletion regions at metal/semiconductor interfaces, with barrier height of $\Phi_{bn} = 0.8$ eV and $\Phi_{bp} = 0.6$ eV for n and p-type material respectively.

When the depletion regions are isolated, i.e., for low cluster density or high doping, the LTBL will be partially compensated but still conducting. Conversely, for high precipitate density or low doping, the material will be totally depleted and semi-insulating. The band diagrams for these two situations are shown schematically in fig. (7. 1), after ref. 17.

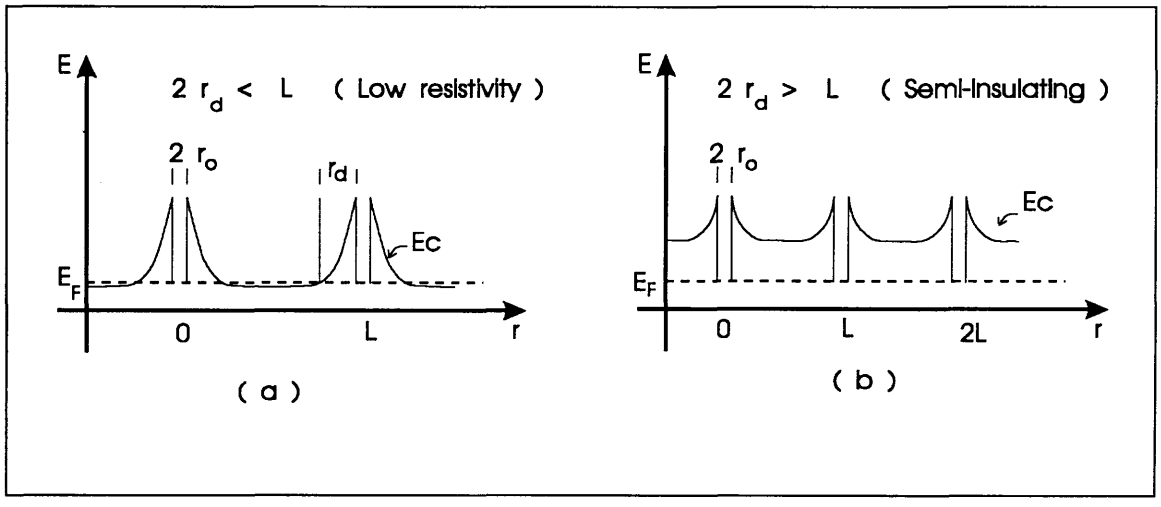

Fig.(7. 1) - Band bending in n-type semiconductor with isolated buried Schottky barrier clusters. L is the average distance between two clusters, r_0 is the cluster radius and r_d is the radius of the depletion region. In (a), $2\ r_d < L$ and the material is partially compensated but still conducts. In (b) the depletion regions overlap, rendering the material semi-insulating.

The depletion radius r_d, cluster radius r_0, barrier height Φ_b and doping N_d are related by:[17]

$$\Phi_b = q\frac{N_d}{6\varepsilon}\cdot\left[\frac{2r_d^3}{r_0} + r_0^2 - 3r_d^2\right] \qquad (7.01)$$

Hence, for a cluster radius of 3 nm, barrier height of 0.8eV and doping level of 10^{18} cm^{-3}, the depletion radius is $\approx$ 19 nm. In this case, the depletion spheres will start overlapping at precipitate densities of 3×10^{16} cm^{-3}.

Therefore, according to this model, there should be a clear relationship between doping, precipitate density and resistivity. Some interesting results obtained recently seem to confirm this.[18] LTBLs doped at 10^{18} and 5 x 10^{18} cm^{-3} (n-type) were grown without annealing, following a procedure similar to that outlined before. The "as-grown" material is totally compensated for both dopings. Rapid thermal annealing at 700, 800 and 900°C activates these doped layers. The density of carriers activated is directly proportional to the annealing temperature. At 900°C, half of the carriers in the LTBL doped with 10^{18} cm^{-3} is activated and the mobility is 1950 $cm^2/V.S$. Such a high mobility shows that the GaAs matrix is of very high quality. The As precipitates grow in size and decrease in density during the annealing. Therefore, isolated depletion regions result, "activating" these doped samples.

Another interesting characteristic of the As distribution in LTBLs is the preferential formation of precipitates in GaAs regions compared to AlGaAs layers. This phenomenon has been used to produce a thin layer of precipitates in 10 nm GaAs quantum wells sandwiched between 100nm AlGaAs layers.[19]

7.4) - LTBL growth and characterization

Four LTBLs were grown in this project. A summary of the layers features is presented below, in table (7.1):

Table (7.1) - LTBLs grown for this project, with different annealing cycles.

Wafer	Layer Thick	Growth Temp	BEP	As Source	Annealing cycle	
	(μm)	(°C)			Temp. (°C)	Time
B108	1	250	10	As_2	600	20 min.
B111	2	230	8	As_2	no	anneal
A484	2	250	24	As_2	600	1 hour
A524	2	250	17	As_4	no	anneal

The first two layers, B108 and B111, were grown on top of a 0.2 μm GaAs buffer. A484 and A524 were grown following the procedure described before. A cross-section diagram of A484 is shown in fig.(7.2).

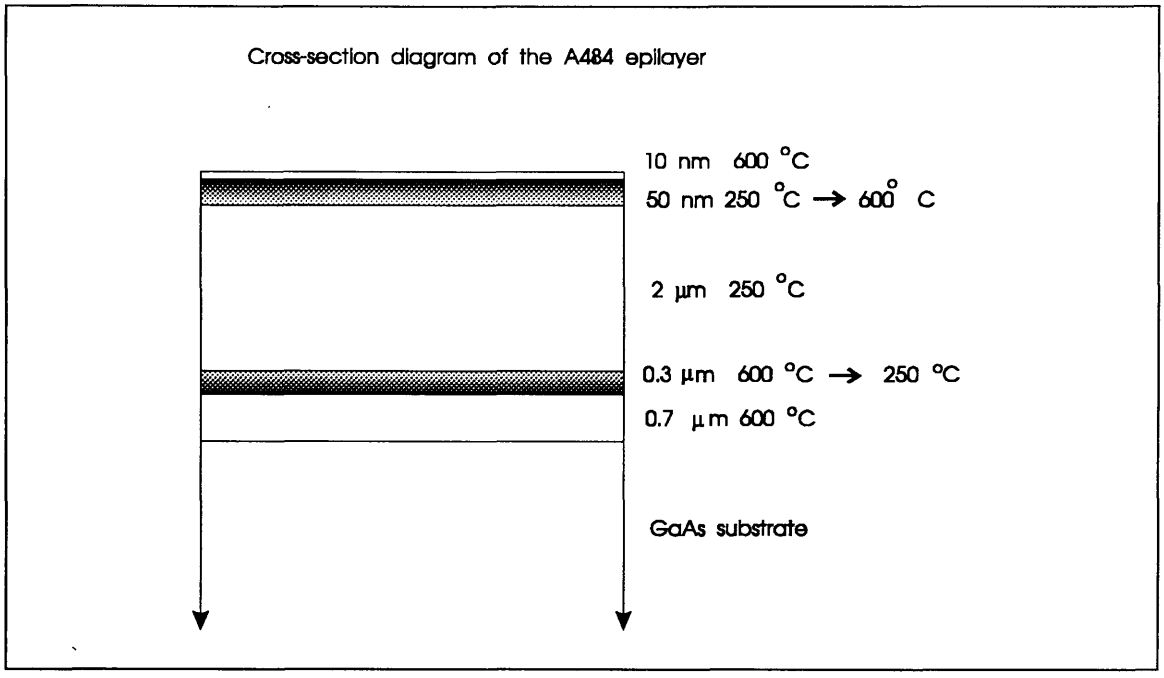

Fig.(7.2) - Cross-section diagram of the A484 epilayer. The temperature is changed continuously over the transition layers above and below the LTBL.

X ray rocking curves were taken from all layers. The annealed layers B108 and A484 show a single narrow X ray diffraction peak as in fig. (7.3). This shows that the MBE layers are single crystals and lattice matched to the substrate.

An X ray rocking curve of the non-annealed layer B111 shows two peaks almost at the limit of resolution of the diffractometer. The two peaks are an indication that the epilayer is not lattice matched to the substrate. This is interpreted as incorporation of As in the LTBL, which expands its lattice.

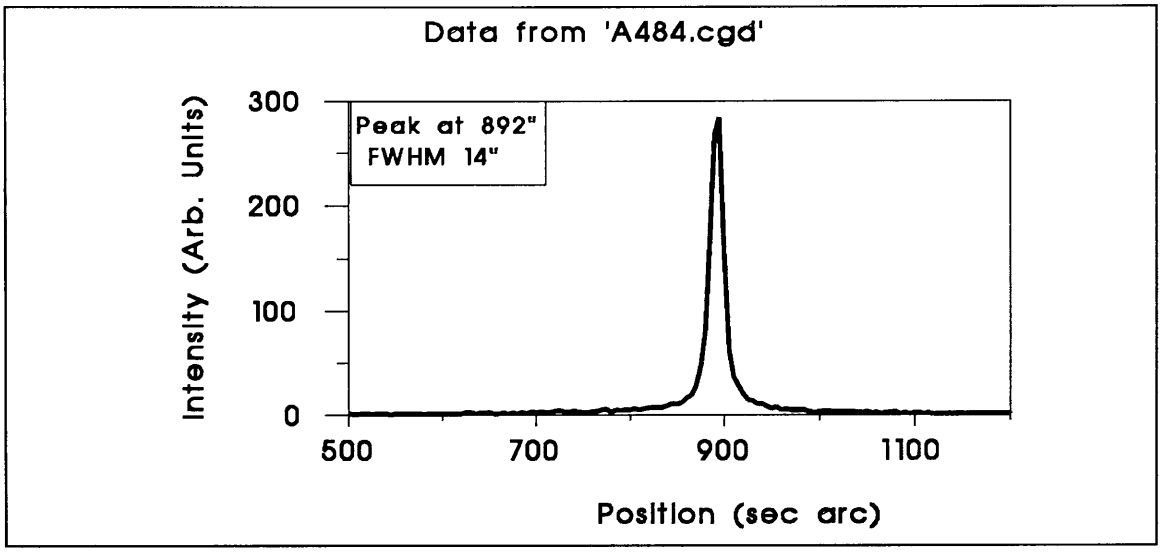

Fig.(7. 3) - X ray diffraction peak for the sample A484, showing that the epilayer is a single crystal, lattice matched to the substrate.

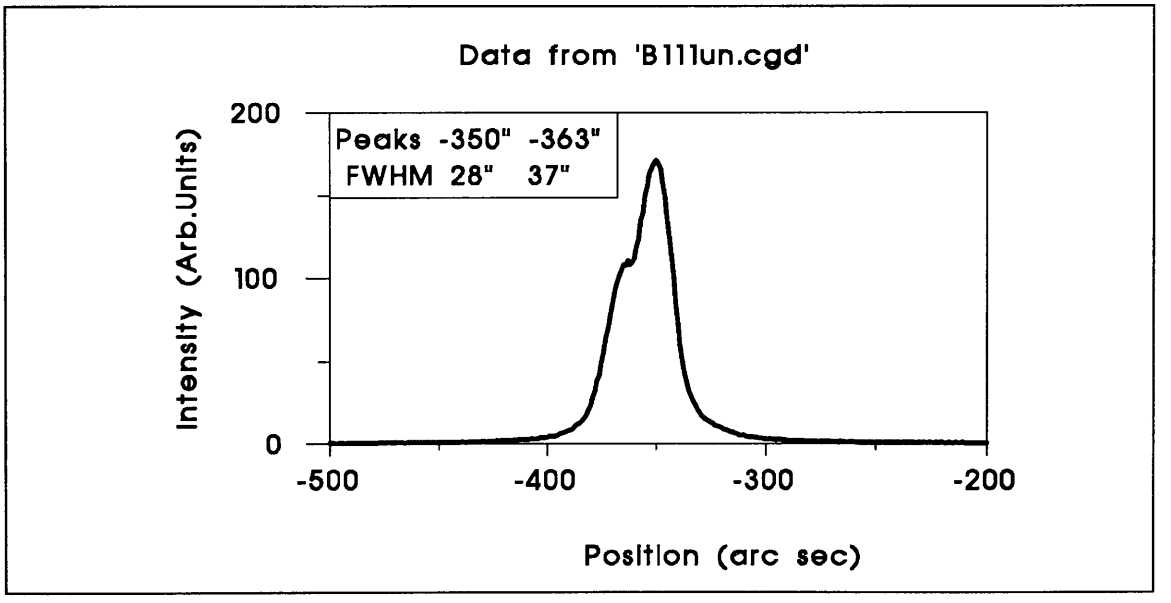

Fig.(7.4) - The X ray diffraction of the B111 wafer. The first peak at -350" is generated by X ray diffraction by the lattice planes in the substrate, whereas the second peak, at -363" is due to the 2 μm epilayer. The existence of the two peaks shows that the epilayer is not lattice matched to the substrate.

The lattice constant and the amount of expansion can be obtained from fig.(7.4), using Bragg's law:

$$2\,a\sin\theta = n\lambda \qquad (7.02)$$

In all X ray measurements, the parameters for the diffraction are:

$\lambda = 1.54$ Å

$\theta = 33.04^{o}$

$n = 4$

The lattice parameter obtained from (7.02) is then 5.649 Å. The deviation from the actual GaAs lattice constant of 5.653Å comes from innacuracies in the measurement of the diffraction angle.

The lattice expansion can be calculated by taking a derivative of (7.02):

$$\Delta a = -\frac{n\lambda}{2\sin\theta\tan\theta}\cdot\Delta\theta \qquad (7.03)$$

The two peaks in fig.(7.4) are separated by $\Delta\theta = -13" = -0.0036^{o} = -6.28 \times 10^{-5}$ rd. Using the value for $\Delta\theta$ in radians in (7.03), together with the other parameters, the lattice expansion is found to be $\Delta a = 5.5 \times 10^{-4}$ Å. The epilayer lattice dilation $\Delta a/a$ is then only 0.0097%.

The other non-annealed wafer (A524) has a much larger lattice mismatch between the epilayer and substrate. This is shown by its X ray rocking curve plotted in fig. (7.5).

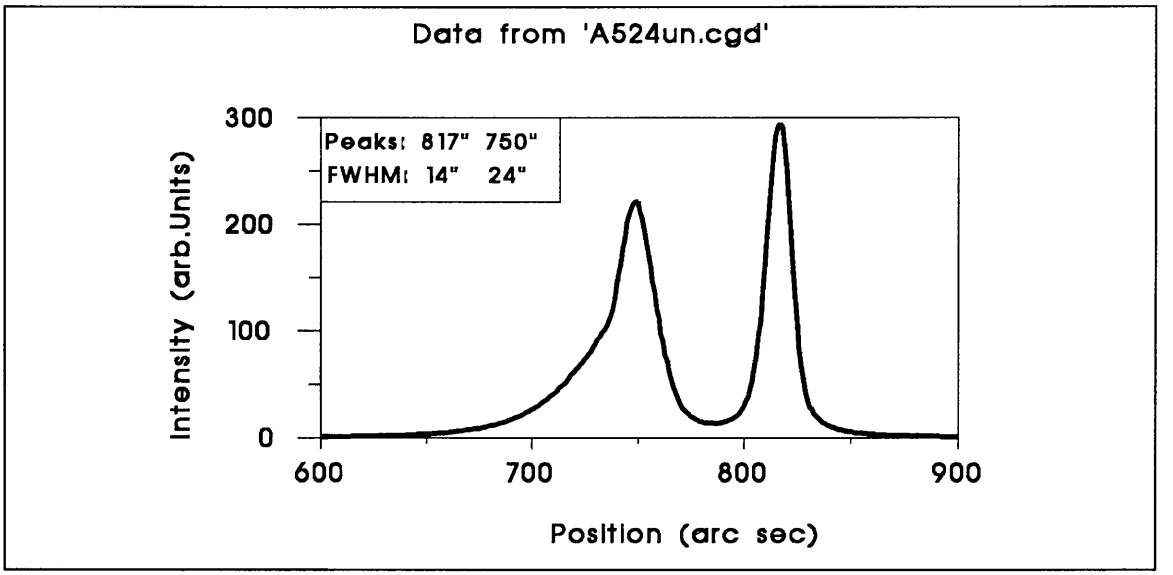

Fig.(7.5) - X ray diffraction of the wafer A524 "as-grown", i.e., prior to annealing. The epilayer has a larger lattice parameter than the substrate, resulting in two diffraction peaks. The lattice expansion in the epilayer can be calculated from the separation between the diffraction peaks.

The two peaks are well resolved and their separation is $\Delta\theta$ = - 67" = -3.25 x 10^{-4} rd. The corresponding lattice expansion is 0.0028 Å, giving $\Delta a/a$ = 0.05%.

A straight line was fitted to the data presented in ref 9, relating the lattice expansion (in percentage points) to the excess arsenic concentration measured by PIXE. The linear dependence obtained is:

$$C(x) = -1.41 + 17.48\ x$$

where C(x) is the excess arsenic (%) incorporated in the lattice and x is the lattice expansion. It is evident that this equation is not valid for very low lattice expansion, as it does not pass through origin. Even for the highest lattice expansion measured in this project, the equation above can not be applied because a negative value for C(x) results. It is interesting to see that the lattice expansion corresponding to 1% excess arsenic is 0.14 %, i.e., about three times larger than the expansion in A524 material.

The sample B111 was annealed in a carbon boat in a furnace with nitrogen atmosphere at 600°C for 10 min. The strain in the epilayer is released as shown the X ray diffraction curve in fig. (7.6), measured after anneal, which has only one peak, 14" wide.

Part of the wafer A524 was cleaved in 9 chips, 5 x 5 mm and annealed in the same furnace. The annealing temperature was 500, 600 and 700°C and the annealing time was 1/2, 1 and 2 hours. These samples were used in the fabrication of

photoconductive switches. Other chips from this wafer were annealed in a Rapid Thermal Annealer. Two chips were annealed at 800°C for 30s and 60s and another one at 900°C for 30s. The X ray curves after annealing have only one peak, 20" wide, very similar to fig. (7.6). Thus, after annealing, the epilayer is lattice matched. At least part of the excess As might have precipitated, if its local concentration in certain areas of the sample reached a critical concentration for the precipitation of the metallic phase.

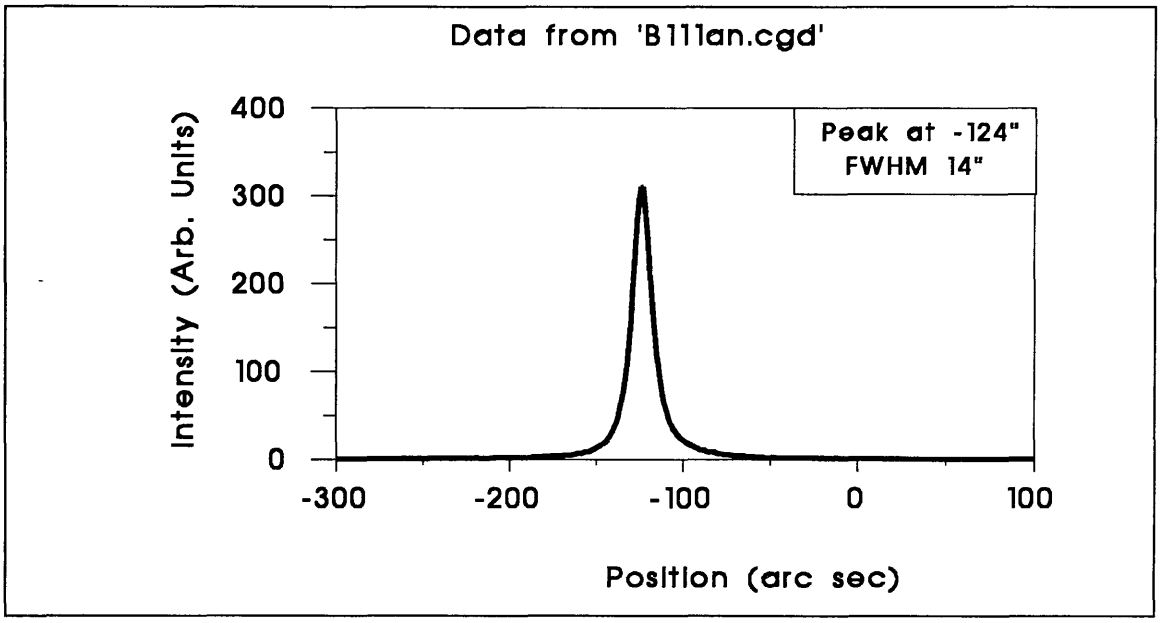

Fig.(7.6) - After annealing the sample B111 at 600 °C for 10 min the strain in the epilayer is released and it becomes lattice matched to the substrate. This is demonstrated by the X ray diffraction measurement above, taken after annealing. Very similar single peaked curves were obtained for the sample A524 after annealing. Compare this curve with the ones in figs.(7.4) and (7.5).

Some of the samples were examined by SEM and TEM. SEM examination reveals a high contrast between the epilayer and the substrate. This is shown by the pictures in figs. (7.7) and (7.8). The reason for this high contrast is not clear. It can be suggested though that the excess As in the epilayers could produce more secondary electrons, making these regions brighter. It is not known if the very small amounts of excess As in the epilayers could produce this effect.

Examination of the epilayer at different points along the wafer shows large variations in the quality and thickness of the layer. This can be seen by comparing figs. (7.7) and (7.8), which were taken from the same sample on A484 material, at two points

a few millimetres apart. This could be caused by temperature non-uniformities on the substrate during growth, but there is no data available to confirm such hypothesis.

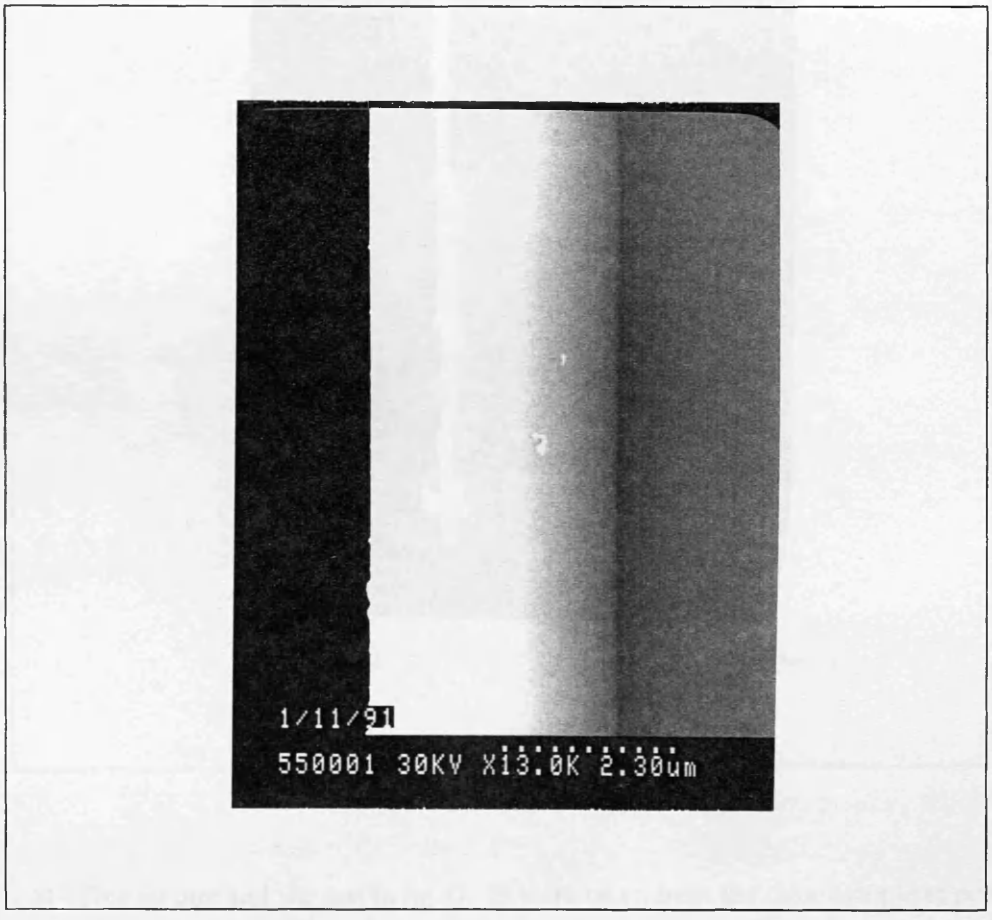

Fig. (7. 7) - SEM picture of the epilayer in A484 material. The high contrast between the epilayer and the substrate could perhaps be caused by excess arsenic.

Only the samples B108 and A484 were examined by TEM and no evidence for the formation of As precipitates was found. Due to the very low density of excess As, few and small precipitates might have formed, which make them extremely difficult to detect. Despite the evidence for excess As in the lattice (double peaked X ray diffraction and high contrast in SEM pictures), its concentration was much lower than the critical concentration of about 1%, for which a high precipitate density has been observed previously. As explained before, the amount of As incorporated is a strong function of growth temperature, increasing with decreasing temperature.

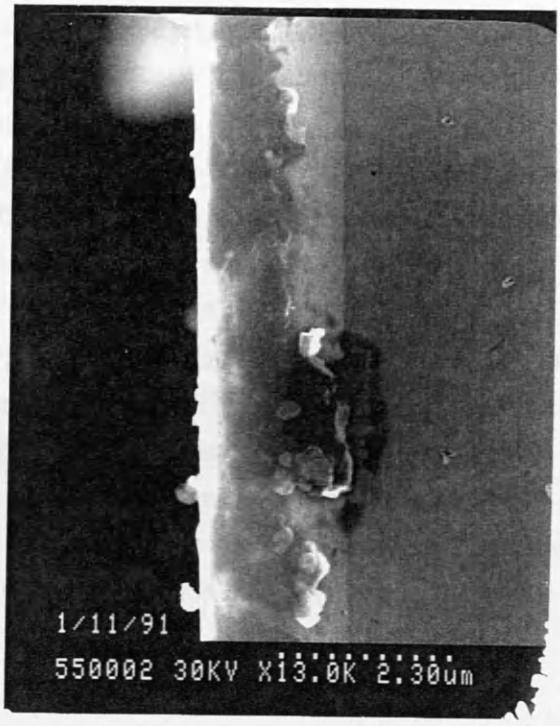

Fig.(7. 8) - This picture and the one in fig. (7. 7) were taken from the same sample at positions a few millimetres apart. There is a large change in the layer quality and thickness in the two pictures.

7.5) - Fabrication of photoconductors and dc measurements.

Photoconductive switches were made on material from all four wafers. The simple test mask for the simplified optoelectronic sampling device shown in fig. (5.12) was used in the lithographic process. The fabrication was done in accordance with the process data sheet given in chapter V.

I-V characteristics of the photoconductors were measured in the dark and under microscope lights illumination. The contacts deviate little from perfect ohmic behaviour. One of such measurements is presented in fig. (7. 9).

The photoconductive region is 14 μm wide and 51 μm long. The resistance of the photoconductors vary with the material in which they are made. B108, A484 and A524 are high resistance materials. The typical resistance of the photoconductors is $\approx$280 MΩ, which gives ρ = 77 MΩ/square. The resistance of B111 material seems to vary across the wafer. Some devices made on this material have very low resistance of only 1 KΩ (ρ = 274 Ω/square). The highest resistance measured on a device made on this material was 17 MΩ, which gives ρ = 4.7 MΩ/square.

7.6) - Sampling Oscilloscope measurements.

The photoconductors were tested using the Ti:Sapphire laser and the sampling oscilloscope with the high frequency CPW probes. The electric pulses switched across a single photoconductor were measured and two of them are shown in figs (7.10) and (7.11).

The devices made on B108, A484 and resistive parts of B111 have a carrier lifetime very similar to SI GaAs. The lifetime is long, being above 150 ps for all devices. The same lifetime was obtained from time resolved photoluminescence experiments at room temperature, done at Heriott Watt University.

In order to compare the lifetime of these materials with a known long lifetime material, some devices were made on a high quality undoped GaAs grown by MBE. The lifetime of this material was measured by time resolved photoluminescence and found to be $\approx$ 2ns. Photoconductors were made on this material and tested in exactly the same conditions as the LTBLs. Fig. (7.12) shows two electric pulses switched across the photoconductors. It shows very long electric pulses, with a FWHM of $\approx$ 2 ns and a very long tail. In fact, the carrier density in the switch does not decay to intrinsic concentration in the time interval between two laser pulses. For this reason, the tail of the electric pulse does not decay to background value. The measurements in this material confirm the accuracy of the sampling oscilloscope lifetime measurements.

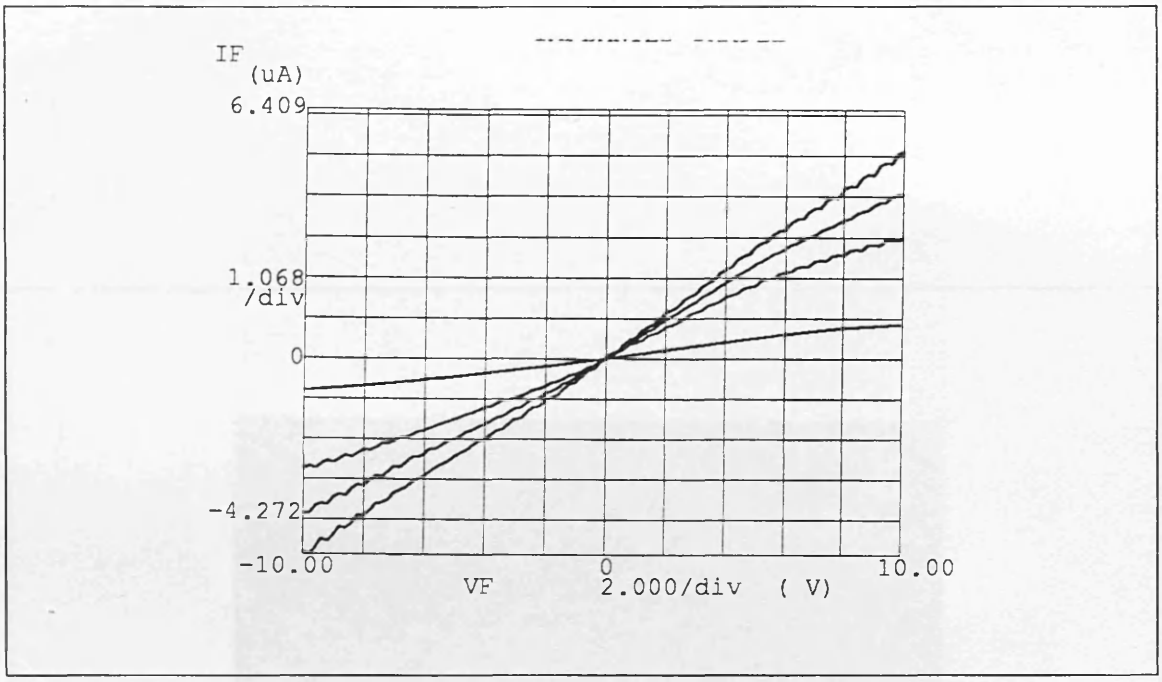

Fig.(7. 9) - I-V characteristics of photoconductors in the dark (line with the smallest slope) and under various levels of microscope lights illumination.

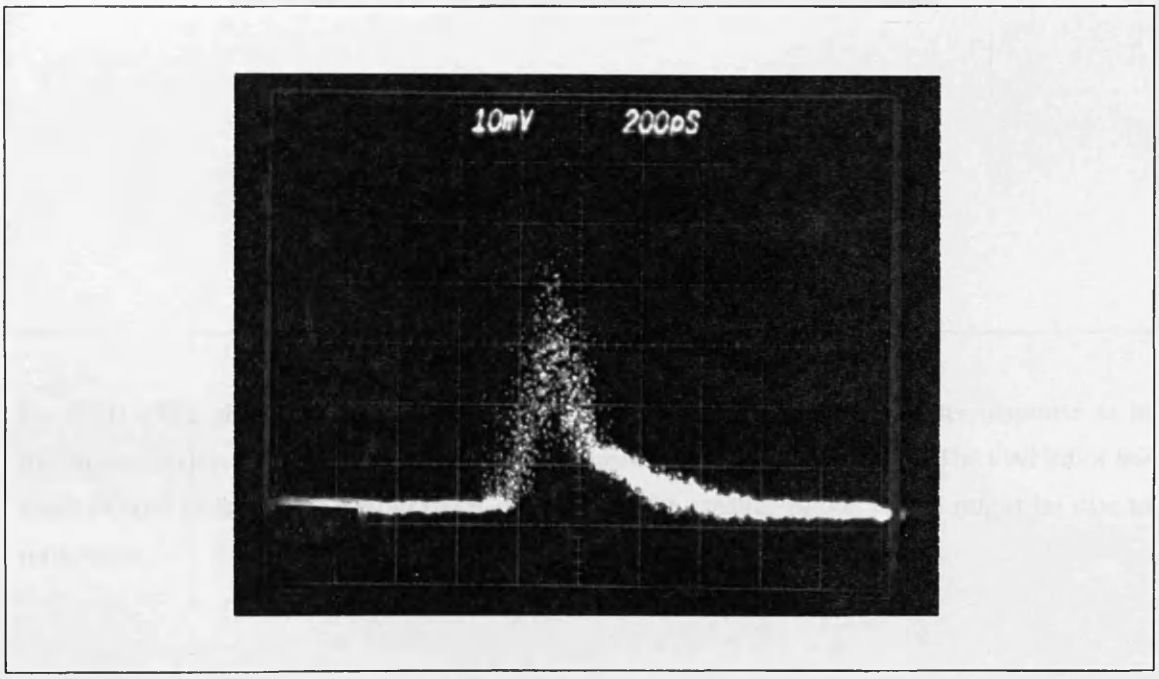

Fig.(7.10) - Electric pulse switched across a single photoconductor on A484 material. The FWHM is $\approx$ 200 ps.

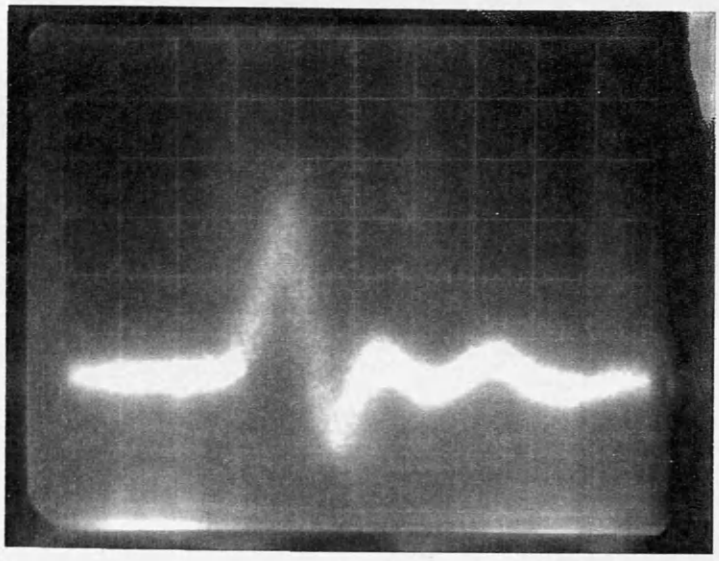

Horizontal: 50ps/division
Vertical: 2mV/division

Fig.(7.11) - The photoconductors made on A524 material seem to show a faster response as in the picture above. This particular sample was annealed at 700°C for 1 hour. The FWHM of the main electric pulse above is $\approx$ 70 ps, if one ignores the smaller peaks, which might be due to reflections.

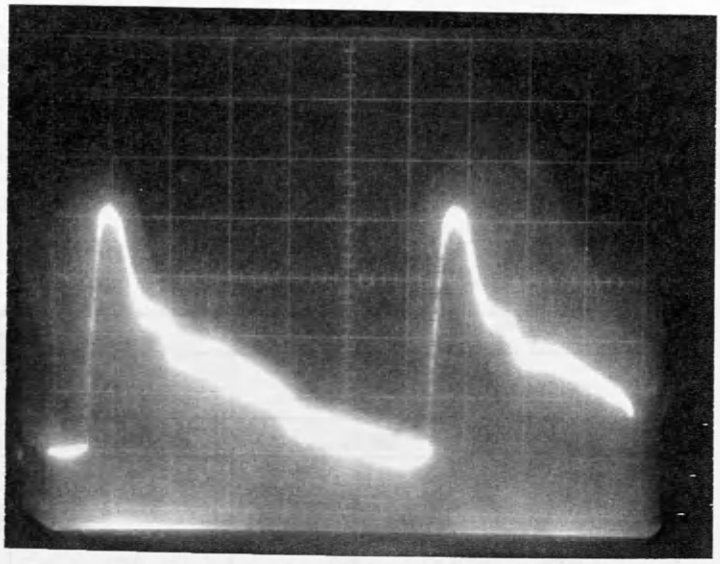

Horizontal: 2ns/division
Vertical: 20mV/division

Fig.(7.12) - Electric pulses switched by a photoconductor made on high purity MBE GaAs. The long lifetime measured by time resolved PL is confirmed by the set-up used in this work.

The devices made on A524 material show some improvement in shortening the lifetime. The table below gives the lifetimes for all A524 samples annealed in the conventional furnace. It is seen that longer annealing time and/or higher temperature tends to produce shorter carrier lifetime. This is in perfect agreement with the model of buried Schottky barriers around the As precipitates. A524 was the only wafer grown using the As_4 as the As source. However, it is unlikely that this is the cause of the shorter lifetime in this material. In fact, As_2 is known to produce larger As incorporation in

epilayers than As_4. Again, both arsenic sources have been used before, in the growth of LTBLs.

Table (7.2) - FWHM in picoseconds of the electric pulses switched across photoconductors fabricated on A524 material annealed at different temperatures and time. These results suggest that long annealing times and/or high annealing temperatures produce short carrier lifetime. The samples annealed at 500°C and at 600°C for 2 hours were destroyed during device fabrication.

Annealing Time	Annealing Temperature (°C)		
	500	600	700
	Measured Lifetime in ps		
1/2 hour	100	80	100
1 hour	120	80	70
2 hours	–	–	70

After the completion of the experimental work in this project, some new results were published[12] relating short carrier lifetime with the growth temperature. These results are reproduced in the plot of fig. (7.13), from ref 12 . According to these results, if the growth temperature is above 200 °C, the carrier lifetime obtained decreases very slowly with decreasing temperature, as found in this work.

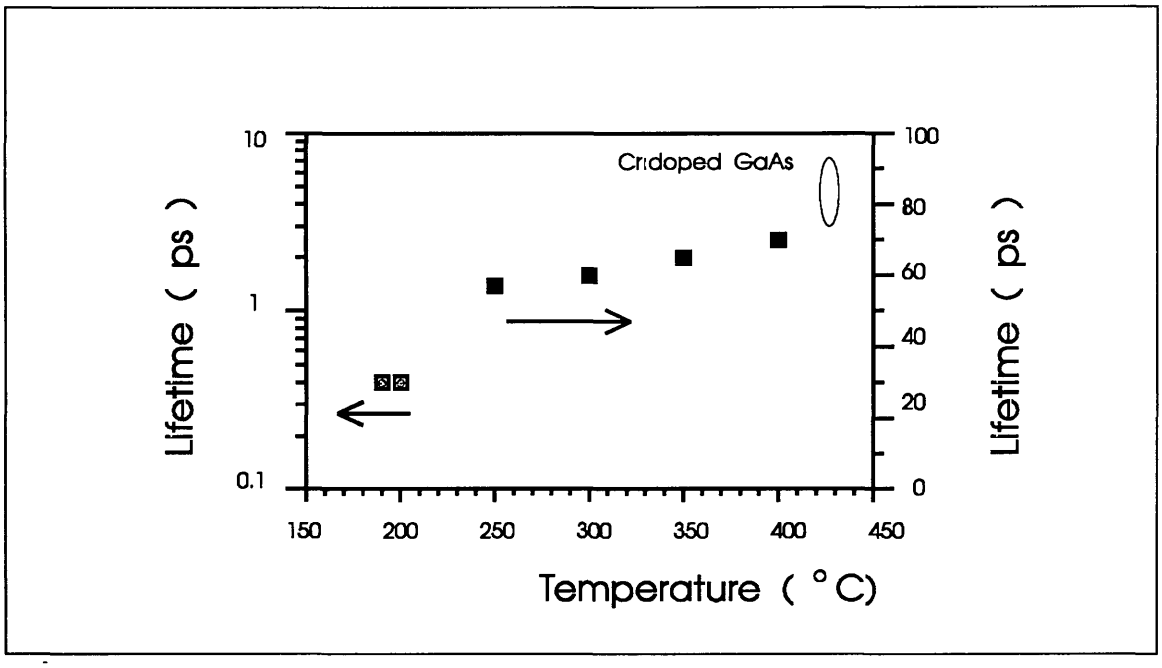

Fig.(7.13) - From ref. 12. Carrier lifetime as a function of growth temperature for a number of unannealed LT-GaAs layers and Cr-doped semi-insulating substrates. Note the different time scales used in the figure.

For a growth temperature around 200 °C the carrier lifetime changes *abruptly* from ≈ 60 ps to 0.4 ps. Such a large reduction in lifetime can be easily explained by the excess As reaching the critical concentration where precipitation takes place. Problems of time and equipment prevented us from proceeding this work by growing epilayers at these very low temperatures and testing for short lifetime.

7.7) - Photoluminescence Measurements

The low temperature buffer layers were compared in their luminescence efficiency with bulk SI GaAs and proton implanted GaAs. Photoluminescence measurements were performed at room temperature and also at 4 K.

Firstly, the proton implanted and SI GaAs were measured at room temperature. The Ti:Sapphire laser, tuned at λ = 745 nm was used to excite the samples.

The average laser power was about 50 mW. The SI GaAs sample shows the characteristic peak at ≈ 870 nm (1.43 eV) due to band-to-band recombination. This is shown in fig. (7.14).

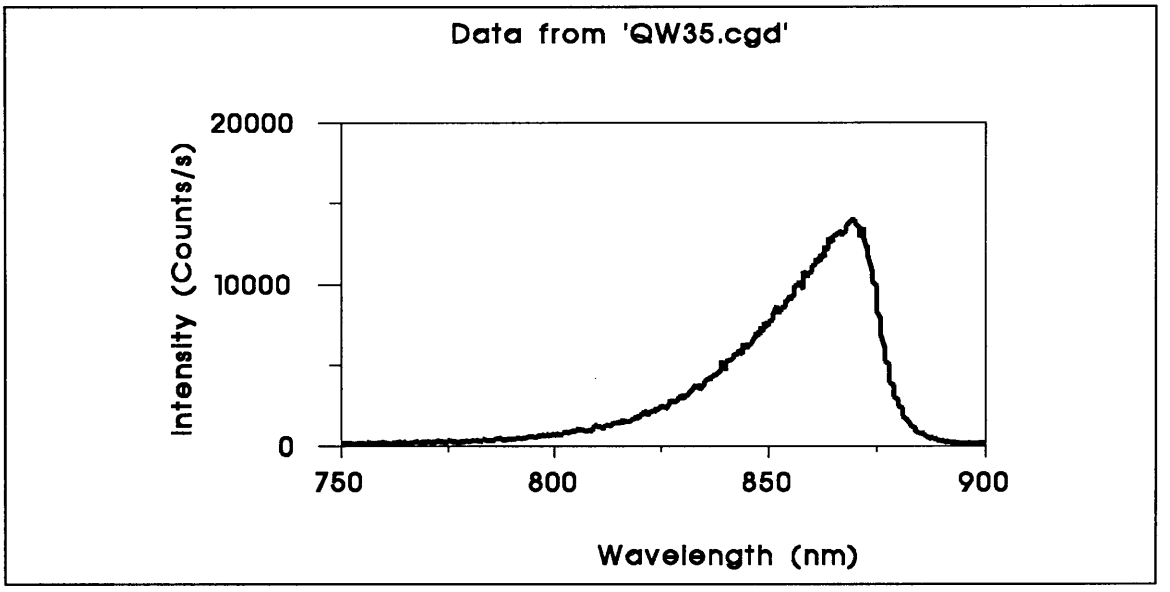

Fig.(7.14) - Photoluminescence (PL) spectrum of bulk SI GaAs at room temperature. The excitation wavelength is $\lambda = 745$ nm.

The proton implantation had the effect of creating new radiative recombination processes. The peak at 1.43 eV obtained from bulk SI GaAs is very much reduced, being just above the background noise. New peaks appear at energies 1.60 eV and 1.53 eV. Fig. (7.15) shows the result of one such measurement. Samples implanted at 2 and 4 x 10^{14} protons/cm^2 were measured and produced virtually identical results. It is difficult to interpret the origin of the new peaks without a more thorough study of luminescence and Raman scattering of these samples. It is interesting to note however that the peak at 1.60 eV is 60 meV below the energy of the pump laser. This is roughly twice the energy of an LO phonon. Thus, one possible cause for the new peaks is a multi-phonon scattering process. The two peaks at energies 1.60eV and 1.53 eV can be viewed as an indication of two metastable states at energies 160meV and 90meV above the bottom of the conduction band. The photoluminescence data seems to suggest that electrons in these levels suffer a transition to the valence band without a cooling step, which would reduce their energy to the energy of the bandgap.

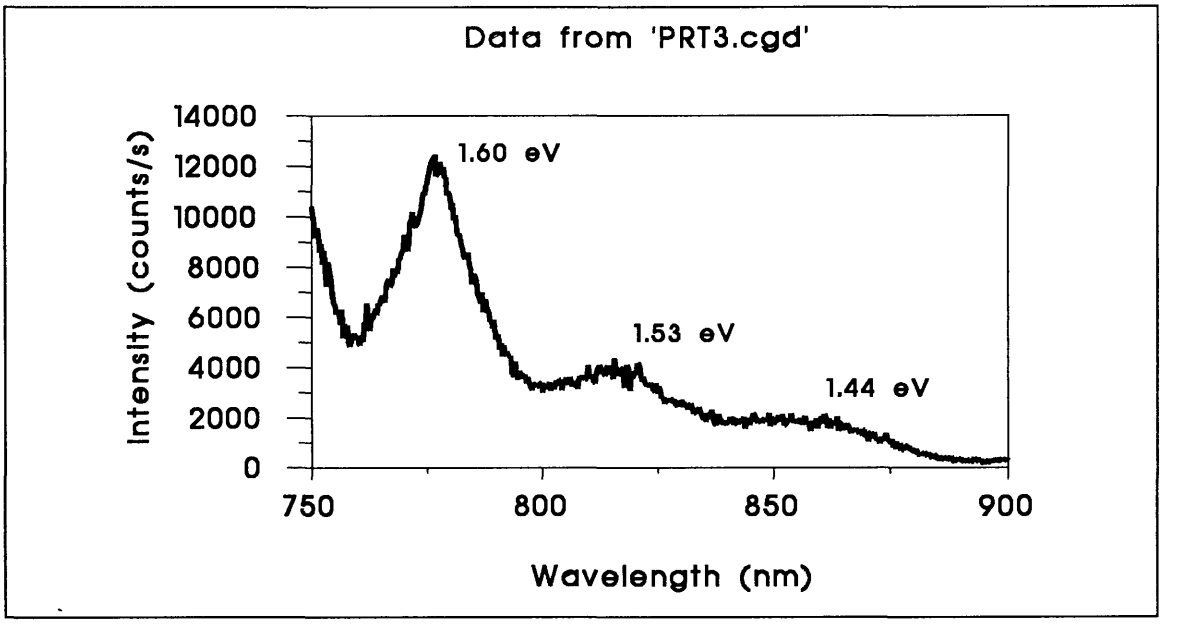

Fig.(7.15) - PL spectrum, at room temperature, of the proton implanted sample. Implant dose is: 2×10^{14} protons/cm^2.

The low temperature buffer layer was measured at room temperature and at 4K. At room temperature, the luminescence efficiency of the LTBL is very poor. The LTBL A484 was measured minutes after the SI GaAs sample, with the photoluminescence apparatus in exactly the same conditions to allow comparisons of luminescence efficiency to be drawn. The PL spectrum obtained is shown in fig. (7.16).

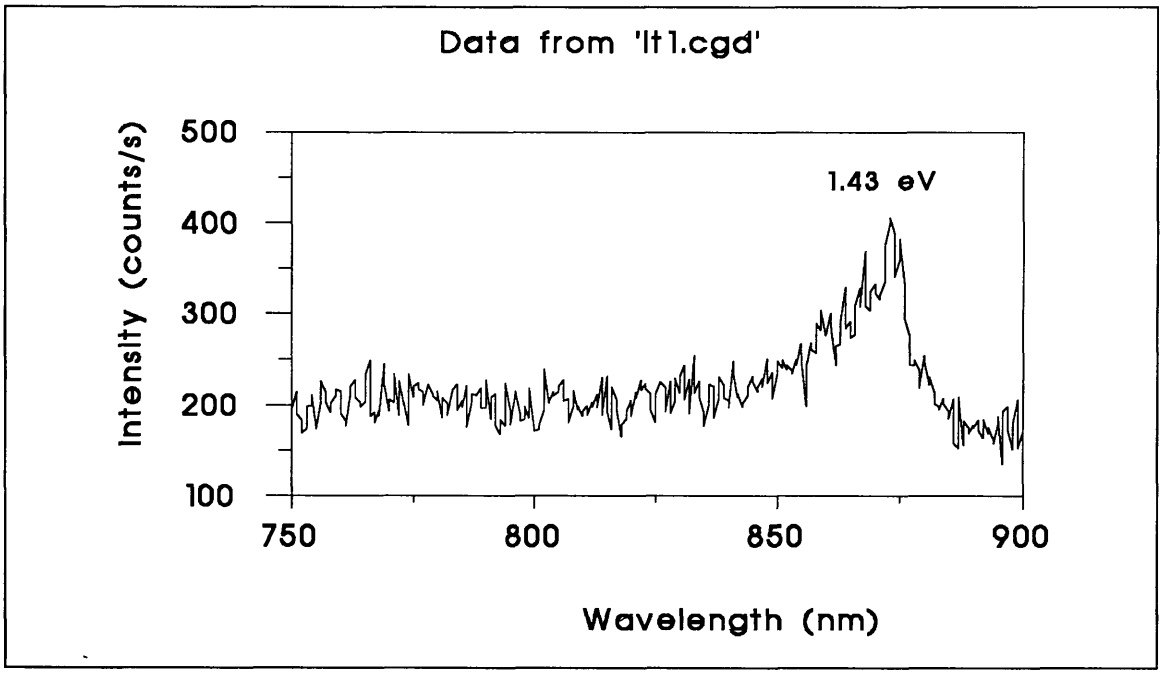

Fig.(7.16) - The photoluminescence spectrum of the A484 LTBL, measured at room temperature, under the same experimental conditions in which fig.(7.14) was obtained.

As the intensity axes in figs. (7.14) and (7.16) are in the same scale, they can be compared. At the peak wavelength λ = 870 nm, the LTBL produces less than 500 counts/s, whereas the high purity GaAs produces about 20000 counts/s. Thus, the luminescence efficiency of the LTBL is less than 2.5% of the SI GaAs efficiency at room temperature.

Some measurements at 4 K were also performed. The band-to-band recombination in the GaAs sample sharpens to a narrow peak. The LTBL does not produce any luminescence from 750 to 900 nm at 4K. The excitation intensity was increased from 50 mW up to about 1W and still no signal was detected. This suggests that the carriers generated by the laser light recombine through non-radiative transitions.

A Ge detector, cooled at 77K, was used to record the PL spectrum at 4K, of the LTBL A484 from 800 to 1600 nm. The excitation intensity used was 1W as lower excitation did not produce any detectable signal. This very high excitation produced a very broad peak centred at 1.04 μm, or 1.19 eV, as shown in fig.(7.17). This peak seems to be connected to deep donor levels, 0.24 eV below the conduction band.

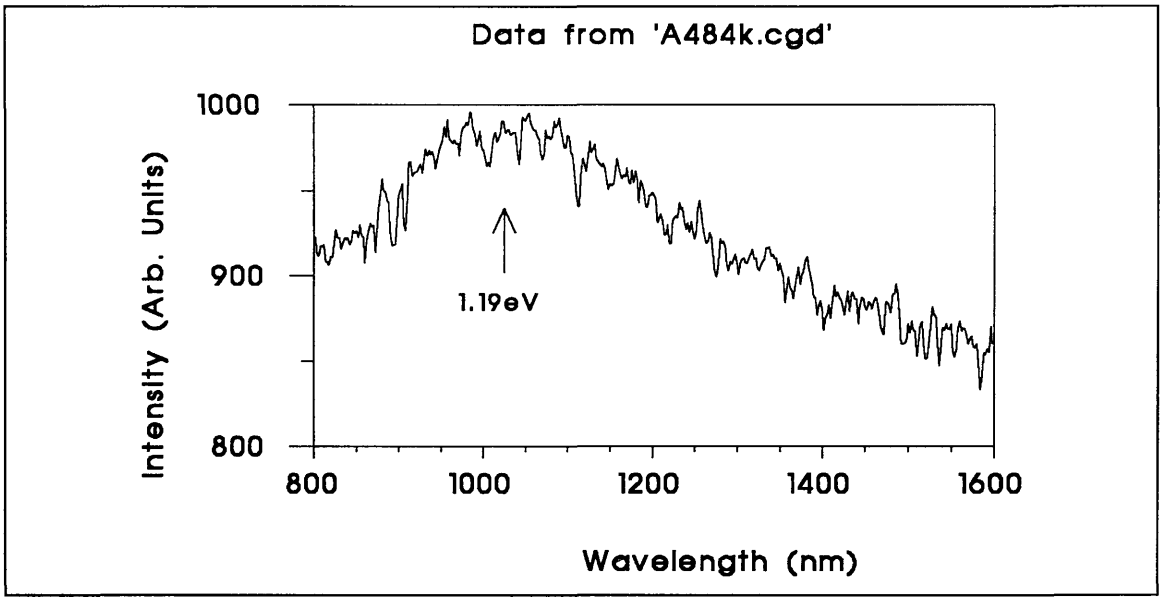

Fig.(7.17) - PL spectrum of A484 at 4K. For wavelengths below 800 nm, the PL intensity goes down to the noise level.

In conclusion, the comparisons between GaAs and the LTBL show that the later has a very poor luminescence efficiency. For typical excitation intensities, the buffer layer is optically inactive. This is to be expected from a material whose carriers recombine through non-radiative transitions.

7.8) - References to chapter VII

[1] - H. Goronkin, M. S. Birrittella, W. C. Seelbach and R. L. Vaitkus, "Backgating and light sensitivity in ion implanted GaAs integrated circuits", IEEE Transactions on Electron Devices, Vol. ED-29, 845-850, 1982.

[2] - T. H. Miers, W. M. Paulson and M. S. Birrittella, "The influence of material parameters on backgating in GaAs integrated circuits", Institute of Physics Conference Series, No. 65, 339-346, 1982.

[3] - C. Kocot and C. A. Stolte, "Backgating in GaAs Mesfets", IEEE Transactions on Electron Devices, Vol. ED-29, 1059-1064, 1982.

[4] - C. P. Lee, S. J. Lee and B. M. Welch, "Carrier injection and backgating effects in GaAs Mesfets", IEEE Electron Device Letters, EDL3, 97-98, 1982.

[5] - W. J. Schaff, L. F. Eastman, B. Van Rees and B. Liles, "Superlattice buffers for GaAs power Mesfets grown by Molecular Beam Epitaxy", Journal of Vacuum Science and Technology B, Vol. 2, 265-268, 1984.

[6] - F. W. Smith, A. R. Calawa, C. L. Chen, M. J. Manfra and L. J. Mahoney, "New MBE buffer used to elliminate backgating in GaAs Mesfets", IEEE Electron Devices Letters, Vol. 9, No.2, 77-80, 1988.

[7] - M. R. Melloch, K. Mahalingam, N. Otsuka, J. M. Woodall and A. C. Warren, "GaAs buffer layers grown at low substrate temperatures using As_2 and the formation of arsenic precipitates", Journal of Crystal Growth, 111, 39-42, 1991.

[8] - Coling Stanley - private communication.

[9] -Z. Liliental-Weber, W. Swider, K. M. Yu and J. Kortright, "Breakdown in crystallinity in Low-Temperature-grown GaAs layers", Applied Physics Letters, 58 (19), 2153-2155, 1991.

[10] - Kin Man Yu and Z. Liliental Weber, "Lattice site locations of excess arsenic atoms in gallium arsenide grown by low-temperature molecular beam epitaxy", Applied Physics Letters, 59 (25), 3267-3269, 1991.

[11] - R. A. Puechner, D. A. Johnson, K. T. Shiralagi, D. S. Gerber, R. Droopad and G. N. Maracas, "Electrical and optical characterization of gas source and solid source MBE low temperature buffers", Journal of Crystal growth, 111, 43-49, 1991.

[12] - S. Gupta, M. Y. Frankel, J. A. Valdmanis, J. F. Whitaker and G. A. Mourou, "Subpicosecond carrier lifetime in GaAs grown by MBE at low temperatures", Applied Physics Letters, 59 (25), 3276-3278, 1991.

[13] - F. W. Smith, H.Q. Le, V. Diadiuk, M. A. Hollis and A. R. Calawa, "Picosecond GaAs-based photoconductive optoelectronic detectors", Applied Physics Letters, 54 (10), 890-892, 1989.

[14] - M. Kaminska, Z. Liliental-Weber, E. R. Weber and T. George, "Structural properties of As-rich GaAs grown by Molecular Beam Epitaxy at low temperatures", Applied Physics Letters, 54 (19), 1881-1883, 1989.

[15] - M. R. Melloch, N. Otsuka, J. M. Woodal, A. C. Warren and J. L. Freeouf, "Formation of Arsenic precipitated in GaAs buffer layers grown by molecular beam epitaxy at low substrate temperatures", Applied Physics Letters, 57 (15), 1531-1533, 1990.

[16] - M. R. Melloch, D. C. Miller and B. Das, "Effect of a GaAs buffer layer grown at low substrate temperatures on a high-electron-mobility modulation-doped two-dimensional electron gas", Applied Physics Letters, 54 (10), 943-945, 1989.

[17] - A. C. Warren, J. M. Woodall, J. L. Freeouf, D. Grischkowsky, D. T. McInturff, M. R. Melloch and N. Otsuka, "Arsenic precipitates and the semi-insulating properties of GaAs buffer layers grown by low-temperature MBE", Applied Physics Letters, 57 (13), 1331-1333, 1990.

[18] - A. C. Warren, J. M. Woodall, J. H. Burroughes, P. D. Kerchner, H. K. Heinrich, G. Arjavalingam, N. Katzenellenbogen, D. Grischkowsky, R. R. Melloch, N. Otsuka, K. Mahalingam, F. H. Pollak and X. Yin, "The electrical and optical properties of GaAs with As precipitates (GaAs:As)", paper presented at the Materials Research Society Fall meeting, 1991.

[19] - M. R. Melloch, N. Otsuka, K. Mahalingam, A. C. Warren, J. M. Woodall and P. D. Kerchner, "Incorporation of excess arsenic in GaAs and AlGaAs epilayers grown at low substrate temperatures by molecular beam expitaxy", presented at the Materials Research Society Fall meeting, 1991.

Chapter VIII - Conclusions

Summary

This work is an investigation on the use of high speed optoelectronic techniques for the characterization of semiconductor devices. A low-frequency electrooptic probe station was demonstrated as well as the optoelectronic sampling scheme. The optoelectronic sampling technique relies on fast photoconductive switches for its operation. The autocorrelation signal detected in optoelectronic sampling was compared with signal detection by conventional techniques employing a sampling oscilloscope and a network analyser.

The optoelectronic techniques described in this work depend critically on short-pulse lasers for the measurement of high speed devices. A fibre-grating pulse compressor was set-up to shorten the 120 ps pulses produced by a mode-locked Nd:YAG laser. Compression by a factor of 40 was demonstrated and nearly transform limited pulses of 3 ps duration were obtained. However, the output of the pulse compressor is very noisy and the output power is not high enough to enable electrooptic sampling experiments, in a jitter-free scheme. The same Nd:YAG laser was frequency doubled and used to synchronously pump a rhodamine 6G dye laser. Autocorrelation measurements obtained with the dye laser are again, very noisy and with poor reproducibility. The noise problems with the pulse compressor and with the dye laser were traced back to the Nd:YAG pump laser. It is concluded that this laser should be avoided as the source of short pulses for the electrooptic and optoelectronic measurement techniques. The use of a feedback loop is likely to reduce the noise in this laser, but drift in the intensity in a long time scale would still be present.

A mode-locked Ti:Sapphire laser was also used for measurements in this project. Autocorrelation measurements taken with this laser are totally reproducible and contain little or no noise.

The devices measured in this project were made by a combination of electron-beam lithography and photolithography. The use of these two lithography techniques together was made possible by the design of a mask set with alignment marks which can be used for registration in a mask aligner and in the electron beam lithography machine.

Discrete devices were made and characterized by electrical techniques. Fabrication procedures were developed for resistors, Metal-Insulator-Metal (MIM) capacitors and for the Optoelectronic Sampling Device (OSD). Discrete Mesfets were fabricated on MBE grown epilayers and their I-V characteristics were measured. A simplified optoelectronic sampling device was designed and made in a single lithographic step. It provides a quick way of producing devices in which autocorrelation measurements can be performed to determine the carrier lifetime in the substrate material.

The optoelectronic sampling devices were made on four different substrate materials. The first one is a high purity, MBE grown GaAs epilayer, with very long lifetime (2ns). The control samples were made on "standard" semi-insulating GaAs, whose carrier lifetime is $\approx$ 200 ps. Proton implantation in some of these devices made on SI GaAs substrate was used as a means of shortening the carrier lifetime, to produce fast turn-off times in the photoconductive switches. The lifetime after implantation of 4 x 10^{14} protons/cm^2 was estimated from an optoelectronic sampling measurement, to be around 40 ps. This is still a very long lifetime for the photoconductive switches. It is thought that self-annealing of the deep electron traps, caused by the lack of temperature control in the implanter, prevented the achievement of short lifetime in the switches.

GaAs epilayers were grown by MBE at a temperature around 250°C, with a high group III to group V beam equivalent pressure. This type of growth conditions can produce an incorporation of up to 1 or 2% excess arsenic in the lattice. Upon annealing, the excess As precipitates into metallic As clusters which act as very fast recombination centres. The material grown in this work was characterized by X ray diffraction and photoluminescence at room temperature and at 4K. The carrier lifetime in photoconductive switches (simplified Optoelectronic Sampling Devices) made on these materials was measured using a sampling oscilloscope and high-frequency probes. The shortest lifetime obtained was roughly 70ps. Based on very recent results published after the completion of this work, it is suggested that the growth temperature of the MBE epilayers should be reduced to 200°C. At temperatures around or below 200°C, the low temperature GaAs epilayers can have a lifetime in the sub-picosecond regime.

Thus, optoelectronic techniques for the characterization of semiconductor devices were demonstrated in this project. Different lasers and substrate materials for device fabrication were investigated. Some more work is still needed to optimize the characteristics of the semiconductor materials used for device fabrication.

The remainder of this chapter summarizes the conclusions to be drawn from materials used in this work, device fabrication and measurements obtained. Also considered are the advantages and disadvantages of the lasers employed in the measurements. Some possible ways of improving the materials and the techniques are also discussed.

8.1) - Device Fabrication

Discrete devices were made before trying the integration into the Optoelectronic Sampling Device (OSD). Fabrication procedures were developed and demonstrated for resistors, capacitors, coplanar waveguides containing photoconductive gap switches and for Mesfets.

NiCr resistors with 50Ω resistance which can be readily integrated were demonstrated. The resistance varied from 47Ω to 52Ω for the 25 devices made in a chip, showing that the resistance variation across a chip can be as low as ± 5%.

MIM (metal-semiconductor-metal) capacitors having a capacitance of 4pF were made using Si_3N_4 as the dielectric material. The parallel resistance of these capacitors is typically 0.5 MΩ, but values as high as 2MΩ were obtained, showing that the capacitors have very low leakage currents. The capacitors were made using the masks designed for the (Optoelectronic Sampling Device) OSD. Thus, their integration is straightforward. Mesfets were made using e-beam lithography and I-V characteristics were obtained.

The Optoelectronic Sampling Device includes 2 resistors, coplanar waveguides, 4 capacitors and 4 photoconductive gap switches made by photolithography. At the centre of the OSD are the registration marks to allow for the alignment of the e-beam levels of the Mesfet or of any other device to be tested by the sampling technique. As the carrier lifetime was not reduced enough to produce an extremely high speed sampling circuit, a complete system of a Mesfet integrated with the measuring OSD was not made.

A simplified OSD which can be made in a single photolithographic level was also designed and fabricated in this project. It provides a quick way of testing the carrier lifetime in photoconductive gap switches.

8.2) - Materials

There are presently two possible ways of producing a semiconductor material with carrier lifetime of a few picoseconds or even in the sub-picosecond range.

The first and more conventional technique employs ion implantation to produce deep electron and hole traps in the substrate material. The effect of the substrate temperature during implant seems to be a critical parameter for short lifetime production. It was found in this work that the implantation, without temperature control, of 180 KeV protons at a dose of 4×10^{14} cm^{-2} produced a reduction in carrier lifetime, by a factor of, at most, 5. Despite this reduction, the lifetime is still about one order of magnitude larger than the desired value. Implantation doses of 1 and 2×10^{14} protons/cm^2 did not produce any observable change in the lifetime, compared with the non-implanted material.

The second way of producing GaAs with very short carrier lifetime is by growing epilayers by MBE at temperatures around 200°C. Growth at these very low temperatures is known to produce the incorporation of up to 1 or 2% excess As in the lattice. Annealing of this material causes the excess As to precipitate, forming metallic As clusters inside the epilayer. The As clusters become capture centres for the electrons in the epilayer. The capture and recombination time can become as short as 0.5 ps.

The four wafers grown in this project produced lifetimes shorter than the control samples, but again, the lifetime is not as short as desired. The reasons for this are related to the growth temperature. It is very likely that the nominal temperatures of about 250°C were too high for the incorporation of large amounts of excess As. A better temperature calibration between pyrometer and thermocouple readings in the MBE machine could help in producing a better extrapolation for the low temperature growth. Following recent results which appeared in the literature, it is suggested that the growth temperature should be reduced to $\approx$ 200°C.

8.3) - Lasers

Normally, state-of-the-art, colliding-pulse mode-locked ring dye lasers producing pulses of less than 100 fs have been used in optoelectronic and electrooptic sampling. The use of simpler laser systems was investigated in this project.

A mode-locked Nd:YAG laser was tried in two different ways. First, a fibre-grating pulse compressor was set-up to compress its 120ps pulses. The laser pulses at the output of the compressor were measured to be 3ps long, giving a compression ratio of 40 and almost transform-limited pulses. The output of the pulse compressor is too noisy and the power is not high enough to use this system in a jitter-free electrooptic sampling scheme.

The same laser, without the pulse compressor, was then frequency doubled and used to synchronously pump a rodhamine 6G dye laser. This dye laser produces visible picosecond pulses. Measurements done with this laser are again very noisy , due to the instabilities in the Nd:YAG pump laser.

Therefore, it was concluded that the mode-locked Nd:YAG laser, without further improvements in its power stability, should be avoided in these optoelectronic sampling measurements.

A mode-locked Ti:Sapphire laser, pumped by an Ar^+ cw laser produces short (<2ps) and stable pulses at a repetition rate of 82MHz. This laser was used in autocorrelation measurements and it was found that the noise problems encountered before were eliminated. The Ti:Sapphire laser was found to be well suited for use in the optoelectronic measurement techniques described in this project. An enhanced version of this laser, producing femtosecond pulses and tuneable from 720nm up to 1060nm will be commercially available soon. With this kind of laser, electrooptic sampling in the manner described in chapter II might come to age.

Mode-locked semiconductor lasers operating at wavelengths between 700 and 800 nm could be another source of laser pulses for these sampling techniques. Recent developments in the fabrication of visible semiconductor lasers and also of mode-locked semiconductor lasers point to the possibility of producing pulses of a few picoseconds or even sub-picosecond pulses with the right wavelength to be used in electrooptic or optoelectronic sampling. Therefore, a small and compact instrument, comprising a picosecond semiconductor laser and a modified Michelson interferometer for delaying one of the laser beams might become feasible in the foreseeable future. Such an instrument would drastically cut the cost and complexity of the optoelectronic sampling technique. Semiconductor lasers might become the best choice for the sampling techniques in the next few years, but they were not explored in this project.

8.4) - Optoelectronic measurements

A low-frequency electrooptic modulator was demonstrated in this project, using a cw infrared laser. Real time recovery of an applied 10KHz signal was found to be very easy. No amplification of the electric signal generated by the intensity modulated laser beam was necessary.

The extension of the electrooptic technique to very high frequencies was made impossible by problems with the production of short and stable infrared and visible laser pulses.

The optoelectronic sampling technique was demonstrated with the measurement of proton implanted and control devices. The mode-locked Ti:Sapphire laser was used in these measurements. Due to the longer than expected lifetime of the proton implanted devices, the autocorrelation peak and a reflection from the open circuit at the end of the line can not be completely resolved. Apart from this, clean and noise-free autocorrelation curves were obtained, demonstrating clearly the validity of this technique.

8.5) - Suggested further work

A thorough investigation of the MBE growth parameters for the Low Temperature Buffer Layers is needed. Growth temperature and beam equivalent pressure are critical parameters for the control of the excess As incorporation in the lattice. The annealing time and annealing temperature on the other hand, control the size and density of As precipitates which are formed from the excess As. More experiments with growth, annealing and characterization of LTBLs is needed, to produce a material with lifetime of the order of a few picoseconds.

As mentioned before, another promising area of research is the use of picosecond semiconductor lasers for electrooptic and optoelectronic sampling. This can lead to the production of a compact optoelectronic sampler with a bandwidth extending up to or above 100 GHz.